Optimized Ensemble Generation for Probabilistic Chemistry Transport Modeling by Coupled Parameter Perturbation

INAUGURAL–DISSERTATION

zur

Erlangung des Doktorgrades

der Mathematisch-Naturwissenschaftlichen Fakultät

der Universität zu Köln

vorgelegt von

Annika Vogel

aus Bergisch Gladbach

Köln, 2020

Gutachter: PD Dr. Hendrik Elbern

Prof. Dr. Yaping Shao

Tag der Abschlussprüfung: 04.02.2020

All models are wrong,
but some are useful.

George Box

Abstract

Progressing developments in atmospheric modeling increase the complexity of modeling systems to improve forecast skills. At the same time, this augmented complexity hampers a reliable and efficient estimation of forecast uncertainties from a limited ensemble of forecasts. Especially chemistry transport models are highly sensitive to uncertainties in model parameters like emissions. Current algorithms for estimating related uncertainties suffer from the high dimensionality of the system. But multiple interactions of chemical compounds also induce multi-variational couplings in model states and uncertainties.

This study introduces an optimized ensemble generation approach in which model parameters are efficiently perturbed according to their coupling. The approach applies the Karhunen-Loève expansion which approximates covariances of the model parameters by a limited set of leading eigenmodes. These modes represent the coupled leading uncertainties from which random perturbations can be sampled efficiently. For correlated model parameters, it is shown that leading uncertainties can be represented by a low number of perturbations driven by a few eigenmodes.

Focusing on model parameters which depend on local atmospheric and terrestrial conditions, state-dependent covariances are approximated from various related sensitivities. As the simulation of all combined sensitivities is computationally demanding, independent input sensitivities are introduced in this study. Assuming tangent linearity, multiple combined sensitivities can be represented by a low number of independent sensitivities. Besides the reduction of computational resources, this setup allows for the integration of different kinds of uncertainties in a convenient way.

The Karhunen-Loève ensemble algorithm is applied to biogenic emissions, dynamical boundary layer parameters and dry deposition in order to account for various uncertainties affecting concentrations of biogenic gases in the atmosphere. A case study in the Po valley in July 2012 indicates exceptionally high sensitivity of biogenic emissions on land surface properties. These sensitivities induce large perturbations of biogenic emissions by the ensemble algorithm. Resulting forecast uncertainties are at least as large as mean concentrations, which is in accordance to high-resolution Zeppelin observations.

Results from the case study demonstrate a sufficient uncertainty estimation for selected model parameters by the Karhunen-Loève ensemble with about 10 members. As total leading uncertainties arise from sensitivities to land surface properties, forecast uncertainties of biogenic trace gases appear to be almost time-invariant. Thus, this study shows that the predictability of biogenic gases is more dependent on regional characteristics than on forecast time.

Kurzzusammenfassung

Fortschreitende Entwicklungen in der atmosphärischen Modellierung erhöhen die Komplexität der Modelle um eine bessere Vorhersagegenauigkeit zu erzielen. Gleichzeitig erschwert diese erhöhte Komplexität eine zuverlässige und effiziente Abschätzung von Vorhersageunsicherheiten mit einer begrenzten Zahl an Ensembleläufen. Besonders atmosphärenchemische Modelle sind sehr empfindlich gegenüber Unsicherheiten in Modellparametern wie Emissionen. Vielfältige Wechselwirkungen chemischer Größen führen aber auch zu internen Kopplungen im Modellzustand sowie deren Unsicherheiten.

In dieser Arbeit wird ein Verfahren zur optimierten Generierung von Ensembleläufen vorgestellt, in der Modellparameter anhand ihrer Kopplungen effizient gestört werden. Das Verfahren nutzt die Karhunen-Loève Entwicklung, mit der Kovarianzen von Modellparametern durch eine begrenzte Anzahl an führenden Eigenmodi genähert werden. Dabei stellen diese Eigenmodi die kombinierten führenden Unsicherheiten dar, von welchen Zufallsstörungen effizient generiert werden können. Es konnte gezeigt werden, dass mit diesem Verfahren die führenden Unsicherheiten von korrelierten Modellparametern durch eine kleine Anzahl von Störungen abgedeckt werden können.

Der Schwerpunkt dieser Arbeit liegt auf Modellparametern, welche von atmosphärischen und terrestrischen Gegebenheiten abhängen. Deswegen werden situationsabhängige Kovarianzen durch verschiedene Sensitivitäten abgeschätzt. Da die Simulation aller kombinierter Sensitivitäten jedoch mit viel Rechenaufwand verbunden ist, werden unabhängige Sensitivitäten eingeführt. Unter der Annahme von tangentialer Linearität kann eine große Zahl von kombinierten Sensitivitäten durch einige wenige unabhängige Sensitivitäten dargestellt werden. Neben der Verringerung des Rechenaufwands ermöglicht dieser Ansatz die Integration verschiedenartiger Unsicherheiten.

Das Karhunen-Loève Ensemble Verfahren wird auf biogene Emissionen, dynamische Grenzschichtparameter und trockene Deposition angewandt um verschiedene Unsicherheitsquellen von biogenen Gasen in der Atmosphäre zu berücksichtigen. Bei einer Fallstudie in der Po-Ebene im Juli 2012 zeigen sich besonders hohe Sensitivitäten von biogenen Emissionen zu Landoberflächen. Diese Sensitivitäten führen zu großen Störungen in biogenen Emissionen durch das Ensembleverfahren. Daraus resultierende Vorhersageunsicherheiten sind mindestens so groß wie mittlere Konzentrationen, was mit hochauflösenden Zeppelin-Beobachtungen übereinstimmt.

Die Ergebnisse der Fallstudie zeigen eine realistische Unsicherheitsabschätzung für die betrachteten Modellparameter durch das Karhunen-Loève Ensemble von etwa 10 Vorhersagen. Da die führenden Unsicherheiten durch Sensitivitäten zu Landoberflächen entstehen, sind Vorhersageunsicherheiten von biogenen Gasen nahezu unveränderlich bezüglich der Vorhersagezeit. Somit zeigt diese Arbeit, dass die Vorhersagbarkeit von biogenen Gasen eher räumlich als zeitlich begrenzt ist.

Contents

1 Introduction

Numerical atmospheric models rely on assumptions about the atmospheric system, which lead to errors in model forecasts. Nevertheless, these models are widely used to provide weather forecasts on an operational basis. Additionally, atmospheric models play an important role in various research fields, such as meteorological hazards, air quality and climate change. Much effort has been made to improve atmospheric forecast models in order to increase the reliability of their forecasts. However, these improvements result in a continuously increasing number of variables and considered processes. Although increasing the models complexity improves forecasts, atmospheric models remain approximations of the high-dimensional dynamical system.

The use of data assimilation techniques aims to reduce some of these uncertainties by pushing relevant quantities towards their observed equivalent. These optimization quantities are assumed to be highly uncertain and have significant impact on the forecast, but can be constrained by available observations. Although the benefit of advanced data assimilation for atmospheric forecasts has been demonstrated for various applications (e.g. Daley [1993]; Kalnay [2003]; Sandu and Chai [2011]; Lahoz and Schneider [2014]), the use of observations and assumptions in the assimilation procedure induce additional sources of uncertainties to the system (e.g. Buizza [2019]).

Generally, every part of the modeling system introduces potential uncertainties to the forecasts. The question is how these uncertainties can be quantified realistically. The specific estimation of forecast uncertainties depends on the actual context. This study introduces an approach for uncertainty estimation of atmospheric forecasts considering three different aspects: Theoretical developments in the context of predictability, technical implementation into chemistry transport models and specific application to biogenic gases. The objectives arising from each of these aspects are consecutively motivated in the following.

From a theoretical point of view, the question of **predictability** estimates forecast uncertainties. Due to the atmosphere's highly nonlinear behavior, forecast uncertainties vary significantly in space and time and differ between variables. In general, atmospheric forecasts are sensitive to uncertainties originating from different types of sources. On the one hand, errors might be introduced by uncertainties in any kind of input – like initial fields and boundary conditions (e.g. Kalnay [2003]; Buizza et al. [2005]). On the other hand, inaccuracies in the formulation of the model itself contribute to forecast uncertainty. These model uncertainties may originate from predefined model parameters, simplified formulations of processes as well as the numerical implementation (e.g. Buizza et al. [1999]; Shutts [2005]).

Different approaches for an analytical formulation of model uncertainties are known in mathematics (see Sec. 2.1). However, the high dimensionality of atmospheric models

makes an analytical formulation of probability densities computationally impracticable (e.g. Ehrendorfer [2006]; Kalnay [2019]). Instead, a set of deterministic forecasts is performed to approximate the probability distribution of the forecast state in numerical weather prediction (NWP). Each member of this *ensemble of forecasts* may be driven by slightly perturbed model inputs or model formulations which represent related uncertatintes.

However, the generation of the ensemble is crucial as it determines the forecast probability distribution. At the same time, the number of *ensemble members* for such high-dimensional systems is limited by computational resources. The major challenge is the generation of ensembles which sufficiently sample the forecast uncertainty with manageable computational effort. Bauer et al. [2015] state that ensemble forecasting is still one of the most challenging research areas in numerical weather prediction. Additionally, a physically based uncertainty estimation may give also insight into model deficiencies (e.g. Xian et al. [2019]). Thus, it can help to further improve the forecast model.

Regarding uncertainties in model parameters, perturbations are usually applied to the whole parameter field or to each location and time separately. However, constant perturbation of the whole parameter field does not allow for any spatial variation. In contrast, independent perturbation of each location and time becomes impractical for high-dimensional systems. Toth and Kalnay [1993] and Palmer [2019] state that sufficient uncertainties in initial conditions cannot be achieved by arbitrary, random perturbations of individual quantities.

Translating this to parameter uncertainties, this study introduces an approach to perturb model parameters in an efficient way. Focusing on leading coupled uncertainty modes of multiple parameters, the developed ensemble algorithm aims to cover the dominating uncertainties even with a small ensemble size.

Regarding atmospheric modeling systems, **chemistry transport models** (CTMs) provide forecasts of atmospheric composition including a large set of trace gases and aerosol compounds. This large number of prognostic variables leads to high dimensionality of the system even compared to NWP (e.g. Zhang et al. [2012a]). Among other implications, this high dimensionality amplifies uncertainties which differ significantly between individual chemical compounds (Emili et al. [2016]). At the same time, multiple interactions by chemical reactions also induce multi-variational correlations of model state and errors.

CTMs are typically driven by NWP forecasts and thus inherit their errors. Besides that, prominent uncertainties of chemical forecasts arise from errors in estimations of emissions, chemical mechanisms and reactions as well as deposition and sedimentation processes. In most cases, the atmospheric composition is mainly determined by balances between emission and deposition processes. Thus, CTMs can be more sensitive to uncertainties in model parameters than initial- and boundary conditions (Elbern et al. [2007]; Bocquet et al. [2015]). However, there are only few attempts for estimating parameter uncertainties within CTMs (see Sec. 2.3). Low level chemical composition is especially sensitive to local transport and mixing within the atmospheric boundary layer. This enhances a general dependency of air quality forecasts on the accuracy of NWP. Zhang et al. [2012b] argue that a (from a meteorological point of view) optimal NWP forecast may

not always result in the best chemical forecasts when applying it to a CTM.

In this study, different sources of parameter uncertainties are combined in order to cover the whole lifecycle of multiple chemical compounds. This is achieved by accounting for chemical parameters – in form of emissions and deposition velocities – on the one hand, and meteorological parameters – determining local transport – on the other hand.

From an atmospheric chemical point of view, **biogenic gases** like biogenic volatile organic compounds (BVOCs) are subject to highly complex formulations and chemical transformations. On the one hand, there is a huge number of volatile organic compounds (VOCs) with fairly low concentrations in the atmosphere (e.g. Goldstein and Galbally [2007]). Being highly reactive, VOCs affect air quality and climate change via formation of aerosols and ozone (see Sec. 2.4). On the other hand, estimations of biogenic emissions rely on rough assumptions about the terrestrial ecosystem. The emitted amount of single BVOC is highly sensitive to local vegetation and surface properties. In CTMs, these properties are usually subject to high uncertainties in terms of their spatial distribution and temporal evolution.

The complexity and variability of biogenic gases motivates the investigation and modeling of related uncertainties. Uncertainties due to multiple dependencies of biogenic emissions and deposition velocities are considered. Based on this, a quantitative and state-dependent uncertainty estimation is achieved for biogenic gases.

The overall purpose of this study arises from the individual objectives described above and can be summarized as follows: (1) Development of an ensemble algorithm for efficient parameter perturbation in atmospheric models focusing on leading coupled uncertainties. (2) Implementation for uncertainties in emissions, transport and deposition covering the whole lifecycle of chemical compounds. (3) Application to biogenic gases with highly state-dependent uncertainties.

Ch. 2 gives a short literature overview including existing approaches in uncertainty estimation and the mathematical basis for the developed algorithm. The model environment in which this work is embedded is described in Ch. 3. Based on this, Ch. 4 describes the development of the ensemble algorithm. The case study to which the ensemble algorithm is applied is introduced in Ch. 5. Results from a sensitivity analysis and the ensemble generation are given in Ch. 6 and 7, respectively. Finally, Ch. 8 evaluates the performance of ensemble forecasts and Ch. 9 concludes this study.

2 Theoretical Background

The predictability of numerical forecasts of dynamical systems is generally limited. This is caused by sources of uncertainties which may be related to both, imperfect input parameters and uncertainties in the numerical model.

This chapter presents a literature overview including established approaches to predictability of numerical forecasts. Sec. 2.1 introduces basic ideas for probabilistic forecasts from a mathematical point of view. Specific approaches for uncertainty estimations for numerical weather prediction and chemistry transport modeling are shortly described in Sec. 2.2 and 2.3, respectively. Sec. 2.4 gives a short introduction to biogenic gases. A theoretical description of the Karhunen-Loéve expansion – which serves as basis for the approach developed during this study – is given in Sec. 2.5.

2.1 Mathematical Basis

In the following, mathematical approaches for probabilistic forecasts in terms of probability density functions (PDF) and covariances are shortly introduced. For a detailed overview see for example Xiu [2010].

Forecast of PDF in Phase Space

The *Liouville equation* known from Hamiltonian mechanics can be used to describe the temporal evolution of the models PDF in phase-space (compare e.g. Epstein [1969]; Ehrendorfer [2006]). It can be expressed by a continuity equation of the probability $\rho(x,t)$ of the model state x at time t

$$\frac{\partial \rho(x,t)}{\partial t} + \sum_i \frac{\partial \left[\rho(x,t)\dot{x_i}\right]}{\partial x_i} = 0 \tag{2.1}$$

With this, the Liouville equation can be interpreted in the way that the probability ρ is constant along a model trajectory in phase-space.

The *Fokker-Planck equation* considers additive white noise to account for model uncertainties in the Liouville equation

$$\frac{\partial \rho(x,t)}{\partial t} + \sum_i \frac{\partial}{\partial x_i}\left[\rho(x,t)\dot{x_i}\right] + \sum_i \sum_j \frac{\partial}{\partial x_i}\left[\frac{\tau_{ij}}{2}\frac{\partial \rho(x,t)}{\partial x_j}\right] = 0 \quad , \tag{2.2}$$

where $\tau_i j$ is the variance of the white noise describing the stochastics. The Fokker-Planck equation provides a theoretical formulation of the probabilistic evolution of uncertainties in time. However, applying the approach to discrete systems becomes computationally

prohibitive even for dimensions far below the ones of atmospheric systems (e.g. Hunt et al. [2007]).

Linear Forecast of the Error Covariance Matrix

As numerical models are formulated in finite-dimensional phase states, a discrete approach to forecast model uncertainties via covariances is presented. For a non-linear model $\mathcal{M}$, the related forecast $x_{t'}$ starting from an initial state x_t at time $t < t'$ is given by

$$x_{t'} = \mathcal{M}_{t \to t'}(x_t) + \varepsilon_{t'} \quad , \tag{2.3}$$

where errors $\varepsilon_{t'}$ in the forecasted state at time t' are induced by both, errors in the initial state x_t and imperfect formulation of the numerical model $\mathcal{M}_{t \to t'}$.

Assuming the existence of a linear approximation of the model, the covariance matrix of the forecast $C_{t'}$ can be calculated using the linearized model $M_{tt'}$ and its transposed $M_{tt'}^T$ (e.g. Daley [1993])

$$C_{t'} = M_{tt'}\ C_t\ M_{tt'}^T \quad . \tag{2.4}$$

This approach requires the knowledge of the covariance matrix C_t at initial time t. It does only account for the development of initial uncertainties given by C_t. In order to consider model uncertainties as well, a model error covariance matrix Q is included as additive term

$$C_{t'} = M_{tt'}\ C_t\ M_{tt'}^T + Q \quad . \tag{2.5}$$

This propagation of error covariances is used in the theoretical formulation of the *Kalman-filter* algorithm for calculating the forecast covariances required for data assimilation. However, the matrix multiplication limits this approach to low-dimensional problems where the size of the matrices is treatable.

2.2 Atmospheric Ensemble Approaches

Early attempts to uncertainty quantification for NWP systems were focusing on sensitivities to initial conditions (e.g. Thompson [1957]). Already in the beginning of the 20^{th} century, Poincaré denoted the existence of *deterministic chaos* which describes the random evolution of uncertainties by imperfect initial conditions even for a perfect model (Poincaré [1914]). This behavior became popular as *butterfly effect* based on the studies of Lorenz [1963].

Leith [1974] introduced the idea of Monte-Carlo forecasts as an ensemble of randomly perturbed atmospheric forecasts according to Gaussian PDFs. Following his idea, different ensemble approaches are currently used on operational NWP systems. The most popular ones dealing with uncertainties in initial conditions or the forecast model are shortly described below.

Initial Value Uncertainties

For uncertainties in initial conditions, *Bred vectors* (Toth and Kalnay [1993]) or *Singular vectors* (Buizza et al. [1993]) are used to detect directions of the fastest growing initial uncertainties over a given time interval. Both approaches aim for generating an efficient ensemble covering the largest uncertainties caused by initial conditions. Another approach estimates uncertainties in initial values by applying random perturbations to observations (PO) which are assimilated into the model (e.g. Houtekamer et al. [1996]).

The *singular vector* (SV) approach developed by Buizza et al. [1993] provides linear estimates of the directions of fastest growing uncertainties. The idea is to detect sensitive system states with large potential for amplification in time. This is achieved by calculating the singular value decomposition of the linear model M

$$M = U \cdot \Sigma \cdot V^T \quad , \tag{2.6}$$

with Σ the diagonal matrix of singular values and U, V being matrices containing the left and right singular vectors, respectively. The length of the time integration by M determines the timescale on which the perturbations are acting (e.g. Sandu et al. [2005]). Here, the singular vectors related to the largest singular values provide the directions of fastest growing initial uncertainties. These directions are scaled by assumed sizes of uncertainties to generate a set of perturbed initial fields.

However, the singular value decomposition requires a local linearization of the often highly nonlinear model operator $\mathcal{M}$ around the most likely model state. This limits the SV approach to the linear regime around the model state (e.g. Hoffman and Kalnay [1983]) in terms of size of perturbations and forecast time. Additionally, the singular vectors – and therefore also the perturbations – appear to be sensitive to the considered time-interval.

To avoid the linearization of the model, the *Breeding* approach was introduced by Toth and Kalnay [1993]. The approach arises from the idea that the directions of fastest growing perturbations naturally develop in the data assimilation process (e.g. Buizza et al. [2005]). Therefore, *Bred vectors* (BVs) are determined from the differences between two forecast. For a repetitive integration of these differences in time, BVs tend to convert to low dimensional subspaces related to the most uncertain directions (e.g. Toth and Kalnay [1993]). At this time, the BVs become independent of the direction of the initial differences. Thus they can be seen as a nonlinear formulation of the leading Lyapunov vectors (e.g. Kalnay [2003]; Buizza et al. [2005]). Finally, stochastic initial fields are created by adding or subtracting perturbations according to the direction of the leading BVs.

Model Uncertainties

Studies have shown that errors in initial conditions are not able to explain forecast uncertainties completely (e.g. Buizza et al. [2005]). The formulation of NWP models itself appears to be another important source of uncertainties. Moreover, model uncertainties trigger initial uncertainties of the ensuing forecast (e.g. Lock et al. [2019]). The two most common types of approaches for model uncertainties are described below.

The first group of methods is related to uncertainties in model parameterizations. These parameterizations rely on simplified assumptions about subgrid-scale processes, which have significant impact on resolved scales. Houtekamer et al. [1996] multiplied random numbers to parameters of parameterization schemes. In this *stochastic parameter perturbation* (SPP) approach, selected parameters in the single parameterization schemes are perturbed according to assumed uncertainties. Thus, uncertainties in the outcome of the parameterizations due to uncertain parameters are featured. Usually, these perturbations are applied to the whole parameter field or to each location and time separately. On the one hand, perturbing the whole parameter field does not allow for any spatial variation and is therefore not able to represent local state-dependent uncertainties. On the other hand, applying perturbations to different locations and times separately suffers from the high dimensionality of the system. Even introducing predefined dependencies to neighboring locations requires a large ensemble size and may not produce reasonable perturbations (e.g. Toth and Kalnay [1993]).

In contrast, Buizza et al. [1999] introduced the *stochastically perturbed parameterization tendencies* (SPPT) scheme. This approach considers uncertainties in the formulation of the parameterization schemes itself. Instead of perturbing parameters, the total tendencies p_D of state variables from all parameterizations are perturbed. These total tendencies are multiplied with random numbers r sampled from an arbitrary PDF by

$$p = (1 + r)\ p_D \quad , \tag{2.7}$$

thus the underlying uncertainties are assumed to be proportional to the total tendency. By perturbing total tendencies resulting form all parameterizations, the balance between different processes is not affected (e.g. Palmer [2019]). Although perturbations are generated in a spatially and temporally correlated way, both correlation scales and standard deviations of the random numbers are predefined as a fixed value (e.g. Leutbecher et al. [2017]; Lock et al. [2019]).

The *stochastic kinetic energy backscatter scheme* (SKEBS, Shutts [2005]) represents a different group of methods focusing on another source of model uncertainty. It is based on the need to account for energy backscattering from subgrid-scales to resolved scales in order to balance energy dissipation (e.g. MacVean [1983]). This two-way exchange of kinetic energy considering subgrid-scale energy sources is assumed to be of stochastic nature (e.g. Shutts [2005]). In SKEBS, stochasticity is realized by adding random noise to the prognostic equation of the stream-function. Where the random noise is proportional to the total energy dissipation rate, multiplied by random numbers. In Shutts [2005], a cellular automaton ensures predefined temporal and spatial correlations of the random numbers within a fixed range.

2.3 Uncertainties in Chemistry Transport Modeling

In chemistry transport modeling, the sensitivity to uncertain model parameters is much more dominant compared to NWPs. Generally, potential sources of uncertainties in CTMs

may be introduced through the whole lifecycle of each compound (for an detailed overview see e.g. Zhang et al. [2012b]). Specifically, chemical sources to the atmosphere in the form of emissions are subject to large errors concerning the spatial and temporal distribution (e.g. Elbern et al. [2007]). Within the atmosphere, chemical compounds are influenced by the atmospheric environment depending on meteorological conditions and reactive chemistry with other compounds including gas-phase chemistry, photolysis and aerosol chemistry (e.g. Bocquet et al. [2015]; Emili et al. [2016]). Finally, different kinds of deposition and sedimentation processes acting as chemical sink also contribute to forecast uncertainties (e.g. McKeen et al. [2007]; Wu et al. [2015]). The longer the forecast horizon, the more are chemical forecasts determined by emission and deposition processes compared to initial conditions (e.g. Elbern et al. [2007]; Bocquet et al. [2015]). Additionally, the general sources of uncertainties in atmospheric models like initial- and boundary conditions as well as the numerical implementation do also apply to CTMs. Besides an uncertainty estimation by multi-model ensembles (e.g. McKeen et al. [2007]; Xian et al. [2019]), there are only few attempts for ensemble generation within a single CTM.

Recent attempts follow two different strategies to account for uncertainties in CTMs. Firstly, former studies aim to account for uncertainties in model parameters or other chemical input fields (compare e.g. Zhang et al. [2012b]). Again, perturbing parameter fields appears to suffer from the high dimensionality of the system. Early studies like the one performed by Hanna et al. [1998] assume predefined uncertainties where perturbations are applied uniformly in space and time, and ignoring any cross-correlation between parameters. This uniform perturbation of model parameters with a fixed standard deviation is still applied to emissions in the context of ensemble data assimilation (e.g. Schutgens et al. [2010]; Candiani et al. [2013]). However, already Hanna et al. [1998] state that introducing state-dependency of uncertainties and cross-correlations between parameters would provide a more realistic representation. More recently, limited spatial correlations are considered in uncertainty estimation by uniform perturbations within arbitrary subregions (Boynard et al. [2011]; Emili et al. [2016]) or isotropic decrease with fixed correlation length scales (e.g. Gaubert et al. [2014]).

Secondly, Vautard et al. [2001] were the first creating an ensemble of ozone forecasts by driving the CTM with an existing meteorological ensemble. This comparably simple approach is based on the assumption that chemical forecasts are more sensitive to meteorology than to chemical uncertainties due to emissions or reactive chemistry (e.g. Zhang et al. [2012b]). In general, uncertainties in NWP may induce uncertainties in CTMs by multiple dependencies. For example, chemical compounds are found to be sensitive to wind fields, temperature, clouds, water vapor and precipitation (e.g. Hess et al. [2004]; McKeen et al. [2007]). Near-surface chemical composition is additionally sensitive to the structure of the boundary layer, for example controlling the boundary layer height, stability, turbulence and surface fluxes (e.g. Hess et al. [2004]; Eder et al. [2006]; Banks et al. [2016]).

2.4 Biogenic Volatile Organic Compounds

Although occurring in small concentrations, there is a huge number of non-methane volatile organic compounds (VOCs) in the atmosphere – and even more compounds are still expected to be found (e.g. Goldstein and Galbally [2007]). VOCs play an active role in tropospheric chemistry, with essential implications for air quality and climate change. On the one hand, VOCs contribute significantly to formation of secondary organic aerosols (SOA, e.g. Geng et al. [2011]; Shrivastava et al. [2017]). SOA act as cloud condensation nuclei and therefore affect aerosol-cloud interaction (e.g. Shrivastava et al. [2017]). On the other hand, VOCs are an important component in the photochemical production of tropospheric ozone (e.g. Geng et al. [2011]; Wu et al. [2015]).

A large fraction of VOCs in the atmosphere is emitted by the terrestrial ecosystem (e.g. Lamarque et al. [2010]). Compared to anthropologically emitted compounds, these biogenic VOCs (BVOCs) are especially sensitive to meteorological conditions. Additionally to the interaction with the atmospheric environment, the emission process of BVOCs is highly dependent on various atmospheric, vegetation- and soil-related properties. Examples for these dependencies are solar radiation, air temperature, soil moisture and biomass density (e.g. Lavoir et al. [2009]; Wu et al. [2015]). Moreover, biogenic emissions as well as dry deposition velocities vary significantly between different vegetation types (e.g. Wesely and Hicks [2000]; Wu et al. [2015]).

With an approximated contribution of about 50%, isoprene is the most dominant BVOC in terms of global annual emissions (Guenther et al. [2012]). In contrast to other BVOCs, isoprene is a direct product of the plants biosynthesis (e.g. Wu et al. [2015]). It has comparably high OH-reactivity (e.g. Fuentes et al. [2000]; Wang et al. [2017]) resulting in a lifetime of about 30 minutes, which is shorter than for other BVOCs (see e.g. Carslaw et al. [2000]; Geng et al. [2011]). The short lifetime of isoprene limits the gas to the local surrounding of the emission location. Therefore, its spatial and temporal distribution may be highly variable with considerable horizontal variations on the order of kilometers (e.g. Guenther et al. [2006]; Wang et al. [2017]).

The huge variability and highly complex dependencies render the modeling of biogenic gases nontrivial. This results in large differences in modeled monoterpene emissions reported for example by Arneth et al. [2008]. Estimates of global uncertainties in biogenic emissions range from a factor of two (Lamb et al. [1987]) to one order of magnitude (Hanna et al. [2005]). Furthermore, uncertainties in biogenic gases induce uncertainties in their chemical products like SOA and ozone formation (Shrivastava et al. [2017]). In contrast, dry deposition velocities of all chemical compounds – including chemical products of BVOC like ozone – differ by about 30% between different models (Wesely and Hicks [2000]).

2.5 Karhunen-Loéve Expansion

The *Karhunen-Loéve* (KL) *expansion* - named after Karhunen [1947] and Loéve [1948] - decomposes a stochastic process into a linear combination of a set of random variables. The KL approach is used in a various fields of applications (compare Wang [2008]). In the context of meteorological data analysis without the stochastic application, its discrete form is called *empirical orthogonal functions* (EOFs) and refers to a *principal component analysis* (PCA) of datasets (eg. Galin [2007]).

A more detailed description of the applied numerical methods can be found in Xiu [2010], the notation of which is adopted in this study.

Let $x(\omega, s)$ be a *stochastic process* with random dimension $\omega \in \Omega$ and location $s \in S$ with S the spatial dimension. The underlying idea is to describe the stochastic process as a linear combination of products of deterministic and stochastic elements

$$x(\omega, s) = \sum_{d=1}^{\infty} f_d(s)\ y_d(\omega) \quad , \tag{2.8}$$

with pairwise-uncorrelated *deterministic functions* $f_d(s)$ and pairwise-uncorrelated *stochastic coefficients* $y_d(\omega)$.

Eq. (2.8) holds for stochastic processes which are centered around zero. If the original distribution does not fulfill this criterion, the stochastic process is shifted by its mean value $\widetilde{x}(s) = x(\omega, s) - \mu(s)$.

The vectors of stochastic coefficients $y_d(\omega)$ are defined to be orthogonal to each other. They need to be sampled from a PDF fulfilling the following properties (compare Appendix B.1):

- The expectation value is zero.
- The standard deviation is given by square root of eigenvalues λ_d.

Thus, $y_d(\omega)$ can be written as

$$y_d(\omega) := \sqrt{\lambda_d}\ Y_d(\omega) \quad , \tag{2.9}$$

which gives the following conditions for the normalized stochastic coefficients $Y_d(\omega)$

$$\mathbb{E}\left[Y_d(\omega)\right] = 0 \quad \forall\ d \qquad , \qquad \mathbb{E}\left[Y_d(\omega)\ Y_d'(\omega)\right] = \delta_{dd'} \quad \forall\ d, d' \quad , \tag{2.10}$$

where $\delta_{dd'}$ is the Kronecker delta.

The selected distribution of the stochastic coefficients takes a similar form as the desired distribution of the stochastic process. In case of a Gaussian stochastic process, the stochastic coefficients are also Gaussian distributed. For other distributions, the definition of the stochastic coefficients becomes much more complicated. Schwab and Todor [2006] mentioned that the assumption of independent stochastic coefficients $Y_d(s)$ might not always be justified which induces an additional error.

The KL approach offers the possibility to use spatial correlations of the stochastic process $x(\omega, s)$ given by their covariance. By interpreting the deterministic functions as eigenfunctions of the covariances $\varphi_d(s)$ and using Eq. (2.9), the *KL expansion* reads:

$$\boxed{x(\omega, s) = \sum_{d=1}^{\infty} \sqrt{\lambda_d}\ \varphi_d(s)\ Y_d(\omega)} \quad , \tag{2.11}$$

where $Y_d(\omega)$ are normalized stochastic coefficients.

The *eigenvalues* λ_d and *eigenfunctions* $\varphi_d(s)$ are determined by the integrative *covariance matrix* $C(s, s') := \mathbb{E}\left[x(\omega, s)\ x(\omega, s')\right]$ of the stochastic process, with $s, s' \in S$

$$\int_S C(s, s')\ \varphi_d(s')\ ds' = \lambda_d\ \varphi_d(s) \quad . \tag{2.12}$$

This eigenvalue problem is usually replaced by an eigenvalue problem of a linear operator defined as

$$T_c(s) : f \to T_c(s) \cdot f = \int_S C(s, s')\ f(s')\ ds' \quad . \tag{2.13}$$

As correlations in $C(s, s')$ are generally symmetric and positive definite, the linear operator is compact and self-adjoint (Schwab and Todor [2006]).

The practical computation of Eq. (2.11) requires a finite approximation of the KL expansion. By defining a finite *truncation* $D < \infty$, the *KL approximation* becomes

$$x(\omega, s) \approx \sum_{d=1}^{\boldsymbol{D}} \sqrt{\lambda_d}\ \varphi_d(s)\ Y_d(\omega) \quad . \tag{2.14}$$

In order to archive an minimal error induced by the truncation, the eigenvalues and related eigenfunctions are sorted by their values: $\lambda_1 \geq \lambda_2 \geq \cdots \geq \lambda_D$. Thus, the first terms contribute most to the stochastic process. The determination of the truncation limit depends on the decay of the eigenvalues and the acceptable error induced by the algorithm.

The main feature of the KL expansion is that a stochastic process is decomposed into orthogonal functions with stochastic coefficients. Thus, KL can be seen as a stochastic extension to Fourier series (eg. Wang [2008]). The determination of the coefficients is optimal in a mean square sense by minimizing the mean square error of the finite representation (eg. Schwab and Todor [2006]). The only required information on the stochastic process are its stochastic mean $\mu(s) = \overline{x(s)}$ and covariances $C(s, s')$. Given this, the KL approximation samples from a subspace of the stochastic space which is given by the covariances. In this context, the leading eigenvalues and corresponding eigenfunctions provide the size and direction of the major uncertainties of the stochastic process, respectively.

The main advantage of the KL algorithm is the consideration of correlations of the stochastic process. First of all, the correlation of the process limits the error of the finite

approximation (eg. Xiu [2010]). As it can be seen in Fig. 2.1, the higher the correlation the faster is the decay of its eigenvalues. This leads to a lower error for a fixed truncation limit or to a lower truncation limit for a fixed error. Thus, the correlated field of stochastic processes can be decomposed into a small number of uncorrelated elements (*principal components*, Hotelling [1933]). Moreover, the low number of principal components only requires a reduced number of stochastic coefficients as they are used globally for all $s \in S$. The reduced dimension of the problem becomes especially important for high dimensional systems being generally limited by computational resources.

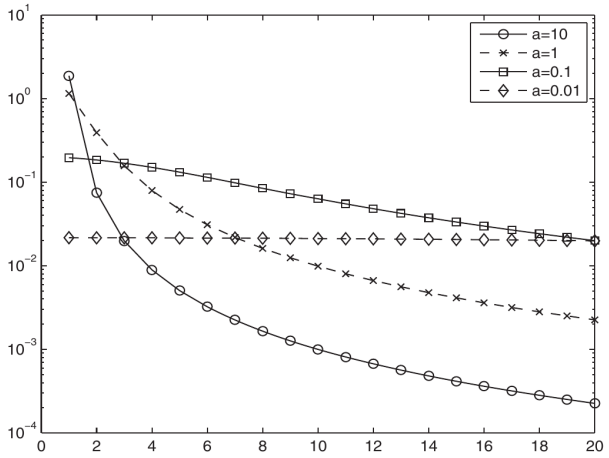

Figure 2.1: Decreasing behavior of leading eigenvalues for exponential covariances with different correlation length a taken from Fig. 4.2 in Xiu [2010].

3 Modeling Framework

This chapter presents an overview of the pre-existing modeling framework on which the developments for this study are based. Three linked modeling systems are used or further developed. On the one hand, the ensemble generation algorithm was applied to two limited-area atmospheric models. While perturbations of meteorological model parameters are considered in WRF (Sec. 3.1), atmospheric chemical parameters are handled in EURAD-IM (Sec. 3.2). The description of both modeling systems focuses on those modules, which are important for the developments performed during this study. On the other hand, an existing ensemble environment for WRF and EURAD-IM is shortly described in Sec. 3.3. Although this ensemble environment was not completely adopted, some parts are used in this study.

3.1 WRF Numerical Weather Prediction System

The WRF (*Weather Research and Forecasting*) model is a mesoscale numerical weather prediction model, which originates from a joint coordination effort of NCAR (National Center for Atmospheric Research), NOAA (National Oceanic and Atmospheric Administration), the U.S. Air Force, the Naval Research Laboratory, the University of Oklahoma and the Federal Aviation Administration. Its code is freely accessible and widely used for various applications. WRF offers two dynamical cores NMM (*Nonhydrostatic Mesoscale Model*) and ARW (*Advanced Research WRF*) as well as additional packages including data assimilation (WRFDA) and atmospheric chemistry (WRF-Chem). A detailed description can be found in Skamarock et al. [2008].

In this study, the WRF-ARW version 3.8.1 is used. The WRF framework consists of a sequence of components allowing for a flexible and comfortable preparation of intended simulations. On a first level, the system can be divided into the *WRF Preprocessor System* WPS and the WRF system. On a second level, WPS consists of three individual components. Firstly, GEOGRID defines the grids and interpolates terrestrial information for all required domains. Secondly, UNGRIB prepares the meteorological input files for the simulation time. Thirdly, METGRID interpolates the prepared meteorological information for the current domain.

The WRF system is fully parallelized and includes the final preparation of initial- and boundary conditions in REAL as well as their interpolation to nested domains in NDOWN. Finally, the forecast of WRF-ARW is performed by solving fully compressible non-hydrostatic prognostic equations. The vertical grid is defined by terrain-following hydrostatic-pressure coordinates and the prognostic variables are horizontally staggered in an Arakawa-C-grid (Arakawa and Lamb [1977]) stencil. Time integration is performed by the 2^{nd} or 3^{rd} order Runge-Kutta scheme.

Multiple schemes for various kinds of parameterizations are available in the WRF model. Available parameterizations account for subgrid-scale processes related to the boundary- and surface layer, land- and urban surface, lake physics, short- and longwave radiation, cloud microphysics and cumulus parameterizations. This study focuses on parameters handled by the boundary- and surface layer schemes as well as the land surface model. Reference options of the parameterization schemes – in which the perturbation of model parameters are implemented during this study – are described in more detail below.

3.1.1 Boundary Layer Parameterization

In numerical weather prediction models, boundary layer parameterizations approximate subgrid scale processes in the *planetary boundary layer* (PBL). As these processes often have a high spatial and temporal variability, boundary layer parameterizations have to provide reasonable averages over a potentially large scale. Different parameterization schemes are based on different assumptions about the treatment of transport, moisture and energy in the PBL (e.g. Hu et al. [2010]). Additionally, these schemes include numerous tuneable parameters, which may be calibrated with a limited number of observations restricted to one specific region (Yang et al. [2016]). Therefore, one primary source of uncertainties in mesoscale atmospheric models is related to boundary layer parameterizations. For example, Pleim [2007] reports significant errors in wind speeds for all considered parameterization schemes. Moreover, parameters describing the PBL structure like the *boundary layer height* (BLH) may also be defined in different ways. These parameters may have especially significant influence for the dispersion of pollutants in atmospheric chemical simulations.

Technically, boundary layer parameterizations approximate mean profiles of atmospheric state variables or their tendencies in the PBL. In general, currently used parameterization schemes can be classified into two approaches. On the one hand, *local closure schemes* are based on K-theory, where the subgrid scale turbulent flux is assumed to be proportional to the local gradient (Stull [1988]). Current local schemes are usually of 1.5^{th} or 2^{nd} order including more detailed formulations than the 1^{st} order K-theory. 1.5^{th} order schemes like MYJ (*Mellor-Yamada-Janjic*, Janjic [1994]), BouLac (*Bougeault-Lacarrere*, Bougeault and Lacarrere [1989]) or MYNN (*Mellor-Yamada-Nakanishi-Niino*, Nakanishi and Niino [2006]) use an additional prognostic equation for the mean *turbulent kinetic energy* (TKE). 2^{nd} order schemes include prognostic equations for flux terms, which require the parameterization of 3^{rd} order terms.

On the other hand, *non-local closure schemes* consider information from surrounding locations or the whole vertical profile to approximate fluxes. Ideally, this approach is more suitable in convective conditions, where the turbulence is buoyancy-driven and vertical gradients become neglectable (e.g Garratt [1994]). Due to the complexity introduced by non-local effects, non-local schemes like YSU (*Yonsei University*, Hong et al. [2006]) or ACM2 (*Asymmetric Convection Model version 2*, Pleim [2007]) are often of 1^{st} order closure. Studies investigating the performance of local and non-local approaches do not show a clear ranking for those. It appears that the performance of each scheme highly

depends on atmospheric conditions (e.g. Yang et al. [2016]).

The *Mellor-Yamada-Janjic* (MYJ, e.g. Janjic [1994]) scheme is a local 1.5^{th} order boundary layer parameterization scheme based on Mellor and Yamada [1982]. As a TKE closure scheme, TKE is treated as additional prognostic state variable determining the eddy diffusion coefficients. In this approach, the diffusivity in the closure of the prognostic TKE equation depends on a master length scale. Being based on the local K-approach, vertical turbulent mixing is defined to be proportional to the eddy diffusion coefficient K_ξ for $\xi \in \{\text{momentum,heat,TKE}\}$ (Janjic [2001])

$$\overline{w'\xi'} := -K_\xi \frac{\partial \xi}{\partial z} \quad . \tag{3.1}$$

Here, different formulations of the coefficients K_ξ are used for momentum (K_m), heat (K_h) and TKE (K_q). The boundary layer height is defined as the height where TKE reaches a threshold of 0.2 $\frac{m^2}{s^2}$. A flowchart of the most important variables of the MYJ PBL scheme as implemented in WRF is given in Appendix A.2.

3.1.2 Surface Layer Parameterization

The surface layer is the lowest part of the PBL and represents the connection between the earth's surface and the atmosphere. According to Stull [1988], the surface layer is defined as the region, where the variation of turbulent fluxes drops below 10% of their magnitude. Due to its direct interaction with the earth's surface, vertical profiles of atmospheric state variables are dominated by large gradients. These gradients induce large fluxes of atmospheric parameters like momentum, heat and moisture between surface and atmosphere (e.g. Arya and Holton [2001]).

In WRF, the surface layer is assumed to be represented by the lowest model layer. Surface layer schemes provide exchange coefficients and surface fluxes of heat and moisture, which are required by the boundary layer parameterizations and the land surface model. Due to close interactions with the boundary layer scheme, surface- and boundary layer schemes should be selected accordingly. Parameterizations of the surface layer are based on the *Monin-Obukhov Similarity Theory* (MOST) derived by Monin and Obukhov [1954]. By applying similarity theory, the approach defines scaling parameters to gain universal relations between dimensionless variables. In the surface layer, scaling parameters for momentum, temperature and humidity are u_* – defined as *friction velocity* –, Θ_* and q_*, respectively. Given these scaling parameters, the *Obukhov length* L can be calculated and is a measure of stability. It is defined as the height where shear production equals buoyancy destruction leading to zero net production of turbulent kinetic energy.

The *Eta-similarity* surface layer scheme (e.g. Janjic [1996]) has been developed to act as lower boundary for the MYJ boundary layer scheme. Over land, the roughness length is defined in a variable way, considering differences when applying to temperature and humidity (Zilitinkevich [1995]). Over water, a viscous sublayer is explicitly defined as the layer in which transport is only determined by molecular diffusion (Janjic [1994]). Additionally, the *Beljaars correction* (Beljaars [1995]) has been applied, which introduces

a velocity scale for free convection w_*. Thus, the adopted friction velocity is formulated as follows:

$$u_*^2 := C_m \cdot \left[u^2 + v^2 + (\beta \cdot w_*)^2\right] \quad , \tag{3.2}$$

where C_m is the momentum transfer coefficient, β a constant scalar and u and v the wind components in zonal- and meredional direction, respectively. The final calculation of surface fluxes, which are provided to the land surface model, is performed iteratively. A flowchart of the most important variables of the Eta-similarity surface layer scheme as implemented in WRF is given in Appendix A.1.

3.1.3 Land Surface Model

The earth's surface represents the lower boundary in atmospheric models. Xiu and Pleim [2001] state that the most important task of a land surface model (LSM) is the estimation of evaporation, which determines the partitioning between sensible and latent heat flux. As the estimated evaporation is determined by local soil and vegetation properties, these parameters have significant effect on the development of the PBL (e.g. Garratt [1994]). Therefore, LSMs are assumed to be especially important when mesoscale meteorological forecasts are applied to CTMs (e.g. Xiu and Pleim [2001]; Gilliam and Pleim [2010]).

In WRF, the earth's surface is divided into water and land surfaces, which are treated separately. Land surface models provide parameterizations of land surface processes and their interaction with the atmosphere. Representing an important component in the earth system, LSMs interact with all other parameterizations. However, their implementation in WRF is one-dimensional and does not include horizontal exchange. Their major outputs are surface fluxes of heat, moisture and momentum as well as upwelling short- and longwave fluxes, which are feed into boundary layer and radiation schemes, respectively.

Except for the *thermal diffusion* scheme, soil temperature and moisture are treated as prognostic variables in LSMs. In the thermal diffusion scheme, soil moisture is set to a fixed value that varies between land use types and seasons. This simplification makes the scheme unpractical for application to forecasts of biogenic gases, where emissions soil moisture-dependent. The number of soil layers ranges from two (*Pleim-Xiu*) to ten (*CLM4*). Examples for featured processes are multi layer snow (*RUC, CLM4*), fractional snow cover (*Noah*), frozen soil physics (*Noah, RUC*) or an explicit consideration of vegetation (*Pleim-Xiu, CLM4*).

The *Pleim-Xiu LSM* (PX LSM, Pleim and Xiu [1995]; Xiu and Pleim [2001]) is a two-layer soil temperature and -moisture model. The surface layer is defined by a depth of 1 *cm* and the root zone layer in 1 *m* depth acting a slowly varying reservoir. The scheme consists of five prognostic equations with corresponding prognostic variables: soil surface temperature $T_s := T\big|_{1cm}$, lower layer temperature $T_2 := T\big|_{1m}$, volumetric soil moisture at the surface $w_g := w\big|_{1cm}$, volumetric soil moisture in the lower layer $w_2 := w\big|_{1m}$, and the amount of canopy water W_r (see Pleim and Xiu [1995]). The formulation of the prognostic equations is based on a force-restore approach (Deardorff [1978]), where the driving forces for temperature and moisture are the surface budgets of energy and moisture, respectively. Evaporation is computed by the sum of direct contributions from

the soil and wet canopies and vegetative evapotranspiration. For the numerical integration of the prognostic equations, the semi-implicit Crank-Nicolson technique is adopted.

3.2 EURAD-IM Chemical Data Assimilation System

The atmospheric chemical data assimilation system EURAD-IM (*EURopean Air pollution Dispersion - Inverse Model*) combines a state-of-the-art chemistry transport model with spatio-temporal data assimilation and inversion methods (Elbern et al. [2007]). The horizontal grid is created by a Lambert conformal projection where the prognostic variables are defined on a staggered Arakawa-C grid stencil (Arakawa and Lamb [1977]). In the vertical, model levels are given in terrain-following σ-coordinates. Additionally, sequential one-way nesting may be applied to multiple nests, which enables the application of continental to local limited-area domains.

The chemistry transport model within EURAD-IM performs forecasts of a large set of gas phase and aerosol compounds up to lower stratospheric levels (e.g. Hass et al. [1995]). The mass mixing ratio c_l of any compound l is subject to different kinds of processes which are formulated as prognostic equation

$$\frac{\partial c_l}{\partial t} = -\nabla\ (\mathbf{v}\, c_l) + \nabla\ \left(\rho\, \widetilde{\mathbf{K}}\, \nabla \frac{c_l}{\rho}\right) + \mathcal{P}_l(\mathbf{c}) + E_l - D_l(c_l) \quad , \tag{3.3}$$

with ρ the air density, $\mathbf{v}$ the 3-dimensional wind vector, $\widetilde{\mathbf{K}}$ the 3-dimensional eddy diffusivity tensor, $\mathcal{P}_l(\mathbf{c})$ the net chemical production from all compounds $\mathbf{c}$, E_l the emission flux and $D_l(c_l)$ the deposition flux of compound c_l.

On the one hand, chemical compounds are influenced by dynamical transformations due to advective and diffusive processes. The advection schemes of Bott [1988] and Walcek [2000] are implemented in the model, of which the Bott scheme is used for this study. On the other hand, chemical production and destruction due to reactive chemistry with other compounds as well as photolysis are considered. Different options for gas-phase chemistry mechanism are implemented, which are all based on RACM (*Regional Atmospheric Chemistry Mechanism*, Stockwell et al. [1997]). For this study, the RACM-MIM (Geiger et al. [2003]) mechanism is selected which considers 221 chemical- and 23 photolysis reactions by 84 gases including condensed isoprene degradation (*Mainz Isoprene Mechanism* MIM, Pöschl et al. [2000]).

These processes build the core of the forecast model $\mathcal{M}$. Due to the different time scales of the included processes, the model is implemented using symmetric operator splitting (Yanenko [1071])

$$\mathcal{M} := \left(\mathcal{D}_h^{\frac{1}{2}}\ \mathcal{T}_h^{\frac{1}{2}}\ \mathcal{T}_v^{\frac{1}{2}}\ \mathcal{D}_v^{\frac{1}{2}}\right) \mathcal{C} \left(\mathcal{D}_v^{\frac{1}{2}}\ \mathcal{T}_v^{\frac{1}{2}}\ \mathcal{T}_h^{\frac{1}{2}}\ \mathcal{D}_h^{\frac{1}{2}}\right) \quad , \tag{3.4}$$

with $\mathcal{D}_{h/v}$ and $\mathcal{T}_{h/v}$ the nonlinear horizontal/vertical operators for diffusion and advection, respectively, and $\mathcal{C}$ the nonlinear chemistry module.

The dynamical processes related to diffusion and transport in horizontal and vertical direction are performed sequentially for half the model time step (denoted by the superscript $\frac{1}{2}$). The large range of time scales in the chemistry mechanism is handled by a sequence of small chemical time steps of variable length within $\mathcal{C}$.

Additionally, emission and deposition fluxes represent the sources and sinks of chemical compounds, respectively. Emissions from anthropogenic- and biogenic sources are treated separately, where anthropogenic emissions provided by the TNO-MACC-II inventory (Kuenen et al. [2014]) are processed by the *EURAD Emission module* EEM (e.g. Memmesheimer et al. [1991]). Dry and wet deposition is considered in the model, where wet deposition is included in the treatment of clouds. According to the focus of this study, the approximation of biogenic emissions and dry deposition are described in more detail in Sec. 3.2.1 and Sec. 3.2.2, respectively.

Besides gas phase chemistry, aerosols and pollen are also part of the model. Aerosol dynamics are realized by the MADE (*Modal Aerosol Dynamics for Europe*), Ackermann et al. [1998] module where aerosols are separated by size into three modes. MADE includes multiple aerosol processes like nucleation, coagulation, particle growth and sedimentation. Due to the coexistence of gases and aerosols, mixed-phase chemistry is also included.

In the EURAD-IM system, *four-dimensional variational data assimilation* (4Dvar) is implemented to identify initial fields $\mathbf{x}_0$ and emission strengths of chemical compounds (Elbern et al. [2007]). The optimization of the emission strength is achieved via the definition of a field of *emission factors* $\mathbf{e}$. It is assumed that the total amount, which is emitted at each location, is more uncertain than the quantitative diurnal cycle. Therefore, the emissions within the assimilation window $[t_0,t_n]$ are multiplied by a constant factor, which can be optimized by data assimilation.

4Dvar is a spatio-temporal technique that estimates the best linear unbiased estimate (*BLUE*). Model variables are optimized by minimizing a cost function $\mathcal{J}$ under the assumption of Gaussian error characteristics of the background model state ($\mathbf{x}_0^b$, $\mathbf{e}^b$) and observations ($\mathbf{y}_t$)

$$\begin{aligned}\mathcal{J}(\mathbf{x}_0,\mathbf{e}) =& \frac{1}{2}\left(\mathbf{x}_0-\mathbf{x}_0^b\right)^T \mathbf{B}^{-1}\left(\mathbf{x}_0-\mathbf{x}_0^b\right) \quad + \frac{1}{2}\left(\mathbf{e}-\mathbf{e}^b\right)^T \mathbf{K}^{-1}\left(\mathbf{e}-\mathbf{e}^b\right) \\ &+ \frac{1}{2}\sum_{t=t_0}^{t_n}\left[\Big(\mathcal{H}\big(\mathcal{M}_{t_0,t}(\mathbf{x}_0)\big)-\mathbf{y}_t\Big)^T \mathbf{R}^{-1}\Big(\mathcal{H}\big(\mathcal{M}_{t_0,t}(\mathbf{x}_0)\big)-\mathbf{y}_t\Big)\right] \quad ,\end{aligned} \tag{3.5}$$

with n_{time} the number of model time steps in assimilation window, $\mathbf{x}_0$ and $\mathbf{x}_0^b$ the initial forecast and background state at initial time step t_0, $\mathbf{e}$ and $\mathbf{e}^b$ the forecast and background emission factors, $\mathbf{y}_t$ the observations at time step t, $\mathcal{M}_{t-1,t}$ the nonlinear forecast model operator (nonlinear), $\mathcal{H}$ the nonlinear observation operator, $\mathbf{B}$ and $\mathbf{K}$ background error covariance matrix for initial values and emission factors and $\mathbf{R}$ the observation error covariance matrix.

In the framework of data assimilation, the chemistry transport model $\mathcal{M}_{t_0,t}$ acts as an operator transferring the model state at time t_0 to time t

$$\mathbf{x}_t = \mathcal{M}_{t_0,t}(\mathbf{x}_0) = \left(\mathcal{M}_{t-1,t}\circ\cdots\circ\mathcal{M}_{t_0,t}\right)\mathbf{x}_0 \quad . \tag{3.6}$$

The observation operator $\mathcal{H}$ maps the model state from the model space to the observation space. For in-situ observations, the mapping reduces to a bilinear interpolation towards the location of the observations, whereas it might include complex radiative transfer calculations for remote sensing observations.

The cost function is iteratively minimized by a quasi-Newton method, the L-BFGS (*Limited-memory Broyden–Fletcher–Goldfarb–Shanno*, e.g. Liu and Nocedal [1989]) algorithm. For this, the gradients of the cost function with respect to initial values and emission factors are required

$$\begin{aligned}\nabla_{(\mathbf{x}_0,\mathbf{e})}\mathcal{J}(\mathbf{x}_0,\mathbf{e}) =& \mathbf{B}^{-1}\left(\mathbf{x}_0-\mathbf{x}_0^b\right) + \mathbf{K}^{-1}\left(\mathbf{e}-\mathbf{e}^b\right) \\ &+\sum_{t=t_0}^{t_n}\Big[\mathbf{M}_{t_0,t}^T\,\mathbf{H}^T\,\mathbf{R}^{-1}\left(\mathcal{H}\big(\mathcal{M}_{t_0,t}(\mathbf{x}_0)\big)-\mathbf{y}_t\right)\Big] \quad ,\end{aligned} \tag{3.7}$$

with $\mathbf{M}_{t-1,t}$ the tangent linear forward model operator and $\mathbf{H}$ the tangent linear observation operator.

The adjoint model $\mathbf{M}_{t-1,t}^T$ is the transposed of the linearized chemistry transport model and integrated a given model state at time t backward in time to $t-1$. Being implemented into the modeling system, the adjoint model can be used to quantify the history of selected airmasses according to Vogel et al. [2020]. Given an input signal $\boldsymbol{\gamma}_k(t_k)$ at time t_k, which is defined to be non-zero at location (x_k, y_k, z_k), the source region of the related airparcel is calculated by

$$\boldsymbol{\gamma}_k(t) = \widetilde{\mathbf{M}}_{t,t_k}^T\,\boldsymbol{\gamma}_k(t_k) = \left(\widetilde{\mathbf{M}}_{t,t+1}^T \circ \cdots \circ \widetilde{\mathbf{M}}_{t_k-1,t_k}^T\right)\boldsymbol{\gamma}_k(t_k) \quad . \tag{3.8}$$

For the purpose of tracking air parcels, chemical conversions are switched off in the *retroplume operator* $\widetilde{\mathbf{M}}_{t,t_k}^T$. This renders the signal $\boldsymbol{\gamma}_k(i)$ acting as a passive tracer being transformed by advection and diffusion backward in time. Therefore, the retroplume approach allows the investigation of source regions of air parcels including the convolution and mixing of different airmasses.

3.2.1 Biogenic Emissions

EURAD-IM includes the MEGAN module for emissions of biogenic species, which is used in a wide range of CTM systems (eg. Wang et al. [2017]; Henrot et al. [2017]; Georgiou et al. [2018]). MEGAN 2.1 (*Model for Emissions of Gases and Aerosols from Nature version 2.1*) accounts for terrestrial emissions including urban, natural, and agricultural sources (Guenther et al. [2012]). In total, 147 chemical compounds are considered, which are grouped into 19 classes according to their emission properties. The emissions of each *component class* g are formulated as

$$F_g = \gamma_g \sum_h \epsilon_{g,h}\,\chi_h \quad , \tag{3.9}$$

where for each *vegetation type* h, the *standard emissions* $\epsilon_{g,h}$ of this class are multiplied by the *vegetation fraction* χ_h. The standard emissions $\epsilon_{g,h}$ can be interpreted as average

emissions of a compound class g from vegetation type h. These average emissions refer to approximations of net primary emissions from the plants into the atmosphere.

The sum of standard emissions over all vegetation types $h \in \{1, \ldots, N_h\}$ at each location is multiplied by the *activity factor* γ_g to account for variations in the environmental conditions. Effects of radiation ($\gamma_{P,g}$), temperature ($\gamma_{T,g}$), leaf age ($\gamma_{A,g}$), soil moisture ($\gamma_{SM,g}$), and CO_2 ($\gamma_{CO_2,g}$) are included in a multiplicative manner

$$\gamma_g = C_{CE}\ LAI\ \gamma_{P,g}\ \gamma_{T,g}\ \gamma_{A,g}\ \gamma_{SM,g}\ \gamma_{CO_2,g} \quad , \tag{3.10}$$

where the *canopy environment coefficient* C_{CE} ensures $\gamma_g = 1$ for standard conditions and LAI is the *leaf area index*.

The emission activity factors for radiation ($\gamma_{P,g}$) and temperature ($\gamma_{T,g}$) are divided into a light dependent and a light independent fraction. The light dependent contribution to $\gamma_{P,g}$ is a function of the incoming shortwave radiation acting as photosynthetically active photon flux density. Both light dependent and independent contributions $\gamma_{T,g}$ have an exponential response to the temperature deviation from standard conditions $\gamma_{P,g} \propto exp\,[(T - T_s)]$.

For the change of emissions depending on the leafs age, four stages of leaf age are considered: new, growing, mature and senescence foliage. Each stage is considered to have different emission patterns either increasing or decreasing with aging. The leaf age activity factor $\gamma_{A,g}$ is calculated as a sum of empirical coefficients $A_{*,g}$ multiplied with the assumed canopy fractions F_*

$$\gamma_{A,g} = A_{new,g}\ F_{new} + A_{gro,g}\ F_{gro} + A_{mat,g}\ F_{mat} + A_{old,g}\ F_{old} \quad , \tag{3.11}$$

where the canopy fractions are approximated by the temporal change of LAI.

Following Guenther et al. [2012], CO_2 concentrations and soil moisture are assumed to have no effect on biogenic emissions from all compounds except isoprene:

$$\gamma_{CO_2,g} = 1 \quad | \forall\ g \neq isoprene \quad , \tag{3.12}$$

$$\gamma_{SM,g} = 1 \quad | \forall\ g \neq isoprene \quad . \tag{3.13}$$

Isoprene emissions are dependent on CO_2 concentrations within the canopy which are proportional to the atmospheric concentration.

Regarding soil moisture effects, isoprene emissions are assumed to decrease linearly with increasing drought stress of the plant. If soil moisture is below the *wilting point* Θ_w, the plants cannot extract any water out for the soil resulting in zero soil moisture activity factor ($\gamma_{SM,isoprene} = 0$). Above the this point, a linear reduction of drought stress over an interval $\Delta\Theta$ is assumed, finally ending with no soil moisture dependency of emissions ($\gamma_{SM,isoprene} = 1$). Thus, Guenther et al. [2012] approximated the soil moisture dependency of isoprene emissions by

$$\gamma_{SM,isoprene} = \begin{cases} 0 & | \quad \Theta < \Theta_w \\ \dfrac{\Theta - \Theta_w}{\Delta\Theta} & | \quad \Theta_w < \Theta < \Theta_w + \Delta\Theta \\ 1 & | \quad \Theta_w + \Delta\Theta < \Theta \end{cases} \quad . \tag{3.14}$$

An overview of the MEGAN 2.1 emission model is shown in Fig. 3.1. Required input parameters are fields of LAI, solar radiation, temperature, soil moisture, CO_2 concentrations, and plant functional types (PFTs). Given these parameters, the model calculates the activity factors of each compound class and the resulting emission estimates. For a detailed description see Guenther et al. [2012].

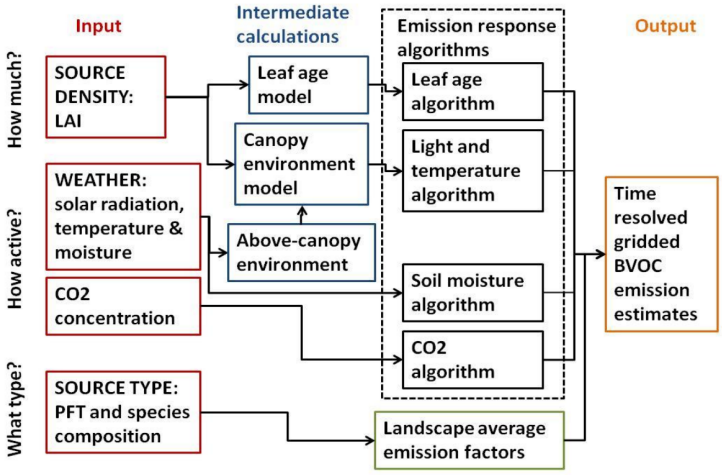

Figure 3.1: Schematic overview of MEGAN 2.1 taken from Fig. 1 of Guenther et al. [2012].

Although biogenic emissions of isoprene should be dependent on soil moisture according to Guenther et al. [2012], the available code of MEGAN 2.1 (Guenther [2011]) does not include this dependency. Nevertheless, multiple publications indicate the significance of moisture-related emission reduction not only for isoprene but recently also for other chemical compounds (eg. Pegoraro et al. [2004]; Lavoir et al. [2009]; Wu et al. [2015]). Thus, the MEGAN approach for linear reduction of isoprene emissions is implemented into EURAD-IM and applied to all compounds for this study. Applying the formulation of Eq. (3.14) requires data of the wilting point Θ_w and the slope of the moisture dependency $(\Delta\Theta)^{-1}$.

In the initial version of MEGAN, Guenther et al. [2006] used a database from Chen and Dudhia [2001] for approximations of the wilting point Θ_w. Chen and Dudhia [2001] provide soil-dependent estimates of Θ_w for 15 different soil types ranging from $0.01\frac{m^3}{m^3}$ for sand to $0.138\frac{m^3}{m^3}$ for clay. As this parameter is a property of the soil and thus independent of plant type and chemical compound, the values from Chen and Dudhia [2001] are also applied to the other compound classes.

While in Guenther et al. [2006] $\Delta\Theta$ was approximated by $0.06\frac{m^3}{m^3}$ based on findings from Pegoraro et al. [2004], Guenther et al. [2012] suggest $\Delta\Theta = 0.04\frac{m^3}{m^3}$ for MEGAN 2.1. Detailed investigations of the moisture dependency on emissions of individual plants indicate large variations of both parameters. Wu et al. [2015] found $\Delta\Theta \in [0.044, 0.19]$ for de novo emissions of monoterpenes from European broadleaf trees (compare Tab. 2 in Wu et al. [2015]). For modeling approaches like MEGAN, an averaged value of $0.08 \pm 0.05\frac{m^3}{m^3}$ is suggested by Wu et al. [2015].

3.2.2 Dry Deposition

Atmospheric trance gases are removed by dry- and wet deposition by precipitation. This study focuses on dry deposition which highly depends on the surface type. The amount of a chemical gases l, which is dry deposited $D_{dep}(l)$ is proportional to the near-surface concentration $c(l)$

$$D_{dep}(l) \propto V_{dep}(l)\ c(l) \quad . \tag{3.15}$$

In EURAD-IM, the dry deposition velocity $V_{dep}(l)$ is modeled according to Zhang et al. [2003]. In the *multiple-path resistance scheme*, considered processes are treated as resistances (in $\frac{s}{cm}$, e.g. Wesely and Hicks [2000]). Three primary resistances are contributing to the dry deposition velocity of a compound i

$$V_{dep}(l) = \frac{1}{R_a + R_b(l) + R_c(l)} \quad . \tag{3.16}$$

Following the approach of Wesely et al. [2002], aerodynamic resistance (R_a) and quasi-laminar sublayer resistance (R_b) are a function of friction velocity.

The overall canopy resistance R_c is decomposed into processes related to stomatal- (R_{st}) and non-stomatal (R_{ns}) uptake

$$R_c(l) = \frac{1 - W_{st}}{R_{st} + R_m(l)} + \frac{1}{R_{ns}(l)} \quad , \tag{3.17}$$

where the fraction of stomatal blocking of deposition W_{st} increases linearly with solar radiation under wet conditions (compare Eq. (5) of Zhang et al. [2003]). Under dry conditions, W_{st} is set to zero. Species-dependent values of the mesophyll resistance R_m are provided by Zhang et al. [2002].

Stomatal resistance R_{st} is implemented by adopting a *two-big-leaf submodel* distinguishing between sun illuminated and shaded leafs (Zhang et al. [2002]). Stomatal uptake is the uptake of leafs via their pores, which only occurs during daytime due to its dependency on photosynthetically active radiation (PAR). Additionally, R_{st} is a function of air temperature, the water-vapor deficit ($e - e*$), and water stress. Although Wesely et al. [2002] proposed the use of soil moisture, water stress is approximated by solar radiation due to limited knowledge of related dependencies (Zhang et al. [2003]).

The parameterization of non-stomatal resistance R_{ns} is based on Zhang et al. [2002]. It consists of a in-canopy aerodynamic resistance (R_{ac}), soil resistance (R_g), and cuticle resistance (R_{cut})

$$R_{ns}(l) = \frac{1}{R_{ac}(l) + R_g(l)} + \frac{1}{R_{cut}(l)} \quad . \tag{3.18}$$

While R_{ac} and R_{cut} depend on LAI and friction velocity, the uptake of soil varies between surface types and chemical compounds. Due to very limited amount of data, only observation-based values of O_3 and SO_2 are used (Zhang et al. [2003]). For SO_2, an additional dependency on canopy wetness is considered using different values of R_g for rain, dew or dry conditions. The resistances for all other considered compounds l are approximated by a combination of the given values:

$$R_{ac/cut}(l) = \frac{\alpha(l)}{R_{ac/cut}(SO_2)} + \frac{\beta(l)}{R_{ac/cut}(O_3)} \quad \Big| \quad \forall\ l\ \text{(dry deposited)} \notin \{SO_2, O_3\} \quad , \tag{3.19}$$

where the scaling factors $\alpha(l)$ and $\beta(l)$ are provided by Wesely [1989] based on solubility and reactivity of each compound.

3.3 ESIAS Ensemble System

The ESIAS (*Ensembles for Stochastic Integration of Atmospheric Systems*) system for ultra-large ensembles of atmospheric models was developed during the last years by Franke [2018] and Berndt [2018]. Its overarching goal is to provide an environment for ensembles with $\mathcal{O}(10^3)$ members, linked to data assimilation by novel algorithms. The developed algorithms are especially designed for high-performance computers aiming at a high degree of parallelization.

The ESIAS system consists of a meteorological- (denoted as ESIAS-met, Berndt [2018]) and an atmospheric chemistry part (denoted as ESIAS-chem, Franke [2018]) realized by ensemble extensions of WRF and EURAD-IM, respectively. Both ensemble systems are based on a second stage of parallelism as shown in Fig. 3.2. Besides the communication between all workers of a single member `MEMBER_COMM` (which replaces `MPI_COMM_WORLD` in the original models), the communication between all workers handling the same part of each ensemble member `ENSEMBLE_COMM` is introduced.

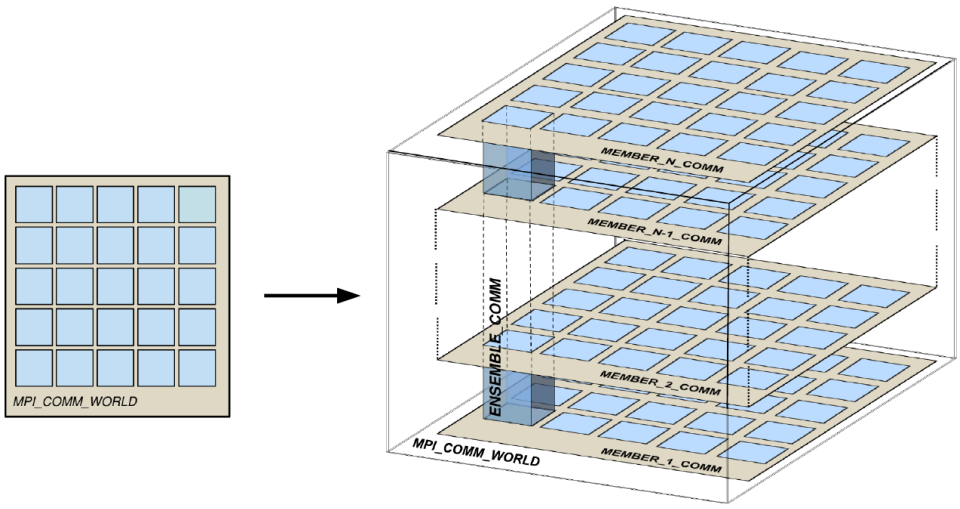

Figure 3.2: Visualization of two stage MPI communication developed for the ESIAS system according to Franke [2018]; Berndt [2018]. Left: original communication, right: two stage communication between worker of each member (`MEMBER_*_COMM`, horizontal) and corresponding worker of each ensemble member (`ENSEMBLE_COMM`, vertical).

The meteorological part of ESIAS is realized by an ensemble extension of the numerical weather prediction model WRF. The second stage of parallelization was introduced to the preprocessing system WPS as well as to the WRF model itself. This creates a stand-alone ensemble system for WRF without restrictions in execution compared to original

model. The ESIAS-met system was developed in order to provide detailed probability distributions of short to medium range wind energy forecasts by an ultra-large ensemble (Berndt [2018]).

The ensemble is generated by considering input uncertainties as well as model uncertainties. For the former, different global meteorological fields (from EPS and GEFS) and perturbed surface parameters are used. Model uncertainties are represented by stochastic incorporation of subgrid-scale energy (SKEBS) and stochastic perturbation of parameterized tendencies (SPPT). Within ESIAS-met, *sequential importance resampling* of the ensemble members is performed according to their attached weight. In this way, data assimilation is used to update the ensemble continuously. While ensemble members with a low weight are rejected, members close to the observations are duplicated to keep a constant ensemble size.

An ensemble extension of the chemical data assimilation model EURAD-IM serves as chemical part of ESIAS. In addition to the implementation of the second stage of parallelization, another modification was performed on process level. The original master-worker setup within EURAD-IM was changed to an all-worker setup including parallel input/output handling. With this setup, the computation time as well as required storage are reduced significantly making the model scaleable to a large number of processes.

ESIAS-chem was used to estimate emission profiles from volcanic eruptions (Franke [2018]). Vertical profiles of volcanic emissions become distinguishable by later observations due to vertical wind shear. The observations are assimilated using a particle-smoother where the each ensemble member is initialized with a reduced emission pattern.

The ensemble system developed during this study is based on the ESIAS software. The two stage parallelization is used within EURAD-IM in order to calculate perturbations and apply these to an ensemble of forecasts by a single executable. However, the focus of this work differs slightly from the idea of ESIAS being designed for a huge number of ensemble members. Instead, the idea of this work is an efficient generation of ensembles representing leading uncertainties with a comparably low ensemble size. Thus, only the second level of parallelism from ESIAS is adopted in this study.

4 Ensemble Generation Algorithm

In this chapter, the setup of the ensemble algorithm which is developed and implemented in the EURAD-IM modeling system is described. The core algorithm based on the Karhunen-Loéve expansion is introduced in Sec. 4.1. Further developments offering supplemental features for the algorithm are presented in Sec. 4.2.

4.1 Core Algorithm

The general application of the KL expansion to ensemble generation for atmospheric models is described in the following.

4.1.1 Application of KL Expansion

Using the KL expansion (see Sec. 2.5) in the context of high-dimensional atmospheric modeling systems, the variable of interest is a field of stochastic processes $x(\omega, s)$ in spatial- $s \in S$ and stochastic space $\omega \in \Omega$. In this context, S can be interpreted as set of all grid boxes for all model parameters considered, with N its total length. The equidistant spatial grid of Eulerian atmospheric models requires a discrete formulation of the finite KL approximation (compare Eq. (2.14)). This implies the following properties:

- $\omega \in \Omega = \{\omega_1, \omega_2, ..., \omega_J\}$ — a finite set of J realizations in probability space Ω
- $s \in S = \{s_1, s_2, ..., s_N\}$ — a set of N discrete locations in physical space S
- $D \leq N$ — exact formulation of the expansion for $N < \infty$ (N eigenmodes of covariance $C \in \mathcal{R}^{N \times N}$)
- $C\ \varphi_d = \lambda_d\ \varphi_d$ — eigenvalue problem reduces to its multiplicative form with eigenvectors $\varphi_d \in \mathcal{R}^N$ (see Appendix B.2)

The stochastic dimension of the KL expansion is generated via the stochastic coefficients $Y_d(\omega)\ \forall\ d \in \{1, \ldots, D\}$ sampled from a predefined PDF (compare Sec. 2.5). Thus, in order to represent uncertainties in the stochastic process, the ensemble is produced by individual sampling of $Y_d(\omega_j)$ for each member $j \in \{1, \ldots, J\}$. For an ensemble size J, this leads to $J \cdot D$ stochastic coefficients independently sampled from the PDF. Here, the transformation into uncorrelated elements of the KL expansion appears to be beneficial. For the generation of a simple Monte-Carlo ensemble, the stochastic process at each location are sampled independently, which requires a huge number of samples. Ideally, each possible combination of realizations should be used which would lead to an exceptionally high number of members required. In the KL expansion, the stochastic coefficients are

sampled in the uncorrelated space and used for all locations $s \in S$. In this sense, the stochastic dimension can be reduced to the leading principal components which describe the stochastic process in an optimal manner. Depending on demands in accuracy of the uncertainty estimation and limitations in ensemble size, the number of leading principal components describing the stochastic process can be selected accordingly. This qualifies the approach for high-dimensional systems while keeping computational costs comparably low.

4.1.2 Definition of Stochastic Process

For a stochastic perturbation of model parameters, the perturbations should continuously be applied to the full forecast time interval. But assuming parameters to be constant in time is not suitable because of their possibly high diurnal variation (eg. for emissions). Therefore, instead of perturbing the absolute value of the parameter, the definition of *amplification factors* of parameters allows the application of perturbations over a time interval (compare Elbern et al. [2007] for emissions). Here, the factor $f(j,s)$ of each ensemble member j at location s is the temporal average of the parameter $q(j,s,t)$ scaled by the related parameter $q(j_{ref},s,t)$ of the reference member j_{ref}

$$f(j,s) := \frac{1}{T}\sum_{t=t_0}^{t_1}\frac{q(j,s,t)}{q(j_{ref},s,t)} \quad , \tag{4.1}$$

where T is the number of discrete time steps in the forecast horizon $[t_0,t_1]$. From definition (4.1) it follows that the factors of the reference member j_{ref} are equal to one for all locations.

In order to perturb stochastic factors f using the Karhunen-Loéve expansion, their PDF should be centered around its expectation value and values should be larger zero. These conditions are fulfilled by a lognormal distribution of the factors f. However, the original form of the KL expansion requires distributions of stochastic processes which allow a direct transformation to the distribution of stochastic coefficients. This is not easily fulfilled for lognormal distributions. But the relation becomes simple for normally distributed processes leading also to normally distributed coefficients (compare Eq. (2.11)). Therefore, the complete calculation of the KL expansion (including the calculation of covariances) is substituted using the natural logarithm of factors

$$x(j,s) := ln\Big(f(j,s)\Big) \quad . \tag{4.2}$$

Additionally, the mean values $\overline{x}(s)$ of the normally distributed stochastic processes are controlled by the stochastic mean of the KL extension (compare Eq. (2.11))

$$\mu(s) \stackrel{!}{=} \sum_{d=1}^{D}\sqrt{\lambda_d}\;\varphi_d(s)\;\overline{Y}_d \quad . \tag{4.3}$$

The mean stochastic coefficients $\overline{Y}_d$ are requested to be zero ($\mathbb{E}_\omega[Y_d(\omega)] = 0$, compare Sec. 2.5) which requires the stochastic processes to be centered around zero

$$\mu(s) := \mathbb{E}_j \left[x(j,s)\right] \stackrel{!}{=} 0 \quad \forall\ s \in S \quad . \tag{4.4}$$

Thus, the ensemble mean values have to be subtracted from the stochastic process.

Given this, the stochastic process is defined as:

$$x(j,s) := ln\Big(f(j,s)\Big) - \mathbb{E}_j \left[ln\Big(f(j,s)\Big)\right] \quad . \tag{4.5}$$

After the calculation of the KL expansion, the mean values are again added during the re-substitution.

4.1.3 Approximation of Covariances

Following the theoretical description of KL expansion in Sec. 2.5, the covariances are the only part of the KL expansion where the perturbations become sensitive to the current model state. In an atmospheric dynamical system, the forecast uncertainty is highly dependent on the current model state which makes the state-dependency being essential for the ensemble generation. This importance of the covariance matrix renders the KL ensemble highly sensitive to the formulation of covariances.

In general, all model parameters can be classified into two different types: independent- and dependent parameters. *Dependent model parameters* are characterized by a physical dependency to the model state or other input fields. This state-dependency may be used by approximating the covariances from a sensitivity analysis.

Sensitivities may be calculated by running the modeling system with different setups or using different external input fields driving the forecasts. The actual selection of reasonable sensitivities depends on the model parameters and will be discussed in Ch. 6.

The sensitivities from the forecasts of stochastic parameters are used for approximating the covariance matrix of the stochastic process. This can be done either by using sensitivities for the specific forecast horizon of the KL ensemble forecast or by pre-calculation of a sufficiently long period to extract statistical covariances for this time period. In case of using statistical covariances, it should be kept in mind that these are averaged uncertatintes and do not account for possible state-dependent temporal variations within the time period.

As described in Sec. 4.1.2, the KL expansion requires stochastic processes which are centered around zero. Using the definition of a stochastic process given in Eq. (4.5), this requirement is fulfilled by definition which simplifies the calculation of the covariance matrix to

$$\begin{aligned} C(s,s') &= \frac{1}{J}\sum_{j=1}^{J}\Big(x_{sens}(j,s) - \mu(s)\Big)\Big(x_{sens}(j,s') - \mu(s')\Big) \\ &= \frac{1}{J}\sum_{j=1}^{J}\Big(x_{sens}(j,s)\Big)\Big(x_{sens}(j,s')\Big) \quad , \end{aligned} \tag{4.6}$$

where J is the number of members from the sensitivity analysis with $j \in \{1, \ldots, J\}$ and $x_{sens}(j, s)$ and $x_{sens}(j, s')$ are the processes of each sensitivity j at location s and s' with ensemble mean $\mu(s) = \mu(s') = 0 \; \forall \; s, s' \in S$.

In case of *independent model parameters*, no dependencies of the parameters are implemented in the model which would allow for a sensitivity analysis. Instead, a-priori knowledge about error statistics of the stochastic parameters is required to approximate the covariance matrix by covariance modeling. In general, exact error statistics of atmospheric model parameter are not known. However, the estimates of standard deviations (or variances) and possible correlations can be used to approximate covariances. This could be done, for example by a statistical evaluation of model errors with respect to observations.

Another way could be the assumption of spatial (and/or temporal) correlation functions. Especially, if the stochastic parameter is dependent on fixed gridbox-related properties, this spatial correlations may be modified according to the distribution of these parameters. An example could be anthropogenic emissions from traffic. For given standard deviations, emissions along similar types of roads might be highly correlated but expected to decrease slightly for higher distances. On the other hand, emissions in grid boxed without traffic may be completely independent from road-emissions. Thus a slowly decreasing correlation function may be used between grid boxes containing roads whereas neglectable correlations can be set between grid boxes with and without roads for traffic emissions. Similar assumptions may be used for other model parameters.

For both approaches, the estimated covariances may be corrected a-posteriori on by validation of the KL ensemble forecasts with observations.

4.1.4 Solution of the Eigenproblem

The KL expansion of a stochastic process requires the calculation of eigenvalues and eigenvectors of the covariance matrix. Due to the high dimension of parameters in atmospheric models, the covariance matrix may easily be of the order of 10^{12} elements. This inhibits explicit storage of the matrix and makes the computation of the eigenproblem very costly. Therefore, it is crucial that the solution algorithm for the eigenproblem is efficient for large-scale problems. The ARPACK (*ARnoldi PACKage*, Lehoucq et al. [1997]) package is a flexible tool for numerical eigen- or singular value decomposition. It is explicitly constructed for large-dimensional problems and includes algorithms for various types of matrices: symmetric, non-symmetric, and generalized. According to the users' requirements, a predefined number of largest or smallest eigenvalues in algebraic or absolute sense can be calculated. Another advantage of ARPACK is that the matrix is only used as an operator acting on a vector within a *reverse communication interface*. This means that the matrix does not have to be available explicitly, which makes the algorithm suitable for large-scale problems. Additionally, the parallel version of ARPACK for the calculation of large-dimensional problems called PARPACK (*Parallel-ARPACK*) is used here. The use of multiple processors highly reduces the computation time in parallelized systems.

APRACK is based on the *Implicitly Restarted Arndoldi Method* (IRAM, Sorensen [1997]) which is related to the implicitly shifted QR-algorithm. It creates a *Krylov subspace*

$$\mathcal{K}_k(A, v) = Span\left(v, Av, A^2v, \ldots, A^{k-1}v\right) \quad , \tag{4.7}$$

which is an invariant subspace of A. Given the input matrix $A \in \mathbb{R}^{n\times n}$ and an unitary matrix $V_m \in \mathbb{R}^{n\times m}$ $(k < m < n)$, the IRAM algorithm for the calculation of k eigenvalues can be summarized as follows:

- reduce matrix A to a tridiagonal form in reduced dimension $H_m \in \mathbb{R}^{m\times m}$:

$$A\ V_m = V_m H_m + f_m e_m^T \tag{4.8}$$

- iterative calculation (until residual vector $f_m \in \mathbb{R}^m$ small):
  - calculate leading eigenvalues and eigenvectors of $H_m \rightarrow Q_m \in \mathbb{R}^{m\times m}$
  - QR-iterations: (apply Schur decomposition to update H_m)
    - update H_m and V_m:

$$H_m \leftarrow Q_m^T H_m Q_m \quad , \quad V_m \leftarrow V_m Q_m \tag{4.9}$$

    - update μ via shifting of QR-iteration
  - calculate Arnoldi factorization of length k:
    - reduce Q_m to k leading columns $\rightarrow Q_k \in \mathbb{R}^{k\times k}$
    - calculate Arnoldi factorization:

$$A\ V_k Q_k = V_k Q_k H_k + f_k e_k^T \tag{4.10}$$

  - extend Arnoldi factorization to length $m \rightarrow H_m, V_m$ (implicit restarting) .

The tridiagonal matrix H_m is an orthogonal projection of matrix A into a Krylov subspace (eg. Lehoucq and Sorensen [1996]). This transformation facilitates the numerical calculation of the leading eigenvalues for example via QR-decomposition. The columns of matrix Q_m are the eigenvectors of H_m. The implicitly restarting of the Arnoldi method is performed by extending the Arnoldi factorization to length m. The extended quantities H_m and V_m are then used for the next iteration. The stopping criterion of the iteration is defined by the length of the residual vector ($|f_m|$) which indicates the accuracy of the solution. The described method provides Ritz values θ and -vectors s which are approximations of the eigenvalues and -vectors of H_k ($H_k\ s = s\ \theta$). From this *Ritz pair* (θ, s), the desired eigenvalues λ, and -vectors φ of the input matrix A can be calculated by

$$\varphi = V_k\ s \quad , \quad \lambda = \theta \quad . \tag{4.11}$$

Using APRACK for the approximation of the eigenproblem in the KL expansion, the matrix of interest is the covariance matrix of the stochastic coefficients. As a covariance

matrix is always quadratic and symmetric by construction, the covariance matrix $C(s, s')$ serves as symmetric input matrix A and the IRAM method reduces to the *Implicitly Restarted Lanczos Method* (IRLM). This simplifies the algorithm compared to general non-symmetric or even non-quadratic problems.

Before using the eigenvectors φ calculated by PARPACK in the KL expansion, they were normalized to unit length.

4.1.5 Generation of Stochastic Coefficients

In the KL expansion, the stochastic property of the process is generated by stochastic coefficients. They are sampled from a predefined PDF, which determines the PDF of the process at each location.

As discussed in Sec. 4.1.2, the lognormally distributed factors are substituted to fulfill the condition for the stochastic process Y being normally distributed

$$PDF(Y) = \frac{1}{\sqrt{2\,\pi}\;\sigma_Y}\;exp\left(-\frac{(Y-\mu_Y)^2}{2\;\sigma_Y^2}\right) \quad . \tag{4.12}$$

Thus, the goal is to archive a normal distribution of the stochastic process via normally distributed stochastic coefficients with parameters $\mu_Y := \mathbb{E}_\omega\Big(Y_d(\omega)\Big)$ and $\sigma_Y := \sigma_\omega\Big(Y_d(\omega)\Big)$ to be determined.

For a normal distribution, the parameter μ_Y is the mean value of the stochastic coefficients Y_d. As described in Sec. 2.5, the expectation value of the stochastic coefficients has to be zero (Eq. (2.10)), which simply leads to

$$\mu_Y = \mathbb{E}\left[Y_d(\omega)\right] = 0 \quad \forall\; d \quad . \tag{4.13}$$

The parameter σ_Y is the standard deviation of the normal distribution. Here a special property of the KL expansion can be used: The variance of the stochastic coefficients is given by the eigenvalues of the covariance matrix (compare Sec. 2.5 and Appendix B.1):

$$\sigma_y^2 := \mathbb{E}\left[y_d(\omega)\;y_d(\omega)\right] = \lambda_d \quad , \tag{4.14}$$

$$\Rightarrow \sigma_Y^2 := \mathbb{E}\left[Y_d(\omega)\;Y_d(\omega)\right] = \frac{\sigma_y^2}{\lambda_d} = 1 \quad . \tag{4.15}$$

The distribution of the stochastic coefficients is given by Eq. (4.12), (4.13) and (4.14). The implemented technical generation of normally distributed random numbers is described in Appendix B.3.

4.1.6 Overview KL Ensemble Algorithm

In the following, the major steps of the KL ensemble algorithm are summarized as set of equations. Assuming lognormally distributed model parameters q and approximating

their covariances from a sensitivity analysis with members $j = \{1, \ldots, J\}$ and reference member j_{ref}, the KL ensemble algorithm is given as follows

$$
\begin{aligned}
&\text{sensitivity analysis} && x_{sens}(j,s) := ln\Big[f_{sens}(j,s)\Big] - \mu(s) \\
&&& \text{with} \quad f_{sens}(j,s) := \frac{1}{T}\sum_{t=t_0}^{t_1}\frac{q(j,s,t)}{q(j_{ref},s,t)} \\
&\text{covariance matrix} && C(s,s') = \frac{1}{J-1}\sum_{j=1}^{J}\Big[x_{sens}(j,s)\Big]\Big[x_{sens}(j,s')\Big] \\
&\text{eigenvalue problem} && \sum_{s'=1}^{S} C(s,s')\ \varphi_d(s')\ \delta s' = \lambda_d\ \varphi_d(s) \\
&\text{stochastic coefficients} && PDF\Big(Y_d(\omega)\Big) = \frac{1}{\sqrt{2\ \pi}\ \sigma_Y}\ exp\left[-\frac{\big(\omega-\mu_Y\big)^2}{2\ \sigma_Y^2}\right] \\
&\text{KL expansion} && x_{KL}(\omega,s) = \sum_{d=1}^{D}\sqrt{\lambda_d}\ \varphi_d(s)\ Y_d(\omega) \\
&\text{perturbed parameters} && q(\omega,s,t) = q(j_{ref},s,t)\cdot f_{KL}(\omega,s) \\
&&& \text{with} \quad f_{KL}(\omega,s) = exp\Big[x_{KL}(\omega,s) + \mu(s)\Big]
\end{aligned}
$$

The implementation of the KL ensemble algorithm in EURAD-IM is based on ESIAS described in Sec. 3.3. For a technical overview of the implementation on the KL ensemble algorithm see Appendix C.

It has to be noted that the statistics of the stochastic process given in the covariance matrix and the mean value are not changed by the KL expansion. This means that for large ensemble sizes the covariances and mean values of the stochastic process generated by the KL ensemble algorithm converge towards their input values. Therefore, the major benefit of the algorithm presented lies in the optimality of the perturbations focusing on leading uncertainties and thus providing an optimal coverage of the uncertainty space even for low ensemble sizes.

Up to now, only one single model parameter was considered as stochastic process with spatial correlations. But the described setup of the KL ensemble algorithm also allows for a generalization including cross-correlations of a set of stochastic parameters. Especially if these parameters are physically linked, like emissions of different biogenic species, the KL ensemble is beneficial. In this case, the high correlation between the parameters reduces the number of principal components to a low number. This means that the highly correlated parameters are perturbed in similar directions according to their cross-correlation. However, it has to be kept in mind that the dimension of the covariance matrix increases quadratically with the number of parameters. This limits the number of model parameters considered in the KL ensemble by computational reasons.

4.1.7 Small Test Case

A small toy model at test setup was created in order to test the different elements of the implementation of the KL ensemble algorithm. The test case contains three gridpoints ($S = 3$, $s \in [1, S]$) for which arbitrary factors $f(j, s)$ have been chosen. The sensitivity analysis consists of three members ($J = 3$, $j \in [1, J]$) where the factors of the reference member were set to 1.0 at all gridpoints by definition (compare Sec. 4.1). In order to investigate the advantages of the KL ensemble algorithm, the factors are defined to have high spatial correlation. The setup of the test case and the related factors are sketched in Fig. 4.1.

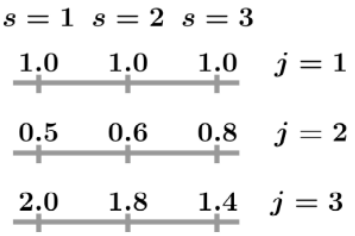

Figure 4.1: Setup and selected values of factors $f(j, s)$ for a small test case of KL ensemble algorithm. The grid pox is given by index s and the member number by j. Gray lines indicate the grid structure for each member.

This test case already gives some insight into the behavior of the KL ensemble algorithm. After substitution to a normally distributed stochastic process $x(j, s) = ln\Big(f(j, s)\Big)$, the covariance matrix becomes

$$C = \begin{pmatrix} 0.480 & 0.381 & 0.194 \\ 0.381 & 0.302 & 0.154 \\ 0.194 & 0.154 & 0.079 \end{pmatrix} \quad . \tag{4.16}$$

The high correlation leads to fast decreasing eigenvalues λ_d of the covariance matrix

$$\lambda_1 \approx 0.861 \qquad \lambda_2 \approx 0.001 \qquad > \lambda_3 \quad . \tag{4.17}$$

The leading corresponding eigenvectors $\varphi_d(s)$ are

$$\varphi_1 \approx \begin{pmatrix} 0.747 \\ 0.592 \\ 0.302 \end{pmatrix} \quad \varphi_2 \approx \begin{pmatrix} 0.536 \\ -0.266 \\ -0.801 \end{pmatrix} \quad . \tag{4.18}$$

The fast decrease of the eigenvalues indicates almost perfect correlation of the stochastic process. Assuming perfect correlation, the approximation of the KL expansion can be truncated after the first element ($D = 1$ in Eq. (4.1.6)). This means that one single stochastic coefficient determines the resulting stochastic process at all locations for each member. Note that in case of low correlation between different locations, the slow decrease of eigenvalues would require more stochastic coefficients to describe the whole stochastic

process. Creating $K = 6$ realizations with the KL ensemble algorithm for the described test case (Fig. 4.1), the re-substituted factors f_k of each ensemble member $k \in \{1, \ldots, K\}$ may look like

$$\begin{aligned} f_1 &\approx \begin{pmatrix} 1.419 \\ 1.320 \\ 1.152 \end{pmatrix} \quad f_2 \approx \begin{pmatrix} 0.481 \\ 0.559 \\ 0.743 \end{pmatrix} \quad f_3 \approx \begin{pmatrix} 1.561 \\ 1.424 \\ 1.198 \end{pmatrix} \\ f_4 &\approx \begin{pmatrix} 0.892 \\ 0.897 \\ 0.946 \end{pmatrix} \quad f_5 \approx \begin{pmatrix} 0.726 \\ 0.776 \\ 0.878 \end{pmatrix} \quad f_6 \approx \begin{pmatrix} 1.095 \\ 1.074 \\ 1.037 \end{pmatrix} \quad . \end{aligned} \tag{4.19}$$

Fig. 4.2 shows the distribution of the stochastic processes created by the KL ensemble algorithm and its re-substitution to factors. For a sufficient large number of samples (=KL ensemble member), the distribution of factors converges to a lognormal form as desired.

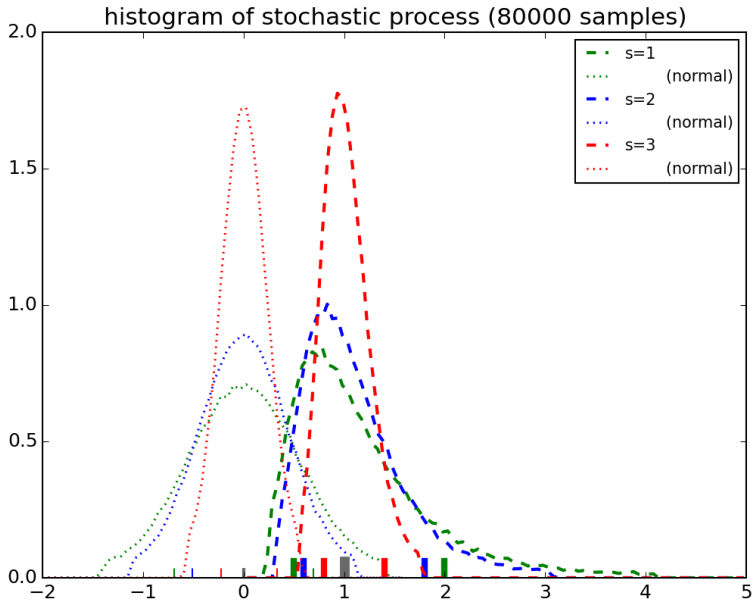

Figure 4.2: Histogram for the distribution density of the stochastic processes for the test case. Each color represents one of the three gridpoints (green: $s = 1$, blue: $s = 2$, red: $s = 3$). The small, thick lines at the x-axis indicate the assumed factors from the sensitivity analysis as given in Fig. 4.1. Their substituted values which serve as input for the KL ensemble algorithm are indicated by small, thin lines. The distributions of stochastic coefficients provided by the KL ensemble algorithm are shown as thin, doted lines. After the re-substitution to factors, the distributions are given by thick, dashed lines. The PDFs are approximated by 80000 samples.

4.2 Extensions

In addition to the core setup described above, some extensions to the KL ensemble algorithm are developed and implemented. These include the use of independent input sensitivities (Sec. 4.2.1) and the combination of different sources of uncertainties in the form of an additional a-priori uncertainty (Sec. 4.2.2). From a technical point of view, nesting of KL perturbations towards nested domains (Sec. 4.2.3) and handling of KL perturbation in WRF (Sec. 4.2.4) are also described shortly.

4.2.1 Independent Input Sensitivities

A main advantage of the KL ensemble algorithm is the efficient generation of perturbations enabling lower ensemble sizes and thus saving computational resources. However, calculating the covariances from a full case-dependent sensitivity analysis requires information on all combined sensitivities to uncertainties. An explicit calculation of these combined sensitivities requires large computational efforts which is in disagreement to the objectives. To overcome this issue, the approach of *independent input sensitivities* is derived in the following.

Generally, atmospheric models are sensitive to a number of *model arguments* of any kind. These arguments may be as diverse as initial conditions, external input information and formulation of model parameterizations. From a mathematical point of view, each model argument at each location $s \in S$ can be interpreted as *random parameter* with R_i different *realizations* $r_i \in \{1, \ldots, R_i\}$ for each random parameter $i \in \{1, \ldots, I\}$. In this context, realizations refer to different available options of each model argument, for example initial fields, sources of input information or selections of model parameterizations. These arguments affect simulated model parameters at all grid points denoted as locations s and $s' \in S$. Here, sensitivities to each random parameter are formulated as deviation from the reference forecast. Then the full set of *combined sensitivities* $Q_j^s, j \in \{1, \ldots, J\}$ consists of the sensitivities from all possible combinations of realizations $Q_j^s = Q_{r_1,r_2,\ldots,r_I}^s$. Thus, the total number of combined sensitivities which needs to be calculated is $J := \prod_{i=1}^{I} R_i$, which is impractically large for most cases.

Now let $q_i^s(r_i)$ be the set of I single sensitivities resulting from the modification of one single model argument $i \in \{1, \ldots, I\}$ with realization r_i. Note that all sensitivities are assumed to be defined in a way that the reference realization $r_i = 1$ of all random parameters results in zero sensitivity $q_i^s(1) = 0 \mid \forall\, i$. Then, the approach of independent input sensitivities is constructed in the following way, provided that the tangent-linear assumption of sensitivities is sufficiently valid:

Each combined sensitivity Q_j^s can be calculated from a linear combination of single sensitivities $q_i^s(r_i)$ by

$$Q_j^s = Q_{r_1,r_2,\cdots,r_I}^s = \sum_{i=1}^{I} q_i^s(r_i) \quad \Big| \quad \forall\, j \in \{1, \ldots, J\}\ ,\ r_i \in \{1, \ldots, R_i\} \quad . \tag{4.20}$$

Then at each location $s \in S$, all combined sensitivities Q_j^s lie within a vector space which is spanned by the set of single sensitivities $q_i^s(r_i)$. Consequently, the assumption of tangent linearity equals the treatment of single sensitivities q_i as independent of each other. Thus, the $q_i^s(r_i)$ are denoted as *independent sensitivities* from which all combined sensitivities can be inferred. Instead of calculating each Q_j^s explicitly, the effect on mean values and covariances are derived generally as presented in Appendix D. The derivation there considered two realizations of each random parameter $R_i = 2, \forall i \in \{1, \ldots, I\}$. In the derivation, all realizations of each random parameter are assumed to have the same probability or weight. During the KL ensemble generation, mean values $\mu(s)$ and covariances $C(s, s')$ are calculated from the set of independent sensitivities

$$\mu(s) = \frac{1}{2} \sum_{i=1}^{I} q_i^s(2) \tag{4.21a}$$

$$C(s, s') = \frac{2^I}{4\,(2^I - 1)} \sum_{i=1}^{I} \left(q_i^s(2) \cdot q_i^{s'}(2) \right) \quad , \tag{4.21b}$$

where $q_i^s(2)$ and $q_i^{s'}(2)$ are alternative realizations of independent sensitivities i at locations s and s', respectively. Note that the assumption of independence does not imply orthogonality between the input sensitivities. Thus, the solution of the eigenproblem for the KL expansion is not affected by this assumption. If independent input sensitivities are selected by the user, Eq. (4.21) replaces the usual calculation of mean value and covariances of the stochastic process. Thus, instead of calculating $J = 2^I$ combined sensitivities for two realizations each, only I independent sensitivities need to be calculated.

Although the equations are exact under the given assumption, the approach should be used with caution. The underlying assumption of independent input sensitivities is a strong criterion and may not be a sufficient approximation in many cases. Most atmospheric processes are dominated by nonlinear effects for which the solution of the KL ensemble would be biased. It has to decided if the computational benefit of independent input sensitivities justifies the neglection of nonlinear effects.

4.2.2 Additional Information about Uncertainties

Uncertainties in dependent model parameter may not only result from sensitivities to uncertain model arguments, additional unceratinties may originate from other sources including the model formulation. The idea of independent input uncertainties allows the inclusion of these additional information in a straightforward way. These additional information about uncertainties can be included as additional independent input uncertainty q_{add}.

Following the approach in Sec. 4.2.1, mean values and covariances are described as function of independent sensitivities $q_i^s(r_i), r_i \in \{1, 2\}, i \in \{1, \ldots, I\}$ at location $s \in S$.

Adding an additional independent uncertainty q^s_{add}, Eq. (4.21) becomes

$$\mu(s) = \frac{1}{2}\sum_{i=1}^{I} q_i^s(2) + q^s_{add} \tag{4.22a}$$

$$C(s,s') = \frac{2^I}{4\,(2^I-1)}\left[\sum_{i=1}^{I}\left(q_i^s(2)\cdot q_i^{s'}(2)\right) + \left(q^s_{add}\cdot q^{s'}_{add}\right)\right] \quad , \tag{4.22b}$$

where the total number of independent factors is now $I+1$.

If the direction of the additional uncertainty is unknown, the original definition of the mean values for independent input sensitivities given in Eq. (4.21a) is used in stead of Eq. (4.22a). This ensures no impact of the additional uncertainty to the mean value of the stochastic parameter.

In general, additional uncertainties may be obtained from any source, for example from validating the model forecasted parameter to available observations. As a example for additional uncertainties, the option of a constant a-priori uncertainty of the stochastic parameter is implemented into the model. Because of unknown direction of this uncertainty, Eq. (4.21a) for the mean values is left unchanged in this case.

The introduction of an additional a-priori uncertainty is especially important because all possible sources of uncertainties can hardly be covered by any sensitivity analysis. Defining an additional minimal uncertainty makes it possible to account for case where the uncertainty estimation by sensitivity analysis tends to underestimate related errors.

4.2.3 Nesting KL Perturbations

In the framework of nested grids, KL perturbations of a mother domain have also to be transferred to its nested domains. This *sequential* or *one-way nesting* of perturbations is required in order to ensure consistent perturbation in the nested domains. In EURAD-IM, horizontal one-way nesting was introduced by Jakobs et al. [1995] following the scheme of Pleim et al. [1991]. According to the implementation of nesting for other fields, the nesting process for KL perturbations is divided into two parts.

The first part consists of operations performed during the run of the mother domain. For each nested domain, a subset of the field of the current domain is written into an output file. The subset is defined by the start- and ending indices of the related nest within the current domain. In the second part, the nested domain reads the input file of the subdomain with the resolution of the mother domain. These coarse fields are then interpolated bi-linearly to the current nested grid.

4.2.4 Handling KL Perturbations in WRF

This work focuses on the perturbation of uncertain parameters in the EURAD-IM modeling system. Nevertheless, the perturbation of meteorological parameters in the WRF model is also tested. Aiming for an easy and appropriate environment to test KL perturbations within WRF, the existing KL ensemble algorithm within EURAD-IM is used.

As first step, the implementation of the KL ensemble algorithm in EURAD-IM is modified to handle meteorological parameters. For each parameter to perturb, a label defines to which model the parameter is referring to. Chemical parameters are handled as described in Sec. 4.1. In case of meteorological parameters, the following changes are implemented.

- If the covariances are calculated from a sensitivity analysis, the sensitivities are read from WRFout files.
- Skip the application of factors calculated by the KL ensemble algorithm.
- If at least one non-chemical parameter is perturbed, skip the complete forecast and finalize the run.

Except these few changes, the standard KL ensemble algorithm is used for calculating perturbations of all kinds of model parameters. Thus, if at least one meteorological parameter is perturbed, the only task of the EURAD-IM run is the generation of KL perturbations which are written into an output file.

During the second step, an ensemble of WRF runs using the KL perturbations is performed. As the original version of WRF 3.8.1 is not implemented in an ensemble environment, the ensemble of WRF runs is realized by a set of single runs. For each run, related perturbations are selected by a member number which can be defined in the namelist. According to this number, KL perturbation factors of the meteorological variables are read at the beginning of the WRF run. Later, the perturbed parameters are multiplied by these factors during the forecast.

As a last step, the set of WRF forecasts perturbed by fields generated by the KL ensemble algorithm may serve as input for an EURAD-IM ensemble forecast. The perturbed meteorology from the WRF runs serves as ensemble of meteorological inputs for the EURAD-IM ensemble. By additionally perturbing chemical parameters, this setup enables the application of joint perturbation of meteorological and chemical parameters.

5 Case Study Description

The developments described above are applied to a case study which tool place in northern Italy in summer 2012. The case study was selected because of excellent campaign measurements obtained from the PEGASOS campaign which is briefly introduced in Sec. 5.1. Sec. 5.2 gives an overview over the meteorological conditions during the campaign in the Po valley for June and July 2012. Sec. 5.3 provides general information on the modeling setup for the simulations shown in the following sections.

5.1 PEGASOS Campaign

The *Pan-European Gas-AeroSOls-climate interaction Study* (PEGASOS) was a project from 26 European partners (`http://pegasos.iceht.forth.gr/`). Its overarching goal was to investigate interactions between anthropogenic and biogenic emitted components and related impacts on air quality and climate change. For this purpose, different regions in Europe are investigated during two campaigns. The first part took place in the Netherlands and Italy between May and July 2012, including the transfer between both. The second part consists of a transfer from southern Germany to Finland in spring 2013.

For all campaigns, a Zeppelin NT (*New Technology*) served as airborne observational platform within the PBL. The Zeppelin offers the ability to fly in low altitudes with low airspeeds allowing for near-surface observations in a high spatial resolution (e.g. Rosati et al. [2016a]). Additionally, the Zeppelin can move into any desired horizontal and vertical direction. For example, vertical profiles can be derived from helical flight patterns. During the campaigns, a large number of in-situ instruments were located on top of the Zeppelin as well as in the gondola. In the latter, the instrument setup changed between different configurations focusing on photochemistry, nucleation or secondary organic aerosols (e.g. Jäger [2013]).

During the first part of the campaign from 18.06. to 13.07.2012, the Zeppelin performed 22 flights in total over the Po valley. This region is known to be one of the most polluted regions in Europe (e.g. Sogacheva et al. [2007]; Israelevich et al. [2012]; Finardi et al. [2014]; Kontkanen et al. [2016]; Sandrini et al. [2016]). On the one hand, the region is highly populated with about 20 million inhabitants (Finardi et al. [2014]). This comes along with a high amount of anthropogenic emissions from traffic, industry and power plants (e.g. Kontkanen et al. [2016]). On the other hand, the topography of the Po valley prevents the mixing and exchange of polluted airmasses (e.g. Sogacheva et al. [2007]). With the Alps in the northwest and the Apennine Mountains in the southwest, the valley is surrounded by mountains at three sides. The inner Po valley is dominated by a flat topography, supporting the development of a nocturnal inversion layer during nighttime (Li et al. [2014]). Thus, air quality in the Po valley is highly affected by both, local

emission and regional advection processes.

During PEGASOS, the base station of the Zeppelin was close to San Pietro Capofiume (SPC) in the south-eastern part of the Po valley. Being located approximately 30 km northeast of Bologna, SPC is classified as a urban background site (Kaiser et al. [2015]; Rosati et al. [2016b]). However, Sandrini et al. [2016] state that it might be affected by the Bologna urban area in case of south-westerly winds. The local surrounding of SPC is dominated by croplands like wheat and corn fields which were subject to intense harvesting during the campaign (e.g. Kaiser et al. [2015]).

Depending on the focus of each specific flight, the instrumental setup of the Zeppelin as well as the flight path and timing was adopted accordingly (see e.g. Jäger [2013] for an overview). Flight patterns are either vertical profiles by helical patters close to SPC or horizontal transects to different part of the Po valley. Flight number *F049* on 12.07.2012 is an example for a helical flight pattern which was performed close to Argenta. With a radius of about 1 km, the Zeppelin spanned altitudes from 50 m up to 750 m above ground between 03:20 and 09:20 UTC. In contrast, horizontal transects were performed to the central Po valley, the Adriatic Sea as well as the Apennine Mountains. During some of the flights to the Apennine Mountains – like flight number *F039* on 01.07.2012 – the Zeppelin followed a large valley towards Monte Cimone (2165 m a.s.l.). Most of the flights were performed in the early morning hours to investigate the morning development of the mixed layer. Using the Zeppelin as observational platform allows the investigation of different coexisting layers within the morning PBL (e.g. Rosati et al. [2016a]). Only on 07.07.2012, flight number *F045* was scheduled between 17:00 and 20:20 UTC to investigate effects of the weakening vertical mixing during the evening hours.

5.2 Meteorological Conditions

During the first half of July 2012, the large-scale weather in Europe was influenced by Rossby wave activity. Starting on 01.07.2012, a through extended from the British islands towards western Spain, causing south-western flow over central Europe. The trough was connected to several surface lows and frontal activity inducing cloudy and rainy conditions from Spain to Poland and Finland (Fig. 5.1a). As the Alps act as orographic boundary, the weather in northern Italy was influenced by a weak high pressure system over the Mediterranean Sea. Clear and partly foggy conditions with calm winds and and temperatures above 20 $°C$ were observed in the Po valley during the morning hours on 01.07.2012.

During the next days, the trough and related low pressure systems propagated in north-eastern direction. Afterwards, a cut-off low developed south of Iceland and started to separate from the polar vortex on 04.07.2012. On 07.07.2012, the center of the cut-off low was located over the British Islands (Fig. 5.1b). Again, a cold front over Poland influenced the local weather north of the Alps but did not affect the Po region. Instead, the weather in the Po valley could still be described by slow varying winds and clear sky conditions. This was still true on 12.07.2012, although a weak stationary front was analyzed in northern Italy (Fig. 5.2). On this day, the cut-off low has weakened and reconnected to the polar vortex over Scandinavia. At the same time, a new cut-off low

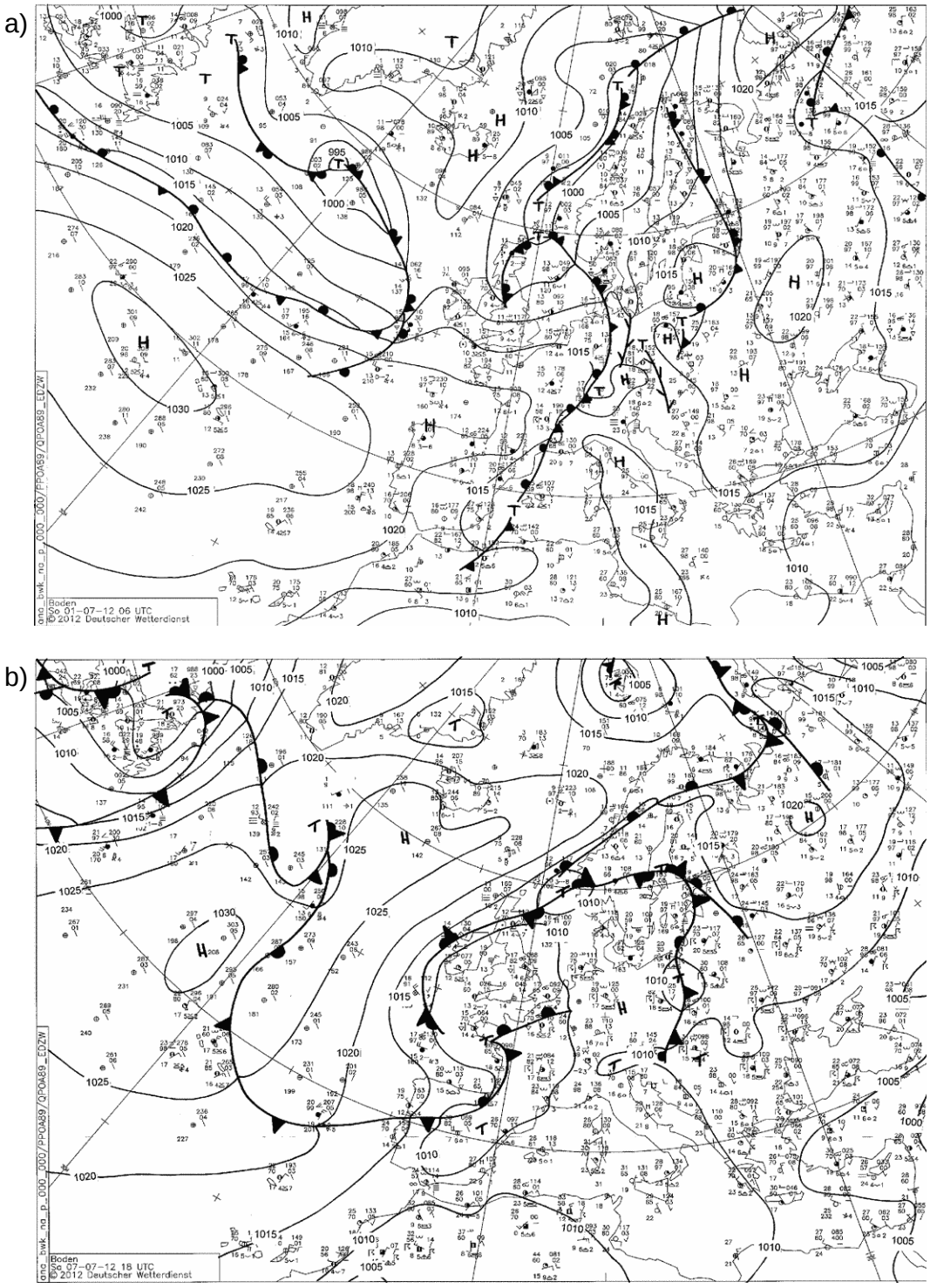

Figure 5.1: Analysis of surface pressure (isobars) and fronts from DWD on 01.07.2012 at 06 UTC (a) and 07.07.2012 at 18 UTC (b) from `http://www1.wetter3.de/archiv_dwd_dt.html` (assessed on 04.11.2019).

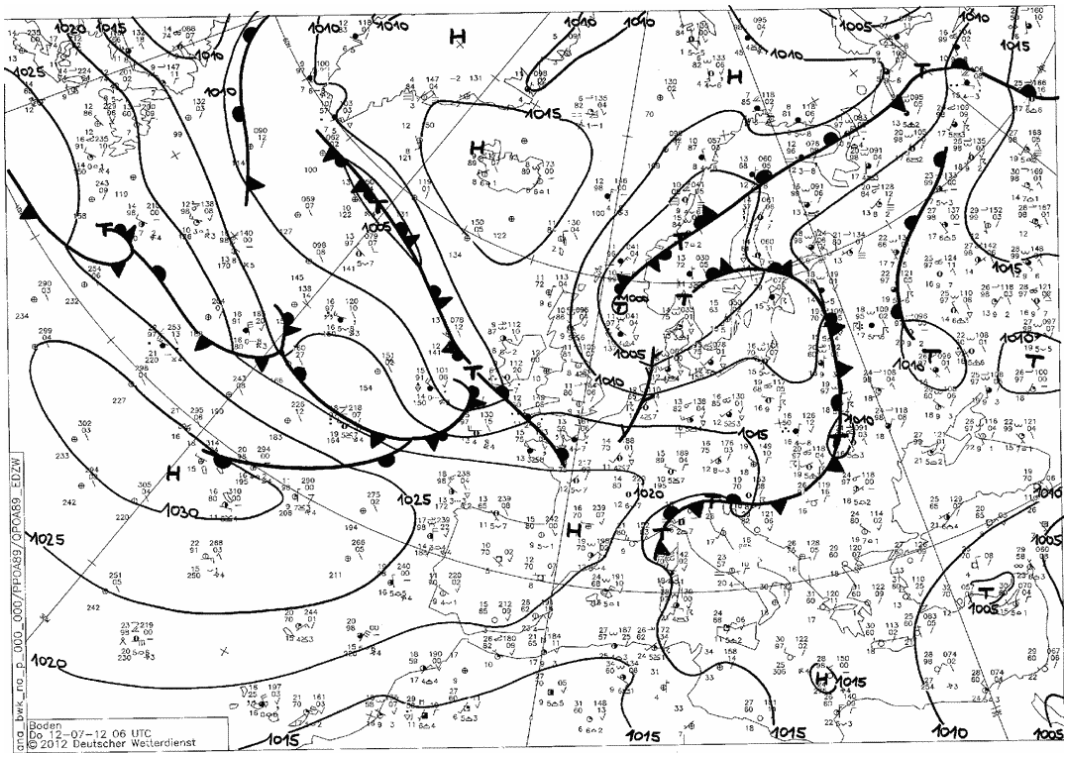

Figure 5.2: Analysis of surface pressure (isobars) and fronts from DWD on 12.07.2012 at 06 UTC from `http://www1.wetter3.de/archiv_dwd_dt.html` (assessed on 04.11.2019).

was formed and moved towards the North Sea. This new cut-off low reconnected again to a number of surface lows over northern Europe. Additionally, a large high pressure system formed over the Atlantic which induced westerly flow towards south-western Europe.

5.3 Model Setup

The results presented in this study focus on three days during the PEGASOS campaign in the Po valley 2012. The days 01.07., 07.07. and 12.07. are selected due to different objectives of related flights (compare Sec. 5.1). Most of the results are taken from the flight on 12.07. in order to show exemplary the behavior of the algorithm.

For the sensitivity analysis, the simulations of WRF and EURAD-IM are initialized one day before at 00 UTC, each. Where the set of meteorological forecasts of WRF serve as meteorological driver for the set of chemical forecasts by EURAD-IM. The simulations with the reference options serve as reference in the sensitivity analysis as well as basis for perturbations in the KL ensemble. Both models share the same domain and projection which is created by a Lambert-conformal projection with 15 km horizontal spacing. Based on this, a 5 km and a 1 km domain are driven by their respective mother domains by initial- and boundary conditions. The three domains of the EURAD-IM model are shown in Fig. 5.3. Depending on the nesting level, WRF domains have some additional grid

points at the lateral boundaries. The number of grid boxes of both models for the three domains as well as time step lengths are given in Tab. 5.1. The vertical layers are defines by terrain-following Sigma-coordinates with 23 levels reaching up to 100 hPa for both models.

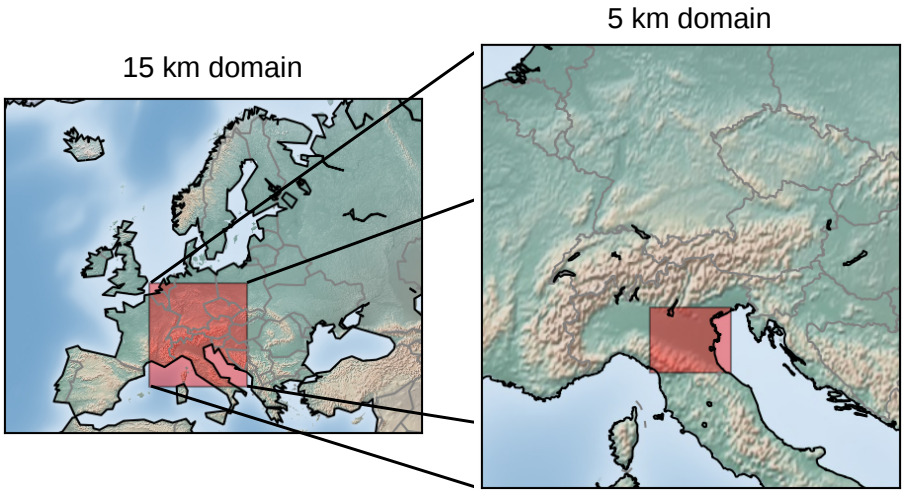

Figure 5.3: 15 km and 5 km domains of EURAD-IM. The nests of each mother domain are indicated in red.

Table 5.1: Number of gird boxes in south-north and west-east direction and time steps of WRF and EURAD-IM for all domains.

domain	**WRF**			**EURAD-IM**		
	S-N dim.	W-E dim.	time step	S-N dim.	W-E dim.	time step
15 km	288	350	30 s	287	349	300 s
5 km	256	241	20 s	253	238	60 s
1 km	191	236	20 s	186	231	20 s

6 Sensitivity Analysis

Ensemble generation based on the KL algorithm highly relies on covariances which are calculated from sensitivities of the model parameters. This section provides an analysis of different sensitivities which are used in the subsequent KL ensemble generation. Dealing with parameters which depend on meteorological fields, the sensitivity analysis focuses on different setups of WRF. Using an existing meteorological ensemble appears to be not sufficient for this application. An investigation of sensitivities from the global GFS (*Global Forecast System*) ensemble from NOAA did not induce significant differences within the boundary layer. Instead, sensitivities to model inputs and parameterizations are identified and investigated for biogenic emissions (Sec. 6.1), dry deposition velocities (Sec. 6.2) and dynamical parameters (Sec. 6.3). For biogenic emissions, the sensitivity to the formulation of soil moisture dependency in MEGAN 2.1 is additionally considered. For all parameters, sensitivities in the Po valley on 12.07.2012 between 03 and 09 UTC are investigated.

In the following, some general remarks regarding different input sources are shortly described. Initial- and boundary conditions for WRF are provided by global meteorological analyses. Here the IFS reanalysis (Hortal [1998]) provided by ECMWF (*European Centre for Medium-Range Weather Forecasts*) is used as reference and the related sensitivities are based on the operational GFS analysis from NOAA (Caplan et al. [1997]).

For WRF and EURAD-IM, reference information on land surface and vegetation types are given in the form of USGS (*U.S. Geological Survey*) land use categories. In WRF information on surface types are provided by the GLCC (*Global Land Cover Characteristics*) database. Based on AVHRR (*Advanced Very High Resolution Radiometer*) observations between April 1992 and March 1993, the surface at each location is classified as one USGS land use category (Loveland et al. [2000]). The USGS data base includes 24 different categories including water, urban, snow and ice as well as various vegetated surface categories (Anderson et al. [1976]). Although the database provides unsupervised surface classification, the occurrence of different surface types is treated by mixed categories (e.g. "Cropland/Woodland Mozaic").
Sensitivities are investigated by using land use information based on MODIS (*MODerate-resolution Imaging Spectroradiometer*) observations. Vegetation products from MODIS and Sentinel-2 satellites can give more recent information on spatial distributions and also temporal evolution of vegetation types. Currently Sentinel-2 provides vegetation products in the highest resolution (up to 10 m horizontal resolution, e.g. Immitzer et al. [2016]; Drusch et al. [2012]). However, these data are not available for 2012 as the satellite was launched in 2015. Thus, MODIS vegetation data are transferred to land use information for this case. Satellite observations by MODIS provide fractional land cover information with 1 km spatial resolution (Friedl et al. [2002]). Multiple studies indicate a more detailed and reliable characterization compared to AVHRR-based products (e.g. Smirnova et al. [2016]; Hansen et al. [2002]). However, the transformation to land use

suffers from missing information on non-vegetated surfaces in vegetation products. Thus, information on land use categories like urban areas, water, snow and ice are not given in the MODIS data. Assuming an appropriate representation of these basic surface types, the related information of USGS were also used in the MODIS-based classification. If the MODIS categories do not sum up to 100 %, the missing fraction is defined according to the USGS land use categories, if they are non-zero.

Predefined values of roughness length in WRF are found to underestimate true roughness in Europe. Related sensitivities to model parameters are investigated by modifying values of roughness length according to Berndt [2018]. A detailed list of original and modified values of different vegetation types is given in Appendix E.

WRF offers various options for different kinds of parameterizations. Here, sensitivities to the LSM, boundary- and surface layer parameterizations and cloud microphysics parameterizations as well as short- and longwave radiation parameterizations are considered. As boundary- and surface layer parameterizations are formulated together, related sensitivities are investigated together. The cumulus parameterization is not considered here as it is only used for the 15 km and 5 km domains. The 1 km resolution of the final domain is assumed to resolve related processes which obviate the need for a cumulus parameterization.

Tab. 6.1 summarizes the selected input sources and parameterization schemes considered in the sensitivity analysis as well as ensemble generation. For the selected case study, both microphysics and radiation schemes do not show significant effects on the selected parameters. Therefore, related sensitivities are not further discussed in this chapter. As significant sensitivities are expected in could cases, these parameterizations are still considered in the KL ensemble generation.

Table 6.1: Selection and description of input sensitivities. ECMWF = IFS reanalysis provided by ECMWF, GFS = GFS analysis provided by NOAA, PX = Pleim-Xiu surface layer parameterization, Du = Dudhia shortwave radiation parameterization. For further information on parameterization schemes in WRF see e.g Skamarock et al. [2008].

input source	**selected options**		**description**
	reference	alternative	
global	ECMWF	GFS	provider of global meteorological forecasts for initial- and boundary conditions in WRF
land use	USGS	MODIS	source of land use information (spatial distribution of PFT, LAI) in WRF and EURAD-IM
land surface	Pleim-Xiu	RUC	land surface model (LSM) in WRF
boundary layer	MYJ + Eta	ACM2 + PX	boundary layer- and surface layer parameterization schemes in WRF
microphysics	WSM6	TGS	cloud microphysics parameterization scheme in WRF
radiation	RRTMG	Du + RRTM	short- and longwave radiation parameterization schemes in WRF

6.1 Biogenic Emissions

According to the formulation of MEGAN 2.1, biogenic emissions may be sensitivities to vegetation type and -fraction, leaf area index, leaf age, solar radiation, air temperature and soil moisture (compare Sec. 3.2.1). In EURAD-IM, most of these data is provided as external input parameter from WRF. Therefore, the sensitivity analysis focuses on the uncertainties of these parameters by the meteorological forecast as described above. Additionally, the implementation of soil moisture dependency introduces additional sources of uncertainties. The sensitivity analysis focuses on isoprene and aldehyde representing different types of biogenically emitted gases. Note that biogenic aldehyde emissions from MEGAN 2.1 include total emissions from acetaldehyde and a set of higher aldehydes which are not treated individually (compare Guenther et al. [2012]).

Fig. 6.1 shows biogenic emissions of isoprene and aldehyde featuring different model input arguments. In general, biogenic emissions increase significantly around sunrise due to increasing solar radiation. The differences between nighttime (03 UTC) and daytime (09 UTC) emissions are more significant for isoprene than for aldehyde. This is because isoprene is a direct product of photosynthesis which is mainly limited to daytime conditions. For the reference setup, daytime isoprene emissions are mainly restricted to the Apennine Mountains and two areas within the the central Po valley north of Modena and Bologna. According to USGS land use, these locations are assigned to "Deciduous Broadleaf Forest" and "Crop/Woodland Mosaic", respectively. In contrast to "Dryland Cropland and Pasture" in the rest of the valley, broadleaf trees generate high amounts of isoprene. Thus, only small numbers of trees result in significantly increased local isoprene emissions. In these regions, increased biogenc emissions are also found for aldehyde. However, the differences between different land use types remain small compared to isoprene.

The high dependency on tree coverage is emphasized by comparing reference biogenic emissions to emissions based on MODIS land use. In contrast to USGS, MODIS does not indicate any tree within the Po valley. This results in neglectable isoprene emissions throughout large parts of the valley. At the same time, the whole Apennine Mountains and southern foothills of the Alps are assigned to high coverage of broadleaf trees. This results in dominating emissions of both biogenic gases in these regions for all presented times. For example, isoprene emissions at 6 UTC reach values of $1.0\frac{kg}{km^2h}$ north of Verona compared to maximal $0.2\frac{kg}{km^2h}$ in the reference case. In the Po valley, also aldehyde emissions of below $0.008\frac{kg}{km^2h}$ remain small compared to $0.02\frac{kg}{km^2h}$ in the reference. This states a exceptionally high sensitivity of biogenic emissions to uncertainties land use information.

The use of GFS global meteorology does not change the general emission patterns. Caused by different initial- and boundary conditions, slight differences are found thought the domain for both gases. At 06 UTC, somehow decreased biogenic emissions are visible in the central valley for GFS global meteorology. As biogenic emissions are not directly affected by roughness length, only minor differences are induced by changed local conditions.

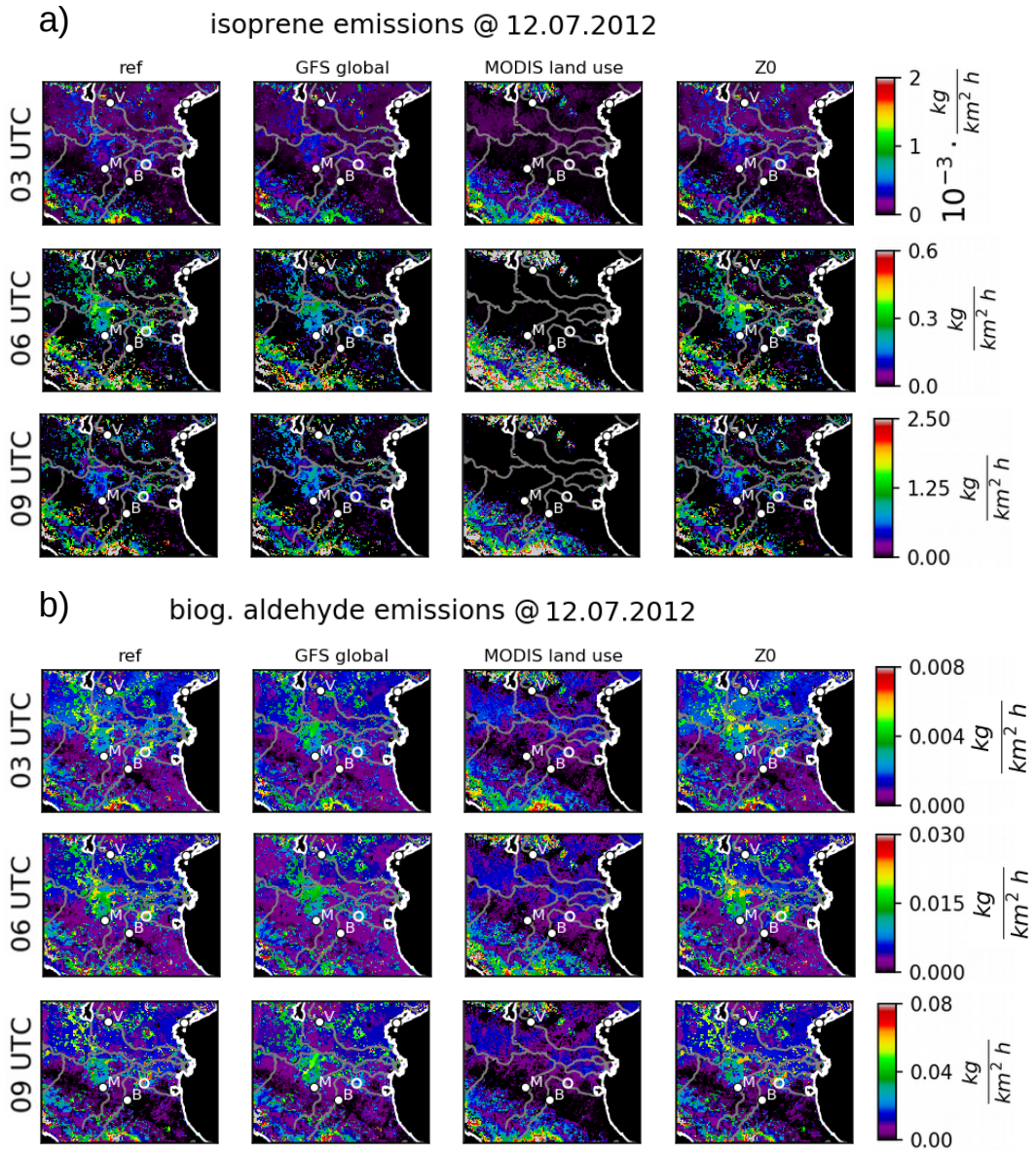

Figure 6.1: Isoprene (a) and biogenic aldehyde (b) emissions on 12.07.2012 at 03, 06 and 09 UTC (coded by colors) for different model input: reference, GFS global meteorology, MODIS land use, and modified roughness length (Z0). Some important cities (Verona, Bologna, Modena) are indicated by their initial letters. The location of the Zeppelin observations on this day is given as small circle.

Sensitivities of biogenic emissions to different options of LSMs and boundary layer parameterizations are shown in Fig. 6.2. Compared to the reference Pleim-Xiu LSM, both isoprene and aldehyde show differences for RUC LSM. For all times, emissions are reduced to almost zero in the south-eastern parts of the Po valley. This reduction is caused by low soil moisture predicted by RUC LSM which results in drought-induced plant stress. Comparing soil moisture predictions from Pleim-Xiu and RUC LSM in the

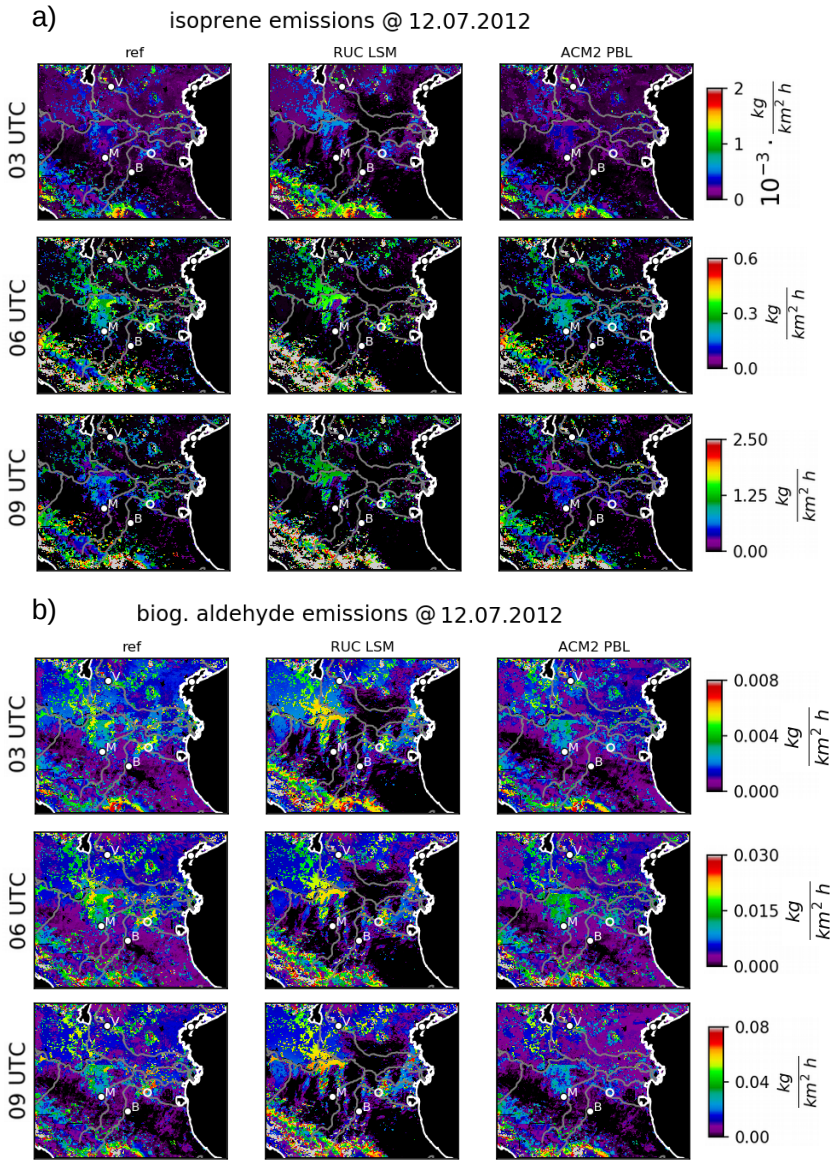

Figure 6.2: Isoprene (a) and biogenic aldehyde (b) emissions on 12.07.2012 at 03, 06 and 09 UTC (coded by colors) for different WRF LSMs and boundary layer schemes: reference (Pleim-Xiu LSM + MYJ PBL), RUC LSM and ACM2 PBL. Plotting conventions as in Fig. 6.1.

Po area shows general differences concerning the temporal evolution. For Pleim-Xiu, soil moisture drops during daytime and fast recovery during nighttime. In contrast, RUC predicts a continuous decrease in soil moisture during these days. Thus, the implemented reduction of emissions for all biogenic gases results in neglectable emissions in these areas for RUC LSM. In the rest of the domain, biogenic emissions are increased by RUC LSM where the largest differences to the reference emissions are found in the Apennines.

The combined effect of boundary layer- (PBL) and surface layer (SL) parameterization is found to be small for both gases. Slight reductions in biogenic emissions are predicted by ACM2 PBL + Pleim-Xiu SL compared to the reference using MYJ PBL + Eta SL schemes. For isoprene, these differences are mainly restricted to the areas of high emissions in the central Po valley. For aldehyde, the reduction extends also towards the north-eastern part of the valley.

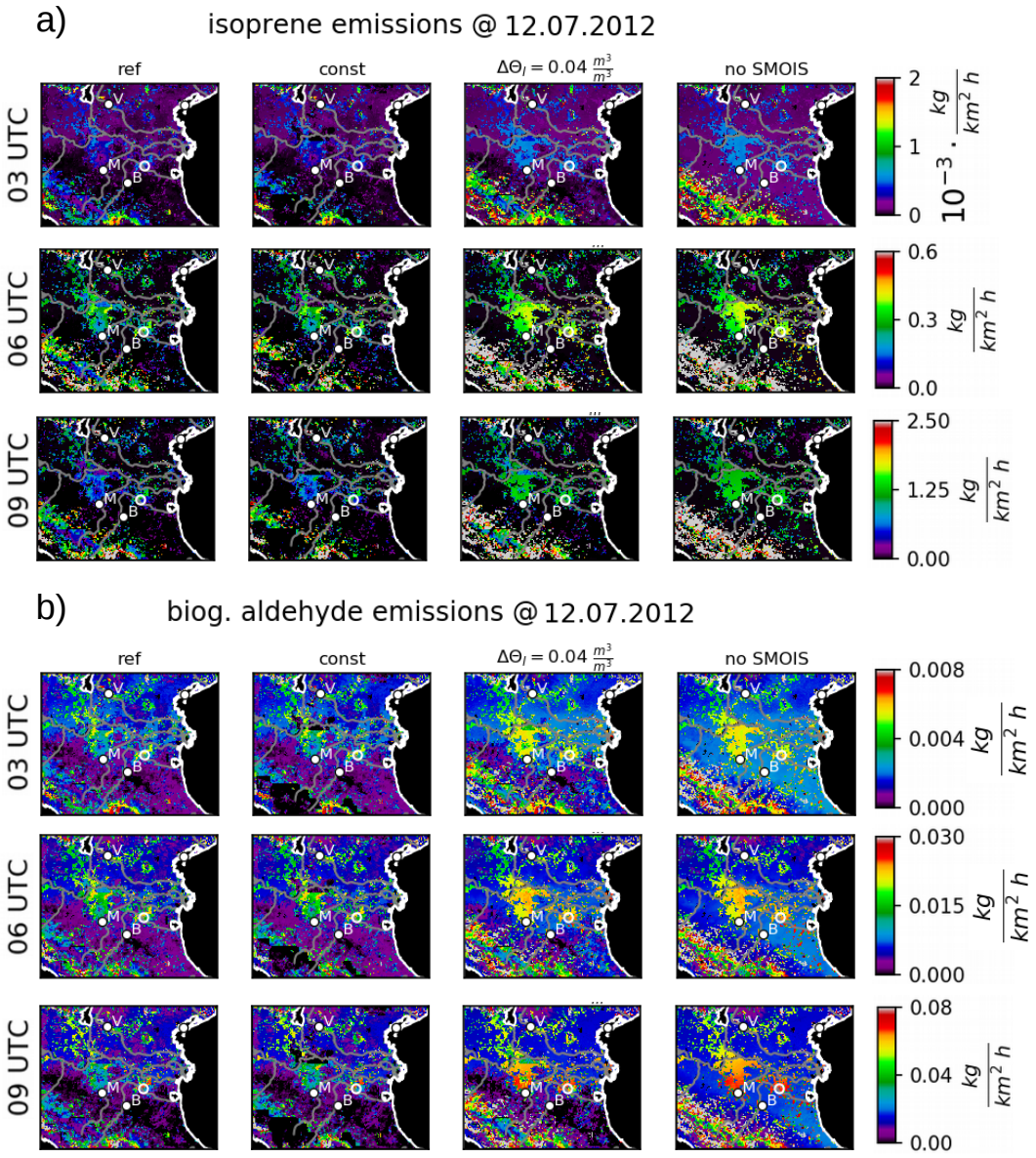

Figure 6.3: Isoprene (a) and biogenic aldehyde (b) emissions on 12.07.2012 at 03, 06 and 09 UTC (coded by colors) for different effects of soil dryness in MEGAN 2.1: reference ($\Delta\Theta = 0.10\frac{m^3}{m^3}$ and Θ_w depending on soil type), constant Θ_w for all soil types, $\Delta\Theta = 0.04\frac{m^3}{m^3}$ and no dependency on soil dryness ("no SMOIS"). Plotting conventions as in Fig. 6.1.

The formulation of emission reduction due to soil dryness influences the biogenic emissions of both gases (Fig. 6.3). Defining a constant wilting point Θ_w for all soil types results in distinct areas of neglectable emissions ("const"). These regions are assigned to "Sandy Loam" and "Loam" soil which are assigned to comparably low wilting points of $0.047\frac{m}{m}$ and $0.066\frac{m}{m}$, respectively. At the same time, the predicted soil moisture is significantly smaller at these locations which almost compensates the low wilting point in the reference case. But if the low wilting points are replaced by a higher constant value, soil-related differences in emissions are not considered and biogenic emissions are dropped to zero - independent of the emitted gas.

Completely ignoring the reduction of biogenic emissions due to soil dryness affects the emissions through the domain ("no SMOIS"). For all times, emissions of both gases are significantly larger than the references, especially in the south-eastern valley and the Apennine Mountains. As soil moisture decreases after sunrise, the largest sensitivities are found at 09 UTC for both gases. At this time, differences in isoprene and aldehyde emissions are of the order of factor 2 to 3. In areas with "(Sandy) Loam" soil, emissions do even differ by a factor up to 5.

Increasing the slope of soil moisture dependency from $\left(0.10\frac{m^3}{m^3}\right)^{-1}$ to $\left(0.04\frac{m^3}{m^3}\right)^{-1}$ results in intermediate biogenic emissions between the reference and "no SMOIS" case. Here, the reduction of emissions is mainly restricted to the south-eastern part of the Po valley close to the Apennines.

6.2 Dry Deposition Velocities

The implemented approach for dry deposition described in Sec. 3.2.2 includes various potential sources of uncertainties. Due to missing information, uncertainties regarding the deposition model itself (errors in the observational basis, approximation of processes, unspecified dependencies) are not considered here. Nevertheless, uncertainties of required input fields are assumed to contribute significantly to the overall uncertainty of dry deposition (eg. Wesely and Hicks [2000]). Following the description in Sec. 3.2.2, simulated dry deposition velocities may be sensitive to land use information as well as meteorological fields like air temperature, water vapor, radiation and friction velocity. Although effects of soil moisture are not directly considered, an possible indirect sensitivity via surface wetness is also analyzed.

Reference dry deposition velocities of HNO_3 and aldehyde in Fig. 6.4 differ significantly between daytime and nighttime conditions. Before sunrise (03 UTC), large HNO_3 deposition velocities are found at the peaks of the Apennine Mountains. While dry deposition at these locations reduces slightly after sunrise, low values in the rest of the domain increase significantly. Although aldehyde deposition velocities are generally smaller, the strong increase of deposition velocities in that area is also visible here. In the Po valley, aldehyde deposition velocities at 03 UTC are approximately one order of magnitude smaller compared to 06 and 09 UTC. Between 06 and 09 UTC, dry deposition velocities of both gases do only increase little at most locations.

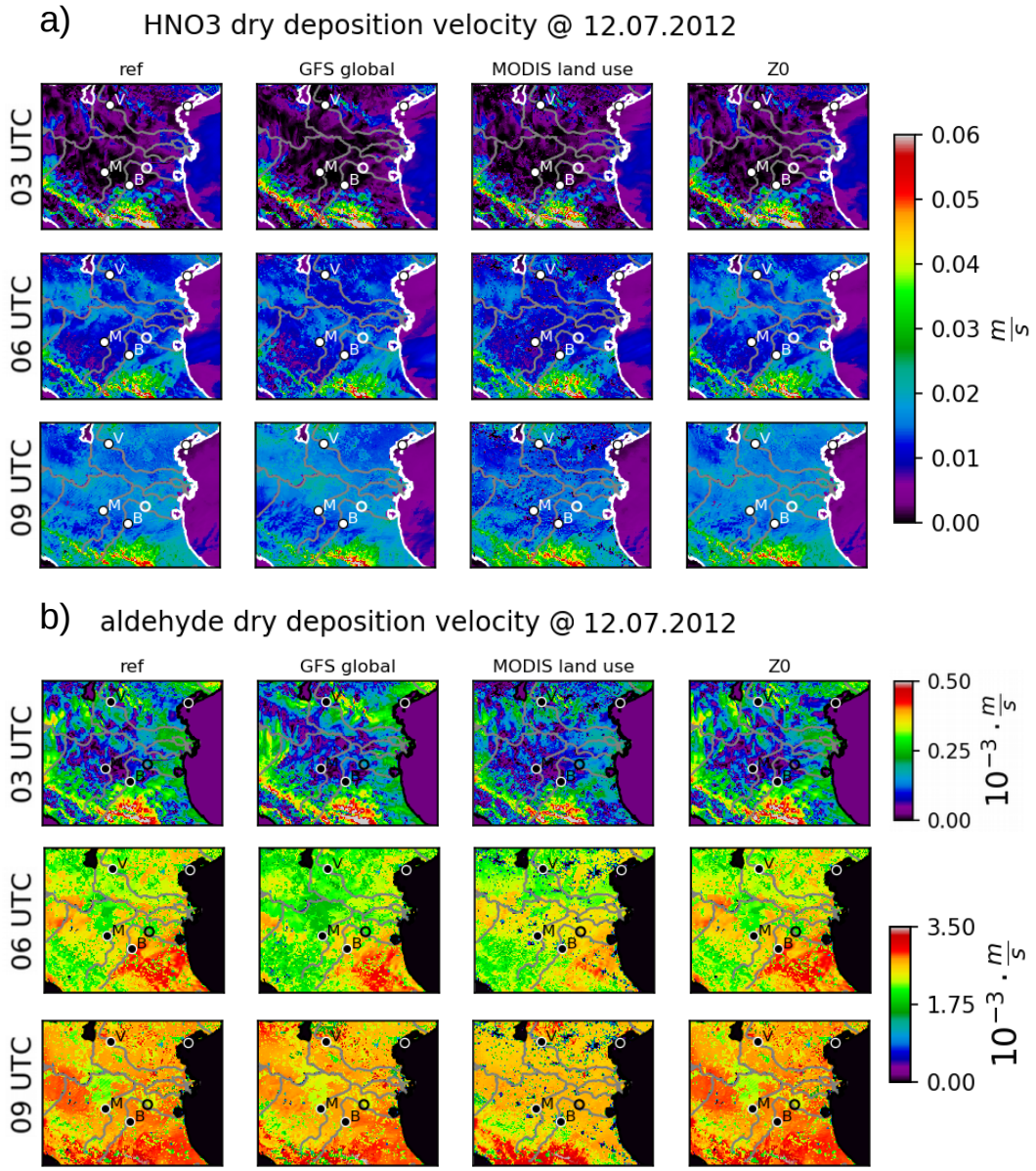

Figure 6.4: Dry deposition velocities of HNO_3 (a) and aldehyde (b) on 12.07.2012 at 03, 06 and 09 UTC (coded by colors) for different model input: reference, GFS global meteorology, MODIS land use, and modified roughness length (Z0). Plotting conventions as in Fig. 6.1.

Several dependencies to meteorological parameters induce sensitivities of dry deposition velocities to global meteorological input. Both gases indicate a small overall reduction of deposition velocities for GFS global meteorology compared to the ECMWF reference. Only at 09 UTC, deposition velocities are slightly increased north of Modena.

Large differences are found in deposition velocities of both gases with respect to land use. Most prominent is a reduction in urban areas according to USGS land use information. This is caused by an imperfect overlap of non-vegetated regions in MODIS and

urban land use in USGS. Usually, USGS urban land use is also applied to locations with missing information in MODIS (see beginning of this Chapter). However in case of non matching locations, missing land use information from MODIS remains, which results in neglectable deposition velocities.

In the rest of the Po valley, dry deposition velocities are slightly reduced for MODIS land use. The same classification of land use in the entire valley results in comparably smooth distributions of dry deposition. At 09 UTC, aldehyde deposition velocities are increased in the southern part of the Apennine Mountains compared to the reference simulation. As expected from the formulation of deposition velocities, changing roughness length does not significantly affect dry deposition velocities of both gases.

Fig. 6.5 shows regional differences in dry deposition velocities with respect to the LSM and boundary layer parameterizations. For both gases, RUC LSM indicates larger deposition velocities in the central Po valley compared to the reference Pleim-Xiu LSM. This region of increased values is found to be almost constant in time as it appears for all times shown. In the rest of the domain, sensitivities due to the LSM remain small.

Also sensitivities to boundary layer- and surface layer parameterizations are similar for both gases. After sunrise, the ACM2 PBL + PX SL schemes indicate locally changed deposition velocities in different parts of the domain. For example, decreased values are found at the north-western edge and south-west of Modena at 06 UTC. At the same time, increased deposition velocities are visible in the north-east around Venice.

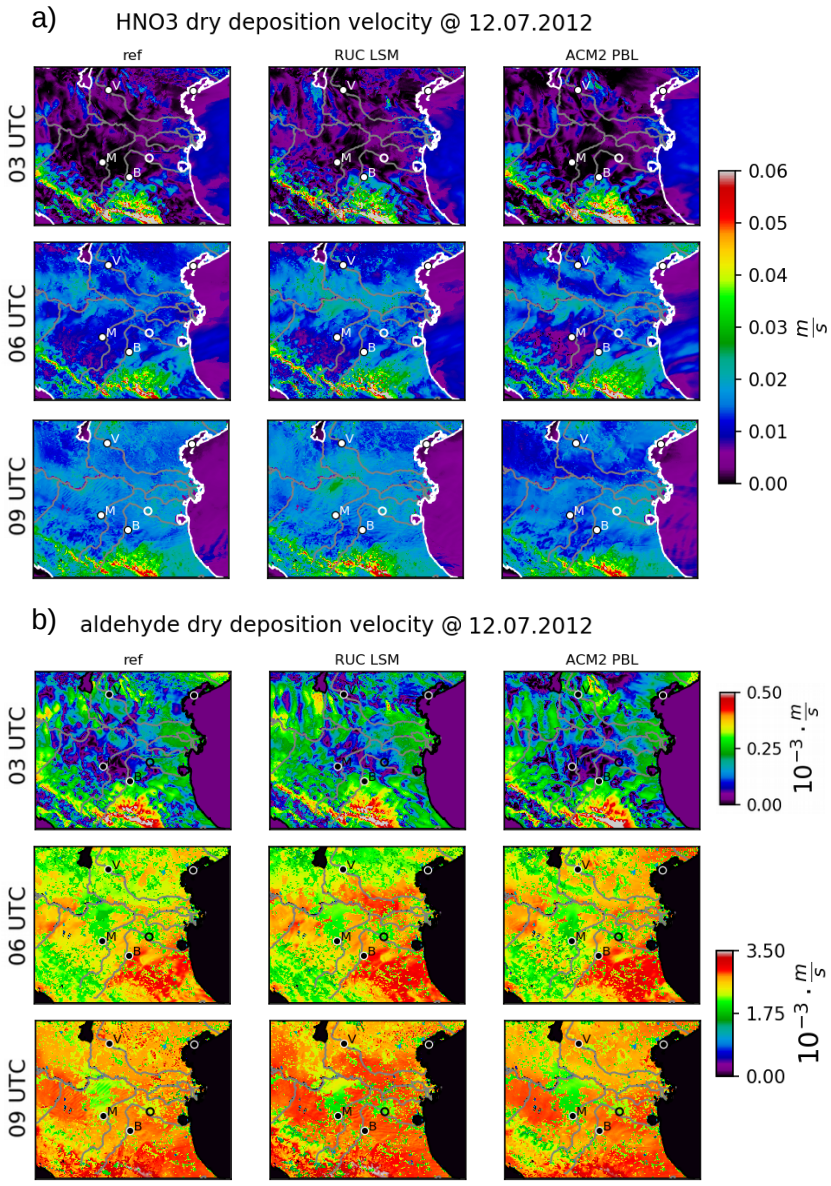

Figure 6.5: Dry deposition velocities of HNO_3 (a) and aldehyde (b) on 12.07.2012 at 03, 06 and 09 UTC (coded by colors) for different WRF LSMs and boundary layer schemes: reference (Pleim-Xiu LSM + MYJ PBL), RUC LSM and ACM2 PBL. Plotting conventions as in Fig. 6.1.

6.3 Dynamics

Besides emissions and deposition, regional atmospheric dynamics may induce significant sensitivities by transport and mixing of pollutants. Firstly, potential effects of local dynamics on the source regions of air masses are analyzed (Sec. 6.3.1). Afterwards, sensitivities of different dynamical parameters are investigated, which might influence local dynamics in the boundary- and surface layer. The sensitivity analysis focuses on friction velocities (Sec. 6.3.2) and surface exchange coefficients (Sec. 6.3.3), which are perturbed by the KL ensemble later on.

6.3.1 Source Regions

Some studies are available that investigate the history of airmasses in the Po valley. However, these studies focus on long-term characteristics based on backward trajectories (Sogacheva et al. [2007]; Pernigotti et al. [2012]). This approach does not account for sensitivities of source regions to uncertainties in transport and mixing. Here, these sensitivities are analyzed using probabilistic retroplumes for an exemplary airparcel. The selected airmass is located at the position of the Zeppelin observations ($44.7°N$, $11.6°E$, "*target location*") on 12.07.2012 at 06 UTC ("*target time*") in 100 m height above sea level. Starting at this time, the retroplume calculation provides relative contributions of source areas of this airmass backward in time.

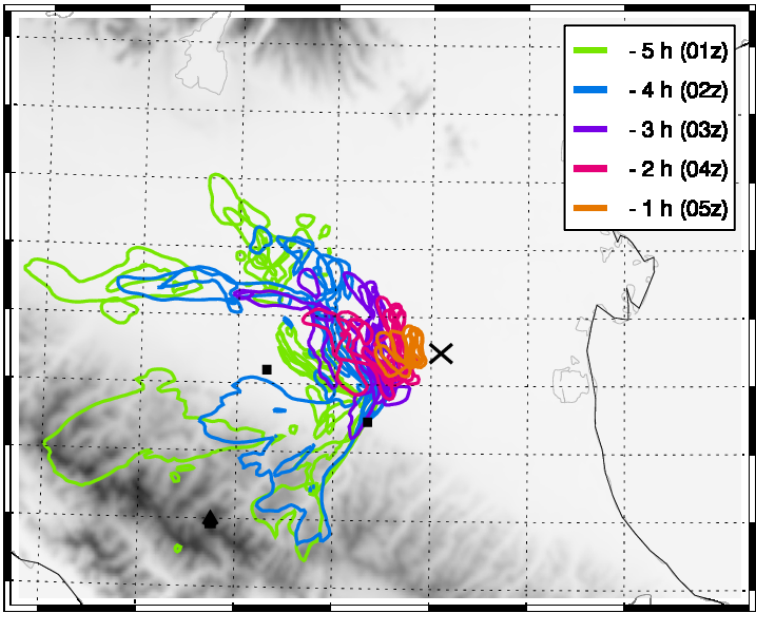

Figure 6.6: Horizontal distribution of source regions for $44.7°N$, $11.6°E$ and 100 m a.s.l. (black cross, "target location") at 12.07.2012, 06 UTC. Significant contributions to vertically integrated source regions for each setup are given as isolines (colored by time according to legend). Gray colors indicate the surface topography. The most important cities (Bologna, Modena) are marked with black squares. The peak elevation of Monte Cimone is indicated by a black triangle.

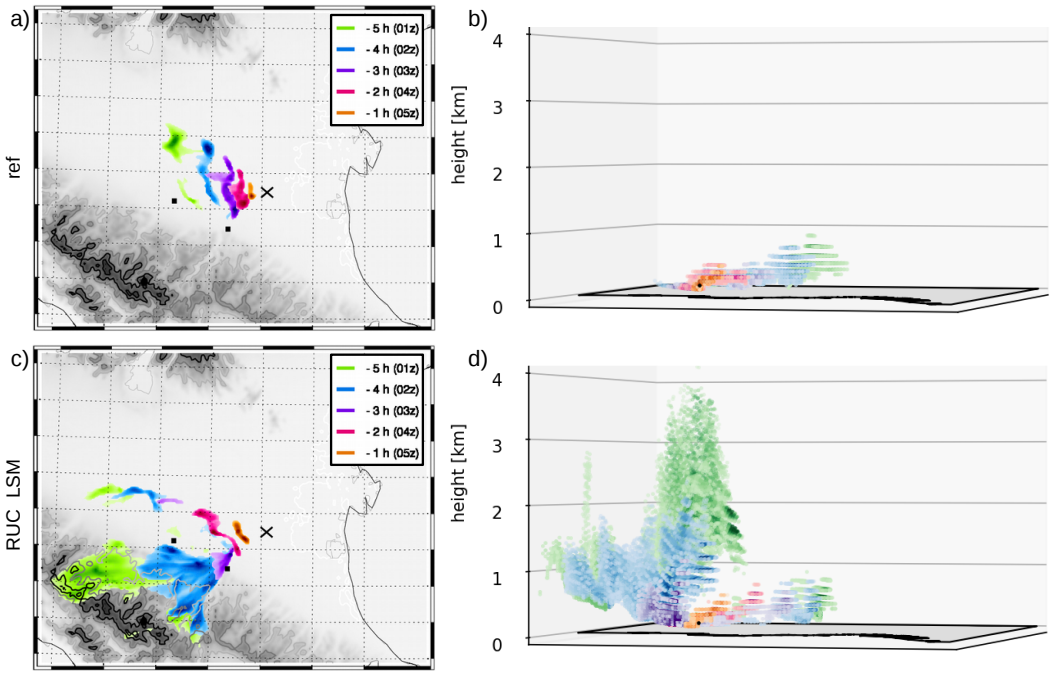

Figure 6.7: Horizontal- and vertical- distribution of source regions for reference (a and b) and RUC land use (c and d). Plotting conventions for (a) and (c) as in Fig. 6.6. For (b) and (d), the viewing direction is from east-northeast towards west-southwest.

Fig. 6.7a+b show the evolution of source regions for the reference setup. The selected airmass is advected from western to north-western directions due to slow westerly winds. During the last 3 hours before the target time, the airmass in influenced by meredional mixing processes. Thus, contributions of this airmass converge from south-western to north-western directions at this time. Going back towards 5 hours before, the major source of the airmass is found north-west of the target location. During the entire time interval, the vertical extension of source areas remains below 1 km altitude (Fig. 6.7a). This is caused by low vertical mixing, which is typical for the early morning hours over flat terrain.

Based on this reference source region, retroplume calculations are performed with changed model input and parameterization schemes given in Tab. 6.1. Horizontal distributions of hourly source areas for the resulting probabilistic retroplumes are shown in Fig. 6.6. The single source regions of the individual sensitivity runs are given in Appendix F. Horizontal source areas of the individual runs start to diverge already during the first hours before the target time. Three hours before, significant contributions are analyzed to range from Bologna in the south-west to the western central Po valley in the north-west.

Five hours before, additional effects can be seen. Transport distances from the selected target location varies more than a factor of two. For example, source regions for the ACM2 boundary layer parameterization almost extend to the western boundary of the domain

within 5 hours. This indicates increased turbulent transport by ACM2 BL + Pleim-Xiu SL compared to the reference MYJ BL + Eta SL. In contrast, Dudhia + RRTM radiation as well as MODIS land use indicate high contributions of western source regions with slow transport. In this case, the airmass originates from urban areas close to Modena and Bologna. Compared to mainly agricultural source areas by the reference and ACM2, these slight changes in local dynamics may result in significant changes in the composition of this airmass.

The RUC LSM has the largest effect on the simulated airmass history (Fig. 6.7c+d). In the horizontal, a major contribution to the airmass was transported from south-western directions crossing Bologna. Before that, it descended from the Apennine Mountains where high winds speeds advect air from comparably remote source regions. This is related to increased mixing processes which result in large extended source regions 4 hours before. Between 4 and 5 hours before, the evolution of horizontal source areas indicates convergence of two main airmasses flowing around the highest peaks of Monte Cimone with altitudes of more than 2000 m a.s.l. (Fig. 6.7c). The overflow above the Apennines forces the airmass to source altitudes of up to 4 km a.s.l. 5 hours before reaching the target time (Fig. 6.7d). Additionally, a small contribution of the airmass originates from a narrow valley south-west of Bologna. This valley is almost perfectly orientated towards the target location, which allows source altitudes of about 0.5 km a.s.l. (lower left part of Fig. 6.7d). Slower wind speeds within the valley force the source signal to stay within the valley even 5 hours before.

This exemplary analysis of source regions of airmasses states high sensitivities to the selected model inputs and parameterizations. Differences in horizontal- and vertical transport as well as mixing of airmasses may induce significant uncertainties to chemical composition. The largest differences of source regions are found with respect to the LSM as well as boundary layer- and surface layer parameterizations. Thus, parameters determining local transport and mixing are assumed to be closely related to these parameterizations.

6.3.2 Friction Velocity

In general, friction velocity does not change substantially between night- and daytime but increase in most areas with increasing local instability. For the reference setup in Fig. 6.8, high values of more than $1.0\frac{m}{s}$ are predicted at 03 UTC over the peaks of the Apennines. In the rest of the domain, friction velocity remains below $0.2\frac{m}{s}$ at this time. These large differences reduce over time by increasing average values and slightly decreasing peak values. At 09 UTC, friction velocity reaches values between $0.3\frac{m}{s}$ and $0.5\frac{m}{s}$ trough the domain except the southern Apennines.

GFS global meteorology indicates a slightly reduced friction velocity in the central Po valley for all times. Additionally, a small area of increased values are predicted east of Verona at 03 UTC. Sensitivities to land use information appear only on small scales. Using MODIS instead of USGS, friction velocity is partly increased in the north-eastern part of the domain. Friction velocity appear also to be not very sensitive to changes in roughness length. Increasing roughness length induces only a very slight tendency to increased of low values after sunrise.

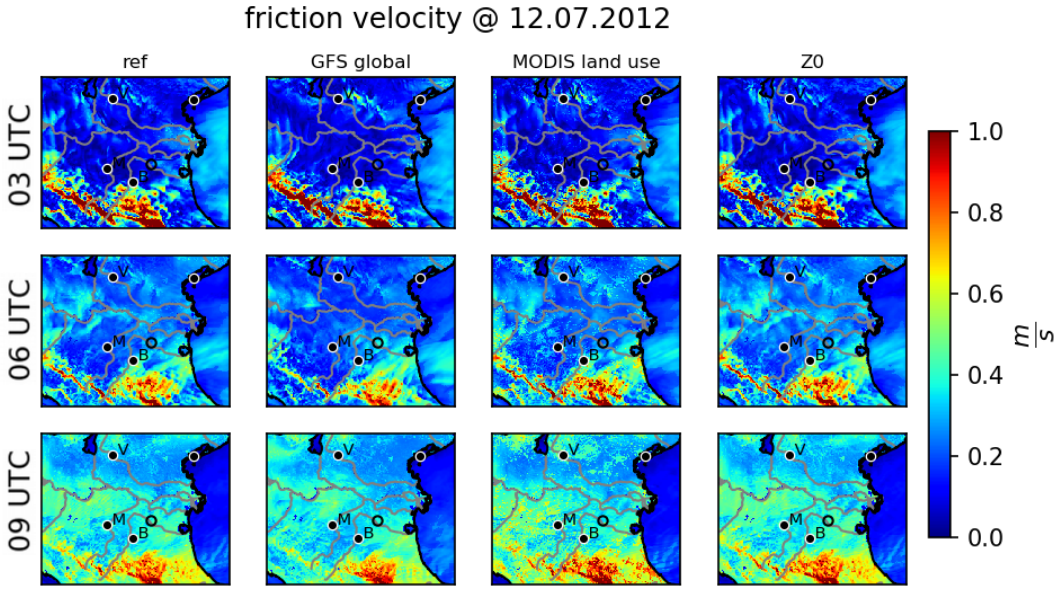

Figure 6.8: Friction velocities on 12.07.2012 at 03, 06 and 09 UTC (coded by colors) for different model input: reference, GFS global meteorology, MODIS land use, and modified roughness length (Z0). Plotting conventions as in Fig. 6.1.

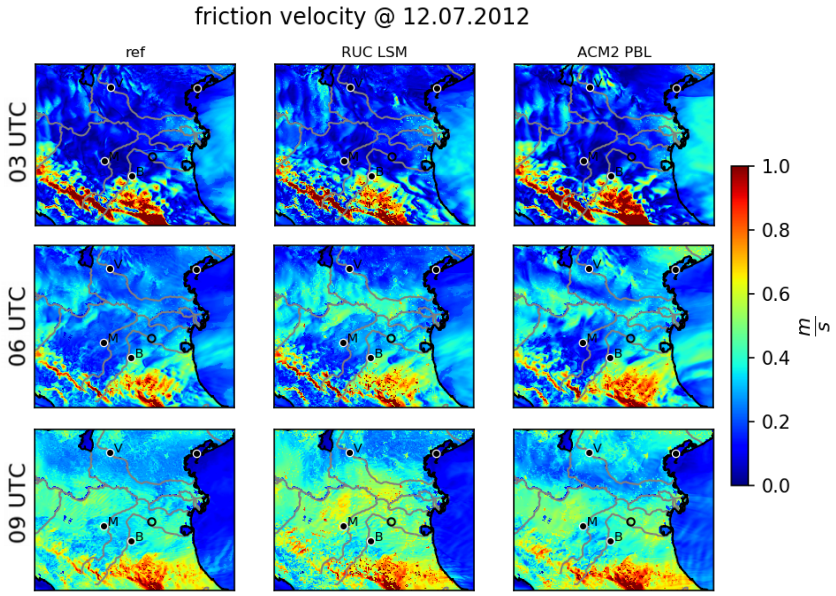

Figure 6.9: Friction velocities on 12.07.2012 at 03, 06 and 09 UTC (coded by colors) for different WRF LSMs and boundary layer schemes: reference (Pleim-Xiu LSM + MYJ PBL), RUC LSM and ACM2 PBL. Plotting conventions as in Fig. 6.1.

According to Fig. 6.9, the selection of the LSM influences friction velocity for all times. Already at 03 UTC, RUC LSM triggers a region of increased values south of Lake Garda. This signal penetrates along the Po river affecting large parts of the valley from 06 to 09 UTC. For example at 06 UTC, friction velocities in the central Po valley are increased by about a factor of 2 compared to the reference Pleim-Xiu LSM.

Using the ACM2 boundary layer parameterization instead of MYJ results also in different local dynamics. Similar to the sensitivity to the LSM, friction velocity is partly increased in the central Po valley. However, this effect is less pronounced and regions of high values change with time. At the north-eastern edge north of Venice, friction velocity is increased for all times.

6.3.3 Surface Exchange Coefficients

Surface exchange coefficients for heat and momentum are defined in the reference Eta surface layer parameterization (see also Appendix A.1). By considering these two parameters, both thermal and dynamical effects are expected. However, these parameters are specific for this parameterization and do not appear in other surface layer schemes in a similar way. This restricts the sensitivity analysis to parameterizations which can be combined with the Eta surface layer scheme. Because this is not the case for the ACM2 boundary layer scheme, the MYNN scheme is used for sensitivities to boundary layer parameterization. Nevertheless it should be kept in mind that the sensitivity to the surface layer parameterization itself cannot be included for these parameters.

At 03 UTC, reference fields of surface exchange coefficients in Fig. 6.10 appear to be very similar for heat and momentum. Both coefficients are by far largest over the peaks of the Apennines with varying low values in the rest of the domain. After sunrise, exchange coefficients increase in low altitudes where momentum coefficients show more noisy patterns. Besides that, coefficients of heat and momentum at 06 UTC are approximately of same size in the Po valley. At 09 UTC, arboreous regions in the Po valley become visible in terms of increased momentum exchange. For all times, peak values of exchange coefficients in the southern Apennines are about twice as large for momentum than for heat.

For GFS global meteorology, both coefficients are reduced in the central Po valley and at the boundary to the Apennines south-west of Modena. However, this effect becomes less prominent at daytime (09 UTC).

Land use information influence exchange of momentum much more than heat. Momentum exchange highly depends on local vegetation distributions related to different surface roughness. Land use specific patterns of momentum coefficient start to evolve around sunrise resulting in significant difference at 06 UTC and 09 UTC. At these times, distinct areas of increased values of about a factor of 2 are visible close to urban areas for MODIS. In contrast, the arboreous regions indicated by USGS in the central Po valley cause somehow increased momentum coefficients in the central valley which are not visible for MODIS.

For increased values of roughness length, momentum coefficients are increased accordingly at all times. This effect is caused by a direct dependency of surface momentum

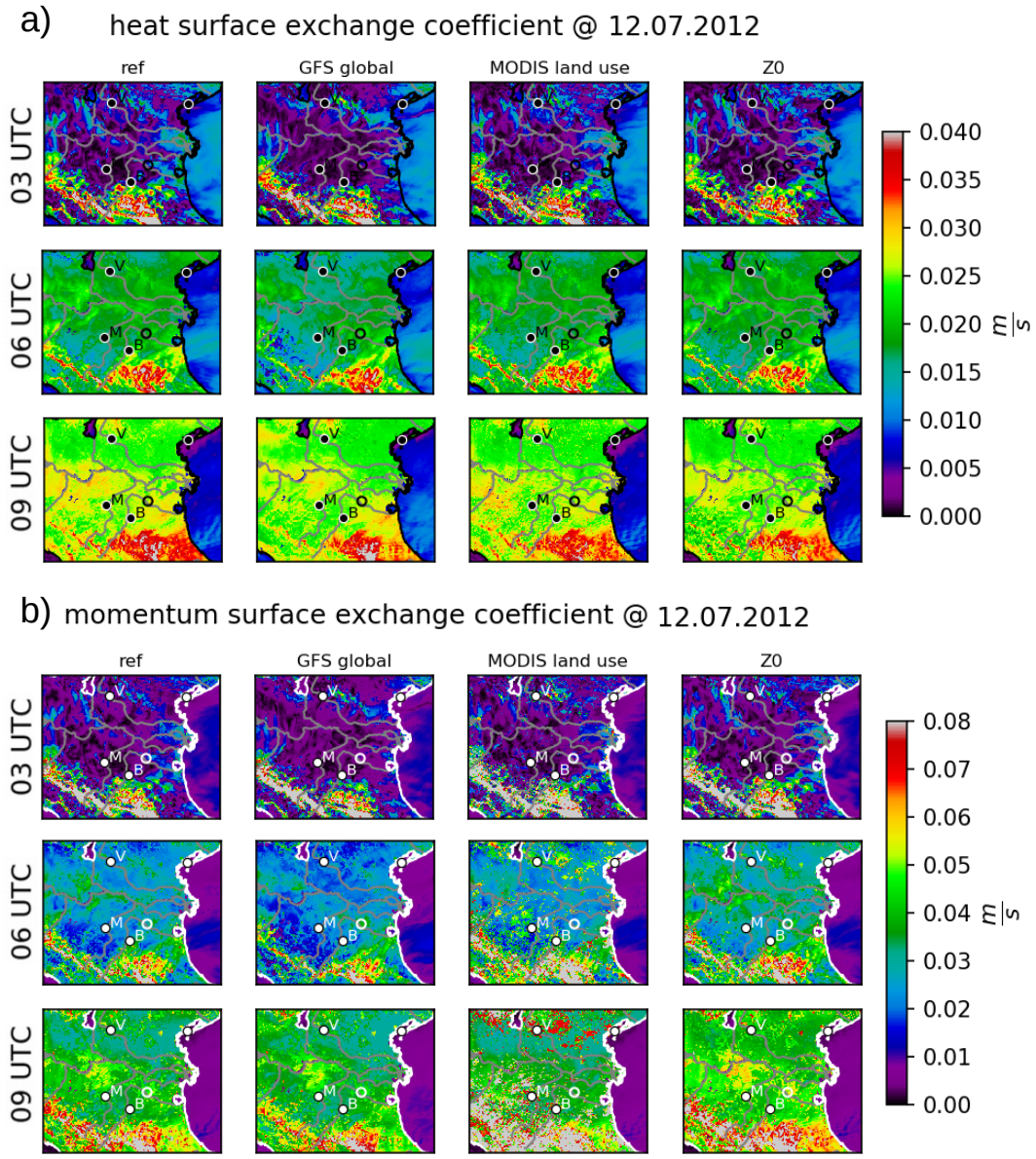

Figure 6.10: Heat- (a) and momentum (b) surface exchange coefficients on 12.07.2012 at 03, 06 and 09 UTC (coded by colors) for different model input: reference, GFS global meteorology, MODIS land use and modified roughness length (Z0). Plotting conventions as in Fig. 6.1.

exchange to the surface roughness. At 09 UTC, heat exchange coefficients are also slightly influenced. Here, the increased roughness length induce a reduction of heat exchange through the domain with largest differences in the south-western Apennines.

Changing the LSM from Pleim-Xiu to RUC in Fig. 6.11 results in generally increased surface exchange for both, heat and momentum. Similar to the sensitivities of other parameterizations, the effect increases with time after sunrise, where absolute differences are largest in the central Po valley. At 06 and 09 UTC, an additional sensitivity appears

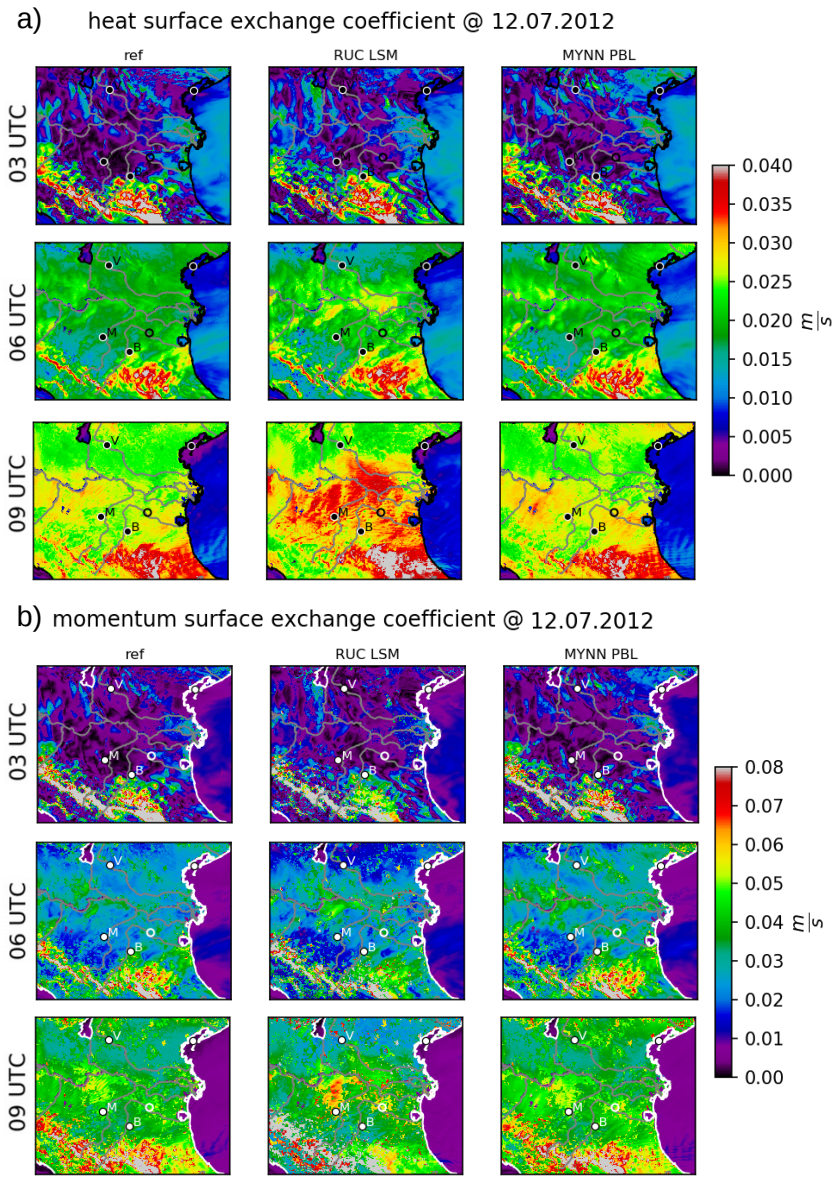

Figure 6.11: Heat- (a) and momentum (b) surface exchange coefficients on 12.07.2012 at 03, 06 and 09 UTC (coded by colors) for different WRF LSMs and boundary layer schemes: reference (Pleim-Xiu LSM + MYJ PBL), RUC LSM and ACM2 PBL. Plotting conventions as in Fig. 6.1.

close to the Alps and Apennines south west of Modena. This signal points into opposite directions for heat and momentum coefficients. While heat exchange is increased in this region, momentum exchange is reduced compared to the reference LSM.

Using MYNN instead of the reference MYJ boundary layer scheme does also result in increased exchange coefficients. Here, largest differences can be found in the north-eastern edge of the domain and a small region west of Modena. But these sensitivities remain smaller than for LSM at all locations and times.

6.4 Implications for KL Ensemble Perturbation

In the following, the results of the sensitivity analysis are summarized with respect to applicability to the KL ensemble algorithm. Firstly, the current setup of the KL ensemble relies on sensitivities from which the covariance matrix is generated. This means that the most important uncertainties of the parameters should be captured by the considered sensitivities. All parameters described above are selected in accordance with this requirement. The sensitivity analysis quantifies significant uncertainties due to the identified input sensitivities. Simulated biogenic emissions and dry deposition velocities are highly dependent on uncertainties of input parameters and meteorology. Dynamical parameters like friction velocity and surface exchange coefficients are by definition determined by the meteorological conditions as well as surface properties affecting local dynamics.

Secondly, constant sensitivity factors with respect to reference values are assumed in the current setup. This assumption is not perfectly true for all parameters, but some assumptions are required in order to apply perturbations over an extended time-interval. Biogenic emissions show almost perfectly constant sensitivities trough the time interval for all sources of uncertainties. For dry deposition velocities, variable structures are observed before sunrise, but sensitivities become much more constant with increasing values after sunrise. Thus, minimal values of biogenic emissions an dry deposition velocities are implemented to limit sensitivity factors from low values. For both parameters, microphysics- and radiation parameterizations have comparably low effects. However, they are expected to have more significant influence in other cases with cloudy conditions.

Compared to biogenic emissions and dry deposition velocities, friction velocities are found to be more variable. This is caused by its definition which induced direct dependence on local near-surface winds. Nevertheless, effects of some sensitivities appear to be at least partly constant over the considered time-interval. Surface exchange coefficients are less closely related to low level wind fields, which results in more constant sensitivities after sunrise. The consideration of joint sensitivities to heat and momentum may induce more consistent perturbations. Both, friction velocity and surface exchange coefficients are driven by highly variable local dynamics before sunrise. Thus, the sensitivity factors for the KL ensemble are restricted to daytime hours.

Regarding local dynamics, other parameters like BLH and surface fluxes have also been investigated. However, both types of parameter turned out be not suitable for perturbation by the current setup of the KL ensemble algorithm. In the context of local mixing of atmospheric pollutants, the BLH is known to be a key parameter. However, the BLH is implemented as diagnostic parameter in WRF and EURAD-IM. Thus, perturbing BLH will not have any effect on the forecasts of both models. The investigation of surface fluxes of heat and moisture shows another problem. Around sunrise, the directions of these fluxes change signs which results in unfavorable conditions for slight variations during the period of zero-fluxes. Sensitivity factors become negative at times were the reference flux is of opposite sign than the one of the sensitivities. Thus, other approaches than constant factors have to be found, if one aims to perturb surface fluxes by the KL ensemble.

7 Ensemble Generation Results

This chapter presents results from the Karhunen-Loéve ensemble generation algorithm applied to different model parameters. According to the availability of observations, the results focus on the early morning hours on 12.07.2012. For this application, covariances of the stochastic parameters are created based on the sensitivity analysis presented in Ch. 6 which was initialized on 11.07.2012 at 00 UTC. Sensitivities to six different input sources are considered by selecting two options for each source. The selected options are the same as for the sensitivity analysis given in Tab. 6.1.

For the meteorological parameters, an additional source of uncertainty is considered. The roughness length for different vegetation types are increased as given in Appendix E. The modifications are based on the findings of Berndt [2018], who observed an underestimation of predefined values of roughness lengths in WRF when applied to European regions.

Forecasted values of considered parameters from the set of simulations are divided by their corresponding value from the reference setup. The sensitivities are defined as temporal average of these factors, which are assumed to be approximately constant over the time interval. The formulation of the sensitivities as factors may induce unrealistic effects in case of low values of parameters. Firstly, if small values are divided by small reference values, factors may become exceptionally small or large even for low absolute differences. These extreme factors tend to dominate the temporally averaged sensitivities, which results in unrealistic values at times with higher reference values. Therefore, factors are limited by *minimal- and maximal factors* defined as 0.1 and 10, respectively. For independent sensitivities, the sensitivities are interpreted relative to the independent mean. In order to handle the minimal- and maximal factors analogously, independent mean and -sensitivities are limited by 0.2 and 5. With this, a maximal deviation of 0.1 and 10 is allowed when the sensitivities are applied to the independent mean which is consistent to the original setup.

Secondly, if reference values are close to zero, high values indicated by other options cannot be produced even for large factors. This may result in underdispersion of the KL ensemble were reference values are small. In order to avoid this effect, model parameters which may become zero are limited by a *minimal value*. This minimal value is applied to parameters from the sensitivity analysis before calculating the KL ensemble as well as in the forecast when KL perturbations are applied. In this study, minimal values for biogenic emissions and dry deposition velocities are set to $1.0 \cdot 10^{-3} \frac{kg}{km^2\ h}$ and $1.0 \cdot 10^{-3} \frac{m}{s}$, respectively.

The ensemble approach is applied to biogenic emissions (Sec. 7.1) and dry deposition velocities (Sec. 7.2) in EURAD-IM as well as surface exchange coefficients (Sec. 7.3) in WRF. The perturbation of friction velocity was also investigated but it turned out to induce numerical instabilities in WRF (compare Appendix G.3). Note that the random

numbers are generated using a predefined random seed. This ensures the same values for the stochastic coefficients of each ensemble member given in Tab. 7.1 for all simulations.

Table 7.1: Stochastic coefficients of the seven leading eigenmodes for all KL ensembles of perturbations.

eigenmode	1^{st}	2^{nd}	3^{rd}	4^{th}	5^{th}	6^{th}	7^{th}
member 001	2.088	-1.710	0.247	-0.896	0.669	0.382	-0.410
member 002	0.065	-0.662	-0.974	0.775	0.437	-1.014	0.564
member 003	-2.379	-0.706	0.852	-0.874	0.065	-0.439	-1.552
member 004	-1.689	0.024	1.289	0.595	-1.400	-0.412	-0.468
member 005	-0.923	1.196	-0.842	0.215	0.556	-0.537	-0.184
member 006	1.227	0.358	0.063	-0.477	0.064	1.420	-1.185
member 007	1.713	0.095	0.180	0.547	0.067	1.260	0.555
member 008	-1.964	0.363	-1.448	0.021	-1.272	1.129	1.139

7.1 Stochastic Biogenic Emissions

Biogenic emissions of five trace gases are perturbed: isoprene, limonene, alpha-pinene, ethene and aldehydes. Because ethene and aldehydes are also anthropologically emitted, their biogenic contributions are denoted as "*biogenic ethene emissions*" and "*biogenic aldehyde emissions*". Note that biogenic aldehyde emissions from MEGAN 2.1 represent the total emission from acetaldehyde and a set of higher aldehydes which are not treated individually (see Guenther et al. [2012] for further details).

This set of five biogenic gases was selected in order to investigate the benefit of coupled perturbation of multiple potentially correlated parameters. As biogenic emissions are restricted to terrestrial vegetation, only land surface gridboxes are considered in the ensemble generation which reduce the total dimension of the problem by about 27 % to 157 725. The simulation time-interval which is considered for the KL ensemble generation is on 12.07.2012 from 00 UTC to 10 UTC. Generally, sensitivities to biogenic emissions are very similar for all five gases leading to highly correlated perturbations by the KL algorithm. Thus, the description focuses on the results of isoprene emissions where additional figures are provided in Appendix G.1.

7.1.1 Full Input Sensitivities

In the following, forecasts of biogenic emissions based on the core KL ensemble algorithm (compare Sec. 4.1) are presented. For this setup, the covariances are calculated from full input sensitivities. In contrast to independent input sensitivities (which will be discussed in the next Section), the full set of possible input options is considered including multiple combinations of the options presented in Tab. 6.1. Due to computational reasons, a subset of 32 full sensitivities is sampled from a total number of $2^6 = 64$ possible combinations. The setup of the selected input combinations in given in Tab. G.1.

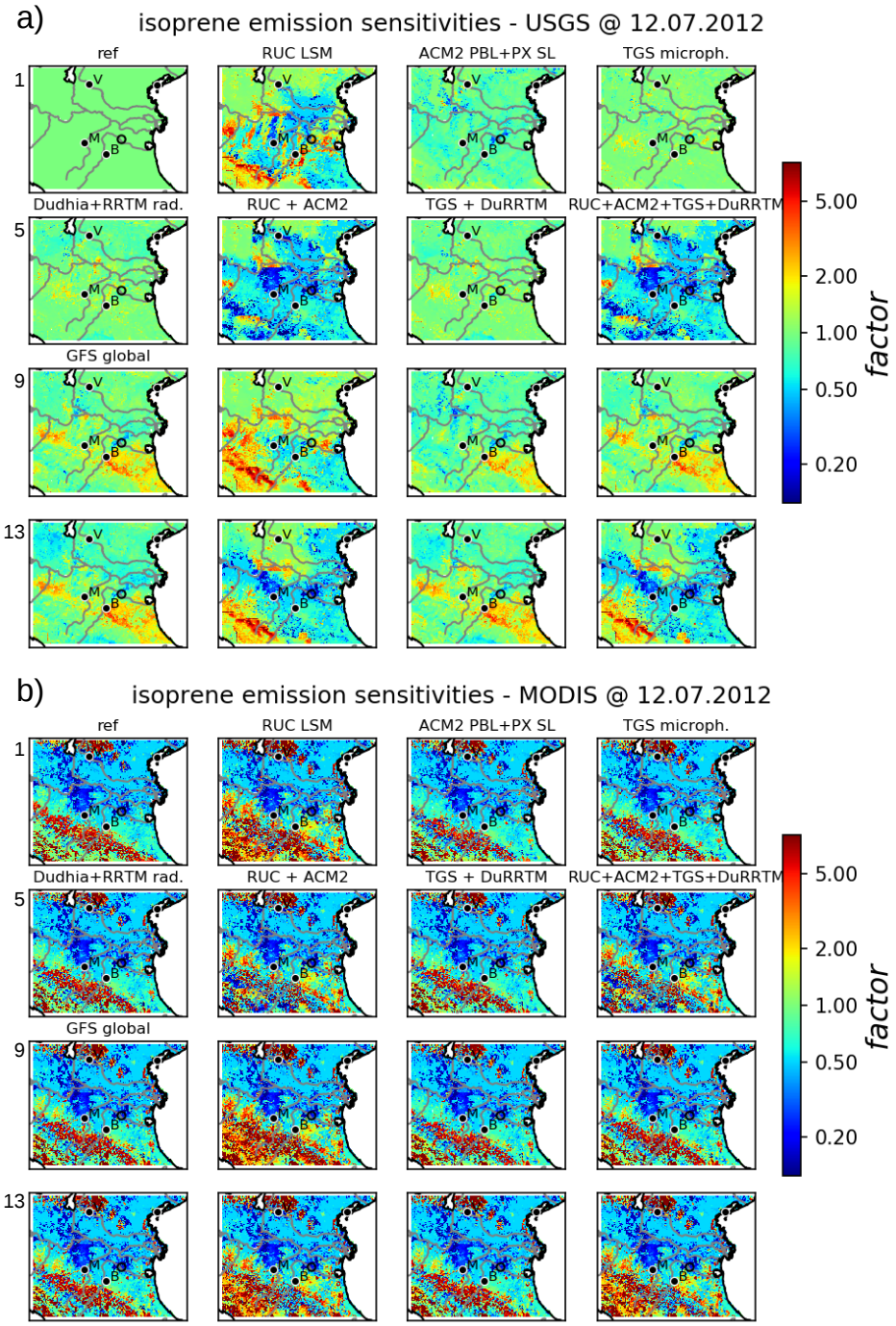

Figure 7.1: Sensitivities of isoprene for full input sensitivities of biogenic emissions splitted for USGS (a) and MODIS (b) land use. The sensitivities are given as factors w.r.t reference emissions and ordered according to Tab. G.1 from left to right and from top to bottom. Some major cities (Verona, Bologna, Modena) are indicated by their initial letters. The location of the Zeppelin observations on this day is given as small circle.

Given the set of 32 fields of biogenic emissions, full sensitivities are calculated as temporal average of the emissions divided by the reference emissions. Fig. 7.1 shows the resulting 32 emission factors. Note that factors of the reference run (subplot 1 of Fig. 7.1a) are always one by definition. The sensitivity factors are dominated by uncertainties in land use ranging from 0.2 to 5 in the mountains and the Po valley, respectively (Fig. 7.1b). These large differences for MODIS instead of USGS land use arise from the indicated amount of broadleaf trees. Significant effects are also found with respect to global meteorology, land surface model and boundary layer scheme, which induce nonlinear combined sensitivities.

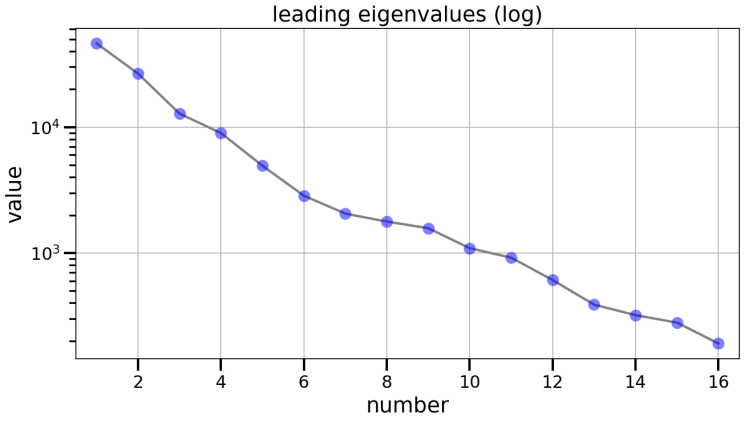

Figure 7.2: Leading eigenvalues of biogenic emissions for full input sensitivities (blue dots). Eigenvalues are plotted on a logarithmic scale.

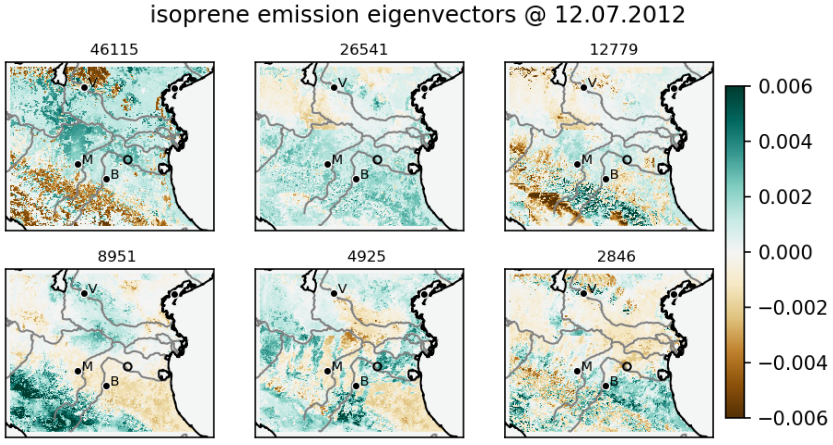

Figure 7.3: Normalized leading eigenvectors of isoprene for full input sensitivities of biogenic emissions. Corresponding eigenvalues are given above each eigenvector. Some major cities (Verona, Bologna, Modena) are indicated by their initial letters. The location of the Zeppelin observations on this day is given as small circle.

Based on the presented sensitivities, the 16 leading eigenvalues and related eigenvectors are calculated. The eigenvalues given in Fig. 7.2 show an approximately steady logarithmic decrease. The five leading eigenvalues decrease rapidly by approximately one order of magnitude. This indicates that the stochastic dimension of the emissions factors is mainly determined by a few leading components. In other words, the fast decrease of leading eigenvalues confirms a high correlation of biogenic emissions through the domain. After the 5^{th} eigenmode, the decrease of the eigenvalues diminishes slightly. The contribution of these leading eigenmodes to the emission factors of the different species is given by the eigenvectors. Looking at the six leading eigenvectors for isoprene emissions given in Fig. 7.3, the contribution of different sensitivities can be analyzed. The first eigenmode can clearly be related to the sensitivity of isoprene emissions to land use information. As the other eigenmodes are not clearly related to single sensitivities, remaining sensitivities are not completely independent to each other.

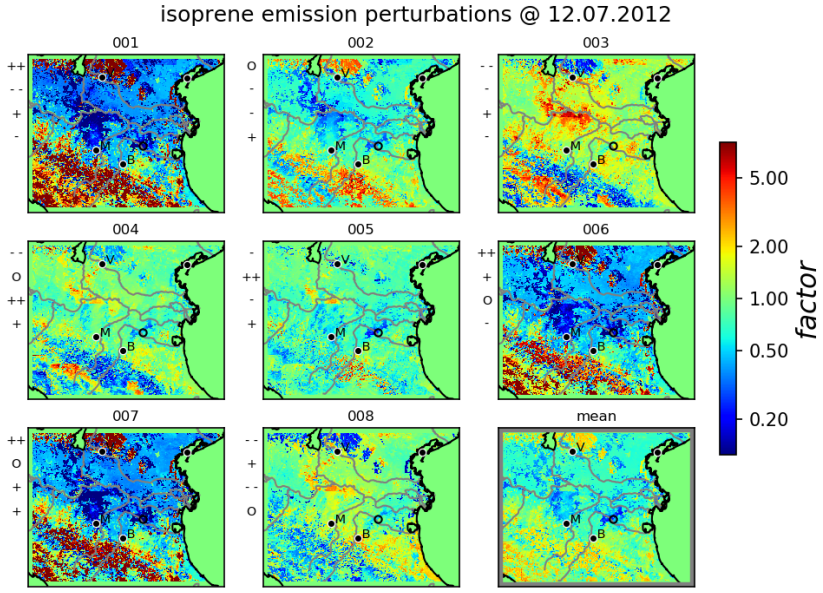

Figure 7.4: Ensemble of perturbations of isoprene for full input sensitivities of biogenic emissions given as factors w.r.t reference emissions. Random numbers for the leading components of each member are indicated left of each subplot ('++': large positive value (> 1.0), '+': small positive value ($< 1.$), 'O': very small absolute value (< 0.1), '–': small negative value (> -1.0), '– –': large negative value ($< -1.$)) (compare Tab. 7.1). The lower right subplot gives the ensemble mean factors. Some major cities (Verona, Bologna, Modena) are indicated by their initial letters. The location of the Zeppelin observations on this day is given as small circle.

The emissions of biogenic gases are now stochastically perturbed according to the leading eigenmodes. Fig. 7.4 shows the emission factors of isoprene for eight different combinations of stochastic coefficients giving an ensemble of eight members which are influenced by different eigenmodes. . In general, the ensemble represents the leading components of uncertainties with respect to the mean emission factors indicated from the

sensitivities (compare Fig. 7.1). On the one hand, members with large positive contribution of the 1^{st} eigenmode are dominated by a large reduction within the valley and increase in the mountainous regions caused by the sensitivities to land use (member 001, 006, 007). On the other hand, emissions similar to the reference run are generated and smaller contributions to emission factors become visible (member 004, 005, 008).

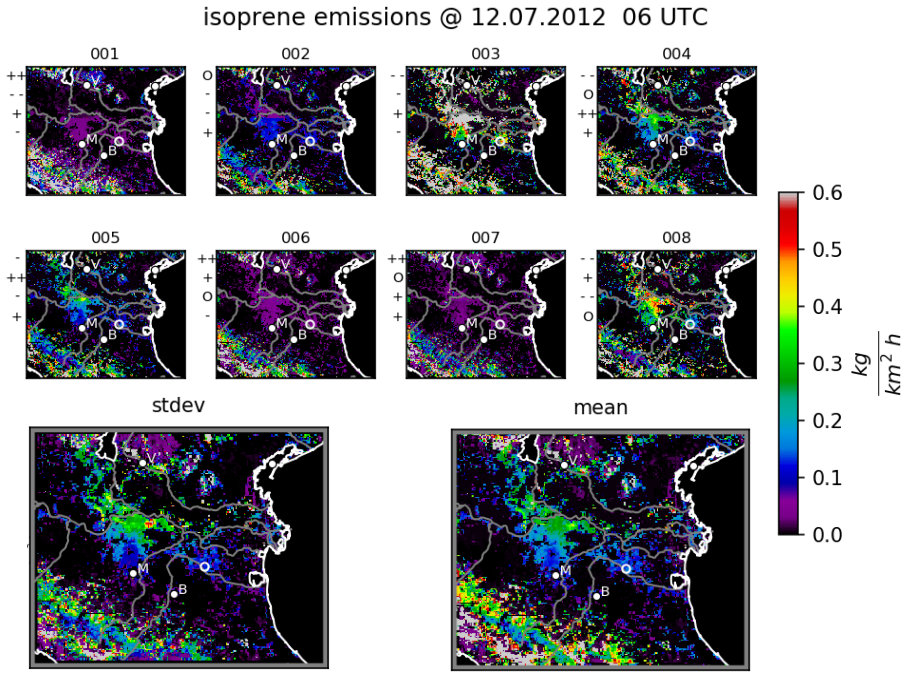

Figure 7.5: Ensemble of isoprene emissions for full input sensitivities of biogenic emissions. Random numbers for the leading components of each member are indicated left of each subplot. The lower left and right subplot gives the ensemble standard deviation and mean, respectively. Some major cities (Verona, Bologna, Modena) are indicated by their initial letters. The location of the Zeppelin observations on this day is given as small circle.

The perturbations are multiplied with the biogenic emissions of the reference setup over the selected time-interval. This creates an KL ensemble of forecasts for 12.07.2012 starting on 00 UTC. Fig. 7.5 shows the resulting KL ensemble of isoprene emissions at 06 UTC. The large range of emission factors generated by the KL algorithm induces highly different isoprene emissions. Largest ensemble spread is predicted at locations with high average isoprene emissions in areas like north of Bologna and Modena as well as the Apennine region. For this small ensemble with eight realizations, the ensemble spread is of the same magnitude as the ensemble mean emissions. Thus, a relative uncertainty of 100 % in isoprene emissions is captured by the KL ensemble. Due to uncertainties in land use information, isoprene emissions vary more than one order of magnitude north of Bologna and Modena. Thus, the range of isoprene emissions indicated by the sensitivity analysis is covered by the comparably small KL ensemble.

7.1.2 Independent Input Sensitivities

Although the core KL ensemble setup is able to produce reasonable probabilistic forecasts, the calculation of full input sensitivities requires large computational efforts. Therefore, the assumption of independent input sensitivities was developed (compare Sec. 4.2.1) and is applied to stochastic biogenic emissions in this section.

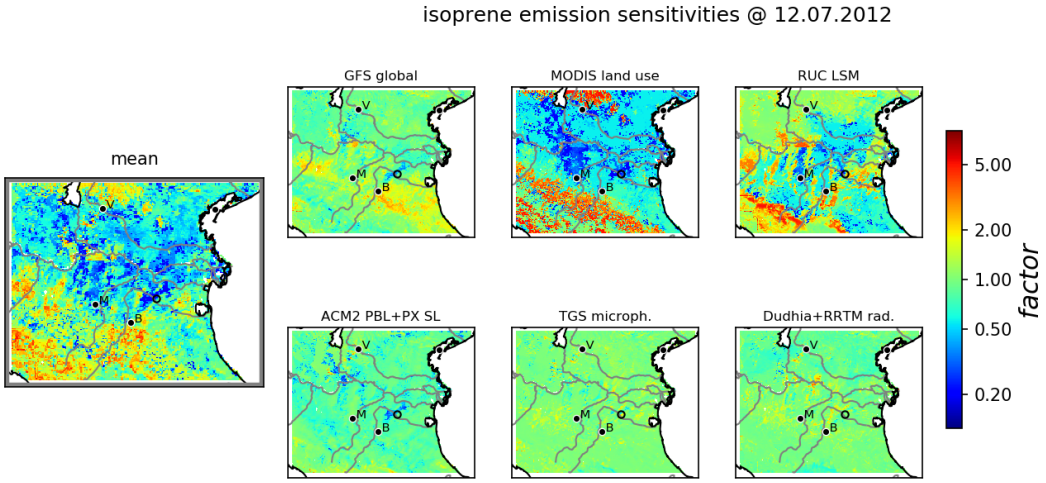

Figure 7.6: Independent- mean and sensitivities of isoprene for independent input sensitivities of biogenic emissions. The sensitivities given as factors w.r.t. to the mean (left subplot). Some major cities (Verona, Bologna, Modena) are indicated by their initial letters. The location of the Zeppelin observations on this day is given as small circle.

For independent input sensitivities, the mean value and covariances of the independent sensitivities are calculated in a different way (compare Eq. (4.21)). Fig. 7.6 shows these corrected independent mean factors and -sensitivities for isoprene emissions. Note that the independent sensitivities shown here are interpreted relative to the independent mean, which are both limited by 0.2 and 5. Independent sensitivities to the six single input sources are considered in this setup. Similar to full sensitivities, land use information and land surface model indicate significantly reduced isoprene emissions within the Po valley which is also represented in the independent mean. Compared to that, the other independent sensitivities induce smaller deviations in isoprene emissions.

The leading eigenvectors of isoprene for independent sensitivities in Fig. 7.8 can clearly be related to the single sensitivities. This is because smaller changes due to combined sensitivities are not considered and the remaining single sensitivities are comparably perpendicular to each other. The leading 1^{st} and 2^{nd} eigenvectors can both be attributed to uncertainties in land use and land surface model. As these two input sources induce the largest sensitivities, the related eigenvalues shown in Fig. 7.7 are almost one order of magnitude larger than the remaining ones.

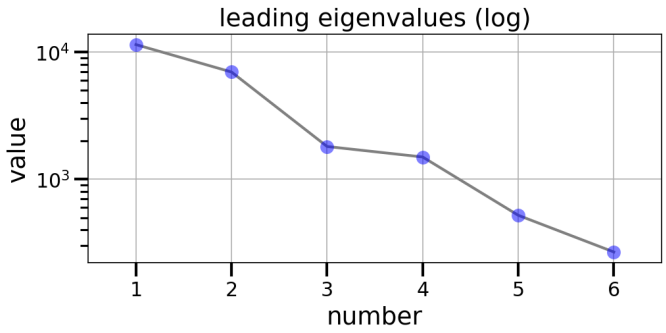

Figure 7.7: Leading eigenvalues of biogenic emissions for independent input sensitivities (blue dots). Eigenvalues are plotted on a logarithmic scale.

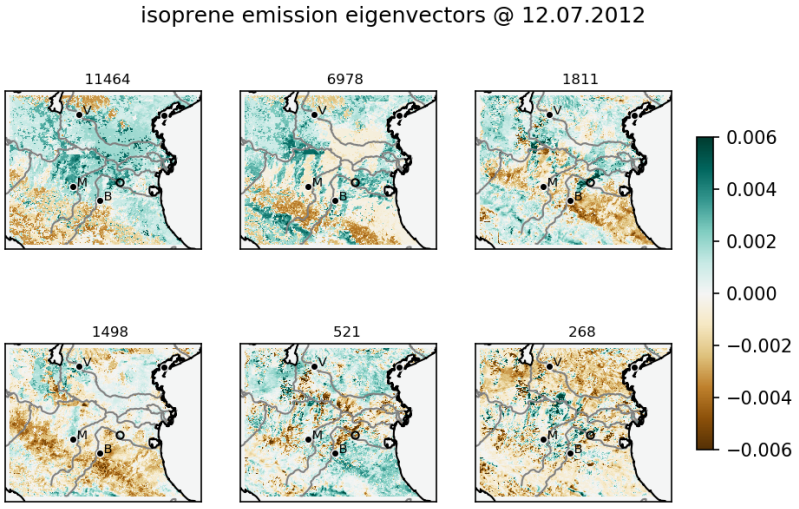

Figure 7.8: Normalized leading eigenvectors of isoprene for independent input sensitivities of biogenic emissions. Plotting conventions as in Fig. 7.3.

Some differences are found when the eigenmodes from the independent sensitivities are compared to the full sensitivity case. In general, independent sensitivities lead to a faster decrease of eigenvalues because of the smaller amount of information used. Using full sensitivities, the 1^{st} eigenmode solely represents uncertainties in land use, while land surface model uncertainties also contribute to this mode for independent sensitivities. Due to the assumption of independent sensitivities, nonlinear effects arising from combinations of input options cannot be captured. For example, the 2^{nd} eigenmode for full sensitivities - which was induced by combining RUC land surface model with ACM2 boundary layer parameterization - cannot be found in the independent case.

Perturbation factors of biogenic emissions are calculated by multiplying the independent mean factors with realizations of the KL expansion. This ensures that the ensemble of perturbations (shown in Appendix G.1.2 for isoprene) are centered around the independent mean. Similar to full sensitivities, the resulting isoprene emissions show standard

deviations proportional to the absolute mean values. However, the ensemble mean in the central Po valley as well as the estimated relative uncertainty of about 50 % is lower compared to the full sensitivity case. This underestimation results from the neglectance of nonlinear effects for independent sensitivities.

7.1.3 Additional A-priori Uncertainties

Up to now, only uncertainties of biogenic emission due to sensitivities to input sources are considered. But the modeling approach itself from which the emissions are calculated may induce additional sources of uncertainties. This is especially important for biogenic emissions where complex processes have to be simplified to a emission module which can be used in chemistry transport models. For MEGAN 2.1, Guenther et al. [2012] assume global annual uncertainty of the MEGAN emission module to be about 200 %, which is interpreted as an emission factor of 2. This additional a-priori uncertainty can be included into the algorithm when independent sensitivities are used (compare Sec. 4.2.2). Additionally, the implemented emission reduction due to soil dryness also induces uncertainties to the emissions approach as the explicit dependency is still under discussion (compare Sec. 3.2.1). As the soil dryness dependency was implemented into MEGAN 2.1 in the reference setup of EURAD-IM, this sensitivity is considered by excluding this dependency in an additional independent sensitivity.

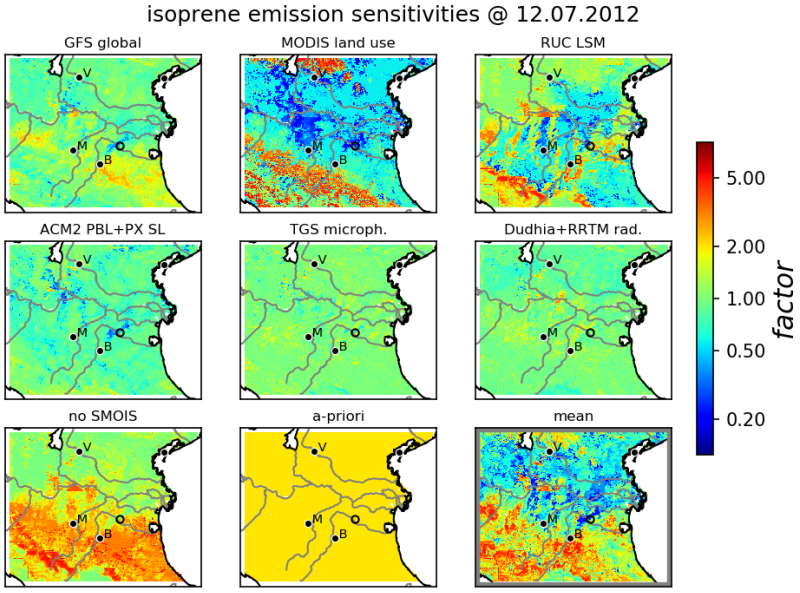

Figure 7.9: Independent- mean and sensitivities of isoprene including additional uncertainties due to soil dryness ('no SMOIS') and emission modeling ('a-priori') of biogenic emissions. The sensitivities given as factors w.r.t. to the mean (lower right subplot). Plotting conventions as in Fig. 7.6.

Adding these two sources of uncertainties, the independent sensitivities and -mean emission factors for isoprene are shown in Fig. 7.9. The additional sensitivity to exclusion of soil dryness effects points towards increased emissions in the southern part of the domain. Indicating emission factors of about 3, this sensitivity increases the independent mean factors in the related regions compared to the original independent case (compare Fig. 7.6). The a-priori uncertainty is represented by a constant factor of 2 though the domain and for all biogenic gases which does not affect the independent mean. The constant uncertainty applying to the whole dimension of the problem results in a dominating contribution with respect to all biogenic gases represented by the 1^{st} eigenvalue. In general, sensitivities for different biogenic gases are highly correlated which lead to very similar signals in the eigenvectors in Fig. G.4.

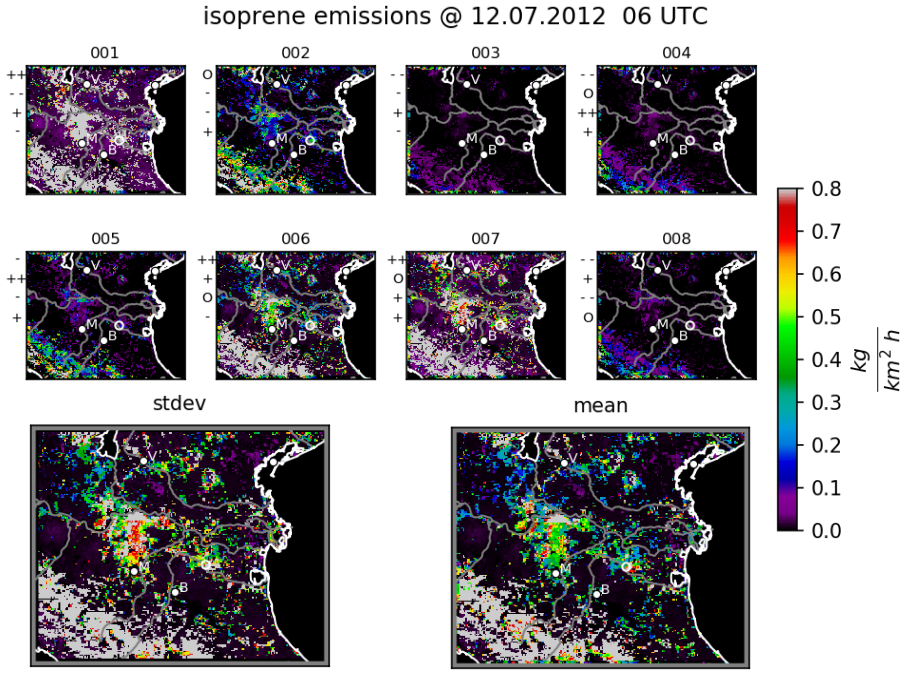

Figure 7.10: Ensemble of isoprene emissions for additional a-priori uncertainties of biogenic emissions. Plotting conventions as in Fig. 7.5. Note the different colorscale compared to the previous cases.

The resulting ensemble of isoprene emissions at 06 UTC in Fig. 7.10 shows a huge spread which even exceeds the ensemble mean emissions in some regions. Compared to the original setup of independent sensitivities, the standard deviation increased by about a factor of 5. The combination of minimal emissions with the introduction of a constant a-priori uncertainty enables significant emissions in the regions of low reference emissions in the valley (e.g. member 001).

7.2 Stochastic Dry Deposition Velocities

In the formulation in EURAD-IM, calculated dry deposition velocities of different gases are formulated similarly. Therefore, dry deposition velocities of four gases are perturbed to show the general behavior for different types of gases. These are: SO_2, HNO_3, O_3 and aldehyde. Note that aldehyde includes acetaldehyde and higher aldehydes, similar to biogenic emissions. From these four gases, the discussion focuses on the results for dry deposition of HNO_3 and aldehyde. Results for the other two gases are given in Appendix G.2.

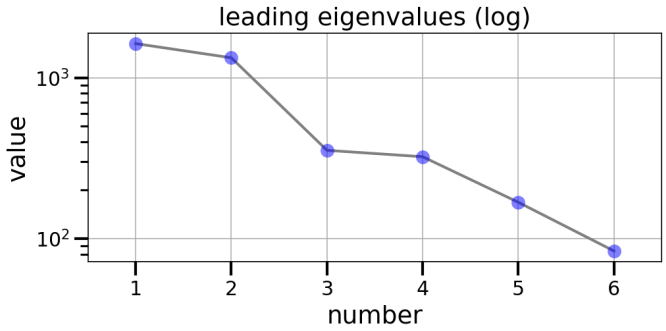

Figure 7.11: Leading eigenvalues of dry deposition velocities for independent input sensitivities (blue dots). Eigenvalues are plotted on a logarithmic scale.

Dry deposition velocities are perturbed using the assumption of independent input sensitivities. The leading eigenvalues in Fig. 7.11 show dominating contributions of the 1^{st} and 2^{nd} eigenmode. According to the eigenvectors in Fig. 7.12, the 1^{st} eigenmode represents the sensitivities to land surface model as well as aligned contributions from global meteorology and boundary layer parameterization. The 2^{nd} eigenmode reflects sensitivities to land use information which deviate from the 1^{st} mode. Contributions of the leading four eigenvectors for the different gases show similar patterns indicating high correlation between those. Smaller sensitivities of aldehyde compared to the other three gases are represented by generally smaller signals in the eigenvectors.

Perturbation factors of dry deposition velocities in Fig. G.7 span a generally smaller range compared to biogenic emissions. The 1^{st} eigenmode dominates the perturbations for HNO_3 because the effects of the 2^{nd} eigenmode are hardly visible because of their small spatial extension. In agreement with the sensitivities, aldehyde dry deposition factors have a smaller spread with maximum factors about 0.5 and 2.

The resulting ensemble of dry deposition velocities in Fig. 7.13 shows patchy structures thought the domain caused by the small extension of perturbations. At most locations, the ensemble standard deviation is proportional to the ensemble mean, whereas it goes almost down to zero at some locations in the eastern valley and above the ocean. For aldehyde, mean dry deposition velocities are more equally distributed over the land surface.

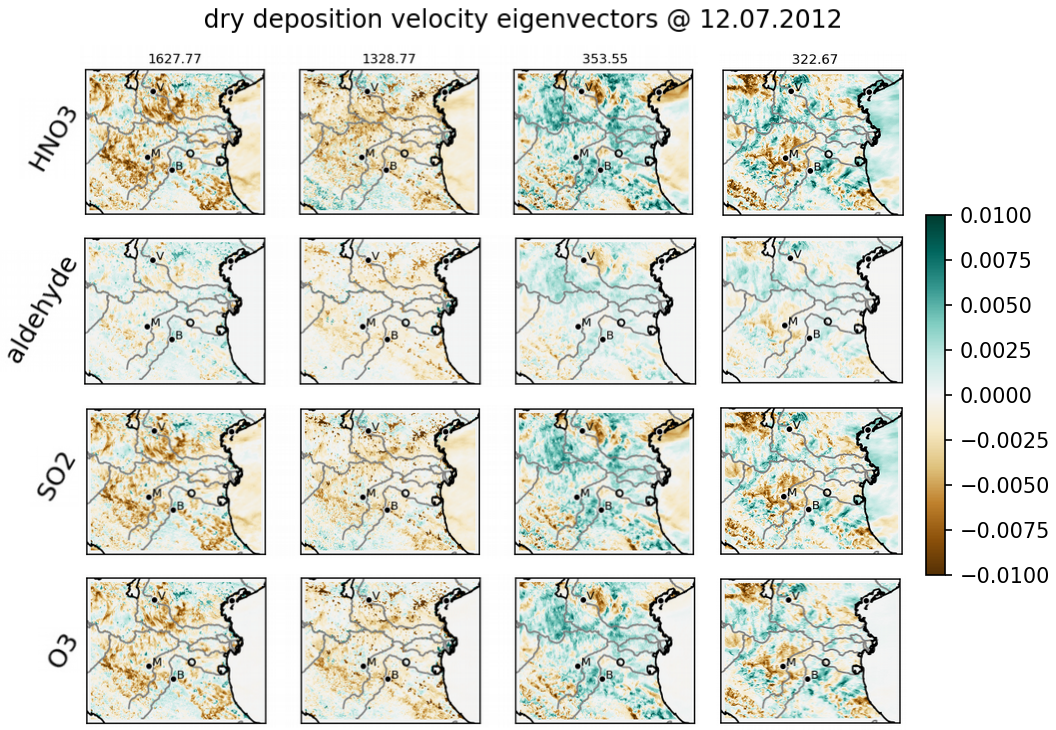

Figure 7.12: Normalized leading eigenvectors of HNO_3 (a) and aldehyde (b) for independent input sensitivities of dry deposition velocities. Plotting conventions as in Fig. 7.3.

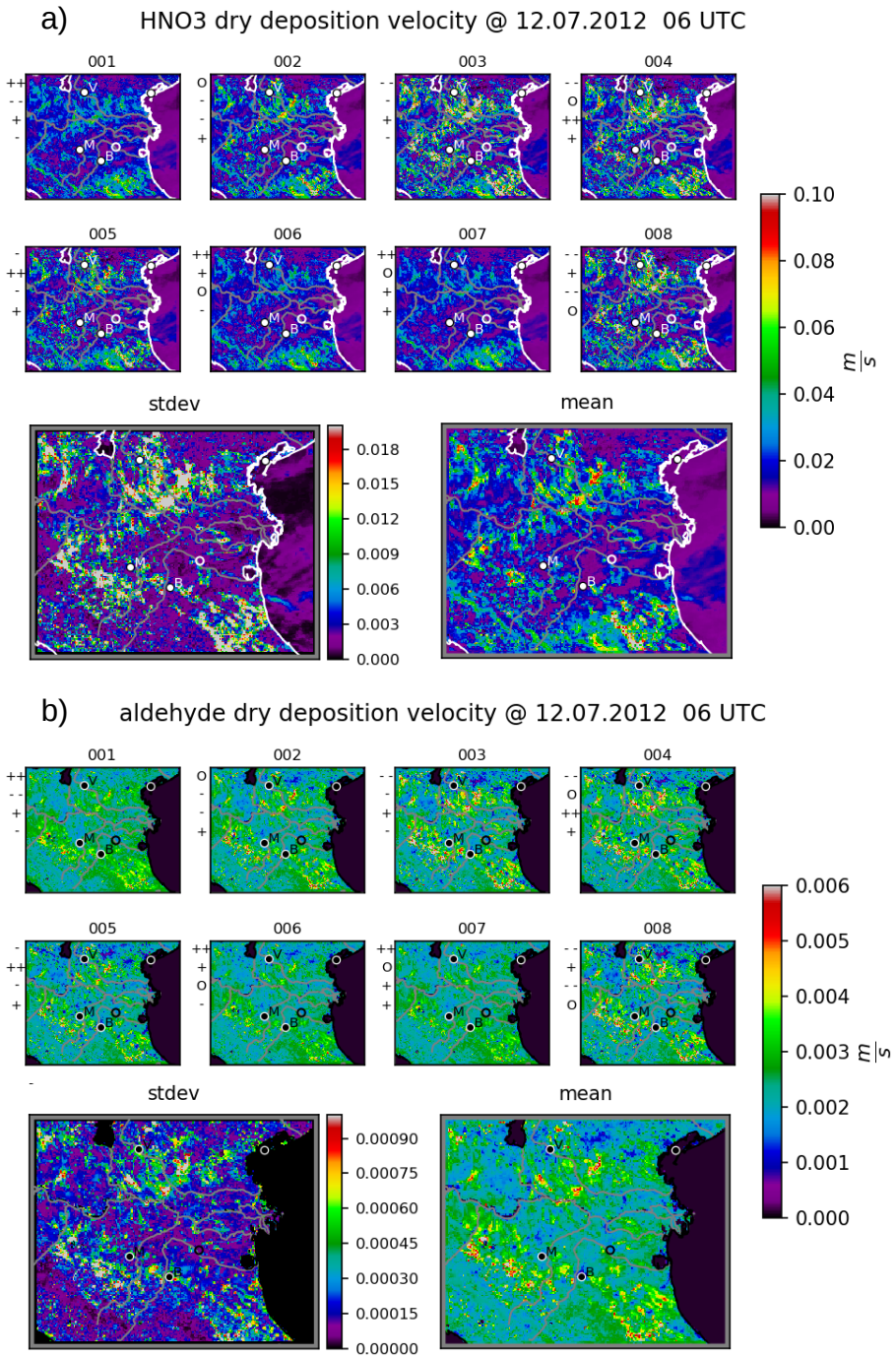

Figure 7.13: Ensemble of HNO_3 (a) and aldehyde (b) dry deposition velocities for independent input sensitivities of dry deposition velocities. Plotting conventions as in Fig. 7.5.

7.3 Stochastic Surface Exchange Coefficients

Surface exchange coefficients for heat and momentum are perturbed as example for dynamical parameters in WRF. As described in Sec. 6.3.3, the MYNN boundary- and surface layer parameterizations had to be replaced by the ACM2 boundary layer scheme in the sensitivity analysis. Thus, sensitivities to the surface layer parameterization itself are not included for these parameters. Note that sensitivities to roughness length are additionally considered for meteorological parameters. The analysis of related sensitivities detected large variations in the early morning before sunrise which are assumed to be non-physical (compare Sec. 6.3.2). Therefore, the ensemble generation is restricted to daytime hours between 06 and 10 UTC. Additionally, the perturbations are restricted to the land surface due to the definition of surface exchange coefficients.

In general, the sensitivities of surface exchange coefficients are larger for momentum than for heat. Mean fields of exchange coefficients show regions of increased and reduced values, where a general tendency to larger values for momentum are mainly induced by land use.

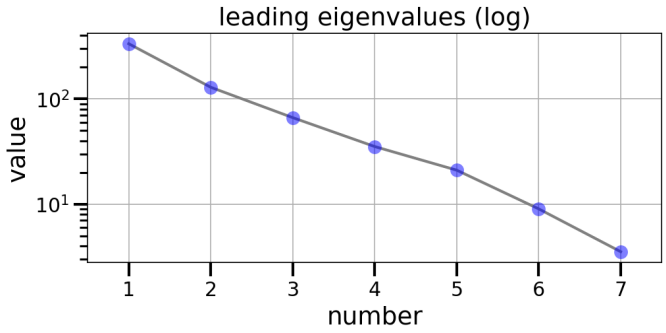

Figure 7.14: Leading eigenvalues of surface exchange coefficients for independent input sensitivities (blue dots). Eigenvalues are plotted on a logarithmic scale.

The eigenmode analysis shows a continuous, almost ideal lognormal decrease of eigenvalues given in Fig. 7.14. Related eigenvectors show clear connections to single sensitivities, which indicates no significant alignment between any of the independent sensitivities. According to the eigenvectors in Fig. 7.15, the 1^{st} eigenmode represents sensitivities due to land use. Although only small contributions are found for heat exchange, large contributions to momentum attach this mode to the largest eigenvalue. The 2^{nd} and 3^{rd} eigenmodes are induced by the sensitivities to land surface model and roughness length, respectively.

The small spatial scale of signals in the eigenmodes leads to patchy structures of perturbations and forecasted surface exchange coefficients shown in Appendix G.12. Due to larger perturbation factors, this is especially the case for momentum exchange. Largest ensemble spread occurs in the south-eastern Apennines at locations, where also the largest values are found.

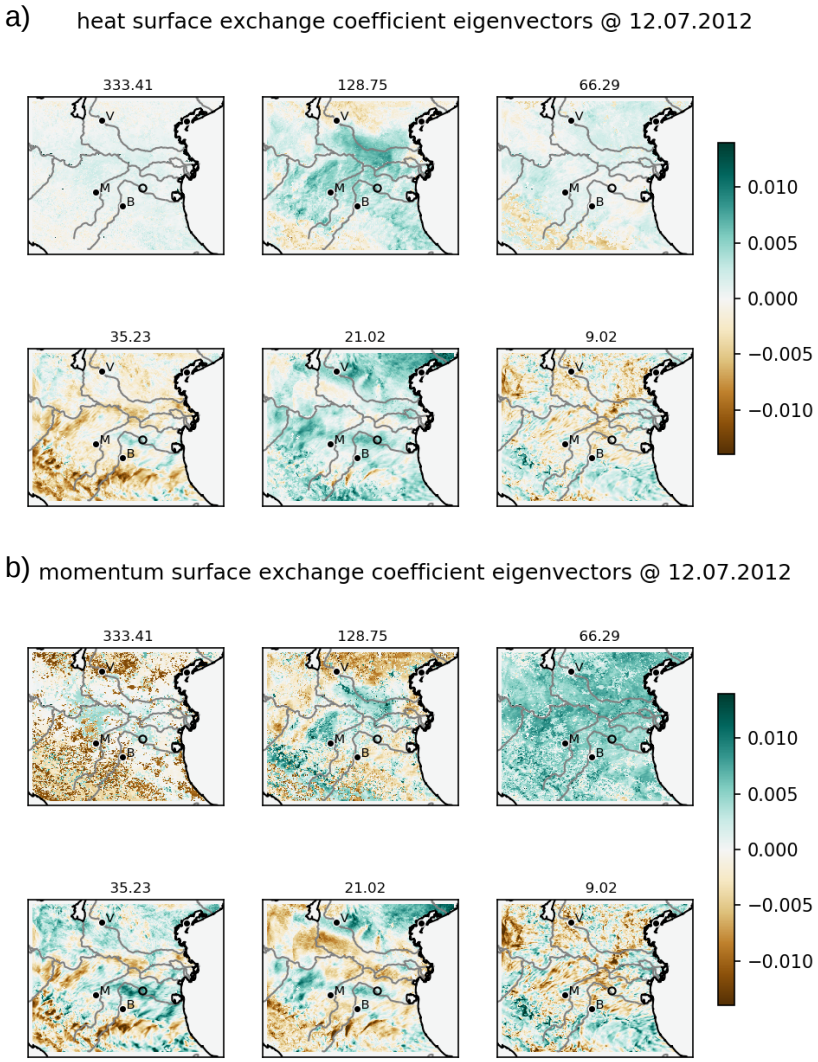

Figure 7.15: Normalized leading eigenvectors of heat- (a) and momentum- (b) surface exchange coefficients for independent input sensitivities. Plotting conventions as in Fig. 7.3.

The KL ensemble of surface exchange coefficients on the 1 km domain of the Po area is mainly driven by small scale perturbations. In comparison, perturbations are generated on the 5 km domain in order to investigate the effect of nesting large-scale perturbations on ensemble forecasts in the 1 km domain. In general, sensitivities calculated on the 5 km domain given in Appendix G.13 do not change significantly compared to the original setup on the 1 km domain. Notable differences can only be found for land use and land surface model due to averaging of patchy surface properties.

Although the sensitivities have only slightly changed compared to the original setup, the leading eigenvalues given in Fig. 7.16 has changed more significantly. This is due to

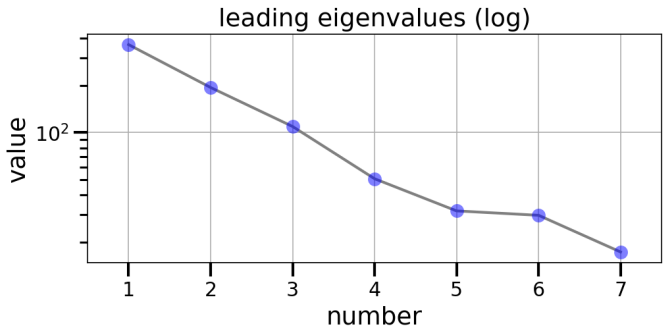

Figure 7.16: Leading eigenvalues of surface exchange coefficients on the 5 km domain for nested perturbations (blue dots). Eigenvalues are plotted on a logarithmic scale.

the fact that the eigenmodes now refer to the parameters of the whole 5 km domain from which only the part within the 1 km domain is shown. Slightly larger eigenvalues indicate on average similar or higher sensitivities in other parts of central Europe compared to the Po valley.

This results in larger perturbation factors of heat exchange coefficients compared to the original setup. Momentum exchange in the Po area is dominated by the leading two eigenmodes. The sensitivities to land use and the land surface model are combined in different ways and produce different perturbation patterns over the mountains.

According to the eigenmodes, the generation of perturbations on the 5 km domain results in more large scale variability of surface exchange coefficients on the 1 km domain in Appendix 7.18. For heat exchange, ensemble mean and standard deviation show much smoother patterns compared to the reference 1 km ensemble. Nevertheless, absolute values did not change significantly in most areas. The smoothing effect is also visible for momentum exchange. However, the peak values of mean and standard deviation due to land use in the original 1 km setup are not captured here. This is caused by the underrepresentation of urban areas by the 5 km land use information.

Perturbing surface exchange coefficients does also affect friction velocity shown in Fig. G.14. Although significant ensemble spread is generated in the mountainous regions, only minor differences are induced in the Po valley. This indicates that leading uncertainties in local dynamics are not represented adequately by the current ensemble setup for surface exchange coefficients. On the one hand, this can be caused by an underestimation of uncertainties in exchange coefficients, for example by neglecting uncertatintes due to the surface layer parameterization. On the other hand, significant contributions to dynamical sensitivities may be driven by other parameters.

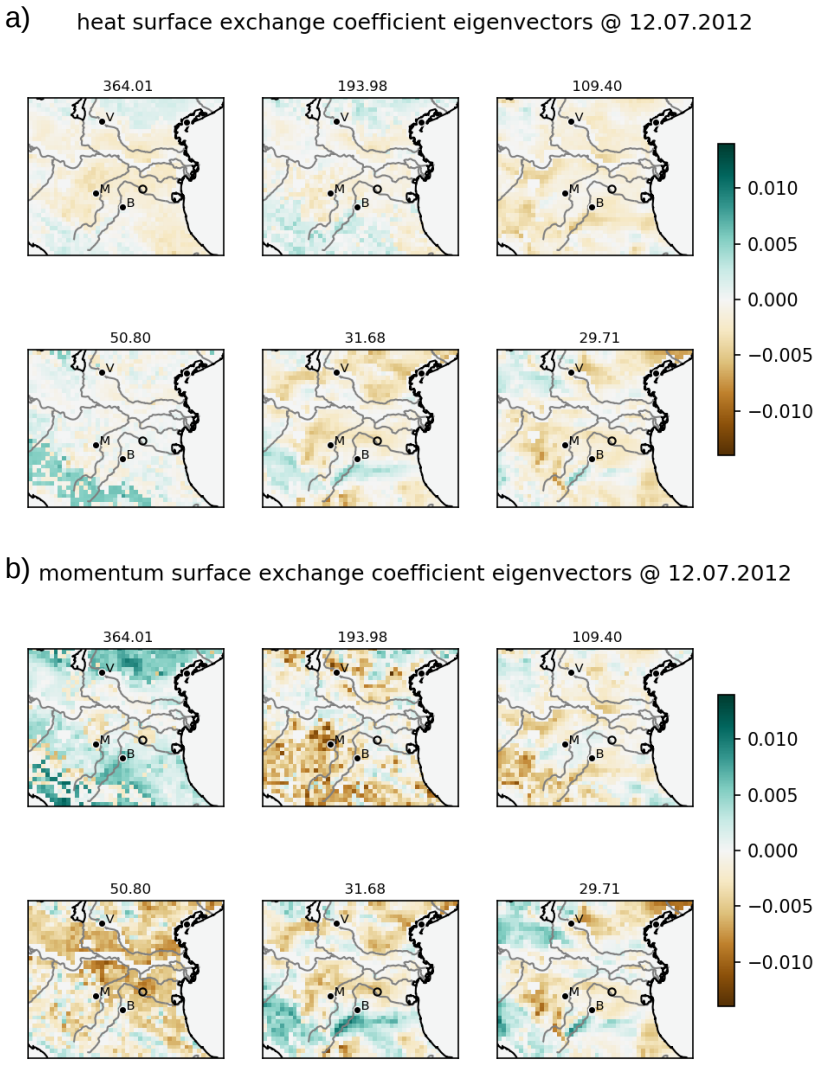

Figure 7.17: Normalized leading eigenvectors of heat- (a) and momentum- (b) surface exchange coefficients on the 5 km domain in the Po valley for nested perturbations. Plotting conventions as in Fig. 7.3.

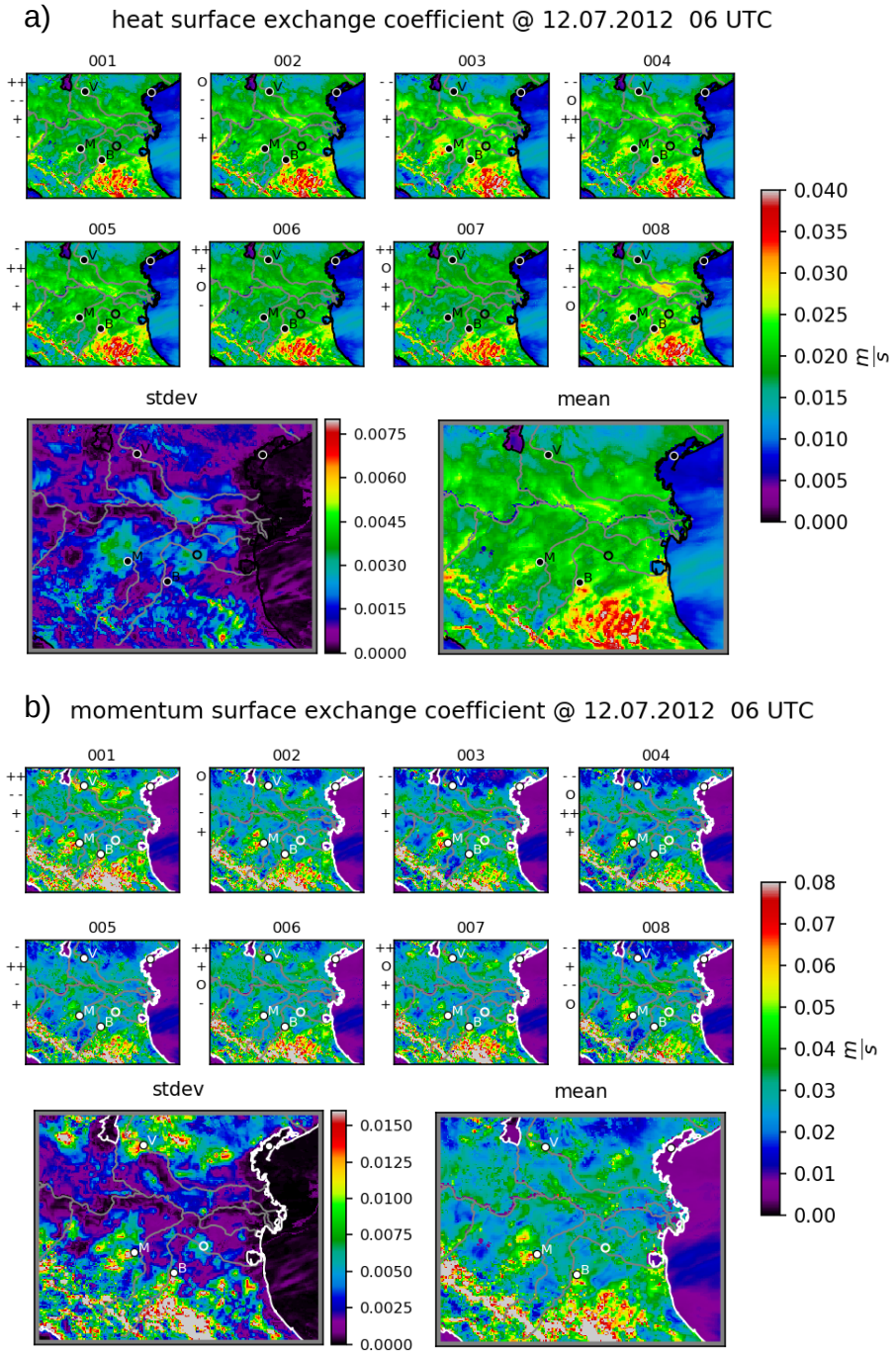

Figure 7.18: Ensemble of heat- (a) and momentum- (b) surface exchange coefficients for nested perturbations. Plotting conventions as in Fig. 7.5.

8 Ensemble Performance

This chapter covers different aspects of the performance of the KL ensemble algorithm. Sec. 8.1 gives an example for joint perturbations of different parameters. Ensemble forecasts for stochastic biogenic emissions are validated to observations under three different conditions in Sec. 8.2. Finally, the computational efficiency of the ensemble generation algorithm is analyzed in Sec. 8.3.

8.1 Joint Perturbation

Based on the results from the KL ensemble generation in Ch. 7, joint perturbations of different model parameters are investigated. Perturbations are restricted to biogenic emissions and dry deposition velocities, because surface exchange coefficients are not completely independent from dry deposition velocities. That means that perturbing surface exchange coefficients does already induce changes in dry deposition velocities via friction velocities. Thus, perturbing both parameters would lead to a double perturbation of dry deposition velocities.

The ensemble generation is based on the setup in Sec. 7.1.2 and Sec. 7.2 assuming independent input sensitivities. Additional a-priori uncertainties are not included due to missing information on uncertainties within the dry deposition approach. Biogenic emissions of five gases and dry deposition velocities of four gases are considered for 12.07.2012 from 00 to 10 UTC. The presented results focus on aldehydes because it is the only gas which is both, biogenically emitted and dry deposited. Note that biogenic emissions as well as dry deposition velocities of aldehyde refer to acetaldehyde and higher aldehydes.

In general, input sensitivities are the same as discussed in Sec. 7.1.2 and Sec. 7.2. Biogenic aldehyde emissions in Fig. 8.1 show similar sensitivities as isoprene emissions (compare Fig. 7.6). Sensitivities to aldehyde tend to be even higher, especially the reduction due to soil dryness in the south-western Po valley related to the land surface scheme. This is caused by a smaller effect of minimal biogenic emissions compared to isoprene, which does not affect reference aldehyde emissions in the early morning. Sensitivities of aldehyde dry deposition have already been discussed in Sec. 7.2. What becomes important here are the generally smaller sensitivities for dry deposition velocities when compared to biogenic emissions of aldehyde. Only sensitivities to land use in urban regions reach sensitivity factors comparable to the ones of biogenic emissions.

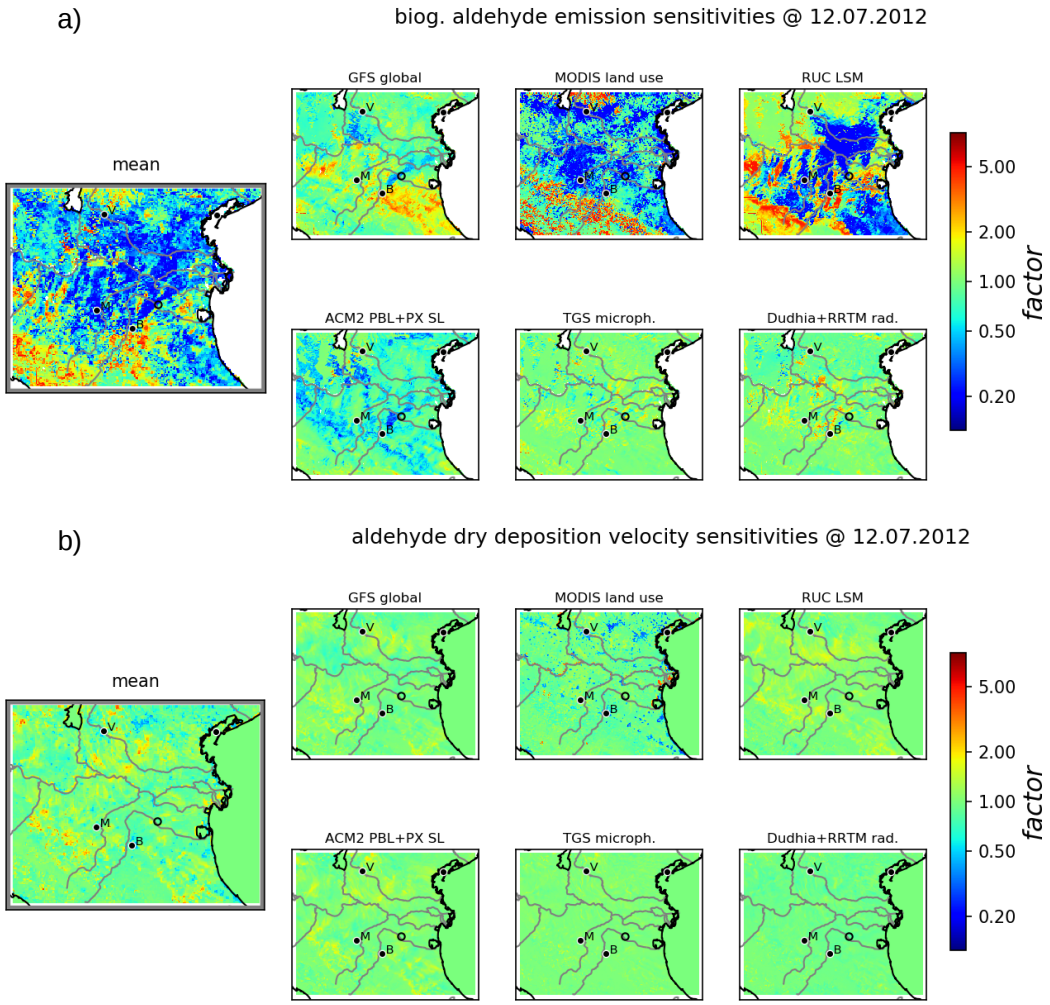

Figure 8.1: Independent- mean and sensitivities of biogenic emissions (a) and dry deposition velocities (b) of aldehyde for joint perturbation. The sensitivities given as factors w.r.t. to the mean (left subplot). Note the different scales for HNO_3 and aldehyde. Plotting conventions as in Fig. 7.6.

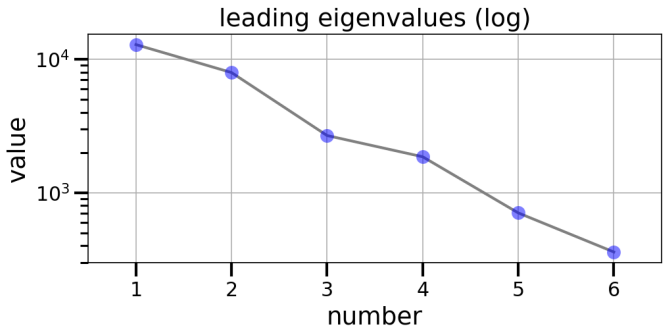

Figure 8.2: Leading eigenvalues for joint perturbations for independent input sensitivities (blue dots). Eigenvalues are plotted on a logarithmic scale.

The leading eigenmodes do thus refer to leading uncertainties with respect to all biogenic emissions and dry deposition velocities. Fig. 8.2 indicate that the size and decrease of eigenvalues is similar to the ones for only biogenic emissions. This is caused by the dominating contribution of biogenic emissions to the total uncertainties of all parameters. Thus, the leading total uncertainties of biogenic emissions and dry deposition velocities can be well approximated by considering biogenic emissions only. This can also be seen from the contributions to the leading eigenvectors in Fig. 8.3. For all eigenmodes, contributions of aldehyde dry deposition velocities remain small compared to aldehyde biogenic emissions.

The dominating uncertainties of biogenic emissions result in much larger differences in related perturbation factors, as shown in Fig. 8.4. Factors of biogenic aldehyde emissions range from less than 0.2 to about 5, whereas factors of dry deposition velocities remain mainly within 0.5 to 2. Only members 003, 004 and 008 with large negative contribution of the 1^{st} eigenmode show significant reduction of aldehyde dry deposition velocities in urban regions of the Po valley.

Although perturbation factors remain relatively small, significant ensemble spread is created for aldehyde dry deposition velocities in Fig. 8.5. In most areas of the domain, deposition velocities range between 0.004 and $0.006\frac{m}{s}$. At the same time, comparably low dry deposition velocities are correlated with large biogenic emissions of aldehyde (e.g. member 001, 006, 007). For the other members, biogenic aldehyde emissions are reduced and dry deposition velocities are increased in the Po valley as indicated by the sensitivity to the land surface model.

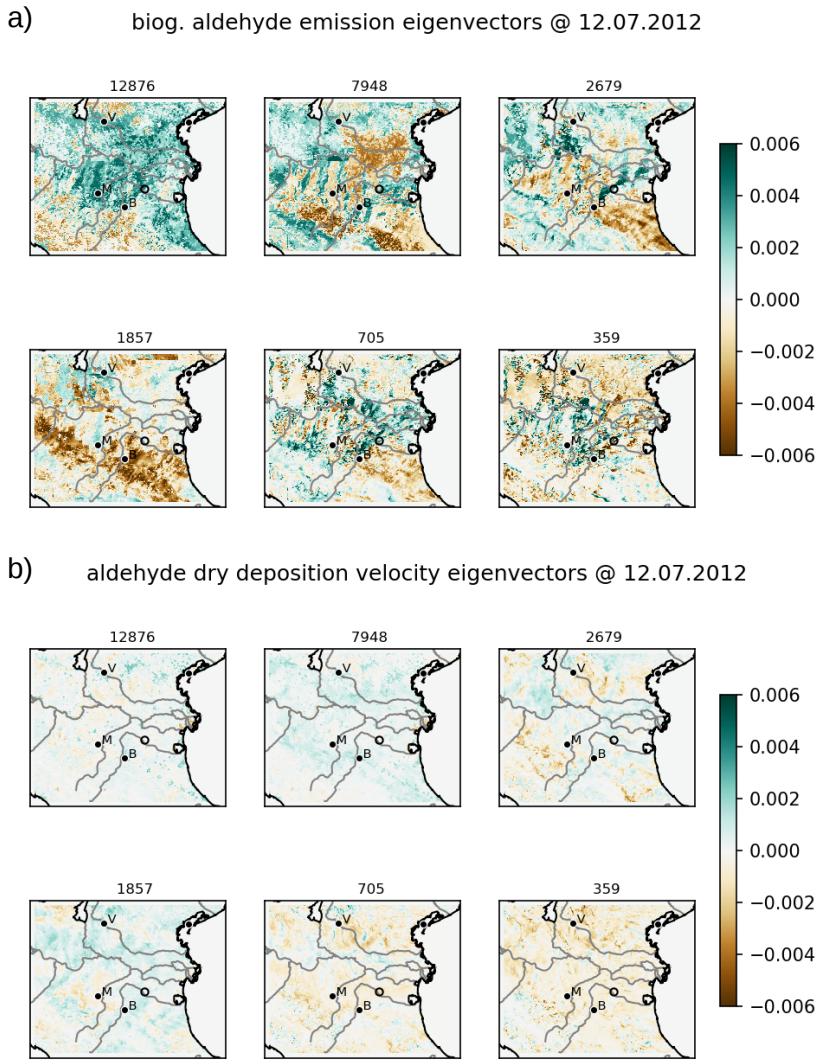

Figure 8.3: Normalized leading eigenvectors of biogenic emissions (a) and dry deposition velocities (b) of aldehyde for joint perturbation. Plotting conventions as in Fig. 7.8.

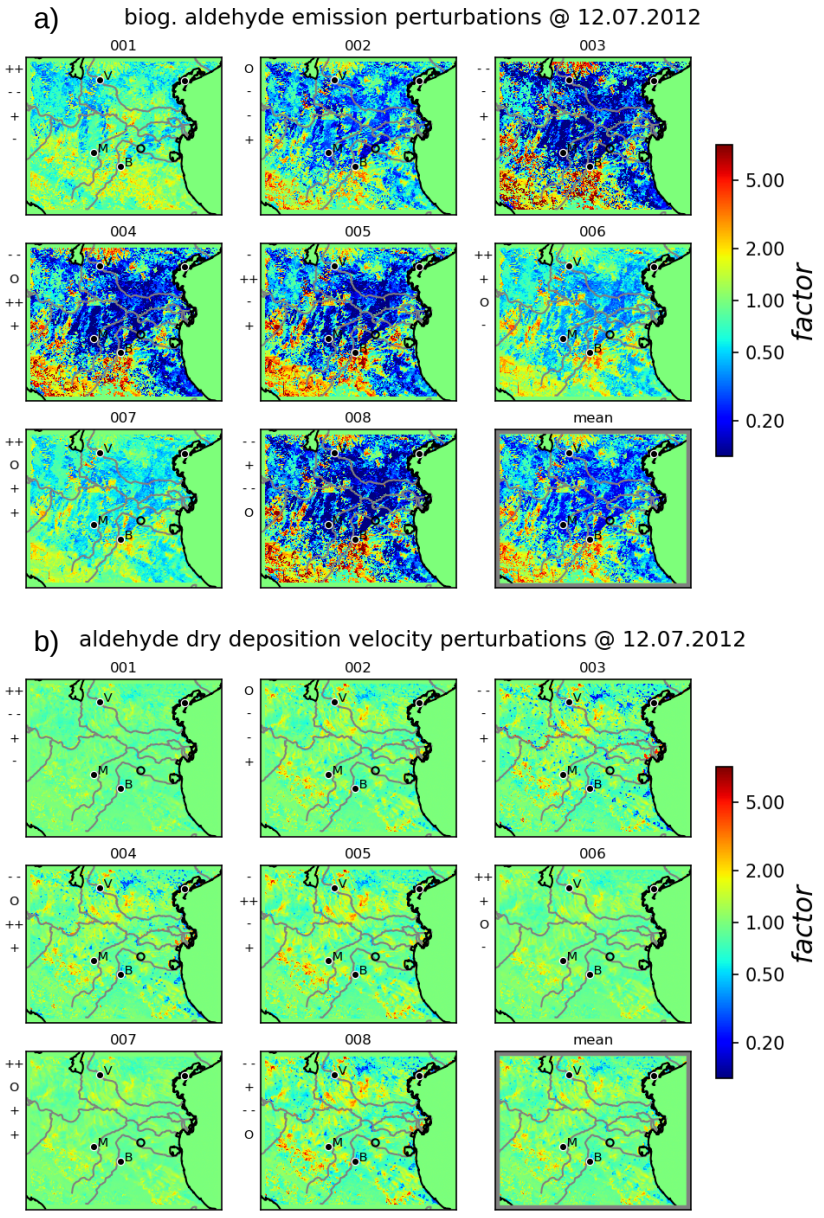

Figure 8.4: Ensemble of perturbations of biogenic emissions (a) and dry deposition velocities (b) of aldehyde for joint perturbation. Plotting conventions as in Fig. G.1.

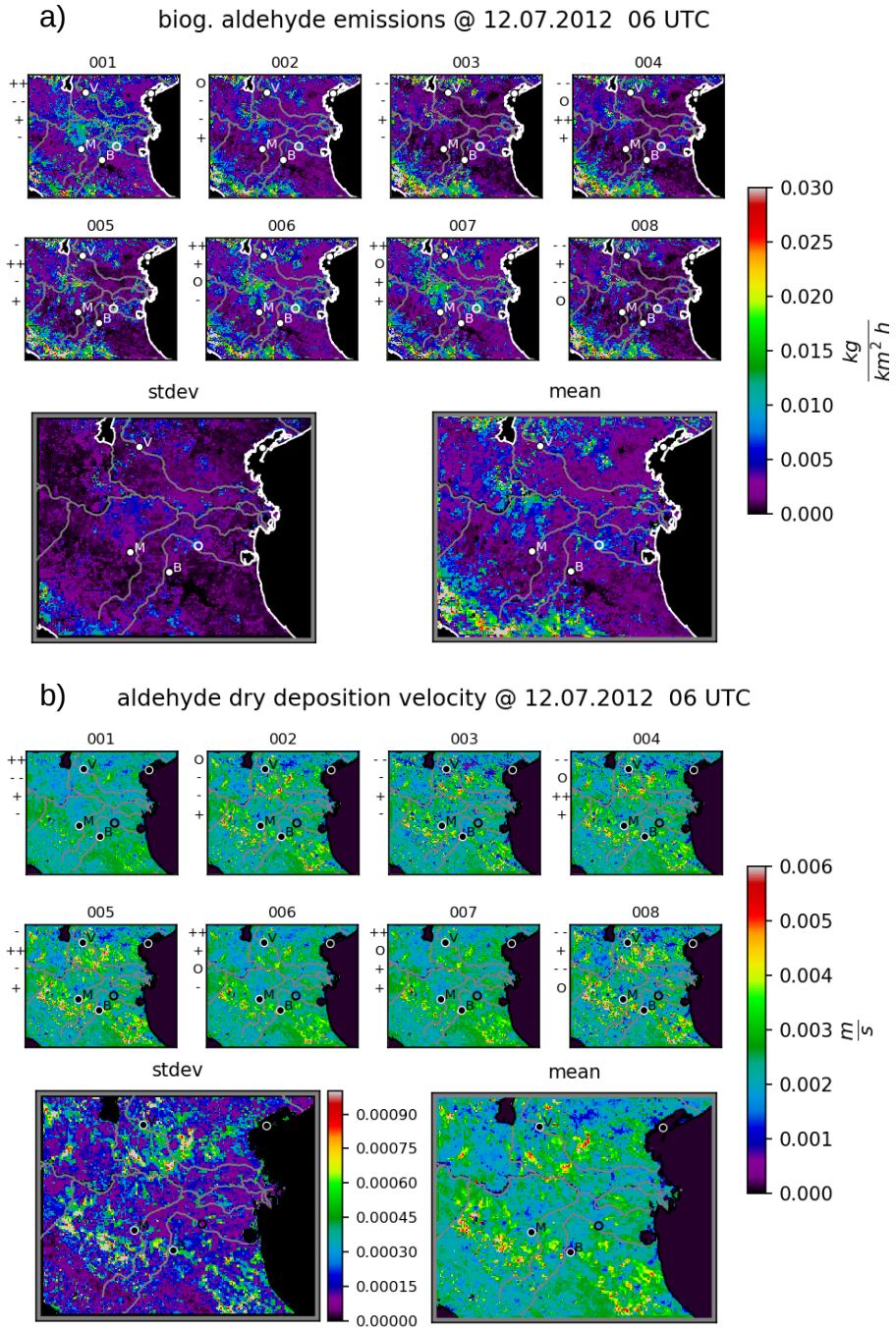

Figure 8.5: Ensemble of biogenic emissions and dry deposition velocities of aldehyde for joint perturbations. Plotting conventions as in Fig. G.2.

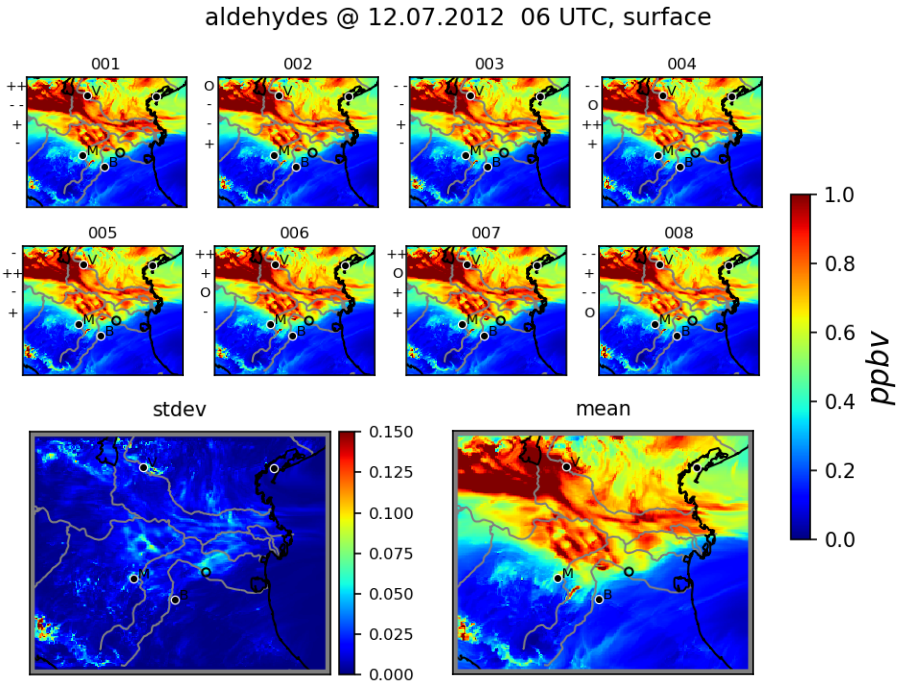

Figure 8.6: Ensemble of aldehyde concentrations for joint perturbations. Plotting conventions as in Fig. G.2.

The resulting ensemble spread of aldehyde surface concentrations in Fig. 8.6 is influenced by both, biogenic emissions and dry deposition velocities. However, aldehyde is mostly determined by high concentrations in the north-western and northern Po valley which originate from anthropogenic sources. Although uncertainties of biogenic emissions dominate in relative terms, their low contribution to total aldehyde emissions results in similar absolute uncertainties as for dry deposition velocities. Thus, uncertainties resulting from perturbed biogenic emissions and dry deposition remain small compared to absolute concentrations. This indicates that uncertainties in anthropogenic aldehyde emissions have to be considered in order to create sufficient uncertainty estimations of aldehyde in this area.

8.2 Ensemble Validation by Flight Observations

Ensemble forecasts from the KL algorithm are validated with high-frequency Zeppelin observations of the PEGASOS campaign 2012. Due to the dominating contribution of uncertainties in biogenic emissions, only these parameters are perturbed using independent input sensitivities and additional uncertainties in the emission approach. Three flights in the Po valley are selected to validate the uncertainty estimation for different situations.

8.2.1 Vertical Flight on 12.07.2012

Ensemble forecasts for flight *F049* which was performed during the early morning hours on 12.07.2012 have already been discussed in Ch. 7. Input sensitivities, eigenmodes, perturbations and emissions of isoprene for independent sensitivities and additional uncertainties are given in Sec. 7.1.3 and Appendix G.1.

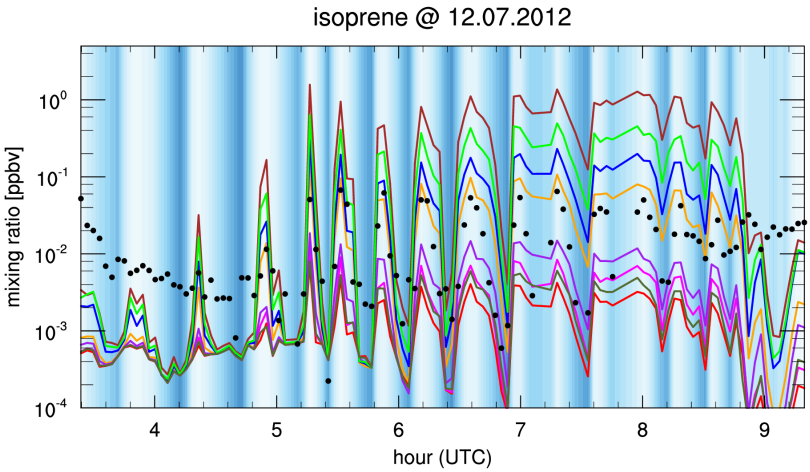

Figure 8.7: Validation of KL ensemble (colored lines) with PEGASOS observations (black dots) for isoprene from vertical flight on 12.07.2012. Background shading indicates the Zeppelins height (white: 0 m, dark blue: 700 m). Forecasted concentrations are interpolated to time and position of the Zeppelin. Member 002 representing the ensemble median is shown as orange line.

Fig. 8.7 shows isoprene concentrations along the flight path on 12.07.2012. The vertical movement of the Zeppelin is clearly related to variations in observed and modeled isoprene concentrations. During the main part of the flight between 05:30 and 09:00 UTC, observed concentrations follow the median predictions of member 002. The significant decrease of observed concentrations in high altitudes is well captured by the median forecast between 06:00 and 07:00 UTC. Between 07:00 and 08:00 UTC, this reduction is less pronounced by the forecasts, which may be caused by differences in the development of the mixed layer. However, the observed concentrations are still covered by the ensemble spread, indicating a reasonable uncertainty estimation.

During the very end of the flight, the Zeppelin headed southbound towards its base station. In this region, the sensitivity analysis indicates low isoprene emissions in all cases leading to an underestimation of isoprene concentrations. Before 5:30 UTC, the observations show a continuous decrease in isoprene concentrations, which is not found in the ensemble forecasts. According to personal communication with instrument experts, this relatively large values are assumed to be artifacts from the calibration procedure. Additionally, the observed values reach down to the detection limit of about 1 *pptv* = 10^{-3} *ppbv* which might influence observed low concentrations through the flight.

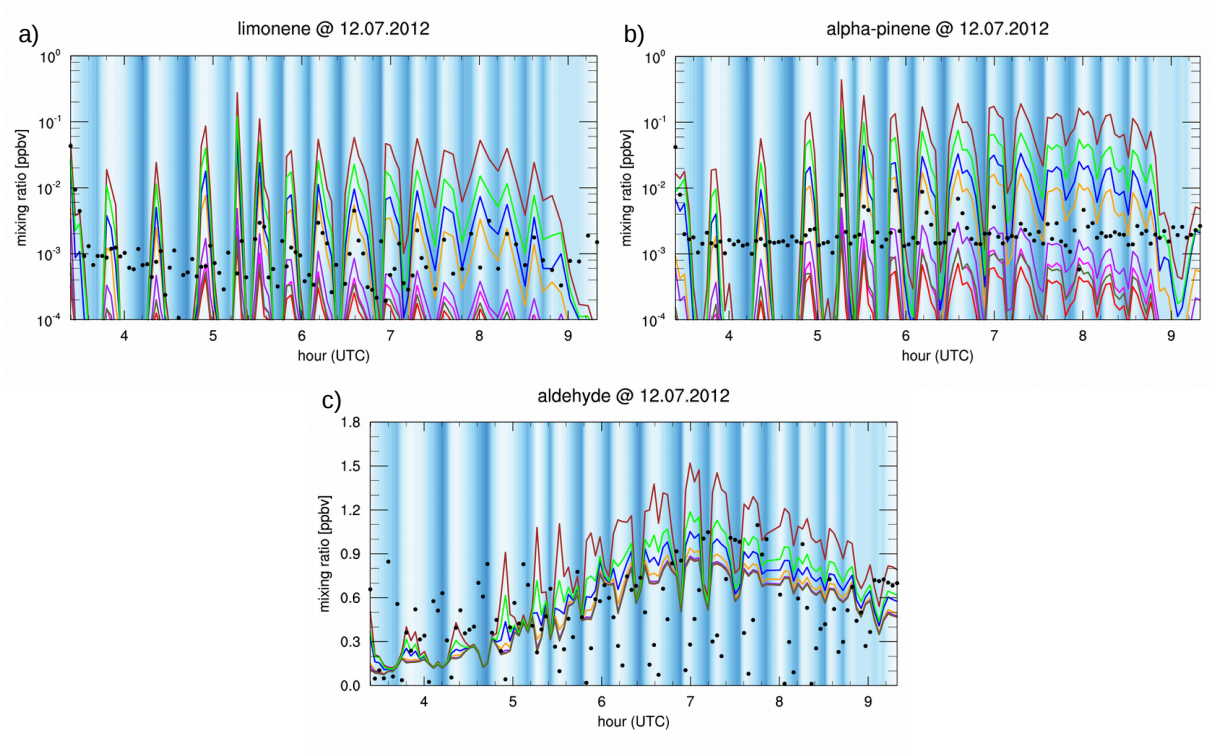

Figure 8.8: Validation of KL-ensemble (colored lines) with PEGASOS observations (black dots) for limonene (a), alpha-pinene (b) and aldehyde (c). Plotting conventions as in Fig. 8.7. Note that aldehyde concentrations are not plotted in the logarithmic scale and observations do only consider acetaldehyde.

Observed and modeled concentrations of limonene, alpha-pinene and aldehyde are shown in Fig. 8.8. The observations of limonene and alpha-pinene are also affected by the instruments detection limits. Thus, much lower modeled concentrations in high altitudes are still in accordance to observations with about 10^{-3} *ppbv*. Near-surface peak concentrations of these two gases agree well with the ensemble median member 002. Only the decrease of observed low level alpha-pinene concentrations after 07:00 UTC is underestimated by the ensemble. This might be caused for example by underestimated emission reduction of alpha-pinene due to soil dryness by the model.

In contrast to the other biogenic gases, observed aldehyde concentrations increase

with height (Fig. 8.8c). This behavior is not represented by the ensemble forecasts and may be caused by advection from larger aldehyde sources above the developing mixing layer. In contrast, low level concentrations are overestimated after 05:00 UTC. This difference is possibly related to the different definitions of the plotted values. While the observations do only refer to acetaldehyde, the model includes also higher aldehydes. Generally, the forecast and uncertainty estimation of aldehyde appears to be influenced by other processes like anthropogenic emissions and transport of residual concentrations as indicated in Sec. 8.1.

8.2.2 Horizontal Flight on 01.07.2012

Zeppelin-borne observations from flight *F039* during the early morning on 01.07.2012 allow the validation of the KL ensemble forecast along a horizontal flightpath towards the Apennines.

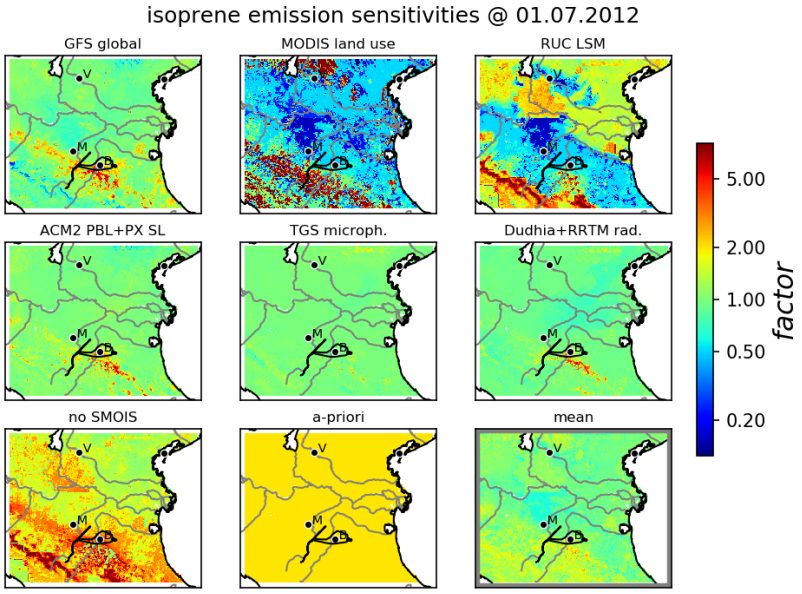

Figure 8.9: Independent- mean and sensitivities of isoprene including additional uncertainties of biogenic emissions for horizontal flight on 01.07.2012. The sensitivities given as factors w.r.t. to the mean (lower right subplot). The Zeppelin flight pattern is indicated as black line. Plotting conventions as in Fig. 7.6.

Fields of independent sensitivities and mean values for isoprene emissions are given in Fig. 8.9. The general signals are similar to the ones on 12.07.2012 with large sensitivities for land use, land surface model and soil-moisture dependency. The soil-moisture dependency affects large parts of the domain leading to increased isoprene emissions when this dependency is not considered. The sensitivity to land use shows similar patterns as on 12.07.2012 but larger signals of increased emissions in the mountains and decreased

values in the Po valley. Areas of strongly increased and decreased emissions are induced by the sensitivity to the land surface model. Reduced values are simulated by RUC LSM in the northern parts of the Apennines and around Verona due to soil dryness. At the same time, isoprene emissions are highly increased in parts of the southern Apennines. Sensitivities to the other input sources remain small with somehow increased emissions south of Bologna for global meteorology, ACM2 BL + PX SL and Dudhia + RRTM radiation parameterizations. Independent mean values of isoprene emissions are close to the reference in the whole domain.

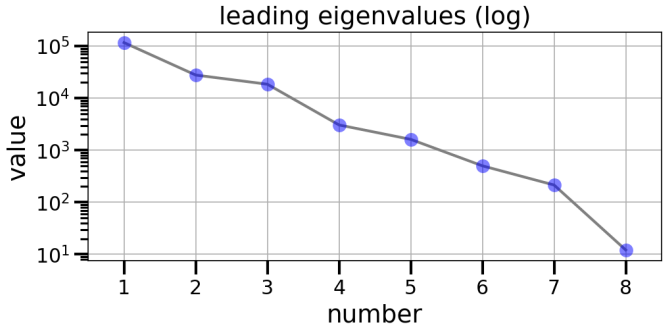

Figure 8.10: Leading eigenvalues of biogenic emissions for additional a-priori uncertainties for horizontal flight on 01.07.2012 (blue dots). Eigenvalues are plotted on a logarithmic scale.

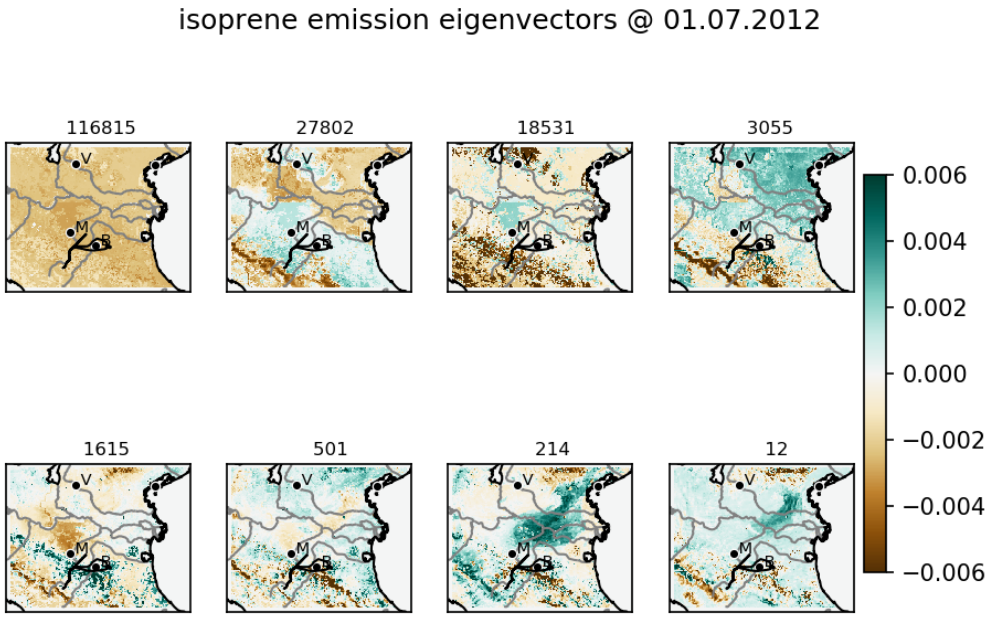

Figure 8.11: Normalized leading eigenvectors of isoprene for additional a-priori uncertainties of biogenic emissions for horizontal flight on 01.07.2012. The Zeppelin flight pattern is indicated as black line. Plotting conventions as in Fig. 7.8.

The eigenvalues in Fig. 8.10 show a fast, but steady decrease. The leading eigenmodes decrease on average by about one order of magnitude every two modes. The 1^{st} eigenmode mainly related to the a-priori uncertainty is dominant but followed by two other modes with large contributions. According to the eigenvectors of isoprene emissions in Fig. 8.11, these 2^{nd} and 3^{rd} eigenmodes are induced by the sensitives to the land surface model and land use information, respectively. The 4^{th} mode represents the remaining sensitivity to soil dryness differing from the direction of the 2^{nd} mode.

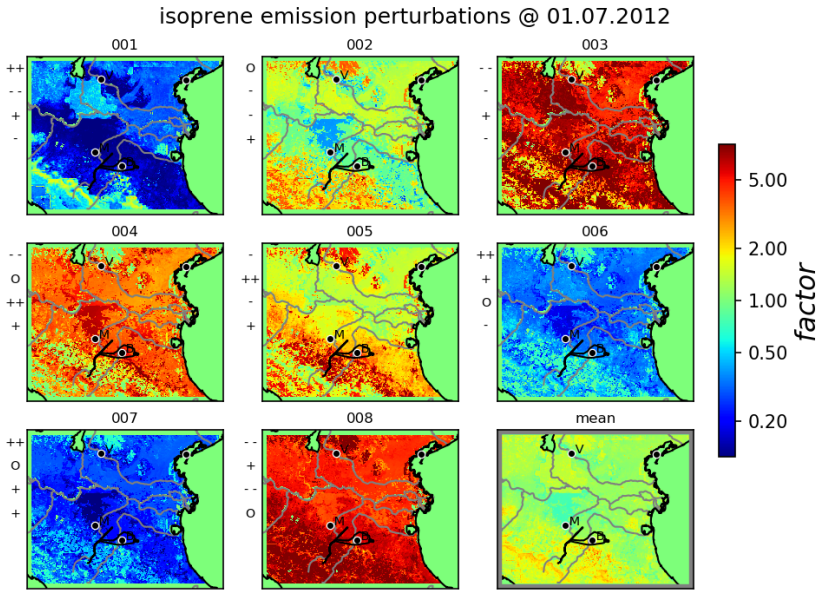

Figure 8.12: Ensemble of perturbations of isoprene for additional a-priori uncertainties of biogenic emissions for horizontal flight on 01.07.2012. The Zeppelin flight pattern is indicated as black line. Plotting conventions as in Fig. G.1.

The perturbation factors of isoprene emissions in Fig. 8.12 are highly influenced by the 1^{st} eigenmode leading to a common direction of perturbation from the independent mean. Additionally, regional differences are induced by contributions of the subsequent eigenmodes. For example, differences between the north-eastern and south-western part of the Po valley for member 001, 002 and 005 are induced by the 2^{nd} mode. The 3^{rd} eigenmode creates different factors between the mountains and the valley for member 004 compared to member 008. Although the ensemble covers perturbation factors of more than one order of magnitude, the ensemble mean remains close to one for the whole domain.

The large range of perturbations results in highly different isoprene emissions shown in Fig. 8.13. Although mean emissions are highest in the Apennines, member 003, 004, 005 and 008 also predict emissions of more than $0.6\frac{kg}{km^2h}$ north of Modena. While emissions in the Po valley do not exceed values of $0.05\frac{kg}{km^2h}$ for member 001, these values are found for member 008 even in regions with neglectable reference emissions. For the whole domain,

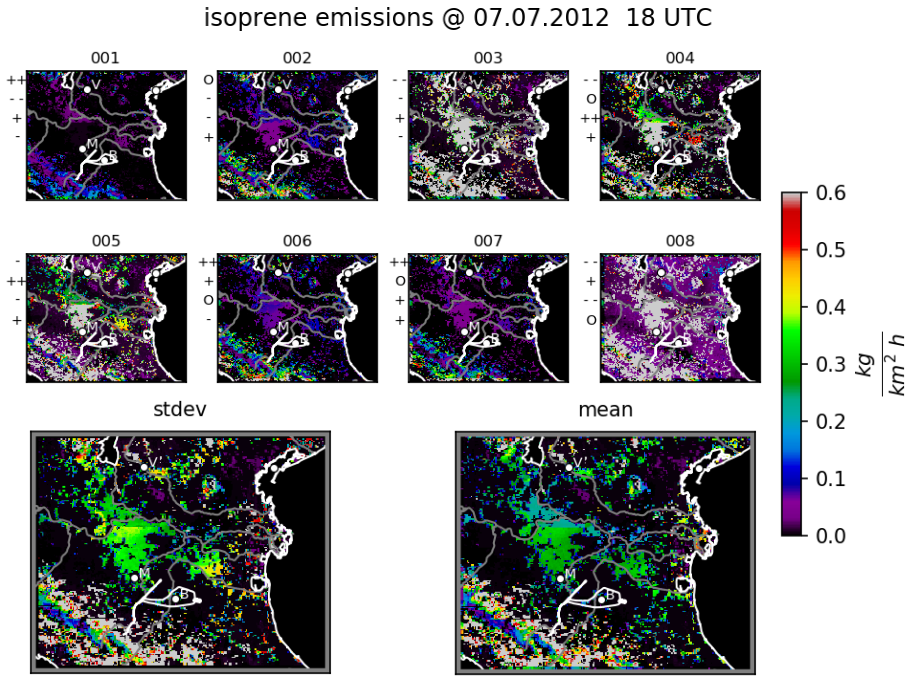

Figure 8.13: Ensemble of isoprene emissions for additional a-priori uncertainties of biogenic emissions for horizontal flight on 01.07.2012. The Zeppelin flight pattern is indicated as while line. Plotting conventions as in Fig. G.2.

the ensemble standard deviation of isoprene emissions is at least as large as the ensemble mean.

In the regions covered by the Zeppelin observations, relatively low isoprene emissions are forecasted by all members. While the Zeppelin moved towards south into a valley of the Apennines, observed concentrations are influenced by higher surrounding emissions of isoprene. This results in two periods of increased isoprene concentrations along the flight path in Fig. 8.14. The observed occurrence and extension of these two periods agrees well with the ensemble median forecasts (orange and purple lines). However, most forecasts indicate slightly decreased concentrations for the second period in the valley, whereas they tend to increase in the observations. This indicates an overestimation of emission reduction due to soil dryness resulting from underestimated soil moisture after sunrise in this area. Additionally, errors in local dynamics within the narrow valley might also play a role here.

At the beginning of the flight, the flight path shows a small descent of the Zeppelin between 05:15 and 05:30 UTC. This results in increased observed isoprene concentrations where most forecasts point towards decreased concentrations. This might be related to an underestimated local source of isoprene which becomes less significant in higher altitudes. At the end of the flight, the ensemble forecast slightly underestimates isoprene concentrations. However, observed values remain close to the member with largest concentrations which indicates reasonable ensemble spread. For this case, reasonable spread

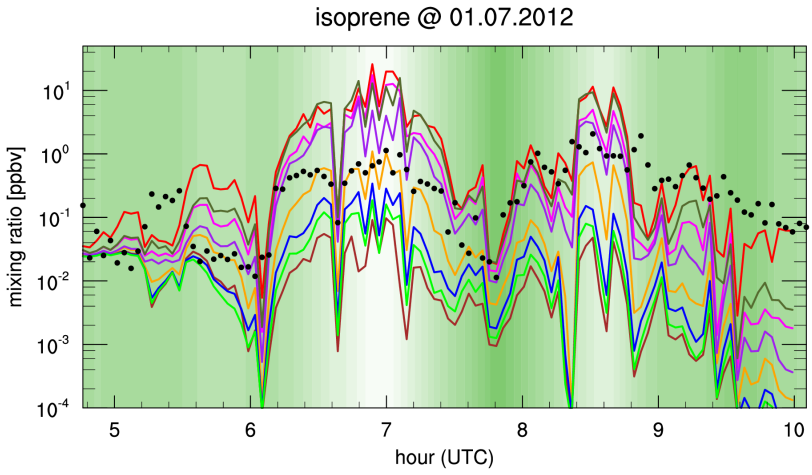

Figure 8.14: Validation of KL ensemble (colored lines) with PEGASOS observations (black dots) for isoprene from horizontal flight on 01.07.2012. Background shading indicates the Zeppelins latitude (white: 44.2°N, dark green: 45.4°N). Plotting conventions as in Fig. 8.7.

is only created because additional uncertainties in the emission approach are considered as independent sensitivities. The KL ensemble for independent sensitivities without these additional sensitivities was not able to estimate forecast uncertainties adequately.

8.2.3 Evening Flight on 07.07.2012

On 07.07.2012, flight *F045* was performed around sunset which offers ensemble validation under evening conditions. For this situation, the sensitivities and KL ensemble forecasts refer to a time-interval between 12 and 22 UTC. Note that the forecasts of the sensitivity analysis are initialized one day before, on 06.07.2012 at 00 UTC.

Independent sensitivities including additional sensitivities to the emissions algorithm are given in Fig. 8.15. Similar to the two cases for the early morning, largest sensitivities are found for land use, land surface model and soil-moisture dependency. MODIS land use information result in a large general reduction of isoprene emissions except in some parts of the mountains. Signals of RUC land surface model and no soil-moisture dependency point towards increased emissions in the southern half of the domain. This common enhancement is caused by large reduction of emissions in the reference case due to low soil moisture in these areas. Although the extension of both signals is very similar, sensitivity factors are larger for the land surface model. The remaining sensitives indicate locally increased emissions on the northern part of the Apennines.

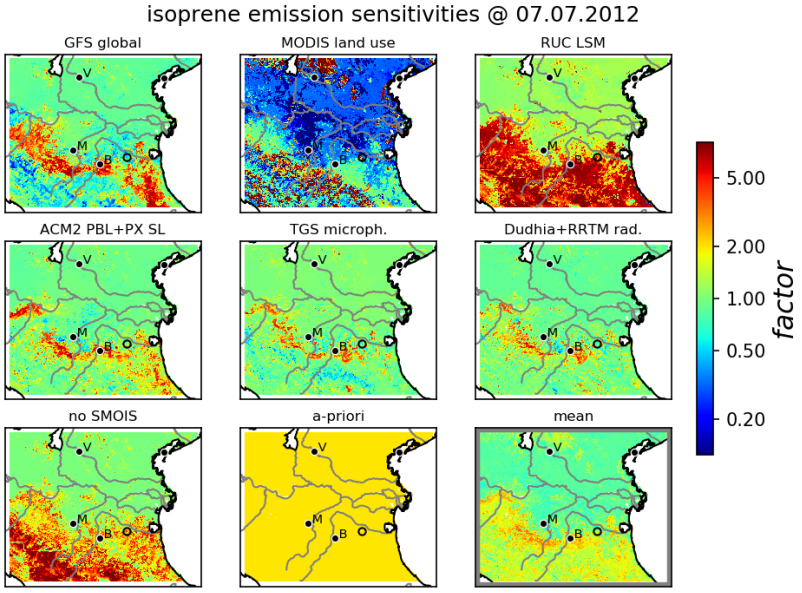

Figure 8.15: Independent- mean and sensitivities of isoprene including additional uncertainties of biogenic emissions for evening flight on 07.07.2012. The sensitivities given as factors w.r.t. to the mean (lower right subplot). Plotting conventions as in Fig. 7.6.

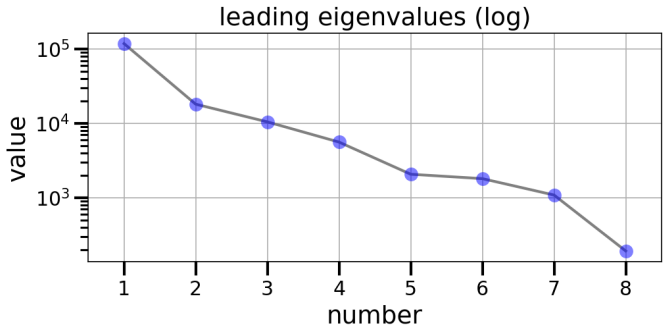

Figure 8.16: Leading eigenvalues of biogenic emissions for additional a-priori uncertainties for evening flight on 07.07.2012 (blue dots). Eigenvalues are plotted on a logarithmic scale.

The eigenmode analysis states the dominant contribution of the a-priori uncertainty. According to Fig. 8.16, the related 1^{st} eigenvalue is almost one order of magnitude larger than the remaining ones. Contributions of isoprene to the 2^{nd} eigenvector in Fig. 8.17 are induced by the sensitivity to land use information. The two subsequent eigenmodes correspond to the common direction (3^{rd}) of land surface model and no soil-dependency as well as their differences (4^{th}).

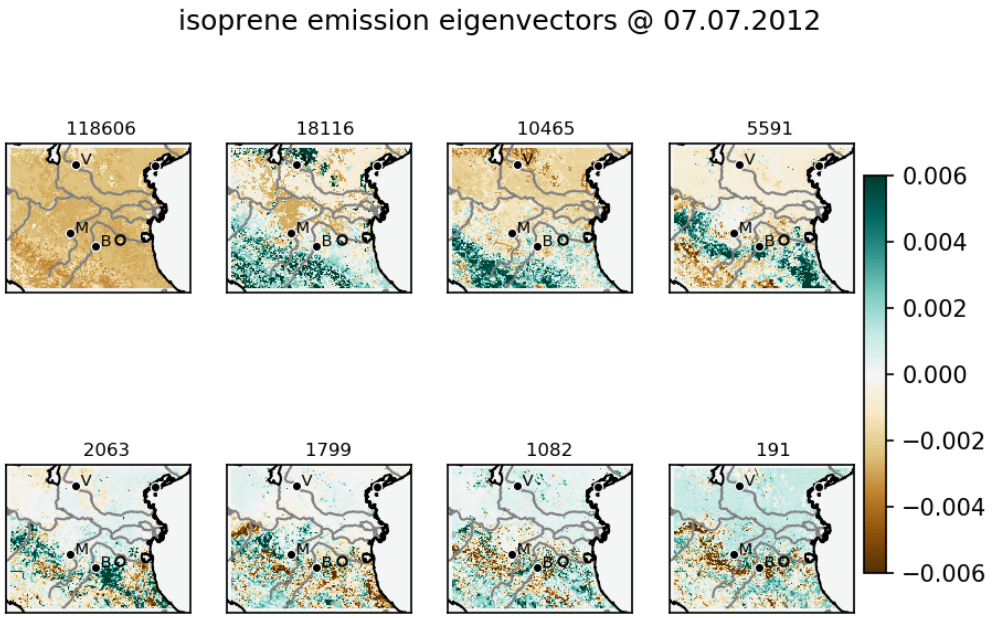

Figure 8.17: Normalized leading eigenvectors of isoprene for additional a-priori uncertainties of biogenic emissions for evening flight on 07.07.2012. Plotting conventions as in Fig. 7.8.

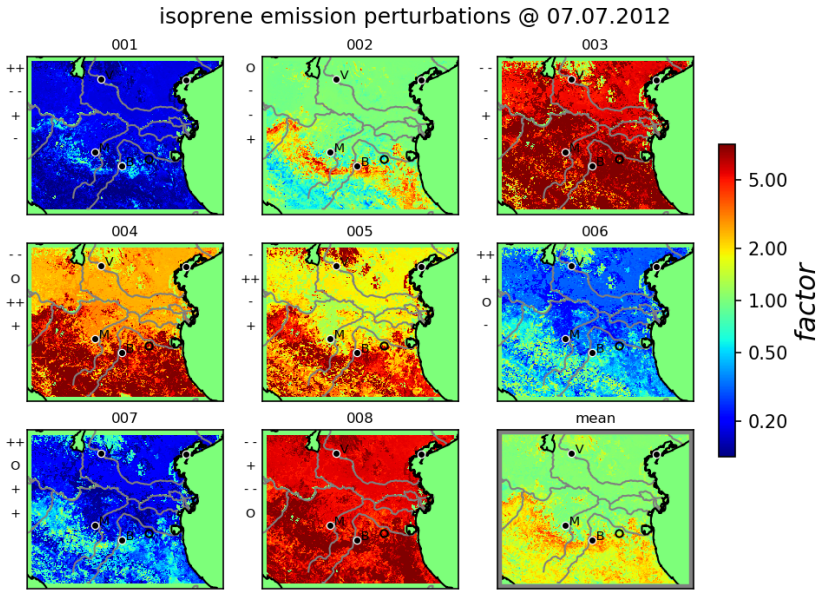

Figure 8.18: Ensemble of perturbations of isoprene for additional a-priori uncertainties of biogenic emissions for evening flight on 07.07.2012. Plotting conventions as in Fig. G.1.

The large uncertainty of the leading eigenmode results in highly different perturbation factors of isoprene in Fig. 8.18. Each member is mainly perturbed either towards decreased or increased emissions for the whole domain. For example, local differences due to the

2^{nd} eigenmode are visible in the central Po valley between member 003 and member 008. Member 002 is the only one with both, increased and decreased local emissions with respect to the reference forecast.

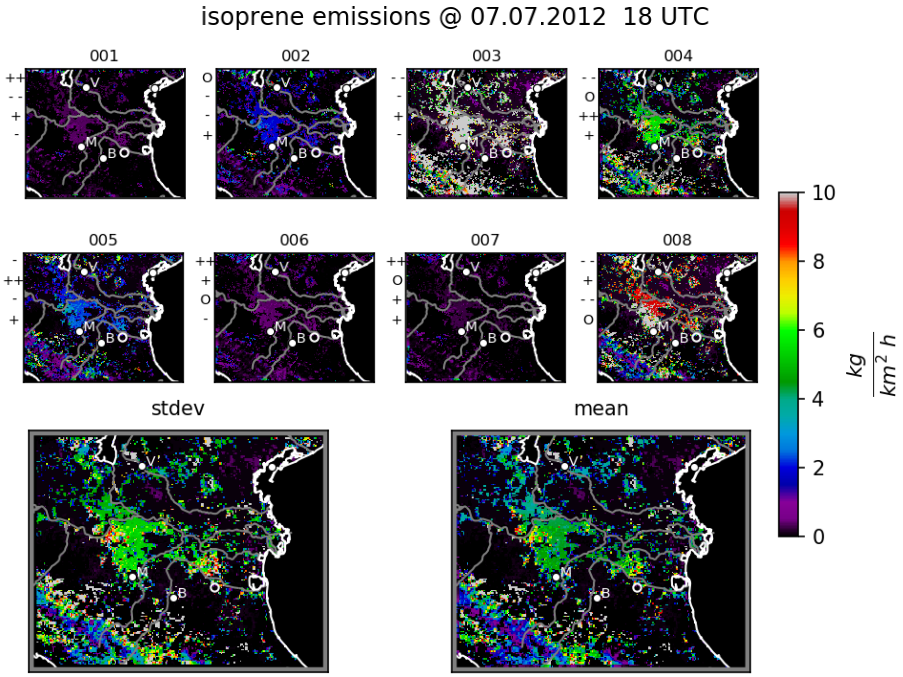

Figure 8.19: Ensemble of isoprene emissions for additional a-priori uncertainties of biogenic emissions for evening flight on 07.07.2012. Plotting conventions as in Fig. G.2.

As shown in Fig. 8.19, the large range of perturbation factors results in highly different isoprene emissions at 18 UTC. Similar to the two cases for the early morning, the isoprene standard deviation is of the same order at the ensemble mean. Local differences in emission strengths can be found in the Apennines and north of Modena when comparing member 008 with member 003 and 004.

Resulting isoprene concentrations along the flight path are given in Fig. 8.20. During the vertical sampling, observed concentrations do not decrease as much as in the two cases in the early morning. The lower vertical gradients are also forecasted by the ensemble and can be explained by still well-mixed conditions during the break-up of the mixed layer. Between 19:00 and 19:30 UTC, the Zeppelin ascends above to altitudes of about 800 m above sea level. Reduced isoprene concentrations in observations and forecasts show the decoupling process of aloft airmasses from the surface. In general, observed concentrations are well predicted by member 005 (purple line) which is close to the median, but the large ensemble spread may indicate an overestimation of forecast uncertainties.

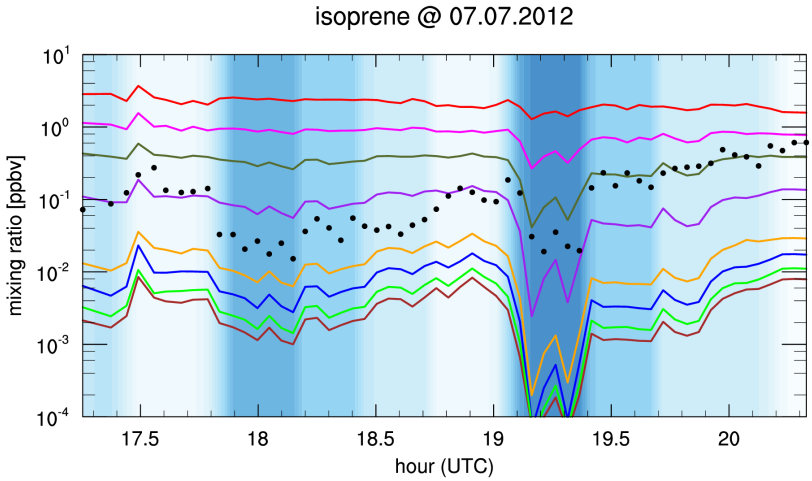

Figure 8.20: Validation of KL ensemble (colored lines) with PEGASOS observations (black dots) for isoprene. Background shading indicates the Zeppelins height (white: 0 m, dark blue: 825 m). Plotting conventions as in Fig. 8.7.

8.3 Computational Scaling

This section analyses the computational efficiency of the eigenmode calculation for ensemble generation in EURAD-IM. Computational scaling with respect to the dimension of the problem, number of sensitivities and -eigenvalues is discussed. The results are based on the computing time for the eigenmode calculation of biogenic emissions with full sensitivities (reference setup as in Sec. 7.1.1). If not mentioned differently, 16 eigenmodes of biogenic emissions of 5 gases are calculated from 32 sensitivities.

Table 8.1: Computing time with respect to the number of parameters. Relative factors refer to the relative increase in computing time compared to 1 parameter.

number of parameters	1	2	3	4	5
CPU time in sec.	44	176	398	710	1108
relative factor	1.0	4.0	9.0	16.1	25.2

The dimension of the problem increases proportional to the number of parameters considered. In this way, the number of parameters perturbed by the KL ensemble algorithm is limited by computational reasons. The increase in computing time with respect to the number of parameters in given in Tab. 8.1 and Fig. 8.21. Going from 1 (isoprene) to 5 biogenic emissions increases the computing time by approximately a factor of 25. A general quadratic increase in computing time with increasing dimension of the parameters is found. This is accordance to the quadratic dimension of the covariance matrix with

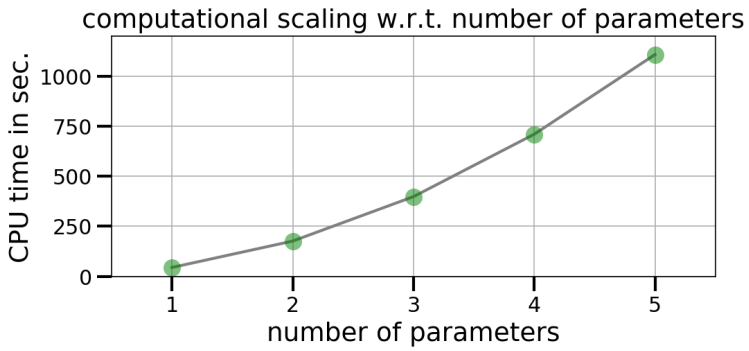

Figure 8.21: Computing time with respect to number of parameters. Exact numbers are listed in Tab. 8.1.

respect to the dimension of the parameters. Thus, the computing time increases linearly with the number of elements in the covariance matrix.

Table 8.2: Computing time with respect to the number of sensitivities. Relative factors refer to the relative increase in computing time compared to 8 sensitivities.

number of sensitivities	8	16	24	32
CPU time in sec.	122	285	417	660
relative factor	1.0	2.3	3.4	5.4

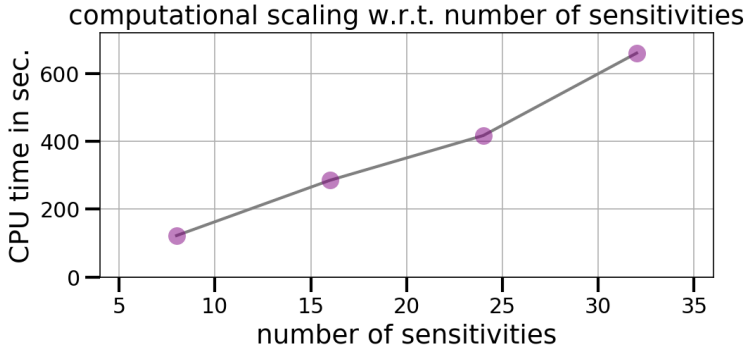

Figure 8.22: Computing time with respect to number of sensitivities. Exact numbers are listed in Tab. 8.2.

The computational scaling with respect to sensitivities uses 8, 16, 24 and 32 sensitivities in the calculation of covariances. As the number of eigenmodes should not extend the number of sensitivities in the covariances, the number of eigenmodes is reduced to 8 for this evaluation. According to Tab. 8.2 and Fig. 8.22, the computing time increases

almost linearly with the number of sensitivities. For this setup, doubling the number of considered sensitivities increases the computing time by about a factor of 2.3.

Table 8.3: Computing time with respect to the number of eigenmodes. Relative factors refer to the relative increase in computing time compared to 4 eigenmodes.

number of eigenmodes	4	8	12	16
CPU time in sec.	359	660	823	1108
relative factor	1.0	1.8	2.3	3.1

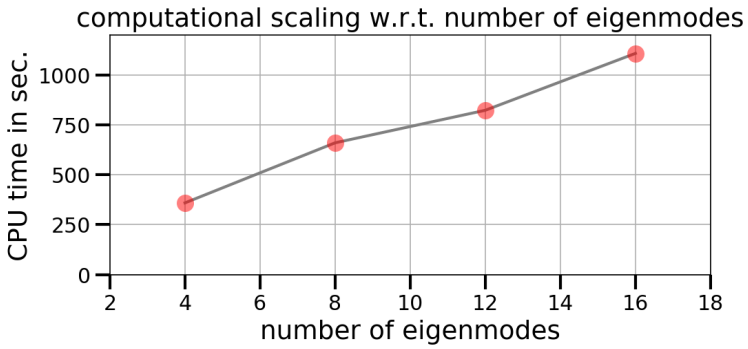

Figure 8.23: Computing time with respect to number of eigenmodes. Exact numbers are listed in Tab. 8.3.

The computational scaling with respect to the calculated number of eigenmodes is given in Tab. 8.3 and Fig. 8.23. Despite small variations, the computing time increases linearly with about one minute per eigenmode for this setup.

9 Conclusion and Outlook

The predictability of prognostic dynamical systems is generally limited. This is due to both, imperfect model input and inaccuracies in the numerical model. Atmospheric models are characterized by high dimensionality and complex nonlinear interactions. This renders an accurate estimation of forecast uncertainties challenging. The major challenge is a reliable and efficient estimation of forecast uncertainties from a limited ensemble of forecasts.

Focusing on uncertainties of model parameters, this study introduces an approach for efficient ensemble generation with respect to leading coupled uncertainties. The approach is based on the Karhunen-Loève (KL) expansion, which decomposes a stochastic process into its leading eigenmodes. In the context of uncertainty estimation in atmospheric models, leading eigenmodes provide information on the dominant coupled uncertainties of model parameters. Based on this, stochastic sampling for ensemble generation is performed in an uncorrelated subspace spanned by the eigenmodes. Through this reduction of the sampling space, it is shown that the stochastic dimension of the problem can be significantly reduced. This makes the algorithm suitable for efficient ensemble generation of high-dimensional atmospheric models where the computational costs are a critical and limiting quantity.

In the KL ensemble algorithm, perturbations are created from covariances of the stochastic process which are not changed by the KL expansion. This means that for large ensemble sizes the statistics of the stochastic process converges towards its input values. Therefore, the major benefit of the KL ensemble lies in the optimality of the perturbations focusing on leading uncertainties, providing an optimal coverage of the uncertainty space even for low ensemble sizes. In this context, the greatest benefit is achieved for high correlations of model parameters. But even for uncorrelated parameters, the approach allows the combination of major uncertainties represented by a low number of perturbations. However, the performance the the resulting KL ensemble highly depends on the statistics of the defined covariances.

For this study, covariances are generated from sensitivities of the model parameters to potential input modifications. Calculating sensitivities form all possible combinations requires large computational efforts, which is in contradiction to the motivation. Therefore, the assumption of independent input sensitivities was derived and applied in this study. Assuming tangent linearity for the sample interval, multiple random control parameters can be handled with limited computational effort. Exemplary results indicate that the major properties of leading sensitivities are captured by independent sensitivities. Moreover, this setup allows the consideration of additional uncertainties in a convenient way. This offers the possibility to combine multiple kinds of uncertainties from different information sources. For example, uncertainties due to input sensitivities are combined with a-priori uncertainty estimations. However, the assumption of independent input sen-

sitivities may not be a good approximation in many cases. The user has to decide if the computational benefit justifies the neglection of nonlinear effects.

The KL ensemble generation algorithm is implemented into the regional chemistry transport model EURAD-IM and the numerical weather prediction model WRF-ARW, where it is applied to a case study in the Po valley in July 2012. Within EURAD-IM, biogenic emissions and dry deposition velocities of different gases are perturbed based on a sensitivity analysis.

The sensitivity analysis indicates two main sources of uncertainties for biogenic emissions. Firstly, small errors in land use information result in large uncertainties for all considered biogenic gases. Especially for isoprene, the presence of a few trees significantly increases isoprene emissions. Secondly, drought stress of plants induces high sensitivities of biogenic emissions to predicted soil moisture. Large differences in the temporal evolution of soil moisture are found for different land surface schemes. Thus, related uncertainties may be reduced by improving land surface models in numerical weather prediction models based on sufficient observations. As both main sensitivities are related to the land surface, forecast accuracy is assumed to improve significantly by more detailed information on vegetation and soil properties. High-resolution vegetation data for example from ESA's Sentinel-2 satellite may be an important future step towards uncertainty reduction.

Based on these sensitivities, the KL ensemble induces a large ensemble spread of biogenic emissions during this case study. Considering different sources of uncertainties, the ensemble standard deviation of all considered biogenic emissions is at least as large as the ensemble mean. The validation with Zeppelin observations indicates good ensemble performance for isoprene in all three studied cases. Under most conditions, observed isoprene concentrations are well represented by the ensemble median. In cases of incorrect median concentrations, related differences to observations are of the same order as the ensemble spread. This confirms reasonable uncertainty estimation by the ensemble forecasts for ensemble sizes of the order of 10 members. Only during evening conditions, the forecast uncertainty may be overestimated with respect to the available observations.

Sensitivities of dry deposition velocities remain small compared to biogenic emissions. This indicates that the overall forecast uncertainty of biogenic gases is mainly driven by errors in terrestrial emissions. However, significant uncertainties may be induced by the deposition approach itself which are not considered here due to missing data. As soon as uncertainties in these error sources are specified, they could be included as additional independent sensitivity in the KL ensemble algorithm.

Applying the KL ensemble generation to dynamical parameters within WRF-ARW appears to be non-trivial. While biogenic emissions and dry deposition velocities act as external driving parameters, dynamical parameters are either prognostic or diagnostic parameters within the dynamical model. Thus, continuous perturbation may result in overestimations or instabilities by highly nonlinear feedbacks. The latter appears for perturbed friction velocities in this case study. Although the perturbation of surface exchange coefficients solved the problem in this case, the problem may still appear in other cases. The KL ensemble is applied to surface exchange coefficients on larger scales in order to increase potential effects on local dynamics. Although this application results

in reasonable perturbations of surface exchange coefficients, limited effects on friction velocities did not create significant spread in low level winds. On the one hand, this may be caused by an underestimation of uncertainties by the considered sensitivities. On the other hand, an exemplary analysis of transport and mixing of airmasses indicates large sensitivity to the land surface model. Thus, leading dynamical sensitivities may be driven by parameters within the land surface model.

Uncertainty estimation of forecasts is closely related to the limits of predictability. A predictability limit in numerical weather prediction (NWP) denotes the forecast time, where the forecast uncertainty starts to increase significantly until becoming worthless. As chemistry transport models (CTMs) are usually driven by NWP forecasts, they inherit their errors. Thus, atmospheric chemical forecasts are effected by the predictability limits of NWP forecasts. Depending on the sensitivities, chemical predictability limits due to uncertainties in NWP may be shortened or prolonged compared to meteorological predictability limits. The exemplary investigation of source regions of airmasses in this study indicates a highly reduced chemical predictability limit. Here, small differences in local transport and mixing may result in large differences in the chemical composition of this airmass within hours.

For biogenic emissions, forecast uncertainties appear to be dominated by sensitivities to vegetation and land surface properties. Errors in these input fields do not change substantially with time which makes the forecast uncertainty almost time-invariant. Thus, the definition of *predictable regions* appears to be more important for biogenic gases than defining a predictability limit.

In numerical weather prediction, ensemble forecasts are often evaluated by rank- or Talagrand-diagrams showing the statistical ranking of observations with respect to the forecasts. However, errors in biogenic emissions tend to be comparably constant in time, which leads to a preferred ranking in the Talagrand-diagram. Thus, an evaluation for biogenic gases could only lead to reasonable results, if observations at multiple locations are considered. But high-resolution observations of biogenic gases are too sparse to extract representative statistics in this case.

The good performance of the KL ensemble for biogenic gases motivates further developments with respect to different aspects. Concerning the KL ensemble algorithm, weighted independent input sensitivities could be implemented in the calculation of the covariances. Such a generalization would allow to consider multiple input modifications, weighted according to their importance or accuracy. In chemistry transport modeling, an application to other model parameters would be of advantage. On the one hand, perturbing anthropogenic emissions would allow uncertainty estimation of all atmospheric trace gases. On the other hand, investigating possibilities to perturb surface fluxes may increase the effect on local transport and mixing. Furthermore, the approach for covariance modeling could be used in the context of chemical data assimilation. However, forecast error covariances in data assimilation demand slightly different properties, which require for example localization of spatial correlations.

A Flowcharts WRF parameterization schemes

A.1 Flowchart Eta surface layer scheme in WRF

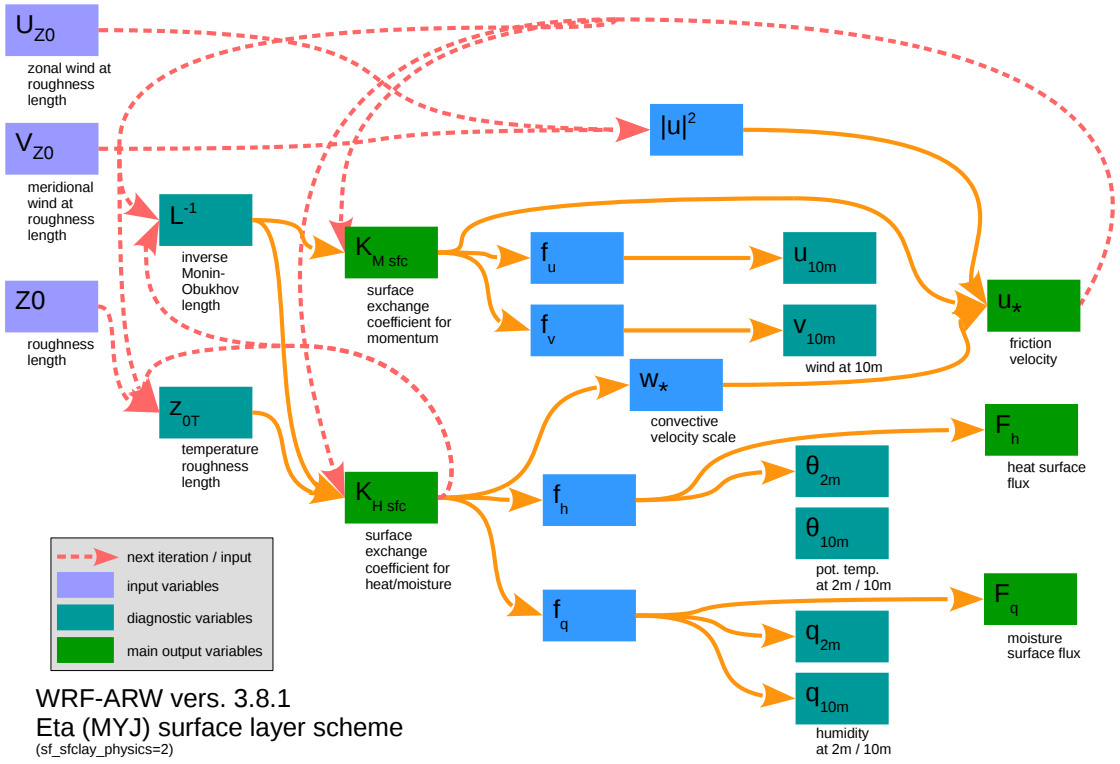

Figure A.1: Flowchart summarizing the implementation of the Eta surface layer scheme in WRF-ARW 3.8.1. Colored boxes represent major variables (colors according to legend). Dependencies between variables calculated within the routine and given as input are indicated by orange and red arrows, respectively.

A.2 Flowchart MYJ boundary layer scheme in WRF

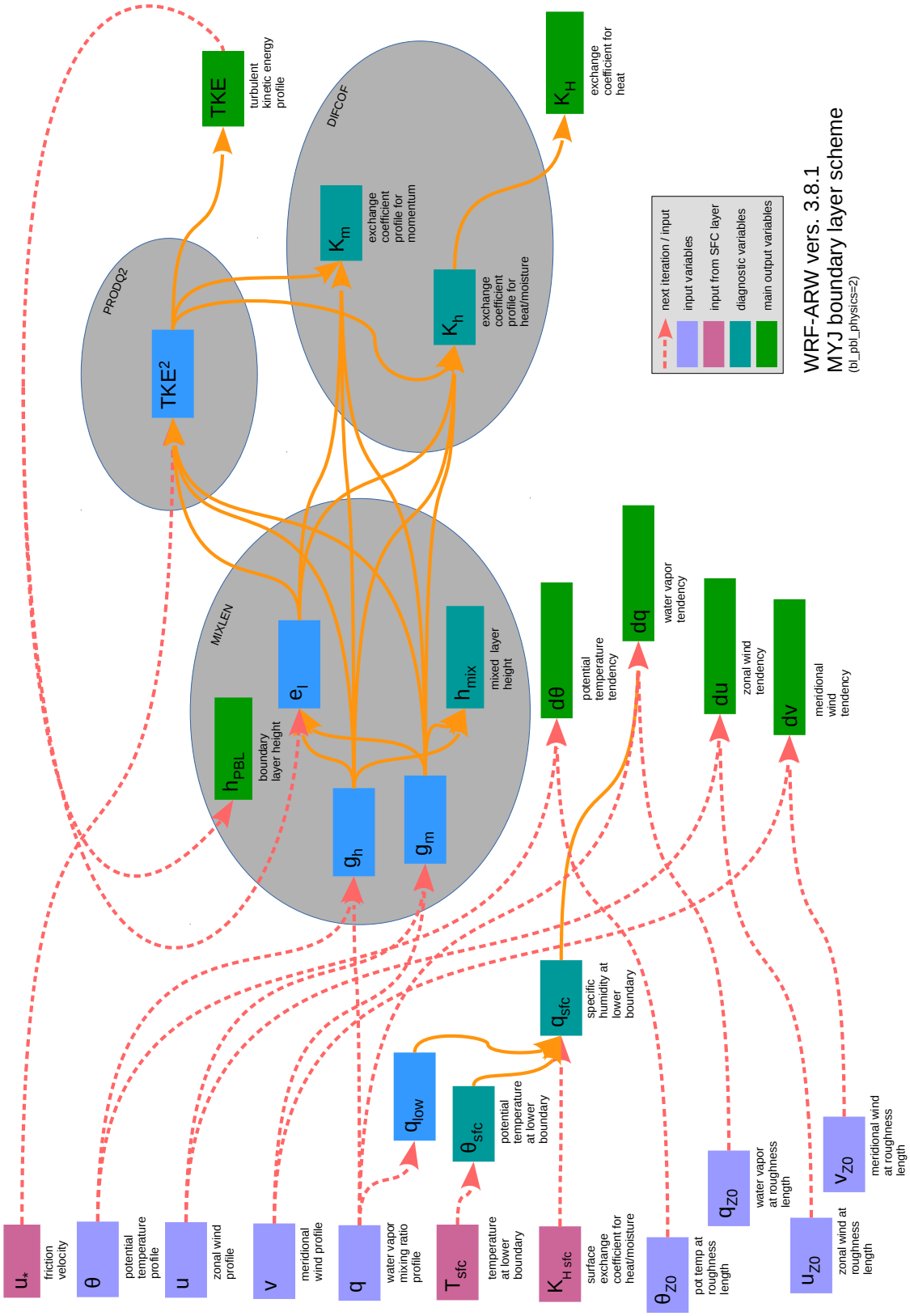

Figure A.2: Flowchart summarizing the implementation of the MYJ boundary layer scheme in WRF-ARW 3.8.1. Colored boxes represent major variables (colors according to legend) and subroutines are shown by gray areas. Dependencies between variables calculated within the routine and given as input are indicated by orange and red arrows, respectively.

B Appendices Development KL Ensemble

B.1 Proof of Random Coefficients

In the KL expansion, the following conditions hold for random coefficients $y_d(s)$, $s \in S$:

- They are uncorrelated: $\mathbb{E}\left[y_d(\omega)\ y_{d'}(\omega)\right] = 0 \quad \forall\ d \neq d'$
- Their variance equals the eigenvalues of the covariance matrix: $\mathbb{E}\left[y_d(\omega)\ y_d(\omega)\right] = \lambda_d$

Proof:

$$
\begin{aligned}
\mathbb{E}\left[y_d(\omega)\ y_{d'}(\omega)\right] &= \mathbb{E}\left[\int_S x(s,\omega)\ f_d(s)ds \int_{S'} x(s',\omega)\ f_{d'}(s')ds'\right] \\
&= \int_{S'}\int_S \mathbb{E}\left[x(s,\omega)\ x(s',\omega)\right] f_d(s) f_{d'}(s')\ ds\ ds' \\
&\qquad \text{use def: } \boxed{C(s,s') := \mathbb{E}\left[x(s,\omega)\ x(s',\omega)\right]} \\
&= \int_{S'}\int_S C(s,s') f_d(s) f_{d'}(s')\ ds\ ds' \\
&= \int_{S'} f_{d'}(s') \int_S C(s,s') f_d(s)\ ds\ ds' \\
&\qquad \text{use Eq. (2.12): } \int_{S'} C(s,s')\ \varphi_d(s')\ ds' = \lambda_d\ \varphi_d(s) \ \ |\cdot\sqrt{\lambda_d} \\
&\qquad\qquad \Rightarrow \boxed{\int_{S'} C(s,s')\ f_d(s')\ ds' = \lambda_d\ f_d(s)} \\
&= \int_{S'} f_{d'}(s')\lambda_d\ f_d(s')\ ds' \\
&= \lambda_d \underbrace{\int_{S'} f_{d'}(s')\ f_d(s')\ ds'}_{=\delta_{dd'}\text{(linear independent)}} = \lambda_d\ \delta_{dd'} = \begin{cases} \lambda_d & (d = d') \\ 0 & (\forall\ d \neq d') \end{cases}
\end{aligned}
$$

□

B.2 Discrete Eigenvalue Problem

Applying KL to a discrete environment with an equidistant grid ($ds = ds' = const$), the eigenvalue problem becomes linear: $C\ \varphi_d = \lambda_d\ \varphi_d$

Proof:

$$\int_{S'} C(s,s')\ \varphi_d(s')\ ds' \overset{ds'=const}{=} \sum_{s'=1}^{N_s} C(s,s')\ \varphi_d(s')\ \delta s'$$

$$\Rightarrow \sum_{s'=1}^{N_s} C(s,s')\ \varphi_d(s')\ \delta s' = \lambda_d\ \varphi_d(s)$$

$$\Rightarrow \begin{pmatrix} c(1,1) & c(1,2) & \dots & c(1,n) \\ c(2,1) & c(2,2) & \dots & c(2,n) \\ \vdots & \vdots & \ddots & \vdots \\ c(n,1) & c(n,2) & \dots & c(n,n) \end{pmatrix} \cdot \begin{pmatrix} \varphi_i(1) \\ \varphi_i(2) \\ \vdots \\ \varphi_i(n) \end{pmatrix} \delta t = \lambda_i \begin{pmatrix} \varphi_i(1) \\ \varphi_i(2) \\ \vdots \\ \varphi_i(n) \end{pmatrix}$$

$$\Rightarrow C\ \varphi_d\ \delta s' = \lambda_d\ \varphi_d$$

□

B.3 Random Number Generation

In Fortran, equally distributed random numbers ω can be generated based on a set of random seeds s. To ensure reproducibility of the results, the random seeds are specified as a function of the member number k with $seed(s) = (37 \cdot s + k) \cdot 811 + 2269$. For unreporduceable numbers during operational use this may be extended by a time-dependence (eg. $seed(s) = time \cdot (37 \cdot s + k) \cdot 811 + 2269$).

Now, this equally distributed numbers are converted to normally distributed random numbers Y with given μ and σ. This is done by applying the inverse of the cumulative function PCF^{-1}:

$$\omega \in [0,1] \qquad \text{equally distributed}$$

$$\omega := PCF(Y) = \frac{1}{2}\left(1 + erf\left(\frac{Y-\mu}{\sqrt{2}\ \sigma}\right)\right)$$

$$\Leftrightarrow \quad 2\ \omega - 1 = erf\left(\frac{Y-\mu}{\sqrt{2}\ \sigma}\right) \qquad \Leftrightarrow \quad \frac{Y-\mu}{\sqrt{2}\ \sigma} = erf^{-1}\left(2\ \omega - 1\right)$$

$$\Leftrightarrow PCF^{-1}(\omega) = Y = \sqrt{2}\ \sigma\ erf^{-1}\left(2\ \omega - 1\right) + \mu \qquad \text{normally distributed}$$

Were the inverse of the error-function $erf^{-1}(x := 2\ \omega - 1)$ is approximated by its Maclaurin series:

$$erf^{-1}(x) = \sum_{n=0}^{\infty} \frac{c_n}{2\ n+1} \left(\frac{\sqrt{\pi}}{2} x\right)^{2n+1}$$

$$\text{with } c_n = \sum_{j=0}^{n-1} \frac{c_j \cdot c_{n-1-m}}{(j+1)\,(2\ j+1)} \quad , c_0 = 1 \quad \Rightarrow c_1 = 1$$

C Implementation of KL Ensemble in EURAD-IM

This section provides an overview over the technical implementation of the KL ensemble algorithm. It also serves as documentation for the major developments in the model during this work. The implementation into the EURAD-IM system is based on ESIAS-chem developed by Franke [2018].

C.1 Namelist Parameters

The overall option `KLens` defines whether the KL ensemble is used. Its reference value is zero, which corresponds to no ensemble generation by KL. If `KLens` is set to one, an KL ensemble forecast is performed with the following namelist parameters to be specified in *ctmrun_'VERSION'_'PLATFORM'.deck.in* .

Table C.1: List of namelist parameters for KL ensemble in EURAD-IM.

parameter	type	description
	–– setup of parameters ––	
KL_VARNAME	character	list of model parameters perturbed by KL
KL_NVAR	integer	number of stochastic parameters perturbed by KL (determined by KL_VARNAME)
KL_REDUCE	logical	flag, if dimension of stochastic process is reduced (if available)
KL_PERTFAC	logical	flag, if factor of parameters are perturbed
	–– setup of perturbations ––	
KL_PERTONLY	character	flag, if only KL perturbations are calculated = TRUE: only calculate perturbation with KL = FALSE: also execute ensemble forecast
KL_PERTSRC	character	source of perturbations = 'cf': calculate KL perturbations from *full sensitivities* = 'ci': calculate KL perturbations from *independent sensitivities* = 'rd': read perturbations from KLout file = 'rn': nest perturbations from KLnest file
KL_CONSTFAC	real	constant factor for artificial increase of all perturbations
KL_APRIUNCERT	real	a-priori defined uncertainty (factor) additionally to sensitivities ≤ 1: no additional uncertainty > 1: a-priori factor of additional uncertainty
	–– setup of sensitivity analysis ––	
KL_PREIDEN	character	runname of sensitivity analysis (required for covariance calculation)
KL_PREMEM	character	list of member-numbers of sensitivity analysis
KL_NPRE	integer	number of members in sensitivity analysis (determined by KL_PREMEM)
KL_ITIME	integer	1st hour of sensitivity analysis to use for calculation
KL_NTIMES	integer	number of hours in sensitivity analysis to use for calculation (≥ 1)
KL_MINVAL	real	limitation of values from sensitivity analysis
KL_MAXFAC	real	limitation of factors from sensitivity analysis
	–– setup of KL expansion ––	
KL_DISTR	character	assumed distribution of stochastic parameters = 'n': normal distribution = 'l': log-normal distribution
KL_NEVAL	integer	number of eigenvalues to approx stochastic process
KL_NMEM	integer	number of members generated by KL

C.2 Structure

All parameters and fields related to the KL ensemble are comprised in the structure KLensemble. The type of this structure TYPE_KL is defined as follows:

Table C.2: Definition of type TYPE_KL.

variable	type	description
nvar	integer	number of stochastic parameters defined by varname
nx	integer	dimension of stochastic process
npre	integer	number of members in sensitivity analysis defined by PreMem
itime	integer	1st hour of sensitivity analysis to use
ntimes	integer	number of hours of sensitivity analysis to use
neval	integer	number of eigenvalues to approx stochastic process
nmem	integer	number of members generated by KL ensemble
reduce	logical	flag, if dimension of stochastic process is reduced
pertFac	logical	flag, if factor of parameters are perturbed
pertOnly	logical	flag, if only KL perturbations are calculated
minVal	real	limitation of values from sensitivity analysis
maxFac	real	limitation of factors from sensitivity analysis
constFac	real	constant factor for increase of perturbations
apriUncert	real	additional a-priori uncertainty (factor)
varname(:)	character (allocatable)	array containing model parameters perturbed by KL
varnameStr	character (len=70)	list of model parameters perturbed by KL
pertSrc	character (len=2)	source of perturbations
pertModel(:)	character (allocatable)	array containing model of parameters
preIden	character (len=20)	CTMiden of sensitivity analysis
preMem(:)	character (allocatable)	array containing member-numbers of sensitivity analysis
preMemStr	character (len=300)	list of member-numbers of sensitivity analysis
distr	character (len=1)	assumed distribution of stochastic parameters
scoef(:)	real (allocatable)	field of stochastic coefficients
sproc(:,:)	real (allocatable)	field of perturbed stochastic processes

C.3 Initialization

This section gives an overview over the initialization of variables related to the KL ensemble. From now on, the major aspects are listed below were subroutines are given in *ITALIC* and model variables in `typewriter` style.

- define KLensemble as type TYPE_KL (*PMCTM*)
- transfer namelist parameters to structure KLensemble (*READNL*)
- allocate KLensemble%preMem(1:KLensemble%npre) and define by cutting KLensemble%preMemStr into substrings separated by spaces (*PMCTM*)
- allocate KLensemble%varname(1:KLensemble%nvar) and define by cutting KLensemble%varnameStr into substrings separated by spaces (*PMCTM*)
- allocate KLensemble%pertModel(1:KLensemble%nvar) and define as 'c' or 'w' depending on KLensemble%varname (*PMCTM*)

- calculate `KLensemble%nx` and allocate `KLensemble%scoef(1:KLensemble%neval)`, `KLensemble%sproc(MDOM%JMAX,MDOM%IMAX,KLensemble%nvar)` (*PMCTM*)
- get stochastic perturbations depending on `KLensemble%pertSrc` (*PMCTM*):
  - if = `'cf','ci'`: call calculation of KL perturbations (→ *KARHUNEN_LOEVE*, compare sec.C.4)
  - if = `'rd'`: call reading of perturbations from KLout file (→ *READ_PERT*)
  - if = `'rn'`: call nesting of perturbations from KLnest file (→ *NEST_PERT*, compare Sec. 4.2.3)

C.4 Generation of KL Perturbations

If the KL perturbations should be calculated (`KLensemble%pertSrc='cf'` or `='ci'`), the core subroutine for handling KL perturbations *KARHUNEN_LOEVE* is called. Fig. C.1 illustrates the interaction of the subroutines and most important fields. Due to the computationally expensive eigenmode calculation, the code is parallelized. The master process of each member calls *KARHUNEN_LOEVE* which includes all parts of the algorithm including the writing of the final perturbations (*KLOUT*) and nesting information (*KLNEST*). At the same time, *PW_KL* is called by worker processes which mainly aids in the solution of the eigenmodes *SOLVE_EVAL*. The implementation follows the algorithm given in Sec. 4.1.6.

As first step, the global master process performs the deterministic part of the calculation:

- allocate `sproc_pre(KLensemble%pre,KLensemble%nx)`
- get fields of factors `SPROC_PRE` from sensitivity analysis (→ *GET_SPROC_PRE*):
  - read parameters from sensitivity analysis
  - limit minimal values of parameters by `KLensemble%minVal`
  - if `KLensemble%pertFac`: calculate factors with respect to reference member
  - limit processes `sproc_pre` based on `KLensemble%maxFac`
  - average processes over times from `KLensemble%itime` to `KLensemble%itime+KLensemble%ntimes-1`
  - if `KLensemble%reduce`: read condition for dimension reduction depending on `KLensemble%varname`
  - reshape to 1D array and if `KLensemble%reduce`: reduce dimension
  - update `KLensemble%nx` according to reduced dimension
- if `KLensemble%distr='l'`: substitute processes `sproc_pre` from sensitivity analysis

- calculate mean value and update field of processes `sproc_pre` depending on `KLensemble%pertSrc='cf'` or `='ci'`
- if `KLensemble%apriUncert` ≥ 1: add a-priori uncertainty
- allocate eigenvalues `eval(KLensemble%nlimit)`
  and eigenvectors `evec(KLensemble%nlimit,KLensemble%nx)`
- solve eigenproblem ($\rightarrow$ *SOLVE_EVAL*) using PARPACK:
  - includes multiplication of input vector with covariance matrix depending on `KLensemble%pertSrc=cf'` or `='ci'` (*COVMUL*)
- if `KLensemble%constFac` $\neq 1$: multiply eigenvalues `eval(:)` with squared `KLensemble%constFac`

After communication of eigenvalues, eigenvectors and mean values, the master process of each member continues independently:

- allocate and generate stochastic coefficients `scoef(KLensemble%nlimit)` ($\rightarrow$ *NORMAL_DISTR*):
  - global master initializes random seeds ($\rightarrow$ *INIT_RANDOM_SEED*) and generated random numbers for all members ($\rightarrow$ *RANDOM_NUMBER*)
  - convert to normally distributed random numbers by inverse cumulative error function
    ($\rightarrow$ *INV_CUM_ERR*)
- allocate and calculate KL expansion of stochastic processes `sproc_kl(KLensemble%nx)`
- if `KLensemble%distr='l'`: resubstitute stochastic processes to factors and put into global field `KLensemble%sproc`
- write KL output file ($\rightarrow$ *KLOUT*)
- if domain has daughter nests: write KL nesting files of daughter subdomains ($\rightarrow$ *KLNEST*)
- deallocate remaining local fields

C.5 Application of Perturbations

After getting stochastic perturbations, these are applied to the referring model variables. Up to now, the application is only implemented for perturbing factors of parameters, but other types of perturbations may be implemented accordingly. The implementations in the code is mainly done in the master subroutine *PMCTM* and can be summarized as follows:

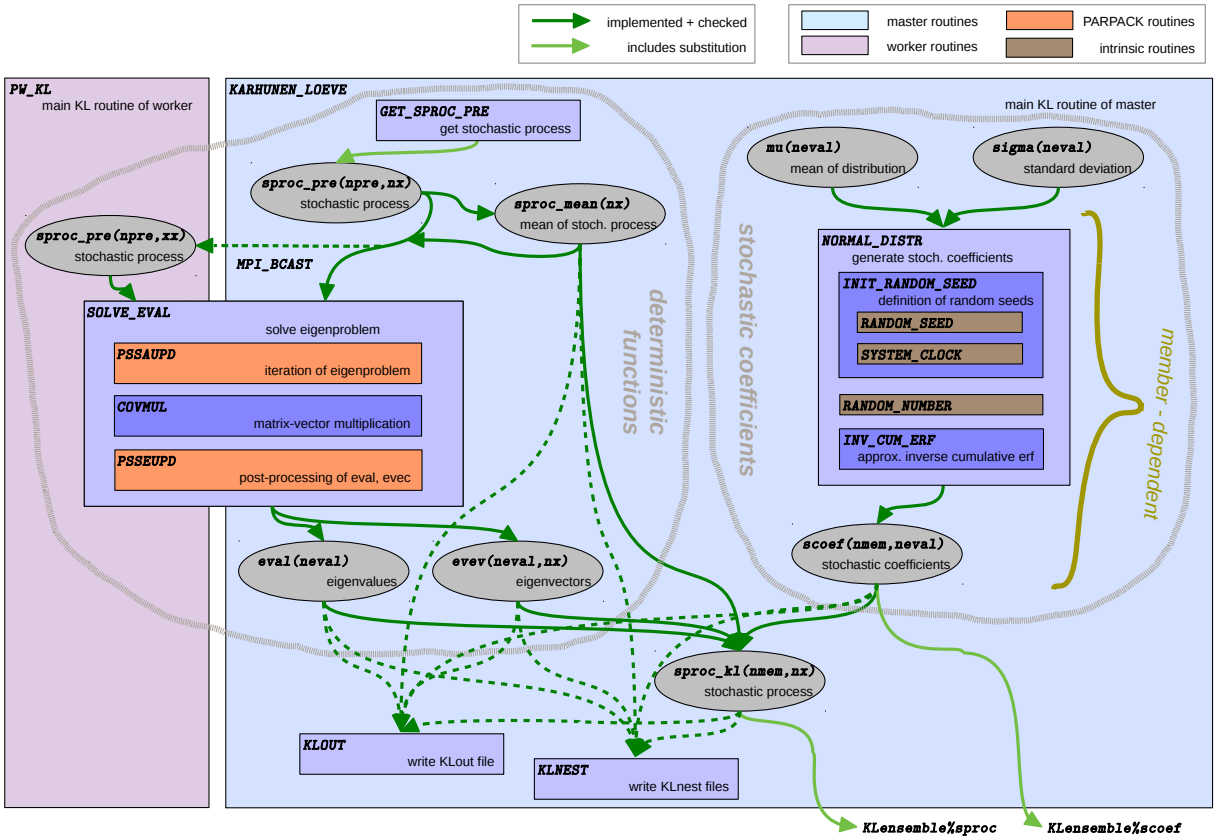

Figure C.1: Implementation of generation of KL perturbations in EURAD-IM. Colored boxes: implemented subroutines. Gray ellipses: major arrays with dimensions. Arrows: evolution and dependencies of array with respect to subroutines.

- define, if the chemical ensemble forecast should be executed (`KL_PERTCTM`)
- if not `KL_PERTCTM`: quit run, else: continue with preparation for forecast
- if `KLensemble%pertFac`: apply stochastic factors to model factors ($\rightarrow$ *PERTFAC_KL*)
- give information about KL ensemble to standard output routine ($\rightarrow$ *NCOUT*)
- deallocate fields in `KLensemble` structure

D Derivation of Mean Values and Covariances for Independent Factors

D.1 Definition of the Problem

Let $q_i^s(r_i)$ be a set of I *independent sensitivities* with two realizations each $r_i \in \{1,2\}$, $\forall\, i \in \{1,\ldots,I\}$ at location $s \in S$, where $q_i^s(1) = 0$ by definition ("*reference*") and $q_i^s(2) \in \mathcal{R}$ ("*alternative*"). Not that, both realizations of each random parameter are assumed to have the same probability or weight. Then let $Q_j^s, j \in \{1,\ldots,J\}$ be the full set of $J = 2^I$ *combined sensitivities* resulting form the sum over independent sensitivities for all possible combinations of realizations under tangent-linear assumption of the sensitivities

$$Q_j^s = Q_{r_1,r_2,\cdots,r_I}^s = \sum_{i=1}^{I} q_i^s(r_i) \quad \Big| \quad \forall\, j \in \{1,\ldots,J\} \quad . \tag{D.1}$$

D.2 Mean Values

The mean values $\mu(s)$ of all combined sensitivities $Q_j^s, j \in \{1,\ldots,J\}$ at location $s \in S$ can be calculated from the set of independent sensitivities $q_i^s(r_i), r_i \in \{1,2\}, i \in \{1,\ldots,I\}$. The resulting formulation for the mean values $\mu(s)$ is derived in the following.

$$\mu^s := \frac{1}{J}\sum_{j=1}^{J} Q_j^s = \frac{1}{2^I}\sum_{r_1=1}^{2}\sum_{r_2=1}^{2}\cdots\sum_{r_I=1}^{2} Q_{r_1,r_2,\cdots,r_I}^s \tag{D.2}$$

- In total, there are 2^I terms $Q_{r_1,r_2,\cdots,r_I}^s$ in Eq. (D.2). Thus, each value of r_i occurs 2^{I-1} times (2^{I-1} times is $r_i = 1$ and 2^{I-1} times is $r_i = 2$).

- Each $Q_{r_1,r_2,\cdots,r_I}^s$ can be decomposed as follows:

$$Q_{r_1,r_2,\cdots,r_I}^s = \sum_{i=1}^{I} q_i^s(r_i) = \sum_{i=1}^{I} q_i^s(r_i)\bigg|_{r_i=1} + \sum_{i=1}^{I} q_i^s(r_i)\bigg|_{r_i=2} \tag{D.3}$$

  $q_i^s(2)$ appears in each term $Q_{r_1,r_2,\cdots,r_I}^s$ with $r_i = 2$.

Thus, each $q_i^s(1)$ and $q_i^s(2) \,|\, \forall\, i \in [1,I]$ appear 2^{I-1} times in Eq. (D.2).

With this, the equation of the mean values becomes:

$$\mu^s = \frac{1}{2^I}\sum_{r_1=1}^{2}\sum_{r_2=1}^{2}\cdots\sum_{r_I=1}^{2} Q^s_{r_1,r_2,\cdots,r_I} = \frac{1}{2^I}\cdot 2^{I-1}\left(\cancelto{0}{\sum_{i=1}^{I} q_i^s(1)} + \sum_{i=1}^{I} q_i^s(2)\right) \tag{D.4}$$

$$\Rightarrow \boxed{\mu^s = \frac{1}{2}\sum_{i=1}^{I} q_i^s(2)} = \frac{1}{2}Q_{2,2,\cdots,2} \tag{D.5}$$

D.3 Covariances

The covariances $\widetilde{C}(s,s')$ of all combined sensitivities $Q_j^s, j \in \{1,\ldots,J\}$ can be calculated from the set of independent sensitivities $q_i^s(r_i), r_i \in \{1,2\}, i \in \{1,\ldots,I\}$. The resulting formulation for the covariances $\widetilde{C}(s,s')$ is derived in the following.

$$\widetilde{C}(s,s') := \frac{1}{J}\sum_{j=1}^{J}\left[\left(Q_j^s - \mu(s)\right)\cdot\left(Q_j^{s'} - \mu(s')\right)\right] = \frac{1}{J}\sum_{j=1}^{J}\left(Q_j^s\cdot Q_j^{s'}\right) - \mu(s)\cdot\mu(s') \tag{D.6}$$

$$= \frac{1}{2^I}\sum_{r_1=1}^{2}\sum_{r_2=1}^{2}\cdots\sum_{r_I=1}^{2}\left(Q^s_{r_1,r_2,\cdots,r_I}\cdot Q^{s'}_{r_1,r_2,\cdots,r_I}\right) - \frac{1}{4}\sum_{i=1}^{I} q_i^s(2)\cdot\sum_{i=1}^{I} q_i^{s'}(2) \tag{D.7}$$

$$= \underbrace{\frac{1}{2^I}\sum_{r_1=1}^{2}\sum_{r_2=1}^{2}\cdots\sum_{r_I=1}^{2}\left(Q^s_{r_1,r_2,\cdots,r_I}\cdot Q^{s'}_{r_1,r_2,\cdots,r_I}\right)}_{(I)} - \frac{1}{4}\underbrace{Q^s_{2,2,\cdots,2}\cdot Q^{s'}_{2,2,\cdots,2}}_{(II)} \tag{D.8}$$

part (I):

- Each "quadratic" term $q_i^s(r_i)\cdot q_i^{s'}(r_i)$ appears every time when $r_i = 2$, which is 2^{I-1} times (compare Sec. D.2).

- "Mixed" terms $q_{i_1}^s(r_{i_1})\cdot q_{i_2}^{s'}(r_{i_2})$ with $i_1 \neq i_2$ appear each time when $r_{i_1} = r_{i_2} = 2$, which is the case 2^{I-2} times ($r_{i_1} = 2$ in half of the terms: 2^{I-1} times, $(r_{i_1} = 2 \wedge r_{i_2} = 2)$ in half of the cases were $r_{i_1} = 2$: 2^{I-2} times):

$$\begin{aligned}&\left(\cdots + q_{i_1}^s(r_{i_1}) + q_{i_2}^s(r_{i_2}) + \cdots\right)\cdot\left(\cdots + q_{i_1}^{s'}(r_{i_1}) + q_{i_2}^{s'}(r_{i_2}) + \cdots\right)\\ &= \cdots + \ q_{i_1}^s(r_{i_1})\cdot q_{i_2}^{s'}(r_{i_2}) \ + \ q_{i_2}^s(r_{i_2})\cdot q_{i_1}^{s'}(r_{i_1}) \ + \cdots\end{aligned}$$

- For any $r_{i_1} = 1$ or $r_{i_2} = 1$ follows $q_{i_1}^s(r_{i_1})\cdot q_{i_2}^{s'}(r_{i_2}) = 0$ (because $q_i(1) = 0$)

part (II):

- The product $Q^{s}_{2,2,\cdots,2} \cdot Q^{s'}_{2,2,\cdots,2}$ contains all possible combinations of $q^{s}_{i_1}(r_{i_1}) \cdot q^{s'}_{i_2}(r_{i_2}) \,\big|\, \forall\, i_1, i_2 \in \{1, \ldots, I\}$

With this, the equation of the covariances becomes:

$$\widetilde{C}(s,s') = \frac{1}{2^I} \sum_{r_1=1}^{2} \sum_{r_2=1}^{2} \cdots \sum_{r_I=1}^{2} \left(Q^{s}_{r_1,r_2,\cdots,r_N} \cdot Q^{s'}_{r_1,r_2,\cdots,r_I} \right) - \frac{1}{4} Q^{s}_{2,2,\cdots,2} \cdot Q^{s'}_{2,2,\cdots,2} \tag{D.9}$$

$$= \frac{1}{2^I} \left[2^{I-1} \sum_{i=1}^{I} \left(q^{s}_{i}(2) \cdot q^{s'}_{i}(2) \right) \Big|_{i=i_1=i_2} + 2^{I-2} \sum_{i_1=1}^{I} \sum_{i_2=1}^{I} \left(q^{s}_{i_1}(2) \cdot q^{s'}_{i_2}(2) \right) \Big|_{i_1 \neq i_2} \right]$$

$$- \frac{1}{4} \sum_{i_1=1}^{I} \sum_{i_2=1}^{I} \left(q^{s}_{i_1}(2) \cdot q^{s'}_{i_2}(2) \right) \Big|_{\forall i_1, i_2} \tag{D.10}$$

$$= \frac{1}{2} \sum_{i=1}^{I} \left(q^{s}_{i}(2) \cdot q^{s'}_{i}(2) \right) + \frac{1}{2^2} \sum_{i_1=1}^{I} \sum_{i_2=1}^{I} \cancel{\left(q^{s}_{i_1}(2) \cdot q^{s'}_{i_2}(2) \right) \Big|_{i_1 \neq i_2}}$$

$$- \left[\frac{1}{4} \sum_{i=1}^{I} \left(q^{s}_{i}(2) \cdot q^{s'}_{i}(2) \right) + \frac{1}{4} \sum_{i_1=1}^{I} \sum_{i_2=1}^{I} \cancel{\left(q^{s}_{i_1}(2) \cdot q^{s'}_{i_2}(2) \right) \Big|_{i_1 \neq i_2}} \right] \tag{D.11}$$

$$= \frac{1}{4} \sum_{i=1}^{I} \left(q^{s}_{i}(2) \cdot q^{s'}_{i}(2) \right) \tag{D.12}$$

As the mean values $\mu(s)$ are not known and calculated from the given data, the sample covariance has to be used. Analogue to Eq. (D.12), the sample covariance becomes

$$C(s,s') := \frac{1}{J-1} \sum_{j=1}^{J} \left[\left(Q^{s}_{j} - \mu^{s} \right) \cdot \left(Q^{s'}_{j} - \mu^{s'} \right) \right] \tag{D.13}$$

$$= \frac{J}{J-1} \widetilde{C}(s,s') = \frac{J}{J-1} \left[\frac{1}{4} \sum_{i=1}^{I} \left(q^{s}_{i}(2) \cdot q^{s'}_{i}(2) \right) \right] \tag{D.14}$$

$$\boxed{C(s,s') = \frac{2^I}{4\,(2^I - 1)} \sum_{i=1}^{I} \left(q^{s}_{i}(2) \cdot q^{s'}_{i}(2) \right)} \tag{D.15}$$

E Modified Roughness Lengths in WRF

Table E.1: Original and modified values of roughness length ($Z0$ in cm) in WRF for USGS vegetation types in summer. Modification are based on Berndt [2018].

number	vegetation type	original	modified
1	Urban and Built-Up Land	80	100
2	Dryland Cropland and Pasture	15	25
3	Irrigated Cropland and Pasture	10	20
4	Mixed Dryland/Irrigated Cropland and Pasture	15	25
5	Cropland/Grassland Mosaic	14	24
6	Cropland/Woodland Mosaic	20	35
7	Grassland	12	12
8	Shrubland	5	5
9	Mixed Shrubland/Grassland	6	6
10	Savanna	15	15
11	Deciduous Broadleaf Forest	50	100
12	Deciduous Needleleaf Forest	50	100
13	Evergreen Broadleaf Forest	50	100
14	Evergreen Needleleaf Forest	50	100
15	Mixed Forest	50	100
16	Water Bodies	0.01	0.01
17	Herbaceous Wetland	20	20
18	Wooded Wetland	40	40
19	Barren or Sparsely Vegetated	1	1
20	Herbaceous Tundra	10	10
21	Wooded Tundra	30	30
22	Mixed Tundra	15	15
23	Bare Ground Tundra	10	10
24	Snow or Ice	0.1	0.1

F Appendix Sensitivity Analysis

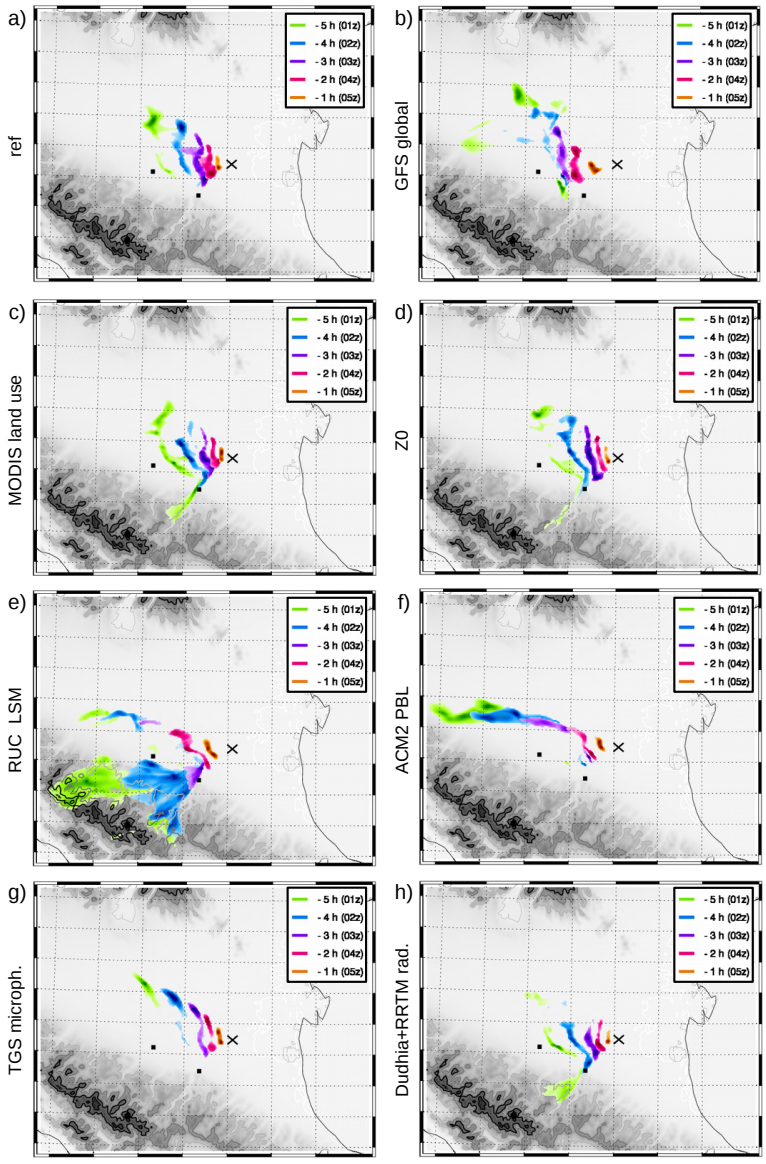

Figure F.1: Horizontal distribution of source regions for $44.7°N$, $11.6°E$ and 100 m a.s.l. (black cross, "target point") at 12.07.2012, 06 UTC. Significant contributions to vertically integrated source regions are colored by time according to legend. See Sec. 6.3.1 for more information.

G Appendices KL Ensemble Results

G.1 Appendix KL Ensemble Results for Biogenic Gases

G.1.1 Setup of Full Sensitivities

Table G.1: Setup of full sensitivities for stochastic biogenic emissions. The abbreviation 'ref' indicates the reference setup to which the KL perturbations are applied in the ensemble forecast. Deviations from the reference setup are give in bold letters ('PX' = Pleim-Xiu surface layer parameterization, 'Du' = Dudhia shortwave radiation parameterization).

	land use	**global**	**land surface**	**boundary layer**	**microph.**	**radiation**
ref	*USGS*	*ECMWF*	*Pleim-Xiu*	*MYJ+Eta*	*WSM6*	*RRTMG*
2	*USGS*	*ECMWF*	**RUC**	*MYJ+Eta*	*WSM6*	*RRTMG*
3	*USGS*	*ECMWF*	*Pleim-Xiu*	**ACM2+PX**	*WSM6*	*RRTMG*
4	*USGS*	*ECMWF*	*Pleim-Xiu*	*MYJ+Eta*	**TGS**	*RRTMG*
5	*USGS*	*ECMWF*	*Pleim-Xiu*	*MYJ+Eta*	*WSM6*	**Du+RRTM**
6	*USGS*	*ECMWF*	**RUC**	**ACM2+PX**	*WSM6*	*RRTMG*
7	*USGS*	*ECMWF*	*Pleim-Xiu*	*MYJ+Eta*	**TGS**	**Du+RRTM**
8	*USGS*	*ECMWF*	**RUC**	**ACM2+PX**	**TGS**	**Du+RRTM**
9	*USGS*	**GFS**	*Pleim-Xiu*	*MYJ+Eta*	*WSM6*	*RRTMG*
10	*USGS*	**GFS**	**RUC**	*MYJ+Eta*	*WSM6*	*RRTMG*
11	*USGS*	**GFS**	*Pleim-Xiu*	**ACM2+PX**	*WSM6*	*RRTMG*
12	*USGS*	**GFS**	*Pleim-Xiu*	*MYJ+Eta*	**TGS**	*RRTMG*
13	*USGS*	**GFS**	*Pleim-Xiu*	*MYJ+Eta*	*WSM6*	**Du+RRTM**
14	*USGS*	**GFS**	**RUC**	**ACM2+PX**	*WSM6*	*RRTMG*
15	*USGS*	**GFS**	*Pleim-Xiu*	*MYJ+Eta*	**TGS**	**Du+RRTM**
16	*USGS*	**GFS**	**RUC**	**ACM2+PX**	**TGS**	**Du+RRTM**
17	**MODIS**	*ECMWF*	*Pleim-Xiu*	*MYJ+Eta*	*WSM6*	*RRTMG*
18	**MODIS**	*ECMWF*	**RUC**	*MYJ+Eta*	*WSM6*	*RRTMG*
19	**MODIS**	*ECMWF*	*Pleim-Xiu*	**ACM2+PX**	*WSM6*	*RRTMG*
20	**MODIS**	*ECMWF*	*Pleim-Xiu*	*MYJ+Eta*	**TGS**	*RRTMG*
21	**MODIS**	*ECMWF*	*Pleim-Xiu*	*MYJ+Eta*	*WSM6*	**Du+RRTM**
22	**MODIS**	*ECMWF*	**RUC**	**ACM2+PX**	*WSM6*	*RRTMG*
23	**MODIS**	*ECMWF*	*Pleim-Xiu*	*MYJ+Eta*	**TGS**	**Du+RRTM**
24	**MODIS**	*ECMWF*	**RUC**	**ACM2+PX**	**TGS**	**Du+RRTM**
25	**MODIS**	**GFS**	*Pleim-Xiu*	*MYJ+Eta*	*WSM6*	*RRTMG*
26	**MODIS**	**GFS**	**RUC**	*MYJ+Eta*	*WSM6*	*RRTMG*
27	**MODIS**	**GFS**	*Pleim-Xiu*	**ACM2+PX**	*WSM6*	*RRTMG*
28	**MODIS**	**GFS**	*Pleim-Xiu*	*MYJ+Eta*	**TGS**	*RRTMG*
29	**MODIS**	**GFS**	*Pleim-Xiu*	*MYJ+Eta*	*WSM6*	**Du+RRTM**
30	**MODIS**	**GFS**	**RUC**	**ACM2+PX**	*WSM6*	*RRTMG*
31	**MODIS**	**GFS**	*Pleim-Xiu*	*MYJ+Eta*	**TGS**	**Du+RRTM**
32	**MODIS**	**GFS**	**RUC**	**ACM2+PX**	**TGS**	**Du+RRTM**

G.1.2 Additional Results for Independent Sensitivities

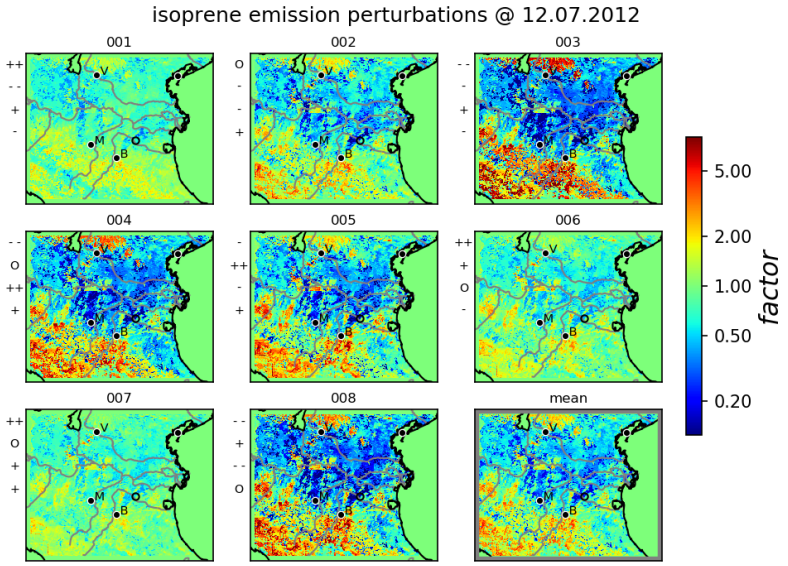

Figure G.1: Ensemble of perturbations of isoprene for independent input sensitivities of biogenic emissions given as factors w.r.t reference emissions. Plotting conventions as in Fig. 7.4.

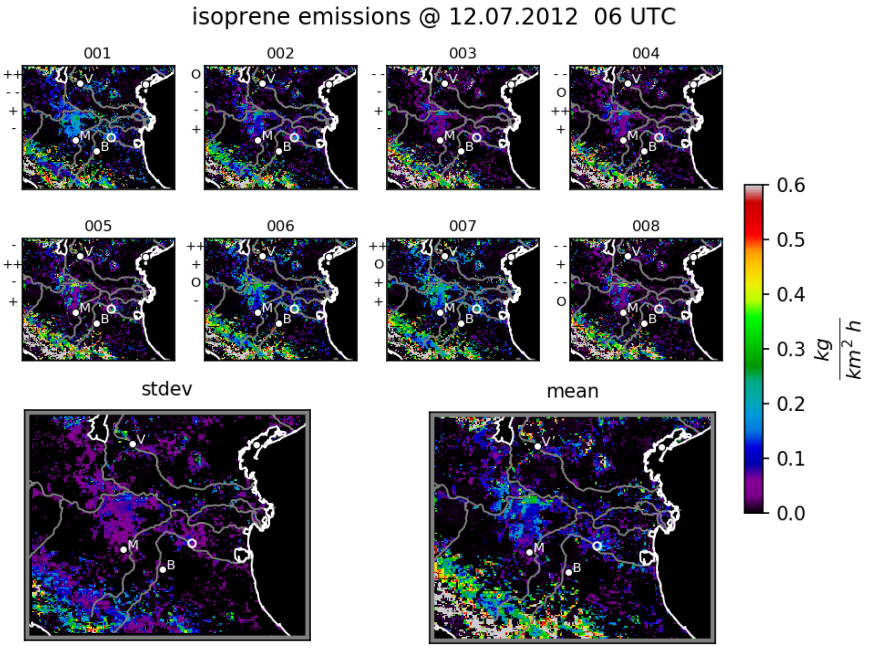

Figure G.2: Ensemble of isoprene emissions for independent input sensitivities of biogenic emissions. Plotting conventions as in Fig. 7.5.

G.1.3 Additional Results for Additional A-priori Uncertainties

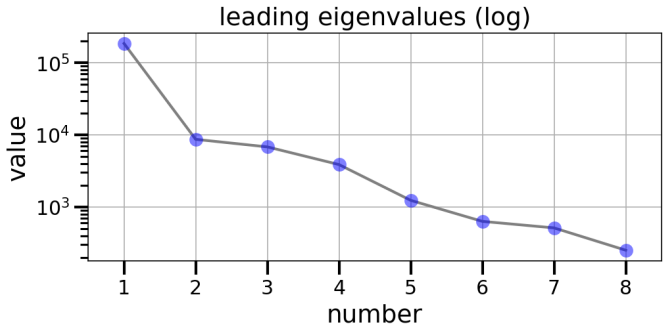

Figure G.3: Leading eigenvalues of biogenic emissions for additional a-priori uncertainties (blue dots). Eigenvalues are plotted on a logarithmic scale.

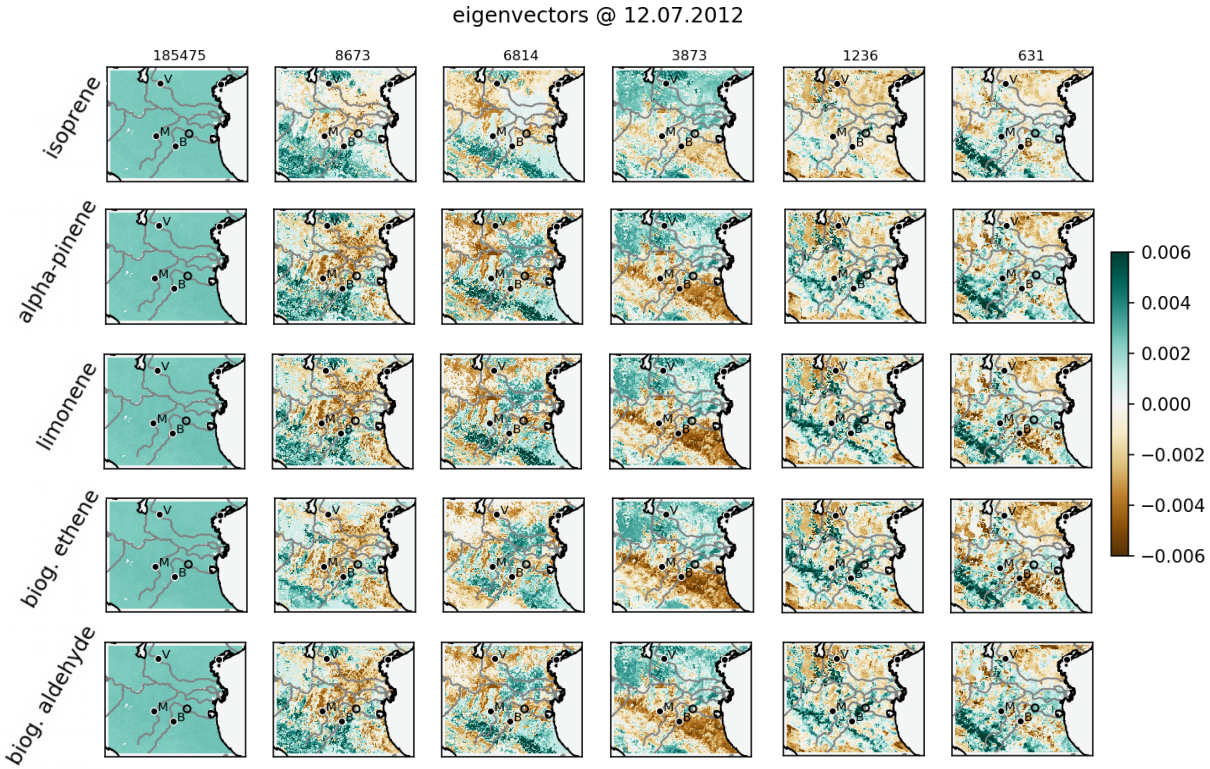

Figure G.4: Normalized leading eigenvectors of all biogenic emissions for additional a-priori uncertainties. Plotting conventions as in Fig. 7.3.

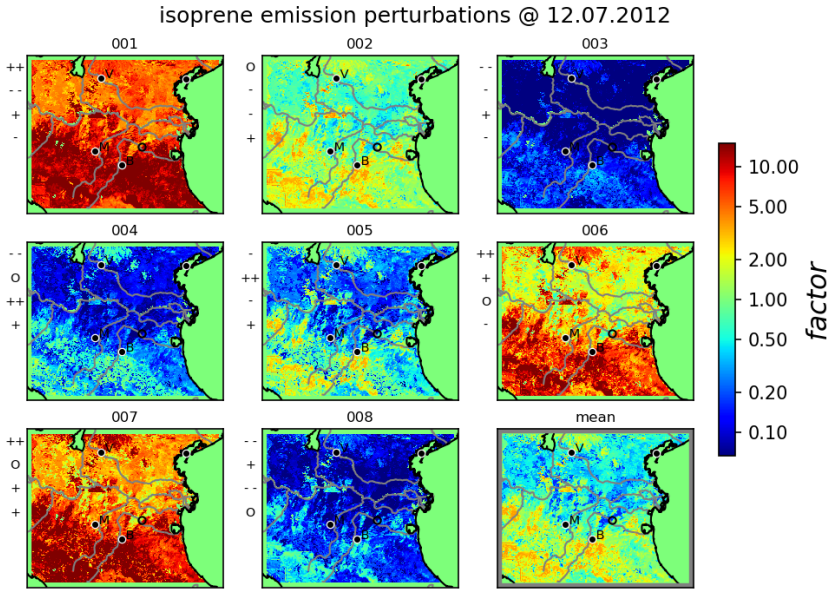

Figure G.5: Ensemble of perturbations of isoprene for additional a-priori uncertainties of biogenic emissions. Plotting conventions as in Fig. 7.4.

G.2 Additional Results for Dry Deposition Velocities

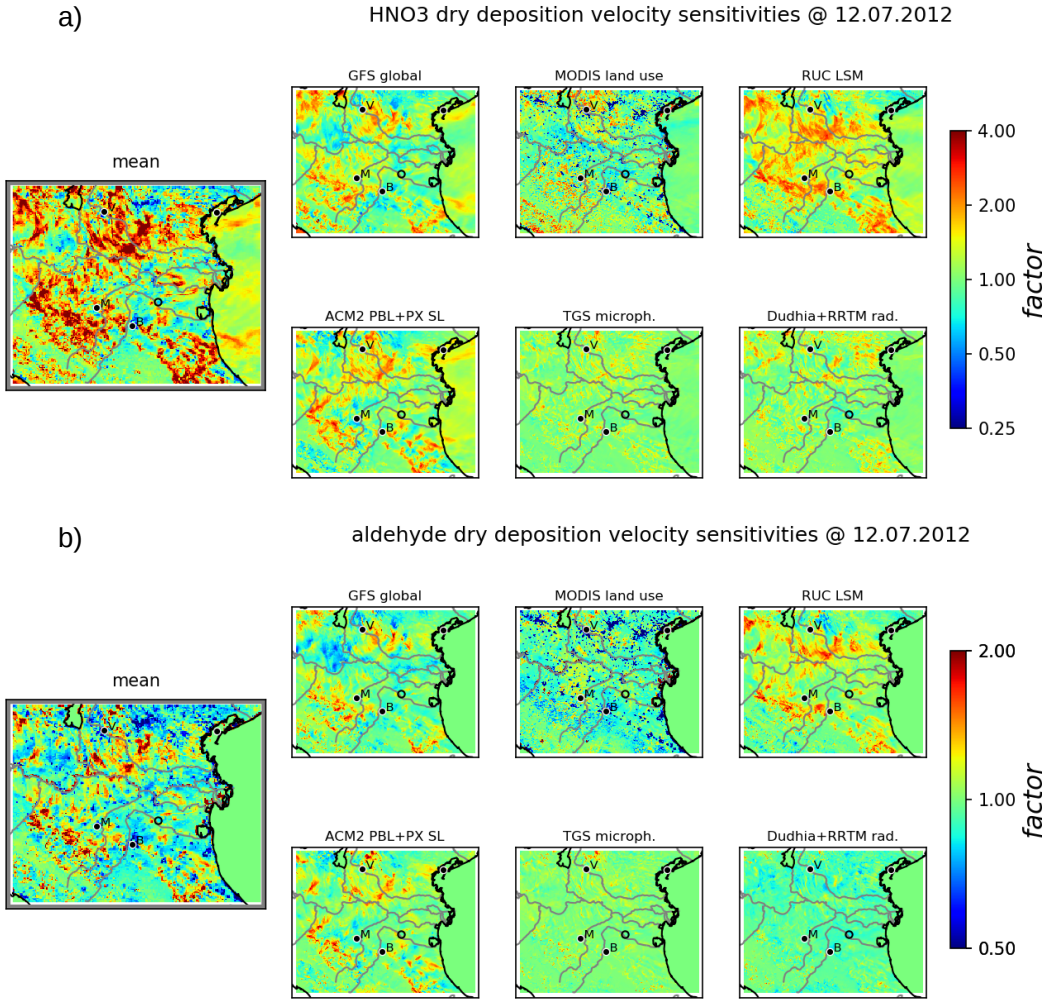

Figure G.6: Independent- mean and sensitivities of HNO_3 (a) and aldehyde (b) for independent input sensitivities of dry deposition velocities. The sensitivities given as factors w.r.t. to the mean (left subplot). Plotting conventions as in Fig. 7.6. Note the different scales for HNO_3 and aldehyde.

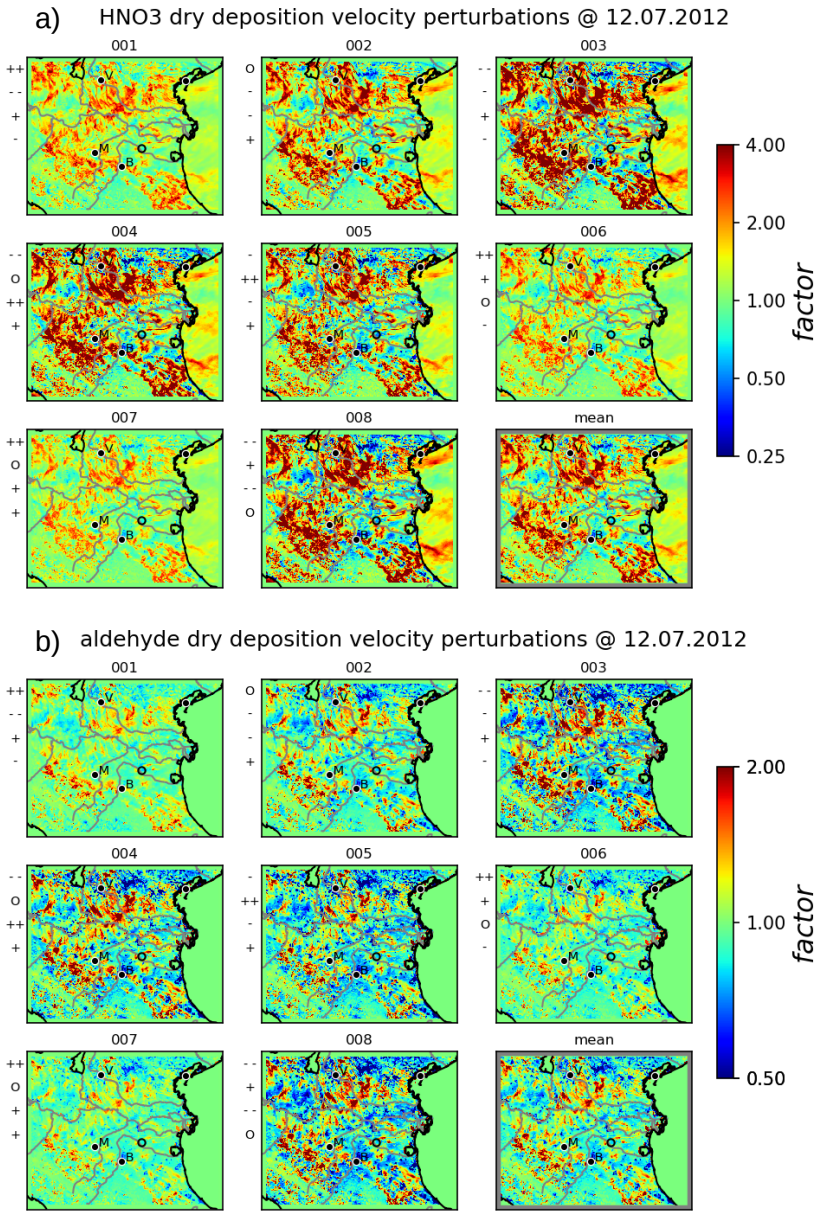

Figure G.7: Ensemble of perturbations of HNO_3 (a) and aldehyde (b) for independent input sensitivities of dry deposition velocities. Note the different scales for HNO_3 and aldehyde. Plotting conventions as in Fig. 7.4.

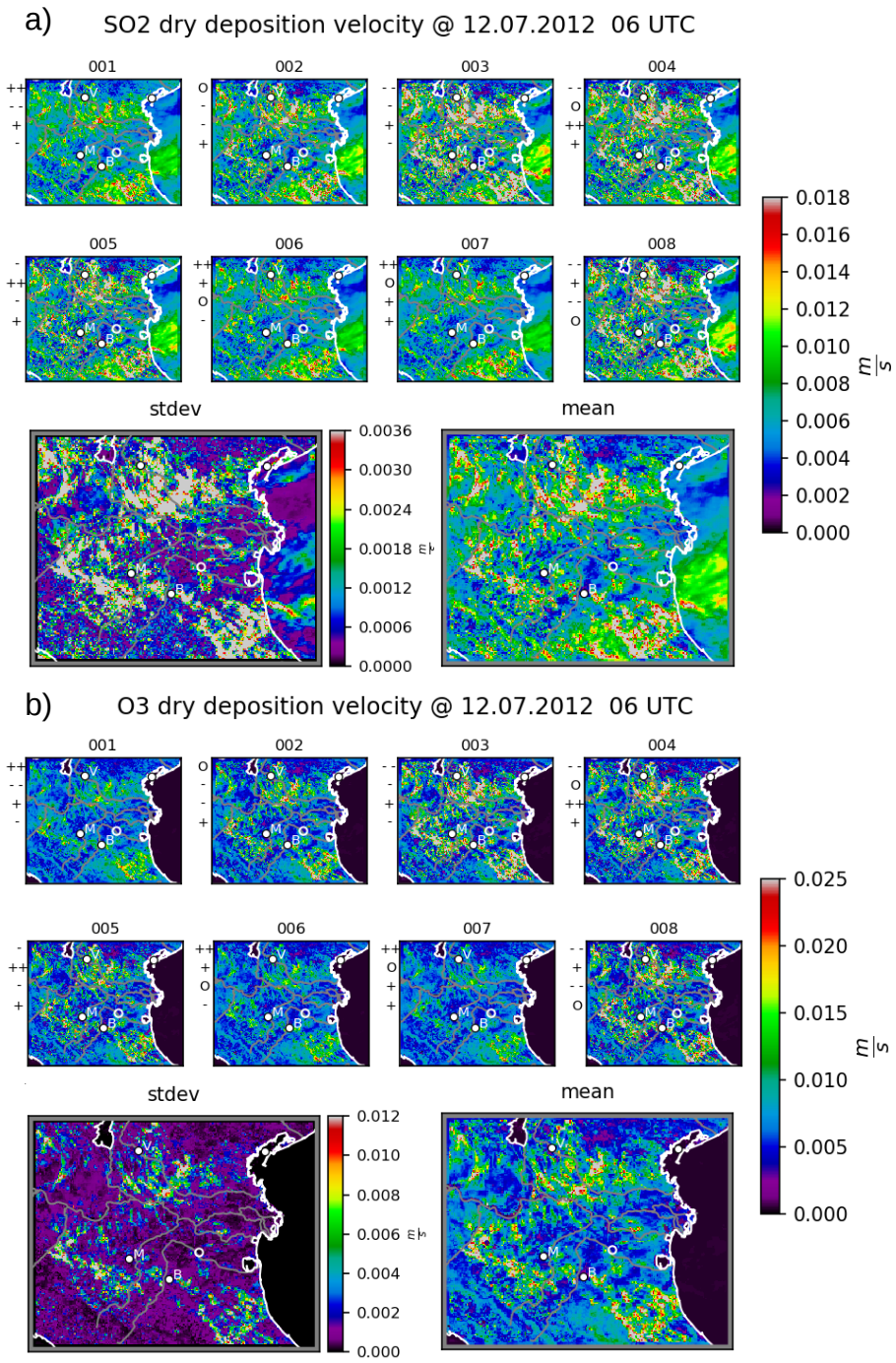

Figure G.8: Ensemble of SO_2 (a) and O_3 (b) dry deposition velocities for independent input sensitivities of dry deposition velocities. Plotting conventions as in Fig. 7.5.

G.3 Results for Friction Velocities

A first attempt to perturb local dynamics by KL considers friction velocity in WRF. Note that sensitivities to roughness length are additionally considered for meteorological parameters. The analysis of related sensitivities detected large variations in the early morning before sunrise which are assumed to be non-physical (compare Sec. 6.3.2). Therefore, the ensemble generation is restricted to daytime hours between 06 and 10 UTC.

Applying the assumption of independent sensitivities, single sensitivity factors of friction velocity are within a range of 0.7 and 2. Larger deviations occurring at specific times are filtered out by the temporal averaging of sensitivity factors (compare Sec. 6.3.2). Thus, the required assumption of constant sensitivity factors may not be perfectly true for friction velocity.

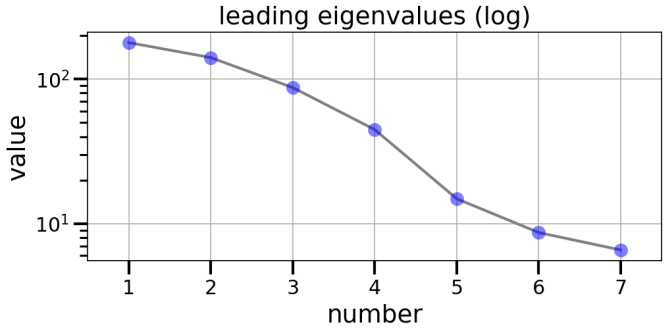

Figure G.9: Leading eigenvalues of friction velocity for independent input sensitivities (blue dots). Eigenvalues are plotted on a logarithmic scale.

The leading eigenvalues in Fig. G.9 show relatively slow decrease until the 4^{th} mode. These four eigenmodes are induced by the sensitivities to land surface model (1^{st}), land use (2^{nd}), global meteorology (3^{rd}) and boundary layer parameterization (4^{th}). The sensitivity to boundary layer parameterization is not completely perpendicular to the former ones and thus contributes partly to the other eigenmodes. The small signals of the renaming sensitivities result in a minor importance of the renaming eigenmodes which consist of much smaller scaled patterns.

For some ensemble members, perturbation factors in Fig. G.11 are dominated by a combination of mean factors and the 1^{th} eigenmode (member 001, 006, 007). For others, signals of the remaining eigenmodes contribute significantly to the perturbation factors. Thus, the slower decrease in eigenvectors compared to biogenic emissions and dry deposition velocities increases the effective dimension of the perturbations.

The generated factors for perturbation of friction velocity include small scale-structures of enhancement for some members. These significant locally increased values trigger dynamical instabilities within WRF. As a result, the ensemble of WRF forecasts with perturbed friction velocity cannot be performed.

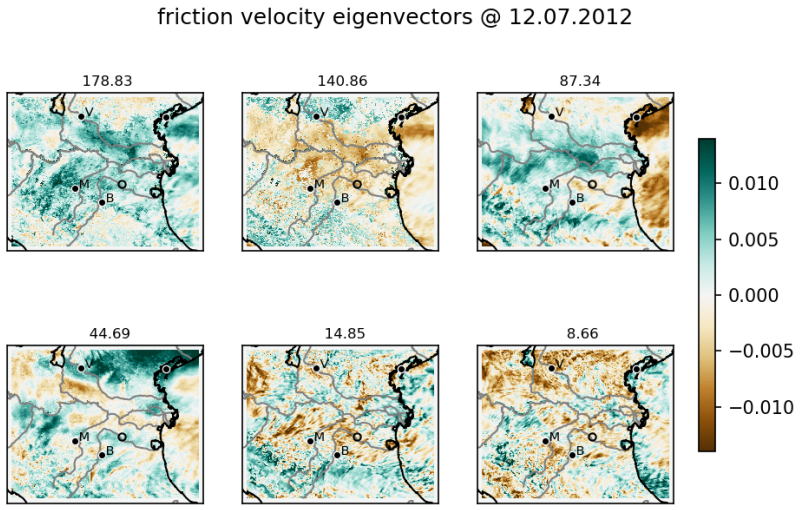

Figure G.10: Normalized leading eigenvectors of friction velocity for independent input sensitivities. Plotting conventions as in Fig. 7.3.

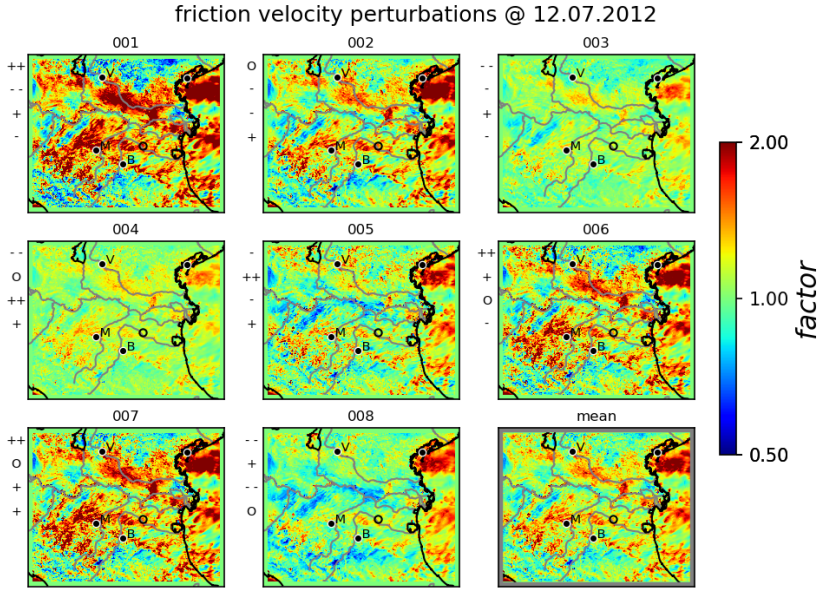

Figure G.11: Ensemble of perturbations of friction velocity for independent input sensitivities. Plotting conventions as in Fig. 7.4.

G.4 Additional Results for Surface Exchange Coefficients

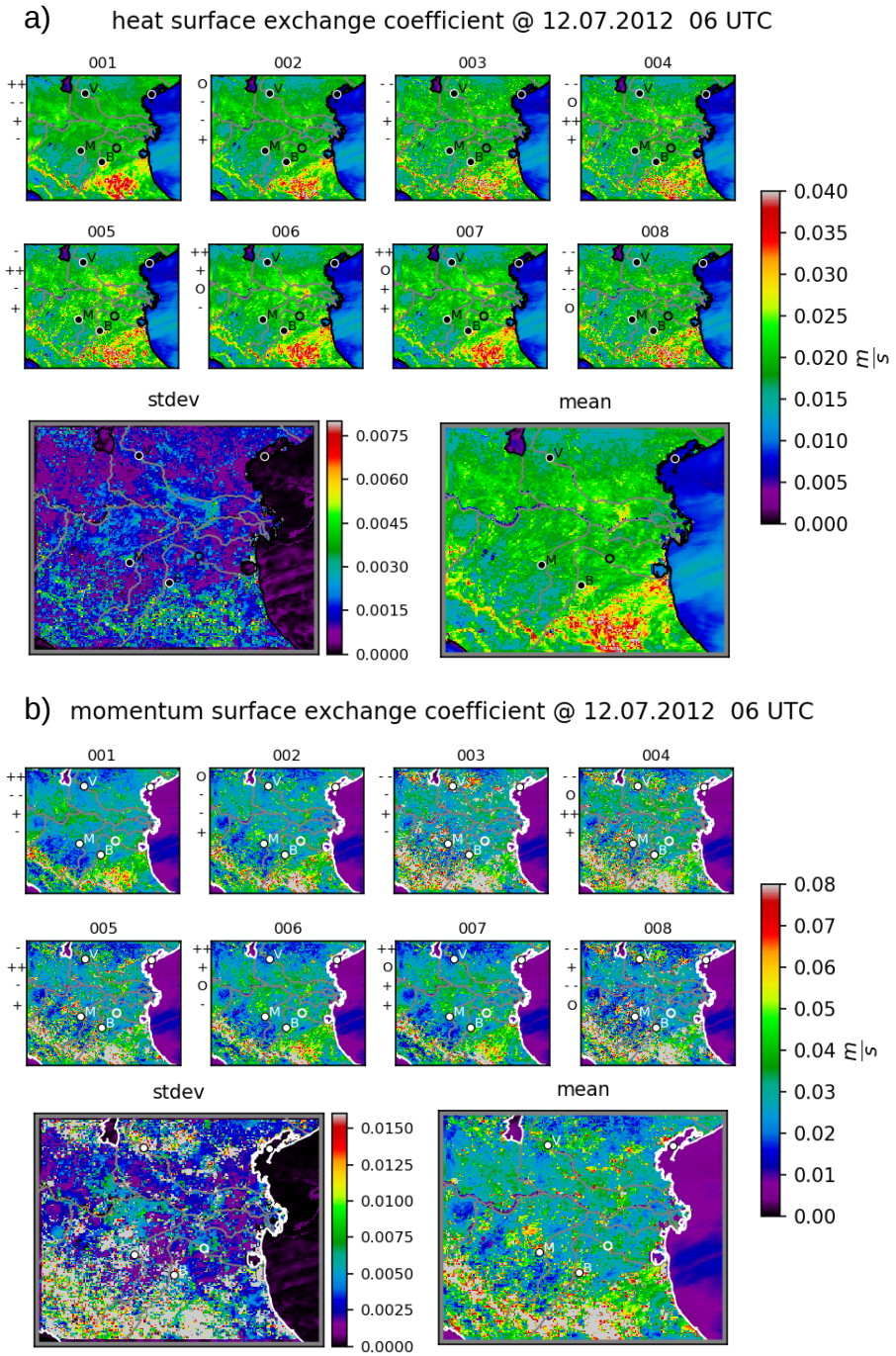

Figure G.12: Ensemble of heat- (a) and momentum- (b) surface exchange coefficients for independent input sensitivities. Plotting conventions as in Fig. 7.5.

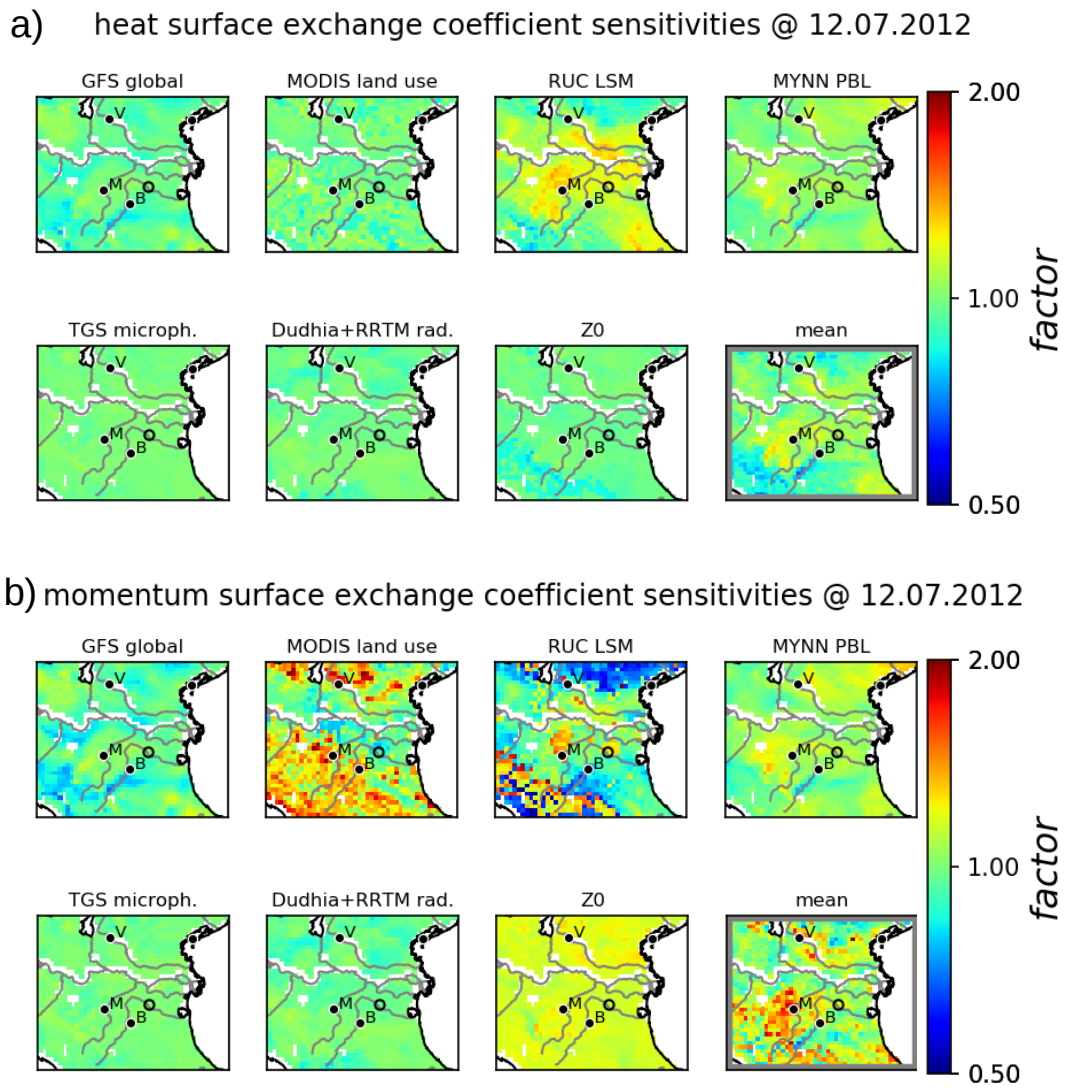

Figure G.13: Independent- mean and sensitivities of heat- (a) and momentum- (b) surface exchange coefficients on the 5 km domain in the Po valley for nested perturbations. The sensitivities given as factors w.r.t. to the mean (lower right subplot). Plotting conventions as in Fig. 7.6.

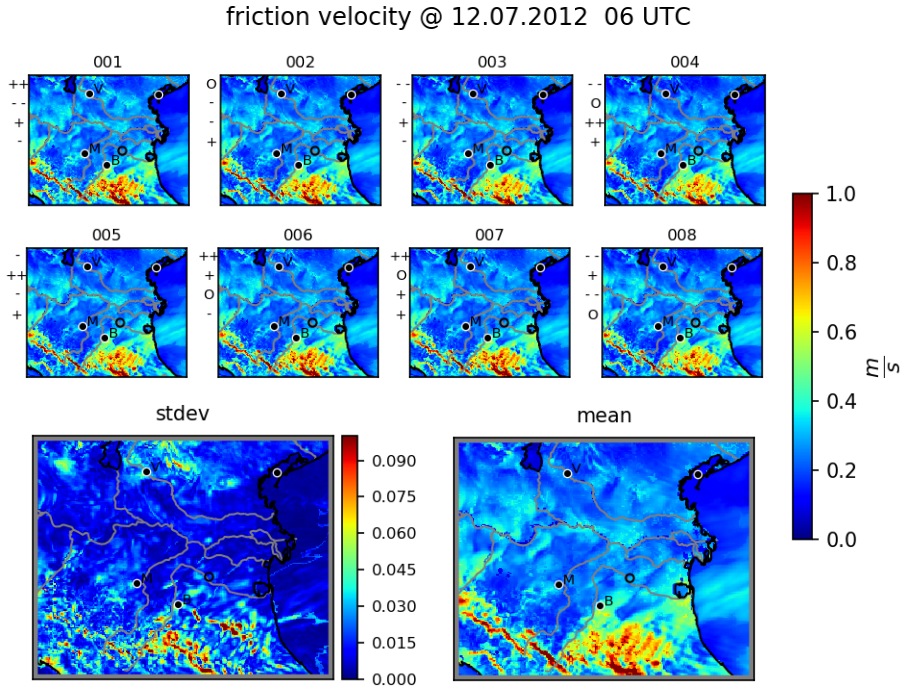

Figure G.14: Ensemble of friction velocity for nested perturbations of surface exchange coefficients. Plotting conventions as in Fig. 7.5.

Bibliography

Ackermann, I. J., Hass, H., Memmesheimer, M., Ebel, A., Binkowski, F. S., and Shankar, U. (1998). Modal aerosol dynamics model for europe: development and first applications. *Atmospheric Environment*, 32(17):2981 – 2999.

Anderson, R., Hardy, E. E., Roach, J. T., and Witmer, R. E. (1976). A land use and land cover classification system for use with remote sensor data. *USGS Prof. Pap*, page 964.

Arakawa, A. and Lamb, V. (1977). Computational design of the basic dynamical processes of the ucla general circulation model. *Methods in Computational Physics*, 17:173–265.

Arneth, A., Monson, R., Schurgers, G., Niinemets, Ü., and Palmer, P. (2008). Why are estimates of global terrestrial isoprene emissions so similar (and why is this not so for monoterpenes)? *Atmospheric Chemistry and Physics*, 8(16):4605–4620.

Arya, P. and Holton, J. (2001). *Introduction to Micrometeorology*. International Geophysics. Elsevier Science.

Banks, R. F., Tiana-Alsina, J., Baldasano, J. M., Rocadenbosch, F., Papayannis, A., Solomos, S., and Tzanis, C. G. (2016). Sensitivity of boundary-layer variables to pbl schemes in the wrf model based on surface meteorological observations, lidar, and radiosondes during the hygra-cd campaign. *Atmospheric Research*, 176:185–201.

Bauer, P., Thorpe, A., and Brunet, G. (2015). The quiet revolution of numerical weather prediction. *Nature*, 525(47).

Beljaars, A. C. M. (1995). The parametrization of surface fluxes in large-scale models under free convection. *Quarterly Journal of the Royal Meteorological Society*, 121(522):255–270.

Berndt, J. (2018). *On the predictability of exceptional error events in wind power forecasting - an ultra large ensemble approach*. PhD thesis, University of Cologne (Germany).

Bocquet, M., Elbern, H., Eskes, H., Hirtl, M., Carmichael, G., Flemming, J., Inness, A., Pagowski, M., Camaño, J., Saide, P., García, R., Sofiev, M., Vira, J., Baklanov, A., Carnevale, C., Grell, G., and Seigneur, C. (2015). Data assimilation in atmospheric chemistry models: Current status and future prospects for coupled chemistry meteorology models. *Atmospheric Chemistry and Physics*, 15:5325–5358.

Bott, A. (1988). A positive definit advection scheme obtained by nonlinear renormalisation of the advective fluxes. *Monthly Weather Review*, 117:1006–1015.

Bougeault, P. and Lacarrere, P. (1989). Parameterization of orography-induced turbulence in a mesobeta–scale model. *Monthly Weather Review*, 117(8):1872–1890.

Boynard, A., Beekmann, M., Foret, G., Ung, A., Szopa, S., Schmechtig, C., and Coman, A. (2011). An ensemble assessment of regional ozone model uncertainty with an explicit error representation. *Atmospheric Environment*, 45(3):784 – 793.

Buizza, R. (2019). Introduction to the special issue on. *Quarterly Journal of the Royal Meteorological Society*, 145(S1):1–11.

Buizza, R., Houtekamer, P., Toth, Z., Pellerin, G., Wei, M., and Zhu, Y. (2005). A comparison of the ecmwf, msc, and ncep global ensemble prediction systems. *Monthly Weather Review*, 133.

Buizza, R., Milleer, M., and Palmer, T. N. (1999). Stochastic representation of model uncertainties in the ecmwf ensemble prediction system. *Quarterly Journal of the Royal Meteorological Society*, 125(560):2887–2908.

Buizza, R., Tribbia, J., Molteni, F., and Palmer, T. (1993). Computation of optimal unstable structures for a numerical weather prediction model. *Tellus A*, 45(5):388–407.

Candiani, G., Carnevale, C., Finzi, G., Pisoni, E., and Volta, M. (2013). A comparison of reanalysis techniques: Applying optimal interpolation and ensemble kalman filtering to improve air quality monitoring at mesoscale. *Science of The Total Environment*, 458-460:7 – 14.

Caplan, P., Derber, J., Gemmill, W., Hong, S.-Y., Pan, H.-L., and Parrish, D. (1997). Changes to the 1995 ncep operational medium-range forecast model analysis forecast system. *Weather and Forecasting - WEATHER FORECAST*, 12:581–594.

Carslaw, N., Bell, N., Lewis, A., McQuaid, J., and Pilling, M. (2000). A detailed case study of isoprene chemistry during the ease96 mace head campaign. *Atmospheric Environment*, 34(18):2827 – 2836.

Chen, F. and Dudhia, J. (2001). Coupling an advanced land surface–hydrology model with the penn state–ncar mm5 modeling system. part i: Model implementation and sensitivity. *Monthly Weather Review*, 129(4):569–585.

Daley, R. (1993). *Atmospheric Data Analysis*. Cambridge Atmospheric and Space Science Series. Cambridge University Press.

Deardorff, J. W. (1978). Efficient prediction of ground surface temperature and moisture, with inclusion of a layer of vegetation. *Journal of Geophysical Research: Oceans*, 83(C4):1889–1903.

Drusch, M., Bello, U. D., Carlier, S., Colin, O., Fernandez, V., Gascon, F., Hoersch, B., Isola, C., Laberinti, P., Martimort, P., Meygret, A., Spoto, F., Sy, O., Marchese, F., and Bargellini, P. (2012). Sentinel-2: Esa's optical high-resolution mission for

gmes operational services. *Remote Sensing of Environment*, 120:25 – 36. The Sentinel Missions - New Opportunities for Science.

Eder, B., Kang, D., Mathur, R., Yu, S., and Schere, K. (2006). An operational evaluation of the eta–cmaq air quality forecast model. *Atmospheric Environment*, 40:4894–4905.

Ehrendorfer, M. (2006). *The Liouville equation and atmospheric predictability*, pages 59–98. Cambridge University Press.

Elbern, H., Strunk, A., Schmidt, H., and Talagrand, O. (2007). Emission rate and chemical state estimation by 4-dimensional variational inversion. *Atmospheric Chemistry and Physics*, 7(14):3749–3769.

Emili, E., Gürol, S., and Cariolle, D. (2016). Accounting for model error in air quality forecasts: an application of 4denvar to the assimilation of atmospheric composition using qg-chem 1.0. *Geoscientific Model Development*, 9:3933–3959.

Epstein, E. S. (1969). Stochastic dynamic prediction1. *Tellus*, 21(6):739–759.

Finardi, S., Silibello, C., D'Allura, A., and Radice, P. (2014). Analysis of pollutants exchange between the po valley and the surrounding european region. *Urban Climate*, 10:682 – 702. Source apportionment and modelling of urban air pollution.

Franke, P. (2018). *Quantitative estimation of unexpected emissions in the atmosphere by stochastic inversion techniques*. PhD thesis, University of Cologne (Germany).

Friedl, M., McIver, D., Hodges, J., Zhang, X., Muchoney, D., Strahler, A., Woodcock, C., Gopal, S., Schneider, A., Cooper, A., Baccini, A., Gao, F., and Schaaf, C. (2002). Global land cover mapping from modis: algorithms and early results. *Remote Sensing of Environment*, 83(1):287 – 302. The Moderate Resolution Imaging Spectroradiometer (MODIS): a new generation of Land Surface Monitoring.

Fuentes, J. D., Lerdau, M., Atkinson, R., Baldocchi, D., Bottenheim, J. W., Ciccioli, P., Lamb, B., Geron, C., Gu, L., Guenther, A., Sharkey, T. D., and Stockwell, W. (2000). Biogenic hydrocarbons in the atmospheric boundary layer: A review. *Bulletin of the American Meteorological Society*, 81(7):1537–1576.

Galin, M. B. (2007). Study of the low-frequency variability of the atmospheric general circulation with the use of time-dependent empirical orthogonal functions. *Atmospheric and Oceanic Physics*, 43(1):15–23.

Garratt, J. (1994). Review: the atmospheric boundary layer. *Earth-Science Reviews*, 37(1):89 – 134.

Gaubert, B., Coman, A., Foret, G., Meleux, F., Ung, A., Rouil, L., Ionescu, A., Candau, Y., and Beekmann, M. (2014). Regional scale ozone data assimilation using an ensemble kalman filter and the chimere chemical transport model. *Geoscientific Model Development*, 7(1):283–302.

Geiger, H., Barnes, I., Bejan, I., Benter, T., and Spittler, M. (2003). The tropospheric degradation of isoprene: An updated module for the regional atmospheric chemistry mechanism. *Atmospheric Environment*, 37:1503–1519.

Geng, F., Tie, X., Guenther, A., Li, G., Cao, J., and Harley, P. (2011). Effect of isoprene emissions from major forests on ozone formation in the city of shanghai, china. *Atmospheric Chemistry and Physics*, 11(20):10449–10459.

Georgiou, G. K., Christoudias, T., Proestos, Y., Kushta, J., Hadjinicolaou, P., and Lelieveld, J. (2018). Air quality modelling in the summer over the eastern Mediterranean using WRF-Chem: chemistry and aerosol mechanism intercomparison. *Atmospheric Chemistry and Physics*, 18(3):1555–1571.

Gilliam, R. C. and Pleim, J. E. (2010). Performance assessment of new land surface and planetary boundary layer physics in the wrf-arw. *Journal of Applied Meteorology and Climatology*, 49(4):760–774.

Goldstein, A. H. and Galbally, I. E. (2007). Known and unexplored organic constituents in the earth's atmosphere. *Environmental Science & Technology*, 41(5):1514–1521.

Guenther, A. (2011). Megan2.1 code. URL: *lar.wsu.edu/megan/docs/MEGANv*2.10*_beta.tar.gz* (accessed: 2018-07-09).

Guenther, A., Karl, T., Harley, P., Wiedinmyer, C., Palmer, P. I., and Geron, C. (2006). Estimates of global terrestrial isoprene emissions using megan (model of emissions of gases and aerosols from nature). *Atmospheric Chemistry and Physics*, 6(11):3181–3210.

Guenther, A. B., Jiang, X., Heald, C. L., Sakulyanontvittaya, T., Duhl, T., Emmons, L. K., and Wang, X. (2012). The model of emissions of gases and aerosols from nature version 2.1 (megan2.1): an extended and updated framework for modeling biogenic emissions. *Geoscientific Model Development*, 5(6):1471–1492.

Hanna, S., Russell, A., Wilkinson, J., Vukovich, J., and Hansen, D. (2005). Monte Carlo estimation of uncertainties in BEIS3 emission outputs and their effects on uncertainties in chemical transport model predictions. *Journal of Geophysical Research: Atmospheres*, 110(D1).

Hanna, S. R., Chang, J. C., and Fernau, M. E. (1998). Monte carlo estimates of uncertainties in predictions by a photochemical grid model (uam-iv) due to uncertainties in input variables. *Atmospheric Environment*, 32(21):3619 – 3628.

Hansen, M. C., DeFries, R. S., Townshend, J. R. G., Sohlberg, R., Dimiceli, C., and Carroll, M. (2002). Towards an operational modis continuous field of percent tree cover algorithm: examples using avhrr and modis data. *Remote Sensing of Environment*, 83:303–319.

Hass, H., Jakobs, H. J., and Memmesheimer, M. (1995). Analysis of a regional model (eurad) near surface gas concentration predictions using observations from networks. *Meteorology and Atmospheric Physics*, 57(1):173–200.

Henrot, A.-J., Stanelle, T., Schroeder, S., Siegenthaler, C., Taraborrelli, D., and Schultz, M. G. (2017). Implementation of the MEGAN (v2.1) biogenic emission model in the ECHAM6-HAMMOZ chemistry climate model. *Geoscientific Model Development*, 10(2):903–926.

Hess, G. D., Tory, K. J., Cope, M. E., Lee, S., Puri, K., Manins, P. C., and Young, M. (2004). The australian air quality forecasting system. part ii: Case study of a sydney 7-day photochemical smog event. *Journal of Applied Meteorology*, 43(5):663–679.

Hoffman, R. N. and Kalnay, E. (1983). Lagged average forecasting, an alternative to monte carlo forecasting. *Tellus A*, 35A(2):100–118.

Hong, S.-Y., Noh, Y., and Dudhia, J. (2006). A new vertical diffusion package with an explicit treatment of entrainment processes. *Monthly Weather Review - MON WEATHER REV*, 134.

Hortal, M. (1998). *Formulation of the ECMWF Forecast Model*, pages 237–251. Springer Netherlands, Dordrecht.

Hotelling, H. (1933). Analysis of a complex of statistical variables into principal components. *Journal of Educational Psychology*, 24:417–441, 498–5204.

Houtekamer, P. L., Lefaivre, L., Derome, J., Ritchie, H., and Mitchell, H. L. (1996). A system simulation approach to ensemble prediction. *Monthly Weather Review*, 124(6):1225–1242.

Hu, X., Nielsen-Gammon, J., and Zhang, F. (2010). Evaluation of three planetary boundary layer schemes in the wrf model. *Journal of Applied Meteorology and Climatology*, 49(9):1831–1844.

Hunt, B. R., Kostelich, E. J., and Szunyogh, I. (2007). Efficient data assimilation for spatiotemporal chaos: A local ensemble transform kalman filter. *Physica D: Nonlinear Phenomena*, 230(1):112 – 126. Data Assimilation.

Immitzer, M., Vuolo, F., and Atzberger, C. (2016). First Experience with Sentinel-2 Data for Crop and Tree Species Classifications in Central Europe. *Remote Sensing*, 8(3).

Israelevich, P., Ganor, E., Alpert, P., Kishcha, P., and Stupp, A. (2012). Predominant transport paths of saharan dust over the mediterranean sea to europe. *Journal of Geophysical Research: Atmospheres*, 117(D2).

Jäger, J. (2013). *Airborne VOC Measurements on board the Zeppelin NT during the PEGASOS campaigns in 2012 deploying the improved Fast-GC-MSD System.* PhD thesis, University of Cologne (Germany).

Jakobs, H., Feldmann, H., Hass, H., and Memmesheimer, M. (1995). The use of nested models for air pollution studies: An application of the eurad model to a sana episode. *Journal of Applied Meteorology - J APPL METEOROL*, 34:1301–1319.

Janjic, Z. I. (1994). The step-mountain eta coordinate model: Further developments of the convection, viscous sublayer, and turbulence closure schemes. *Monthly Weather Review*, 122(5):927–945.

Janjic, Z. I. (1996). The mellor-yamada level 2.5 scheme in the ncep eta model. *11th Conference on Numerical Weather Prediction, American Meteorological Society*, page 333.334.

Janjic, Z. I. (2001). Nonsingular implementation of the mellor-yamada level 2.5 scheme in the ncep meso model. *Office note (National Centers for Environmental Prediction (U.S.))*, 437.

Jülich Supercomputing Centre (2018). JURECA: Modular supercomputer at Jülich Supercomputing Centre. *Journal of large-scale research facilities*, 4(A132).

Kaiser, J., Wolfe, G. M., Bohn, B., Broch, S., Fuchs, H., Ganzeveld, L. N., Gomm, S., Haeseler, R., Hofzumahaus, A., Holland, F., Jaeger, J., Li, X., Lohse, I., Lu, K., Prevot, A. S. H., Rohrer, F., Wegener, R., Wolf, R., Mentel, T. F., Kiendler-Scharr, A., Wahner, A., and Keutsch, F. N. (2015). Evidence for an unidentified non-photochemical ground-level source of formaldehyde in the Po Valley with potential implications for ozone production. *Atmospheric Chemistry and Physics*, 15(3):1289–1298.

Kalnay, E. (2003). *Atmospheric Modeling, Data Assimilation and Predictability*. Cambridge University Press.

Kalnay, E. (2019). Historical perspective: earlier ensembles and forecasting forecast skill. *Quarterly Journal of the Royal Meteorological Society*, 145(S1):25–34.

Karhunen, K. (1947). über lineare methoden in der wahrscheinlichkeitsrechnung. *Annales Academiae Scientarum Fennicae*, 37:3–79.

Kontkanen, J., Järvinen, E., Manninen, H. E., Lehtipalo, K., Kangasluoma, J., Decesari, S., Gobbi, G. P., Laaksonen, A., Petäjä, T., and Kulmala, M. (2016). High concentrations of sub-3nm clusters and frequent new particle formation observed in the po valley, italy, during the pegasos 2012 campaign. *Atmospheric Chemistry & Physics*, 16:1919–1935.

Kuenen, J. J. P., Visschedijk, A. J. H., Jozwicka, M., and Denier van der Gon, H. A. C. (2014). Tno-macc_ii emission inventory; a multi-year (2003-2009) consistent high-resolution european emission inventory for air quality modelling. *Atmospheric Chemistry and Physics*, 14(20):10963–10976.

Lahoz, W. A. and Schneider, P. (2014). Data assimilation: making sense of earth observation. *Frontiers in Environmental Science*, 2:16.

Lamarque, J.-F., Bond, T. C., Eyring, V., Granier, C., Heil, A., Klimont, Z., Lee, D., Liousse, C., Mieville, A., Owen, B., Schultz, M. G., Shindell, D., Smith, S. J., Stehfest, E., Van Aardenne, J., Cooper, O. R., Kainuma, M., Mahowald, N., McConnell, J. R.,

Naik, V., Riahi, K., and van Vuuren, D. P. (2010). Historical (1850 - 2000) gridded anthropogenic and biomass burning emissions of reactive gases and aerosols: methodology and application. *Atmospheric Chemistry and Physics*, 10(15):7017–7039.

Lamb, B., Guenther, A., Gay, D., and Westberg, H. (1987). A national inventory of biogenic hydrocarbon emissions. *Atmospheric Environment (1967)*, 21(8):1695 – 1705.

Lavoir, A.-V., Staudt, M., Schnitzler, J. P., Landais, D., Massol, F., Rocheteau, A., Rodriguez, R., Zimmer, I., and Rambal, S. (2009). Drought reduced monoterpene emissions from the evergreen mediterranean oak quercus ilex: results from a throughfall displacement experiment. *Biogeosciences*, 6(7):1167–1180.

Lehoucq, R. B. and Sorensen, D. C. (1996). Deflation techniques for an implicitly restarted arnoldi iteration. *SIAM Journal on Matrix Analysis and Applications*, 17(4):789–821.

Lehoucq, R. B., Sorensen, D. C., and Yang, C. (1997). Arpack users guide: Solution of large scale eigenvalue problems by implicitly restarted arnoldi methods.

Leith, C. E. (1974). Theoretical skill of monte carlo forecasts. *Monthly Weather Review*, 102(6):409–418.

Leutbecher, M., Lock, S.-J., Ollinaho, P., Lang, S. T. K., Balsamo, G., Bechtold, P., Bonavita, M., Christensen, H. M., Diamantakis, M., Dutra, E., English, S., Fisher, M., Forbes, R. M., Goddard, J., Haiden, T., Hogan, R. J., Juricke, S., Lawrence, H., MacLeod, D., Magnusson, L., Malardel, S., Massart, S., Sandu, I., Smolarkiewicz, P. K., Subramanian, A., Vitart, F., Wedi, N., and Weisheimer, A. (2017). Stochastic representations of model uncertainties at ecmwf: state of the art and future vision. *Quarterly Journal of the Royal Meteorological Society*, 143(707):2315–2339.

Li, X., Rohrer, F., Hofzumahaus, A., Brauers, T., Häseler, R., Bohn, B., Broch, S., Fuchs, H., Gomm, S., Holland, F., Jäger, J., Kaiser, J., Keutsch, F. N., Lohse, I., Lu, K., Tillmann, R., Wegener, R., Wolfe, G. M., Mentel, T. F., Kiendler-Scharr, A., and Wahner, A. (2014). Missing gas-phase source of hono inferred from zeppelin measurements in the troposphere. *Science*, 344(6181):292–296.

Liu, D. C. and Nocedal, J. (1989). On the limited memory bfgs method for large scale optimization. *Mathematical Programming*, 45(1):503–528.

Lock, S.-J., Lang, S. T. K., Leutbecher, M., Hogan, R. J., and Vitart, F. (2019). Treatment of model uncertainty from radiation by the stochastically perturbed parametrization tendencies (sppt) scheme and associated revisions in the ecmwf ensembles. *Quarterly Journal of the Royal Meteorological Society*, 145(S1):75–89.

Loéve, M. (1948). Fonctions aleatoires du second ordre. *Processus Stochastiques et Mouvement Brownien*, 42e éd.

Lorenz, E. N. (1963). Deterministic nonperiodic flow. *Journal of the Atmospheric Sciences*, 20(2):130–141.

Loveland, T. R., Reed, B. C., Brown, J. F., Ohlen, D. O., Zhu, Z., Yang, L., and Merchant, J. W. (2000). Development of a global land cover characteristics database and igbp discover from 1 km avhrr data. *International Journal of Remote Sensing*, 21(6-7):1303–1330.

MacVean, M. K. (1983). The effects of horizontal diffusion on baroclinic development in a spectral model. *Quarterly Journal of the Royal Meteorological Society*, 109:771–783.

McKeen, S., Chung, S. H., Wilczak, J., Grell, G., Djalalova, I., Peckham, S., Gong, W., Bouchet, V., Moffet, R., Tang, Y., Carmichael, G. R., Mathur, R., and Yu, S. (2007). Evaluation of several pm2.5 forecast models using data collected during the icartt/neaqs 2004 field study. *Journal of Geophysical Research: Atmospheres*, 112(D10).

Mellor, G. L. and Yamada, T. (1982). Development of a turbulence closure model for geophysical fluid problems. *Reviews of Geophysics*, 20(4):851–875.

Memmesheimer, M., Tippke, J., Ebel, A., Hass, H., Jakobs, H. J., and Laube, M. (1991). On the use of emep emission inventories for europeanscale air pollution modelling with the eurad model. In Pankrath, J., editor, *Proceedings of the EMEP workshop on photooxidant modelling for long range transport in relation to abatement strategies*, pages 307–324. UBA.

Monin, A. and Obukhov, A. (1954). Basic laws of turbulent mixing in the atmosphere near the ground. *Tr. Akad. Nauk SSSR Geofiz. Inst*, 24(151):163–187.

Nakanishi, M. and Niino, H. (2006). An improved mellor–yamada level-3 model: Its numerical stability and application to a regional prediction of advection fog. *Boundary-Layer Meteorology*, 119(2):397–407.

Palmer, T. (2019). The ecmwf ensemble prediction system: Looking back (more than) 25 years and projecting forward 25 years. *Quarterly Journal of the Royal Meteorological Society*, 145(S1):12–24.

Pegoraro, E., Rey, A., Greenberg, J., Harley, P., Grace, J., Malhi, Y., and Guenther, A. (2004). Effect of drought on isoprene emission rates from leaves of quercus virginiana mill. *Atmospheric Environment*, 38(36):6149 – 6156.

Pernigotti, D., Georgieva, E., Thunis, P., and Bessagnet, B. (2012). Impact of meteorology on air quality modeling over the po valley in northern italy. *Atmospheric Environment*, 51:303 – 310.

Pleim, J. E. (2007). A combined local and nonlocal closure model for the atmospheric boundary layer. part ii: Application and evaluation in a mesoscale meteorological model. *Journal of Applied Meteorology and Climatology*, 46(9):1396–1409.

Pleim, J. E., Chang, J. S., and Zhang, K. (1991). A nested grid mesoscale atmospheric chemistry model. *Journal of Geophysical Research: Atmospheres*, 96(D2):3065–3084.

Pleim, J. E. and Xiu, A. (1995). Development and testing of a surface flux and planetary boundary layer model for application in mesoscale models. *Journal of Applied Meteorology*, 34(1):16–32.

Poincaré, H. (1914). *Science and Method*. T. Nelson, London.

Pöschl, U., Kuhlmann, R., Poisson, N., and Crutzen, P. (2000). Development and intercomparison of condensed isoprene oxidation mechanisms for global atmospheric modeling. *Journal of Atmospheric Chemistry*, 37:29–52.

Rosati, B., Gysel, M., Rubach, F., Mentel, T. F., Goger, B., Poulain, L., Schlag, P., Miettinen, P., Pajunoja, A., Virtanen, A., Baltink, H. K., Henzing, J. S. B., Gross, J., Gobbi, G. P., Wiedensohler, A., Kiendler-Scharr, A., Decesari, S., Facchini, M. C., Weingartner, E., and Baltensperger, U. (2016a). Vertical profiling of aerosol hygroscopic properties in the planetary boundary layer during the PEGASOS campaigns. *Atmospheric Chemistry and Physics*, 16(11):7295–7315.

Rosati, B., Herrmann, E., Bucci, S., Fierli, F., Cairo, F., Gysel, M., Tillmann, R., Groess, J., Gobbi, G. P., Di Liberto, L., Di Donfrancesco, G., Wiedensohler, A., Weingartner, E., Virtanen, A., Mentel, T. F., and Baltensperger, U. (2016b). Studying the vertical aerosol extinction coefficient by comparing in situ airborne data and elastic backscatter lidar. *Atmospheric Chemistry and Physics*, 16(7):4539–4554.

Sandrini, S., van Pinxteren, D., Giulianelli, L., Herrmann, H., Poulain, L., Facchini, M. C., Gilardoni, S., Rinaldi, M., Paglione, M., Turpin, B. J., Pollini, F., Bucci, S., Zanca, N., and Decesari, S. (2016). Size-resolved aerosol composition at an urban and a rural site in the po valley in summertime: implications for secondary aerosol formation. *Atmospheric Chemistry and Physics*, 16(17):10879–10897.

Sandu, A. and Chai, T. (2011). Chemical data assimilation—an overview. *Atmosphere*, 2(3):426–463.

Sandu, A., Constantinescu, E. M., Liao, W., Carmichael, G. R., Chai, T., Seinfeld, J. H., and Dăescu, D. (2005). Ensemble–based data assimilation for atmospheric chemical transport models. In Sunderam, V. S., van Albada, G. D., Sloot, P. M. A., and Dongarra, J. J., editors, *Computational Science – ICCS 2005*, pages 648–655, Berlin, Heidelberg. Springer Berlin Heidelberg.

Schutgens, N. A. J., Miyoshi, T., Takemura, T., and Nakajima, T. (2010). Applying an ensemble kalman filter to the assimilation of aeronet observations in a global aerosol transport model. *Atmospheric Chemistry and Physics*, 10(5):2561–2576.

Schwab, C. and Todor, R. A. (2006). Karhunen-loève approximation of random fields by generalized fast multipole methods. *J. Comput. Phys.*, 217(1):100–122.

Shrivastava, M., Cappa, C. D., Fan, J., Goldstein, A. H., Guenther, A. B., Jimenez, J. L., Kuang, C., Laskin, A., Martin, S. T., Ng, N. L., Petaja, T., Pierce, J. R., Rasch, P. J., Roldin, P., Seinfeld, J. H., Shilling, J., Smith, J. N., Thornton, J. A., Volkamer, R.,

Wang, J., Worsnop, D. R., Zaveri, R. A., Zelenyuk, A., and Zhang, Q. (2017). Recent advances in understanding secondary organic aerosol: Implications for global climate forcing. *Reviews of Geophysics*, 55(2):509–559.

Shutts, G. (2005). A kinetic energy backscatter algorithm for use in ensemble prediction systems. *Quarterly Journal of the Royal Meteorological Society*, 131(612):3079–3102.

Skamarock, W. C., Klemp, J. B., Dudhia, J., Gill, D. O., Barker, D. M., Duda, M. G., Huang, X.-Y., Wang, W., and Powers, J. G. (2008). A description of the advanced research wrf version 3. *NCAR technical note*.

Smirnova, T. G., Brown, J. M., Benjamin, S. G., and Kenyon, J. S. (2016). Modifications to the Rapid Update Cycle Land Surface Model (RUC LSM) Available in the Weather Research and Forecasting (WRF) Model. *Monthly Weather Review*, 144(5):1851–1865.

Sogacheva, L., Hamed, A., Facchini, M. C., Kulmala, M., and Laaksonen, A. (2007). Relation of air mass history to nucleation events in Po Valley, Italy, using back trajectories analysis. *Atmospheric Chemistry and Physics*, 7:839–853.

Sorensen, D. (1997). Implicitly restarted arnoldi/lanczos methods for large scale eigenvalue calculations. In Keyes, D., Sameh, A., and V, V., editors, *Parallel Numerical Algorithms. ICASE/LaRC Interdisciplinary Series in Science and Engineering*, volume vol 4. Springer, Dordrecht.

Stockwell, W. R., Kirchner, F., Kuhn, M., and Seefeld, S. (1997). A new mechanism for regional atmospheric chemistry modeling. *Journal of Geophysical Research: Atmospheres*, 102(D22):25847–25879.

Stull, R. (1988). *An Introduction to Boundary Layer Meteorology*. Atmospheric and Oceanographic Sciences Library. Springer Netherlands.

Thompson, P. D. (1957). Uncertainty of initial state as a factor in the predictability of large scale atmospheric flow patterns. *Tellus*, 9(3):275–295.

Toth, Z. and Kalnay, E. (1993). Ensemble forecasting at nmc: The generation of perturbations. *Bulletin of the american meteorological society*, 74(12):2317–2330.

Vautard, R., Blond, N., Schmidt, H., Derognat, C., and Beekmann, M. (2001). Multimodel ensemble ozone forecasts over europe: analysis of uncertainty. *Mesoscale Transport of Air Pollution. OA15. EGS XXXVI General Assembly. European Geophysical Society, Nice, France. Katlenburg-Lindau, Germany*, 26.

Vogel, A., Ungermann, J., and Elbern, H. (2020). Analyzing highly uncertain source regions in the ex-utls and their effects on small-scale atmospheric composition using probabilistic retroplume calculations. *Atmospheric Environment*, 220:117063.

Walcek, C. J. (2000). Minor flux adjustment near mixing ratio extremes for simplified yet highly accurate monotonic calculation of tracer advection. *Journal of Geophysical Research: Atmospheres*, 105(D7):9335–9348.

Wang, L. (2008). *Karhunen-Loeve expansions and their applications.* PhD thesis, London School of Economics and Political Science (United Kingdom).

Wang, P., Schade, G., Estes, M., and Ying, Q. (2017). Improved megan predictions of biogenic isoprene in the contiguous united states. *Atmospheric Environment*, 148:337 – 351.

Wesely, M. (1989). Parameterization of surface resistances to gaseous dry deposition in regional-scale numerical models. *Atmospheric Environment (1967)*, 23(6):1293 – 1304.

Wesely, M. and Hicks, B. (2000). A review of the current status of knowledge on dry deposition. *Atmospheric Environment*, 34(12):2261 – 2282.

Wesely, M. L., Doskey, P. V., and Shannon, J. D. (2002). Deposition parameterizations for the industrial source complex (isc3) model.

Wu, C., Pullinen, I., Andres, S., Carriero, G., Fares, S., Goldbach, H., Hacker, L., Kasal, T., Kiendler-Scharr, A., Kleist, E., Paoletti, E., Wahner, A., Wildt, J., and Mentel, T. F. (2015). Impacts of soil moisture on de novo monoterpene emissions from european beech, holm oak, scots pine, and norway spruce. *Biogeosciences*, 12(1):177–191.

Xian, P., Reid, J. S., Hyer, E. J., Sampson, C. R., Rubin, J. I., Ades, M., Asencio, N., Basart, S., Benedetti, A., Bhattacharjee, P. S., Brooks, M. E., Colarco, P. R., da Silva, A. M., Eck, T. F., Guth, J., Jorba, O., Kouznetsov, R., Kipling, Z., Sofiev, M., Perez Garcia-Pando, C., Pradhan, Y., Tanaka, T., Wang, J., Westphal, D. L., Yumimoto, K., and Zhang, J. (2019). Current state of the global operational aerosol multi-model ensemble: An update from the international cooperative for aerosol prediction (icap). *Quarterly Journal of the Royal Meteorological Society*, 145(S1):176–209.

Xiu, A. and Pleim, J. E. (2001). Development of a land surface model. part i: Application in a mesoscale meteorological model. *Journal of Applied Meteorology*, 40(2):192–209.

Xiu, D. (2010). *Numerical Methods for Stochastic Computations: A Spectral Method Approach*. Princeton University Press, Princeton, NJ, USA.

Yanenko, N. N. (1071). *The Method of Fractional Steps*. Springer, New York, NJ, USA.

Yang, B., Qian, Y., Berg, L. K., Ma, P. L., Wharton, S., Bulaevskaya, V., Yan, H., Hou, Z., and Shaw, W. J. (2016). Sensitivity of turbine-height wind speeds to parameters in planetary boundary-layer and surface-layer schemes in the weather research and forecasting model. *Boundary-Layer Meteorology*, 162(1).

Zhang, L., Brook, J. R., and Vet, R. (2003). A revised parameterization for gaseous dry deposition in air-quality models. *Atmospheric Chemistry and Physics*, 3(6):2067–2082.

Zhang, L., Moran, M. D., Makar, P. A., Brook, J. R., and Gong, S. (2002). Modelling gaseous dry deposition in aurams: a unified regional air-quality modelling system. *Atmospheric Environment*, 36(3):537 – 560. Seventh Internatioonal Conference on Atmospheric Science and Applications to Air Quality (ASAAQ).

Zhang, Y., Bocquet, M., Mallet, V., Seigneur, C., and Baklanov, A. (2012a). Real-time air quality forecasting, part i: History, techniques, and current status. *Atmospheric Environment*, 60:632 – 655.

Zhang, Y., Bocquet, M., Mallet, V., Seigneur, C., and Baklanov, A. (2012b). Real-time air quality forecasting, part ii: State of the science, current research needs, and future prospects. *Atmospheric Environment*, 60:656 – 676.

Zilitinkevich, S. (1995). Non-local turbulent transport pollution dispersion aspects of coherent structure of convective flows. *Air Pollution III, Air pollution theory and simulation (H Power, N Moussiopoulos, C A Brebbia, eds) Computational Mechanics Publ , Southampton, Boston*, 9:53–60.

Index

Acknowledgements

This work has been funded by the Helmholtz Climate Initiative REKLIM (Regional Climate Change), a joint research project of the Helmholtz Association of German research centers (HGF) under grant: REKLIM-2009-07-16.

The author gratefully acknowledges the computing time granted through JARA-HPC on the supercomputer JURECA Jülich Supercomputing Centre [2018] at Forschungszentrum Jülich.

Danksagung

In aller erster Linie möchte ich ganz herzlich meinem Doktorvater PD Dr. Hendrik Elbern für die langjährige Unterstützung und Betreuung dieser Arbeit bis zum letzten Tag danken. Durch vielfältige Diskussionen - aber auch die nötige Freiheit für eigene Ideen - habe ich in den letzen Jahren sehr viel gelernt und meinen Horizont auch über meine Arbeit hinaus erweitert.

Zudem danke ich herzlich Prof. Dr. Yaping Shao für sein reges Interesse, die Ko-Korrektur dieser Arbeit und das Enganement für zukünftige Perspektiven.

Stellvertretend für das Institut IEK-8 des Forschungszenrums Jülich danke ich Prof. Dr. Andreas Wahner und Prof. Dr. Astrid Kiendler-Scharr für die Bereitstellung der Beobachtungsdaten, sowie die Möglichkeit, diese Arbeit durchführen zu können und das wissenschaftliche Umfeld zu erweitern.

Desweiteren danke ich allen (ehemaligen) Mitarbeitern der EURAD-Gruppe des Rheinischen Instituts für Umweltforschung (RIU) an der Universität zu Köln für die produktive, angenehme und familiäre Arbeitsatmosphäre. Insbesondere danke ich Georg Piekorz für die große Hilfe bei IT Problemen, sowie Philipp Franke für die Unterstützung bei der technischen Ensemble Konfiguration und Jonas Berndt für diverse Diskussionen u.a. über Zufallsverteilungen.

Beim Institut für Geophysik und Meteorologie der Universität zu Köln für möchte ich mich für die Bereitstellung des Büros und die damit verbundene Integration in das Institutsleben bedanken.

Besonderer Dank geht auch an Birte Solveig Kulla, Cornelia von Krüchten, Frauke Tabertshofer, Lukas Pfitzenmaier und Philipp J. Griewank für die regelmäßigen Freizeitaktivitäten abseits der Arbeit, vor allem in den letzen Monaten.

Zu guter Letzt danke ich meiner gesamten Familie, sowie Mathias Richling ganz herzlich für die große Unterstützung und Rückendeckung auf verschiedenste Weise über die letzten Jahre. Besonderer Dank gilt zudem meinem Vater Karl Vogel für die ausgedehnten, mathematischen Disskusionen.

Zudem danke ich vor allem Hendrik Elbern, aber auch Cornelia von Krüchten, Frauke Tabertshofer, Anne Caroline Lange, Philipp Franke, Mathias Richling und Birte Solveig Kulla für die hilfreichen Hinweise und Korrekturen beim Erstellen dieser Arbeit.

Erklärung

Ich versichere, dass ich die von mir vorgelegte Dissertation selbständig angefertigt, die benutzten Quellen und Hilfsmittel vollständig angegeben und die Stellen der Arbeit – einschließlich Tabellen, Karten und Abbildungen –, die anderen Werken im Wortlaut oder dem Sinn nach entnommen sind, in jedem Einzelfall als Entlehnung kenntlich gemacht habe; dass diese Dissertation noch keiner anderen Fakultät oder Universität zur Prüfung vorgelegen hat; dass sie – abgesehen von unten angegebenen Teilpublikationen – noch nicht veröffentlicht worden ist, sowie, dass ich eine solche Veröffentlichung vor Abschluss des Promotionsverfahrens nicht vornehmen werde. Die Bestimmungen der Promotionsordnung sind mir bekannt. Die von mir vorgelegte Dissertation ist von PD Dr. Hendrik Elbern betreut worden.

Es liegen keine Teilpublikationen vor.

Annika Vogel